Semianalytical and Numerical Studies of Relativistic Heavy Ion Collisions

By

Todd Mendenhall

July, 2023

Director of Dissertation: Dr. Zi-Wei Lin

Department: Physics

Abstract

The quark-gluon plasma (QGP) has been produced by relativistic heavy ion collisions, and understanding its properties is a primary goal in the field of nuclear physics. This research first elucidates recent semianalytical developments that improve the estimates of the initial energy and net conserved-charge densities and enable the calculation of trajectories in the quantum chromodynamics (QCD) phase diagram for the matter produced by nuclear collisions. A semianalytical model of the initial densities is developed by including the finite nuclear thickness for parton production. The new maximum energy density is found to have an analytical upper bound and satisfy an approximate scaling relation. QCD phase diagram trajectories are extracted from the semianalytical densities using several nuclear equations of state, and the calculated QGP lifetimes are found to depend significantly on the values of the model's parameters. The study next presents a comparison between two solutions of the relativistic Boltzmann equation (RBE): one, a numerical solution using parton transport; the other, a theoretical solution for a homogeneous gas of massless particles. Parton transport in Zhang's parton cascade (ZPC) is found to reproduce the results of a recent exact analytical solution of the RBE with an unexpected effectiveness at high densities when using new generalized collision schemes. Finally, the work discusses some open questions related to parton transport in ZPC and suggests some possible directions to uncover their answers. These future research goals include discovering the cause of an unexpected problem

arising in simulations with three-dimensional (3D) expansion, understanding the theoretical distribution of the total center-of-mass (CM) energy squared for two-parton collisions, and studying curved parton motion in the presence of strong electromagnetic fields. Overall, the results presented in this dissertation improve the theoretical and numerical descriptions of the QGP and should be useful for future studies.

Semianalytical and Numerical Studies of Relativistic Heavy Ion Collisions

A Dissertation

Presented to the Faculty of the Department of Physics

East Carolina University

In Partial Fulfillment of the Requirements for the Degree

Doctor of Philosophy, Biomedical Physics

By

Todd Mendenhall

July, 2023

Director of Dissertation: Zi-Wei Lin, PhD

Dissertation Committee Members:

Martin Bier, PhD

Michael Dingfelder, PhD

Guglielmo Fucci, PhD

Gregory Lapicki, PhD

ACKNOWLEDGEMENTS

First, I would like to thank my parents for the many sacrifices they have made in providing me with the opportunity to gain this tremendous education. They have always taught me to do my best and I could not have accomplished this undertaking without their constant support. Second, I would like to thank my wife for her encouragement and unshakable belief in my capacity to succeed, especially during these last few months. I am truly blessed to have found a partner who shares my passion for discovery, and I look forward to being lifelong learners together. Third, I would like to thank my advisor for his guidance, patience, and respect; he has exemplified what it means to be a teacher-scholar, and I would be lucky one day to be half the scientist that he is today. Not only has he constantly challenged me to learn more difficult concepts and think more deeply, but he has also helped me see the beauty in studying physics while doing so. Fourth, I would like to thank my peers and close friends among the graduate students, including those who have already graduated, for the many happy memories we have made together on this journey. Finally, I would like to thank the entire faculty and staff of the physics department for a wonderful past six years; I know that their hard work teaching, advising, and organizing has helped me grow as a student, a teacher, and a researcher. I am thankful to have been a part of this program and could not have hoped for a better experience pursuing my graduate education.

This work has been supported by the National Science Foundation under Grant No. 2012947.

Table of Contents

List of Tables

List of Figures

List of Symbols

c	Speed of light in a vacuum
$\hbar$	Reduced Planck constant
k_B	Boltzmann's constant
m_{N}	Nucleon mass
$\hat{s}$	Mandelstam s variable
$\hat{t}$	Mandelstam t variable
$\hat{u}$	Mandelstam u variable
$\sqrt{s_{\mathrm{NN}}}$	Center-of-mass collision energy per nucleon pair
E_0	Threshold collision energy
τ_{F}	Parton proper formation time
y	Rapidity
η	Pseudorapidity
η_s	Spacetime-rapidity
ϵ	Energy density
n_{B}	Net-baryon density
n_{Q}	Net-electric charge density
n_{S}	Net-strangeness density
T	Temperature
μ_{B}	Net-baryon chemical potential
μ_{Q}	Net-electric charge chemical potential
μ_{S}	Net-strangeness chemical potential
P	Pressure
s	Entropy density
p	Momentum

p_{T}	Transverse momentum
p_z	Longitudinal momentum
μ	Debye screening mass
χ	Opacity
σ	Cross section
λ	Fugacity
t_c	Collision time

Chapter 1

Introduction to Relativistic Heavy Ion Collisions

1.1 The Quark-Gluon Plasma and Experimental Observables

Relativistic heavy ion collisions have been used to create the new phase of matter called the quark-gluon plasma (QGP) [1, 2, 3]. From experiments at the Relativistic Heavy Ion Collider (RHIC) at Brookhaven National Laboratory (BNL) to the Large Hadron Collider (LHC) at the European Organization for Nuclear Research (CERN), studying the properties of the QGP is currently a primary goal in the field of nuclear physics [4, 5, 6, 7, 8]. Besides the many experimental successes in producing and measuring the QGP's properties, there have also been numerous advancements in the field's theoretical understanding [9] using tools such as hydrodynamical modelling [10], transport simulations [11], and lattice QCD calculations [12]. The body of knowledge related to the production of the QGP by nuclear collisions is constantly growing as new discoveries are made and novel works are produced. Therefore, the purpose of this research work is to study relativistic heavy ion collisions with semianalytical and numerical tools in order to produce useful results that will advance the field's understanding of the QGP. Experimentally, a plethora of observables may be used to characterize the hot, dense QCD matter produced during heavy ion collisions, and these may in general be separated into several distinct classes. For instance, one may classify a particular observable as being based on the properties of a single particle, a pair or small

group of particles, or of many particles. Importantly, the connections between these observables and the properties of the QGP, such as its equation of state (EoS) or shear and bulk viscosities, provide a rich groundwork on which theoretical and experimental research programs in nuclear physics are based.

When it comes to describing the thermodynamic properties of the QGP, perhaps the most useful tool is the QCD EoS [13]. In general, an EoS describes the relationship between thermodynamic variables like the temperature T, chemical potential μ, energy density ϵ, particle density n, or entropy density s and the pressure P. Final state observables such as the collective flow and final particle spectra depend on the specific form of the EoS because the QGP is subjected to large pressure gradients. Since the EoS determines the speed of sound $c_s = \sqrt{\partial P/\partial \epsilon}$ in the medium, it has a direct relationship to the experimental observables that depend on P. On the other hand, the shear viscosity η and its ratio η/s to the entropy density s, and the bulk viscosity ζ influence the transverse flow patterns of the partonic system. Notably, this ratio can be found for an anti-de Sitter/conformal field theory (Ads/CFT) that is dual to QCD, and its value suggests $\eta/s \geq \hbar/4\pi k_B$ for a QGP [14]. Here, $\hbar$ is the reduced Planck constant and k_B is the Boltzmann constant; they are written explicitly, but are commonly suppressed for the remainder of this research work since the choice of units in which $c = \hbar = k_B = 1$ is more natural. The unexpectedly small value of η/s for the QGP implies that it may be the most perfect fluid yet discovered; for reference, the same ratio for liquid helium is nearly an order of magnitude larger. While the hot QCD matter produced by heavy ion collisions may be the most perfect fluid, it would also be the tiniest fluid ever observed. If one approximated the volume of the QGP with the volume of a colliding nuclei, then the QGP would only take up $\approx 10^{-42}$ m^3. Thus, experimental observables are limited to those which depend on the partonic matters' momentum space variables only, since the produced fireball is so small and fleeting.

Some of the most commonly considered experimental observables include those that can be measured based on the properties of a single species of final state particles. Perhaps the

most basic analysis of heavy ion collisions one can perform is simply to count the number of produced particles of a certain species. This method commonly is limited to the region of momentum space in which the produced particles have a relatively small longitudinal (along the beam axis) momentum p_z. Normally, this is caused by the fact that a particle detector has a ring-like shape surrounding the beam pipe at its center, since other shapes would interfere with the paths the two nuclei must take to ensure successful collisions. Information about the conditions at chemical freezeout may be inferred by fitting the ratios of particle yields to a thermal model [15] in which all particle species are assumed to freeze out at the same temperature. Rapidity distributions such as the particle number per unit rapidity dN/dy are also commonly measured and their shape is related to the stopping power of the colliding nuclei [16]. Information about a particle's transverse momentum p_{T} can also be detected experimentally, which means that generating a histogram of dN/dp_{T} for detected particles typically is quite useful. Specifically, the measured dN/dp_{T} can be fit to a blast-wave model and an effective temperature, which is often referred to as the slope parameter, can be extracted [17].

One can also imagine proton-proton (p + p) collisions as A+A collisions with A = 1 and perform a similar analysis to obtain the transverse momentum spectrum of produced particles. Here, A refers to the nuclear mass number of a colliding nuclei in heavy ion collisions. The nuclear modification factor R_{AA} is defined as the ratio of dN/dp_{T} for A+A collisions normalized by the average number of binary nucleon-nucleon (NN) collisions to dN/dp_{T} for p + p collisions [18]. In A+A collisions, interactions between high-p_{T} final-state hadrons with the medium lead to $R_{\mathrm{AA}} < 1$ and is referred to as jet-quenching [19]. Another key feature of the QGP is the suppression of charmonia, or bound states of charm c and anti-charm $\bar{c}$ quarks like the J/ψ [20], due to the color screening. In fact with a mass of $m_c \approx 1.3$ GeV/c^2, which is far larger than the temperatures expected to be achieved during heavy ion collisions, charm and other heavy flavor production is not expected to follow the normal thermal models. The suppression of heavy quark flavors can be quantified by R_{AA},

whereas measuring the elliptic flow parameter v_2 of open heavy flavor mesons could reveal the mass dependence of the interactions with the QGP. For example, understanding how heavy flavor quarks thermalize is still an open question in heavy ion physics [21].

Another set of experimental observables that are measured in heavy ion collisions are those which depend on two or a few particles. This category of observable can be thought of as a probability measurement of detecting a particle with a certain property given that another particle with another (possibly the same) property has already been detected in the same event. One such theoretically tractable observable is the photon-hadron correlation in which a direct photon is the trigger particle; this measurement has established the importance of gluon g degrees of freedom at RHIC [2]. While the photon energy tightly constrains the energy of the original parton in a hard process, this observable is difficult to measure experimentally because of the contamination in the photon yield. Among the most numerous hadrons produced in heavy ion collisions are pions, and the π^0 undergoes the electromagnetic decay $\pi^0 \to \gamma + \gamma$ with a branching ratio of $\approx 99\%$. Furthermore, one can also imagine a charge asymmetry arising in the initial state of a heavy ion collision if the QCD vacuum fluctuations lead to an asymmetric production of up u and down d quarks with respect to the reaction plane. As the initial incoming nuclei and the subsequent nuclear remnants proceed along the beam (z-) axis, the spectator protons induce a strong magnetic field that could, in principle, separate those quarks with $Q_u = +2/3$ and $Q_d = -1/3$ and induce the chiral magnetic effect (CME) [22]. Unfortunately, this observable requires the detection of at least three particles and therefore has a large and unspecific background, which complicates the analysis of the experimental data.

Various correlations between particles could help us understand the underlying properties of the QGP. First, one may investigate correlations between two particles, called di-hadron correlations, in order to study jet energy loss in the medium. Experimentally, one can measure the difference in the azimuthal angle ϕ in the transverse plane of the trigger particle (typically chosen to have $p_{\mathrm{T}} > 5$ GeV/c) and an associated particle with a slightly lower

$p_{\mathrm{T}} > 3$ GeV/c in hard interactions for which perturbative QCD (pQCD) is valid. Since hard parton scatterings generally result in back-to-back final state particles in momentum space, one can define the near-side and far-side particles as corresponding to the high-p_{T} and lower-p_{T} particles, respectively [23]. The ratio of the far-side particle yield in A+A collisions to that in p + p collisions given a trigger particle is defined to be I_{AA}. By virtue of being a conditional measurement, I_{AA} may contain more detailed information about the in-medium energy loss. On the other hand, one may also measure correlations between one high-p_{T} and one low-p_{T} particle. The trigger particle will emerge from the medium earlier because it has a higher momentum and loses only a small fraction of its energy as it does so. Since it has a smaller momentum, the associated particle should undergo a larger modification by the QGP; these effects may be studied by calculating multi-particle correlations for several p_{T} ranges and differentially over the azimuthal ϕ and longitudinal (η-) phase space [24]. Here, η is the pseudorapidity of a particle and is related to its energy and longitudinal momentum p_z. Finally, one may also measure untriggered angular correlations in which there is no lower threshold for the p_{T} of detected hadrons. Studies of $d^2N/d\eta/d\phi$ have revealed a structure along the η-direction that is often called a ridge [25].

Another category of experimental observables is those that depend on many particles and which reflect the collective behavior of the entire system. The collective flow of particles may be the single most important observable in heavy ion collisions [1]; it is described by the Fourier components v_n of the azimuthal distribution of the final particles in the momentum space [26]. Elliptic flow, quantified by v_2, is a prominent flow parameter and originates from the transverse pressure gradients or particle interactions in non-central ($b > 0$) collisions. The impact parameter b is commonly used to describe the centrality of A+A collisions; it refers to the distance between the centers of the colliding nuclei in the transverse direction. Because the pressure gradients or particle interactions drive the elliptic flow, v_2 is highly sensitive to the QCD EoS and the shear viscosity of the medium. Therefore, the dependence of v_2 on the collision energy $\sqrt{s_{\mathrm{NN}}}$ could indicate that a transition from hadronic matter to

the QGP has occurred [27]. Note that $\sqrt{s} = \mathrm{A}\sqrt{s_{\mathrm{NN}}}$ refers to the Mandelstam variable s that quantifies the total energy of the two colliding nuclei. The anisotropy in the flow coefficients v_n is considered to be a key feature of the QGP formation, and it can be analyzed using numerical methods [28].

Noether's theorem states that for every symmetry there exists a corresponding conserved charge, but the varying initial conditions in heavy ion collisions mean that fluctuations in conserved charges should be measurable. The net baryon number B, the net electric charge Q, or the net strangeness S have event-by-event fluctuations that are excellent signals of the phase transition from hadronic to partonic states [29]. This is understandable since baryons have $B = 1$ and mesons have $B = 0$, while quarks carry $B = 1/3$ and gluons have $B = 0$. The case is similar for the other conserved charges so that event-by-event fluctuations will be quite different depending on whether a hadron gas or a QGP is formed. Additionally, one expects fluctuations in the mean of the transverse momentum distribution to indicate variations in the temperature since $\langle p_{\mathrm{T}} \rangle \propto T$. One can imagine temperature fluctuations to be the relics of quantum fluctuations in the initial state similarly to that of the cosmic microwave background. While these and other fluctuations are experimentally measurable, lattice QCD methods [12] allow one to calculate and predict how they should behave which provides an important link between the data and theory.

1.2 Early Models of the Initial Energy Density

One key variable for studying the QGP's properties is the energy density ϵ produced during heavy ion collisions because its time evolution and maximum value affect the trajectory of the event in the $T - \mu_{\mathrm{B}}$ plane of the QCD phase diagram [30, 31]. The location of the event trajectory relative to that of the conjectured critical endpoint (CEP) of the first order phase transition [32, 33] could significantly alter the experimental observables. Thus, a better understanding of the produced energy density will give insight into the event trajectory's

sensitivity to the CEP [32, 34] and could be critically important for the lower collision energies like those at the Beam Energy Scan (BES) program at RHIC [35, 36, 37, 38]. On the other hand, the spatial and temporal dependencies of the initial energy density is an essential input for hydrodynamic models which predict the subsequent evolution of the dense matter produced by relativistic heavy ion collisions [39, 40, 41]. Among the many methods one can utilize to estimate the initial produced energy density are one attributed to Bjorken [42] and a later extension [43].

The method of Bjorken takes the simple approach to estimate the initial energy density produced by central heavy ion collisions [42]. Note that central collisions refer to collisions in which the impact parameter b is zero. If one were to look along the beam (z-) axis, one would see that the circular cross sections of the two nuclei in the transverse plane are separated by some distance: this distance is the impact parameter b. Under the assumptions that partons are produced at $(z, t) = (0, 0)$ and do not interact with one another as they free-stream toward an observation time t, the Bjorken formula gives the time-dependence of the energy density ϵ as

$$\epsilon_{\mathrm{Bj}}(t) = \frac{1}{A_{\mathrm{T}}} \frac{1}{t} \frac{dE_{\mathrm{T}}}{dy}. \tag{1.1}$$

The full transverse overlap area of the two nuclei in central A+A collisions is $A_{\mathrm{T}} = \pi R_{\mathrm{A}}^2$ where R_{A} is the radius of a nucleus with mass number A. The transverse energy per unit rapidity at mid-rapidity ($y \approx 0$) dE_{T}/dy in Eq. (1.1) above is often taken from the experimental observable [44]. The transverse energy E_{T} of a parton is typically defined as $E_{\mathrm{T}}^2 = p_{\mathrm{T}}^2 + m^2$, where p_{T} is the momentum in the transverse plane and m is the mass, although other definitions may also be used [44]. Recall that the natural choice of units in which $c = \hbar = k_B = 1$ is used throughout this research work and is evident in the above definition of E_{T}. Whereas the A+A collision starts at $t = 0$, the Bjorken formula predicts a diverging ϵ as $t \to 0$. Thus, one must choose a finite initial time τ_{F}, which can be defined as the parton formation time, for Eq. (1.1). In the picture of the Bjorken energy density formula [42], partons are assumed to be non-interacting after they are produced and become on-shell

after $\tau_{\rm F}$.

In the derivation of Eq. (1.1), not only is it assumed that all the initial partons are produced at an instant ($t = 0$) in time, but they are also assumed to be produced at a single point ($z = 0$) along the beam axis [42]. In other words, the duration in time d_t of the nuclear crossing and the finite width of the overlap region in the z-direction are ignored. When the collision energy is large enough, such as for the highest RHIC energy of $\sqrt{s_{\rm NN}} = 200$ GeV, Eq. (1.1) is valid because the crossing time is given by $d_t = 2R_{\rm A}/\sinh(y_{\rm CM})$, which decreases as $\sqrt{s_{\rm NN}}$ increases. The duration time d_t defined here is for the hard sphere model of the nucleus which also has $R_{\rm A} = 1.12{\rm A}^{1/3}$ fm. Here, $y_{\rm CM}$ is the rapidity of the projectile nucleus in the CM frame. Furthermore, the Lorentz contraction of the relativistic nuclei causes the width of the overlap region also to decrease with increasing $\sqrt{s_{\rm NN}}$. Therefore, the duration time and the finite thickness of the overlap region may be neglected at high collision energies when the finite thickness is small compared to the typical $\tau_{\rm F}$ value, which means that Eq. (1.1) is valid in the high energy limit.

On the other hand, Eq. (1.1) breaks down [2] for lower collision energies where $d_t/\tau_{\rm F} \gtrsim 1$. For example, $d_t/\tau_{\rm F} \approx 0.5$ when using the typical estimation of the parton formation time of $\tau_{\rm F} = 1$ fm/c and occurs for central Au+Au collisions at $\sqrt{s_{\rm NN}} = 50$ GeV. Note that the above result used A = 197 for gold nuclei in the hard-sphere model. Thus, one expects the Bjorken energy density formula to become invalid when $\sqrt{s_{\rm NN}} \lesssim 50$ GeV for central Au+Au collisions [43, 45]. Additionally, the Bjorken energy density formula also neglects the effect of overlap volume's transverse expansion, which is known to occur even for the lower collision energies of the BES program at RHIC [37]. Finally, the slowing down of participant nucleons and secondary partonic and hadronic scatterings are neglected in Eq. (1.1). Nevertheless, the Bjorken energy density formula [42] still provides a useful estimation of the initial energy density averaged over the full transverse overlap area of a relativistic heavy ion collision because it is conveniently concise.

Given the limitations of the Eq. (1.1), a later study extended the Bjorken energy density

formula by considering the finite time duration d_t of the initial energy production [43]. In that work, the partons contribute to the energy density at mid-rapidity ($y \approx 0$) and are assumed to be produced at times $x \in [0, d_t]$, but also at $z = 0$. A relatively straightforward analysis of the total energy in a narrow volume at time t averaged over $A_{\rm T}$ yields the following expression for the initial energy density

$$\epsilon(t) = \frac{1}{A_{\rm T}} \int_0^{t-\tau_{\rm F}} \frac{d^2 E_{\rm T}}{dy\, dx} \frac{dx}{t-x}. \tag{1.2}$$

The obvious differences between this result [43] and that of Eq. (1.1) are the differential production of $E_{\rm T}$ over time and that this result is valid for times when the two nuclei are still crossing ($t \leq d_t + \tau_{\rm F}$). On the other hand, the Eq. (1.2) is similar to the Bjorken energy density formula in that it also has $\epsilon(t < \tau_{\rm F}) = 0$. In fact, Eq. (1.1) may be obtained from Eq. (1.2) using the substitution $d^2E_{\rm T}/dy/dx = \delta(x) dE_{\rm T}/dy$. Notably, this extension of the Bjorken energy density formula allows one to choose a specific time profile for the energy production [43].

For some relatively simple time profiles, Eq. (1.2) has analytical solutions that lend themselves to a straightforward comparison with the Bjorken energy density formula [43]. In the case of a uniform production of energy over time, the extension has a maximum energy density $\epsilon^{\rm max}$ that grows as $\ln(1/\tau_{\rm F})$ which is much slower than the $1/\tau_{\rm F}$ behavior of Eq. (1.1) for low collision energies [43]. This means that the updated estimate of the energy density is less sensitive to the uncertainty of the formation time; $\tau_{\rm F}$ is generally taken to have a value $\tau_{\rm F} \in [0.1, 1]$ fm/c. On the other hand, Eq. (1.2) diverges as $1/\tau_{\rm F}$ for higher $\sqrt{s_{\rm NN}}$ when $\tau_{\rm F}/d_t \gtrsim 1$ because its analytical result approaches the Bjorken formula there. Therefore, the recent extension [43] of the Bjorken formula significantly improves the estimation of the energy density produced by heavy ion collisions at low collision energies. In addition to the lower $\epsilon^{\rm max}$ values, Eq. (1.2) also has a much slower evolution in time of ϵ compared with the Bjorken formula if one considers the length in time when $\epsilon > \epsilon^{\rm max}/2$.

Because neither the Bjorken energy density formula [42] nor the recent extension [43] account for the finite longitudinal width along the beam (z-) direction for the initial energy production, one primary goal of this research is to develop a Bjorken-like formula for the initial energy production that accounts for the finite nuclear thickness. In Ch. 2, a semianalytical model is developed which includes both the finite duration time d_t and the finite z-width of the initial energy production. Initially, the same assumptions underlying Eqs. (1.1) - (1.2) are used [45], but later an implementation of transverse expansion is included to make the model more accurate [46]. The behavior of the newest semianalytical model is compared to the earlier results qualitatively and quantitatively, and several notable differences are discussed. After that follows a discussion of the results for extending the semianalytical model to calculate other net conserved-charge densities such as the net-baryon density n_{B}. Note that all of these models study the time evolution of the produced densities in the central spacetime-rapidity region ($\eta_s \approx 0$) in the CM frame for central A+A collisions, and the results are applied specifically to Au+Au collisions that are relevant to current experimental nuclear physics research [37, 47, 48]. Finally, recall that subsequent interactions among the produced particles are neglected for these models. Instead, the initial production is assumed to originate in the primary NN collisions between the participant nucleons of the projectile and target nuclei. However, the secondary interactions can be modeled by transport [49, 50] or hydrodynamic simulations [39, 40].

1.3 The QCD Phase Diagram and Critical Endpoint

Key experimental results from the RHIC and LHC, including the large nuclear suppression of jets and the patterns of collective flow, indicate that the QGP has indeed been formed by ultra-relativistic nuclear collisions [17, 51]. While normal nuclear matter has a number density around $\rho_0 \approx 0.17$ fm^{-3} at $T = 0$ and since the mass of a nucleon is $m_{\mathrm{N}} \approx 1$ GeV, the energy density of the strongly interacting medium has been shown to be around two orders of

magnitude larger than this. These large energy densities are well beyond the deconfinement transition near $T \approx 170$ MeV as calculated by lattice QCD simulations [12]. Quantum chromodynamics (QCD) is the fundamental theory of the Standard Model that describes the strong interactions between the quarks and gluons and is responsible for the structure of hadrons and also nuclei [51]. Because the underlying QCD gauge symmetry is non-Abelian, the strongly interacting quarks and gluons are typically confined inside hadrons; however, the large energy densities and temperatures achieved by heavy ion collisions promote the transition from bound hadronic states to deconfined partonic ones [1]. One can picture this transition as the melting of the protons and neutrons in the colliding nuclei into an exotic phase of matter: this is the QGP [1]. Because the QGP is a system of unbound quarks and gluons, it can only exist for a short time before the partons must recombine into hadrons because of the confinement in QCD. Therefore, experimentally studying the QGP is quite difficult, and its features must be inferred from the behavior of the final state hadrons.

Still though, learning about the QGP's properties would enable the testing of QCD as the fundamental theory governing the strong interaction [52]. Better understanding the QGP could also elucidate the early stages of the universe just after the Big Bang or on the nature of the matter that exists inside the cores of neutron stars. The field of nuclear physics is particularly interested in understanding the phase transition from hadronic to partonic matter in the QCD phase diagram [53] because lattice QCD results [54] show that it is a smooth crossover at vanishing baryon chemical potential ($\mu_{\mathrm{B}} = 0$), but calculations at finite μ_{B} are currently intractable [55]. Specifically, the (μ_{B}, T) location of the hypothesized CEP is of interest because its coordinates will help answer several deep questions about the nature of thermal QCD matter. For example, one may ask how the QGP's behavior becomes more gas-like or liquid like as μ_{B} changes at a given T. The answers to this and other questions motivate the BES program's search for the CEP at RHIC using Au+Au collisions at a variety of collision energies [47, 56, 57]. After averaging over many events, the matter created in a given collision system, which is to say at a given collision energy $\sqrt{s_{\mathrm{NN}}}$ and centrality b,

follows a unique trajectory and has a unique freezeout point in the QCD phase diagram [46]. One must consider the average over many events because of the large statistical fluctuations in the behavior of the formed matter. As the matter follows its event-averaged trajectory, one can imagine that the temperature T and baryon chemical potential μ_{B} have individual time evolutions, and that together they would determine the matter's history in the QCD phase diagram. When $\sqrt{s_{\mathrm{NN}}}$ reaches a certain value, the trajectory of the matter would pass near the CEP, and event-by-event fluctuations in certain conserved quantities could signify the existence of the CEP [58]. For example, analyzing the event-by-event net-proton cumulant ratios could be helpful in determining the location of the CEP.

The thermodynamic properties of the QGP are difficult to correlate directly with the experimental measurements because heavy ion collisions produce matter that progresses through several stages [46]. These stages can be thought of in terms of the semianalytical model of Ch. 2 as the overlapping stage in the beginning, the expansion stage at intermediate times, and the freezeout stage at late times [46]. Both hydrodynamic and transport models have been used to study the evolution of the thermodynamic properties of the QCD matter that is created by relativistic nuclear collisions [50, 59, 60, 61] On the other hand, the semi-analtyical models of the initial production have progressively improved the fields' analytical understanding of the early time evolution of the energy and net conserved-charge densities produced by heavy ion collisions [42, 43, 45]. In particular, the finite nuclear thickness of the initial production must be accounted for in any model because it drastically modifies the peak energy density $\epsilon^{\max}$ and the time evolution at low collision energies [45, 46]. Therefore, one expects the trajectories of the QCD matter to depend significantly on including the finite nuclear thickness effect, and the results of the BES program in particular should depend on this fact [46].

Recently, the string melting version of a multiphase transport (AMPT) model was used to study the temperature T and chemical potentials μ of a parton system using both Boltzmann and quantum statistics [61]. As its name suggests, the AMPT model describes the

matter formed in heavy ion collisions with different stages throughout the evolution [62]. Therefore, its purpose is to model the matter produced during relativistic nuclear collisions in a comprehensive and self-consistent manner. First, the heavy ion jet interaction generator (HIJING) [63] is used to generate the initial conditions of the partonic matter for a given collision system. Second, the partonic interactions are modelled by Zhang's parton cascade (ZPC) [64] until the partons freezeout, after which no further parton-parton interactions occur. Third, the partons recombine into hadrons via a quark coalescence model [62, 65] in which two nearest partons form mesons and three nearest partons form baryons according to their individual flavors. Finally, the hadronic interactions are modelled by a relativistic transport (ART) [66] model that accounts for baryon-baryon, baryon-meson, and meson-meson elastic and inelastic scatterings using the cascade method. Due to its ability to generate an initial state of partonic matter and then model all further interactions, the AMPT model is a useful tool for studying the thermodynamic properties of partonic or hadronic matter formed by relativistic heavy ion collisions.

In a recent work, the evolution trajectories were found to depend on several physical factors including the finite nuclear thickness [61]. Extracting the evolution of the thermodynamic properties from the AMPT model is not a simple task, though it is well-defined. For a given volume V, the energy-momentum tensor $\Pi^{\mu\nu}$ can be calculated according to

$$\Pi^{\mu\nu} = \frac{1}{V}\sum_i \frac{p_i^\mu p_i^\nu}{p_i^0}. \tag{1.3}$$

Here, the summation runs over all particles in the volume V and the final result is then averaged over many events. Also, p^μ is the energy-momentum four-vector and the Greek indices take on the values $\{0, 1, 2, 3\}$ where $p^0 = E$ and p^1, p^2, and p^3 are the x, y, and z components of the three-momentum $\vec{p}$, respectively. The energy density $\epsilon = \Pi^{00}$ and the spatial components of the pressure are $P_x = \Pi^{11}$, $P_y = \Pi^{22}$, and $P_z = \Pi^{33}$ in the rest frame of the volume V [61]. The calculated $\Pi^{\mu\nu}$ and the net conserved-charge densities

n_{B}, n_{Q}, and n_{S} were used to extract the temperature and chemical potentials μ from two QGP EoS [61]. After constructing the event-averaged evolution trajectories in the $T - \mu_{\mathrm{B}}$ plane of the QCD phase diagram, several important features were noted. The location of the trajectories depends significantly on the EoS in the sense that certain commonly used simplifying assumptions about the electric charge or strangeness chemical potentials μ_{Q} and μ_{S}, respectively, lead to very different results [61]. Specifically, the trajectories moved to lower μ_{B} for Au+Au collisions at all energies when $\mu_{\mathrm{Q}} = \mu_{\mathrm{S}} = 0$. Additionally, the authors found that ignoring the finite nuclear thickness effect drastically increased the maximum μ_{B} of a given trajectory and slightly decreased the maximum T [61].

Given that a numerical study has calculated the event trajectories of the matter formed by relativistic heavy ion collisions, Ch. 3 presents another primary goal of this research work that is to use the semianalytical model results to calculate similar QCD phase diagram trajectories. Accomplishing this task would be a useful test of the semianalytical model's validity if the resulting trajectories agree with the numerical results from the AMPT calculations. On the other hand, the successful completion of this goal will improve the analytical or intuitive understanding of how the initial density production leads to the behavior of the matter in the QCD phase diagram. To that end, central Au+Au collisions at a variety of collision energies up to $\sqrt{s_{\mathrm{NN}}} = 200$ GeV and parton formation times τ_{F} are used to semianalytically calculate $\epsilon(t)$, and $n_{\mathrm{B}}(t)$. Note that the behavior of $n_{\mathrm{Q}}(t)$ and $n_{\mathrm{S}}(t)$ are described in Sec. 2.4. A massless parton system is assumed to be formed, and the EoS of an ideal gas using either Bose-Einstein and Fermi-Dirac statistics or Maxwell-Boltzmann statistics is used to extract the T, μ, similarly to Ref. [61]. The ideal gas EoS are conformal; therefore, their applicability is limited since they cannot account for complex behaviors which may be expected of QCD matter at low temperatures or chemical potentials.

Thus, a more realistic EoS for finite chemical potentials is needed in order to accurately model the dynamics of a partonic matter at high temperatures and also correctly account for the hadronic degrees of freedom at low temperatures. Recently, one such lattice QCD-based

EoS [67] has been constructed using a Taylor series expansion of the pressure P in terms of the temperature T and three chemical potentials μ_{B}, μ_{Q}, and μ_{S}. Because the lattice QCD results are only calculated in a limited temperature range, $T \in [135, 220]$ MeV, and this is not wide enough to cover the expected full evolution of the matter produced by heavy ion collisions, the coefficients of the Taylor expansion were merged with hadron resonance gas (HRG) [68] model results at low T. In the high-T limit, each Taylor coefficient is imposed to smoothly merge with its expected value as calculated using the Stefan-Boltzmann limit, which is a reasonable assumption given that the partonic matter should be non-interacting at sufficiently high temperatures. This more realistic EoS has also been used to extract the QCD phase diagram trajectories from the semianalytical densities, and some important features are found to be qualitatively different from the trajectories extracted from the ideal gas EoS [46]. Importantly, limitations of the lattice QCD-based EoS at high μ_{B}/T prevent the calculation of observables such as the QGP lifetime for lower collision energies [46]. Specifically, the BES program has recently shown that the matter formed by $\sqrt{s_{\mathrm{NN}}} = 3$ GeV Au+Au collisions does not exhibit parton degrees of freedom [48], but the lattice QCD-based EoS cannot extract trajectories below $\sqrt{s_{\mathrm{NN}}} \lesssim 7.7$ GeV [46].

1.4 Parton Transport and the Relativistic Boltzmann Equation

Since hard and semihard interactions dominate the processes in the matter produced by relativistic heavy ion collisions, numerical simulations of the strongly interacting medium will aid in the study of the deconfinement phase transition and the chiral symmetry restoration. The final state interactions in particular are prime candidates for linking the experimental observables to predictions from pQCD regarding the space-time evolution of the QCD matter produced in such collisions. Therefore, the final state interactions and the density distribution in the phase space may be studied by numerically solving the relativistic Boltzmann

equation (RBE) for a system of quarks and gluons [64]

$$\begin{aligned} p^\mu \partial_\mu f_a(\mathbf{x},\mathbf{p},t) = &\sum_m \sum_{b_1,b_2,\ldots,b_m} \int \prod_i^m \frac{d^3 p_{b_i}}{(2\pi)^3 2E_{b_i}} f_{b_i}(\mathbf{x},\mathbf{p},t) \\ &\times \sum_n \sum_{c_1,c_2,\ldots,c_m} \int \prod_j^n \frac{d^3 p_{c_j}}{(2\pi)^3 2E_{c_j}} |M_{m\to n}|^2 \\ &\times (2\pi)^4 \delta^4 \left(\sum_{k=1}^m p_{b_k} - \sum_{l=1}^n p_{c_l} \right) \\ &\times \left[-\sum_{q=1}^m \delta_{ab_q} \delta^3(\mathbf{p} - \mathbf{p_{b_q}}) + \sum_{r=1}^n \delta_{ac_r} \delta^3(\mathbf{p} - \mathbf{p_{c_r}}) \right]. \end{aligned} \tag{1.4}$$

In the above $f_a(\mathbf{x},\mathbf{p},t)$ is the single-particle distribution function for a particle of type a at time t, and the matrix element for multi-parton interactions is written as $M_{m\to n}$ and is defined according to [64]

$$\langle c_1 c_2 ... c_n | S | b_1 b_2 ... b_m \rangle = M_{m\to n} (2\pi)^4 \delta^4 \left(\sum_{k=1}^m p_{b_k} - \sum_{l=1}^n p_{c_l} \right). \tag{1.5}$$

Here, the four dimensional delta function ensures the overall conservation of energy and momentum using the standard four-vector notation. If one were to consider only two-to-two interactions, then Eq. (1.4) reduces to the following relatively simple form

$$p^\mu \partial_\mu f(\mathbf{x},\mathbf{p},t) \propto \int \sigma f(\mathbf{x_1},\mathbf{p_1},t) f(\mathbf{x_2},\mathbf{p_2},t) \tag{1.6}$$

where the integration is performed over the momenta of the other three particles. Note that the integrand of Eq. (1.6) also contains other factors such as a delta function to conserve the total energy and momentum [62]. The cross section σ is defined as the integral of the differential cross section that is proportional to the amplitude squared [69]: $d\sigma/d\hat{t} \propto |M_{2\to 2}|^2$ where $\hat{t}$ is the standard Mandelstam variable for the momentum transfer.

Using the semiclassical Eqs. (1.4) and (1.6) to study the parton dynamics of a QGP at high temperatures is justified because the asymptotic freedom of QCD matter at high tem-

peratures means that the quarks and gluons are weakly interacting. Therefore, final state observables such as the hadron spectra [70], collective flows [48], and event-by-event fluctuations [47] can be studied with reasonable accuracy by numerically simulating a relativistic gas of partons. Because the RBE gives the time evolution of the single-particle distribution function in phase space, it is general enough that it has a wide range of applications in heavy ion collisions [11] and even in astrophysical phenomenon [71, 72]. Unfortunately, analytical solutions of even the simplified Eq. (1.6) are quite rare because solving nonlinear integro-differential equations is difficult in general. Therefore, analytical solutions are more commonly found under further assumptions such as the relaxation time approximation (RTA) [73, 74]. Despite the theoretical difficulties deriving analytical solutions of the RBE, one such solution was found nearly a decade ago for a system undergoing Gubser flow [75, 76]. Furthermore, the exact solution for a system of expanding massless particles with isotropic scatterings was found more recently [77, 78]. The theoretical results solving the RBE continue to expand, and the future developments will enable more accurate studies of the QGP and unveil previously hidden connections between its properties and the experimental observables.

ZPC is a Monte Carlo program that numerically solves the RBE of Eq. (1.6) by simulating many two-to-two parton scatterings such as $gg \to gg$ using the cascade method [64]. Two partons will scatter with each other if they approach each other and if their distance of closest approach is smaller than $\sqrt{\sigma/\pi}$. A system of massless gluons has the following differential scattering cross section according to the leading order QCD calculations

$$\frac{d\sigma_{gg}}{d\hat{t}} = \frac{9\pi\alpha_s^2}{2\hat{s}^2}\left(3 - \frac{\hat{u}\hat{t}}{\hat{s}^2} - \frac{\hat{u}\hat{s}}{\hat{t}^2} - \frac{\hat{s}\hat{t}}{\hat{u}^2}\right) \approx \frac{9\pi\alpha_s^2}{2}\left(\frac{1}{\hat{t}^2} + \frac{1}{\hat{u}^2}\right). \tag{1.7}$$

Here, α_s is the strong coupling constant, and $\hat{s}$ and $\hat{u}$ are the other Mandelstam variables. The right-hand side in the above equation arises after keeping only the leading divergent terms for a fixed $\hat{s}$. Since the scattering angle for identical particles ranges from 0 to $\pi/2$, if one

considers the range 0 to π, the $1/\hat{t}^2$ and $1/\hat{u}^2$ terms in the above equation are redundant [64]. With a medium generated Debye screening mass μ that regulates the singularity of the total cross section, the differential cross section and the cross section become for two gluon scattering

$$\frac{d\sigma_{gg}}{d\hat{t}} \approx \frac{9\pi\alpha_s^2}{2(\hat{t}-\mu^2)^2}, \tag{1.8}$$

$$\sigma_{gg} = \frac{9\pi\alpha_s^2}{2\mu^2}\frac{1}{1+\mu^2/\hat{s}}. \tag{1.9}$$

Because μ is generated by the medium, it is related to the phase space density, and $\mu \approx 1$ fm^{-1} for Au+Au collisions at RHIC is expected [62].

Three built-in geometric initial conditions in ZPC are used to study systems like the minijet gluon systems produced at RHIC, or systems undergoing Bjorken-like longitudinal expansion, or systems in a box with periodic boundary conditions [64]. The first geometrical setup initializes 4000 partons to be uniformly distributed in pseudorapidity $\eta \in [-5, 5]$ and within a transverse disk of radius 5 fm at $t = 0$. The partons have their energies generated from a thermal distribution with a temperature T and are formed after a proper formation time $\tau_0 = 0.1$ fm/c. This initial condition allows the numerical simulation of the QCD matter that is produced at RHIC energies because the partons are allowed to expand arbitrarily in the three spatial dimensions. The second geometrical initial condition also allows partons to expand, but only along the beam (z-) direction, in order to make studies of the Bjorken flow possible. This initial condition uniformly distributes the partons over the same pseudorapidity range, but also in a square in the transverse plane with has a user-defined side length. The simulations in a periodic box initialize all the partons at $t = 0$ uniformly in a cube with a side length chosen by the user, typically to allow the number of simulated partons to reach equilibrium. Again, the partons' energies are often generated from a thermal distribution, and this last geometric setup is primarily used for testing ZPC, though it can also be useful for generating results for partonic matter inside a box with

periodic boundary conditions [64].

The cascade method in ZPC simulates the collisions of many particles not by calculating and updating the positions and momenta for all N partons at regular steps in time, but instead by calculating and storing all future interactions then proceeding to the next earliest collision [64]. Thus, the program would in general need to search through $N(N-1)/2 \approx N^2/2$ parton pairs to find the next earliest collision; this is computationally expensive. Therefore, ZPC also provides a method to decrease the running time of the same event: space-cell division [64]. Updating a given parton's next collision partner then only requires the program to search through the partons in the same and neighboring cells, which drastically reduces the computational cost to $\propto N \times n$ where n is the average number of partons per cell. The default setting for the space-cell division is to divide the side-length of the box into ten for a total of 1000 cells and 4 partons per cell on average (for the typical box simulation with 4000 partons). For simulations with three- or one-dimensional expansion, the cells are allowed to expand uniformly in time to maximize the number of partons in the box, which improves the efficiency [64]. Note that the cell size should be chosen to be larger than the interaction length $\sqrt{\sigma/\pi}$, otherwise the results may be incorrect (different from the corresponding simulation without space-cell division).

In general, parton cascades suffer from the causality violation which arises due to the geometric interpretation of the cross section. Thus, one naïvely expects ZPC to be accurate only in the dilute limit where the interaction length $\sqrt{\sigma/\pi}$ is much smaller than the mean free path λ [79]. The dilute limit is mathematically defined as $\chi \ll 1$ where $\chi = \sqrt{\sigma/\pi}/\lambda$ is called the opacity. Techniques like the test particle method, also known as the parton subdivision method, are useful for reducing the inaccuracies due to causality violation [80]. This can be understood in terms of a transformation in the RBE of Eq. (1.6) in which $f \to f \times l$ and $\sigma \to \sigma/l$. This transformation decreases the opacity by $\chi \to \chi/\sqrt{l}$, where l is the subdivision factor [69, 79], but the RBE remains unchanged. Unfortunately, the parton subdivision method is computationally expensive because the number of particles

increases from $N \to N \times l$ and the number of simulated collisions grows proportionally by a factor $\approx N^2$. Recently, a new parton subdivision transformation for massless partons in a box with periodic boundary conditions was shown to be equivalent to the old subdivision technique [69]. This new parton subdivision method increases f not by increasing the number of partons, but by decreasing the volume $V \to V/l$ and is much faster since the number of particles is not changed [69]. The subdivision technique allows one to produce highly accurate results and can be used to predict the behavior of a dilute QGP.

In a relativistic transport model like ZPC, one is also free to choose the scattering prescription, which leads to different results in general [64, 81]. Recently, it has been shown that different scattering prescriptions are useful for reducing the causality violation [69], although the effectiveness also depends on the χ of the medium. A scattering prescription, or collision scheme, refers to the choice of the collision frame, the collision space-time point, the ordering frame, and the ordering time [64]. Each two-parton collision occurs in the collision frame and is ordered in time in the ordering frame, which is chosen to be the CM frame of the parton gas [64]. The original collision scheme in ZPC chooses the two-parton CM frame as the collision frame and the position of each parton in the collision frame when the partons are closest as the collision space-time point [64]. In general, the single collision space-time point in the collision frame results in two different collision times $t_{c,1}$ and $t_{c,2}$ for the partons in the ordering frame, due to Lorentz transformations [69]. The ordering time and collision times for both partons are then chosen to be $(t_{c,1}+t_{c,2})/2$ in the original ZPC collision scheme [64]. By changing the collision and ordering times with a generalized collision scheme, one can in principle reduce the effect of the geometric interpretation of σ so that ZPC would more accurately model the hot dense matter produced by relativistic heavy ion collision.

Recently, various collision schemes were studied in box simulations using ZPC without parton subdivision, and a new collision scheme that significantly improves the results compared to the old collision scheme was discovered [69]. Recall that using the parton subdivision method with a subdivision factor l increases the time needed to simulate an event by a fac-

tor $\approx l^2$. Therefore, finding an accurate collision scheme implies that the parton subdivision method will not need to be used to obtain accurate results in future studies using ZPC [64] or AMPT [62]. In the new collision scheme, the collision frame and collision space-time point are the same as in the old collision scheme; however, the ordering time and collision times for both partons are changed to $\min(t_{c,1}, t_{c,2})$ [69]. This new collision scheme was found to significantly improve the accuracy of the entire time-evolution of the $\langle p_{\mathrm{T}} \rangle$ and $\mathrm{var}(p_{\mathrm{T}})$ when compared with the subdivision results which are expected to be accurate for a range of opacities [69]. Note that the momentum distributions for a system of massless particles following the Maxwell-Boltzmann statistics can be easily calculated, and the results for the transverse and longitudinal momentum distributions are presented in Appendices B.1 - B.2, respectively. The collision rate and the shear viscosity to entropy density ratio were also significantly improved when using the new collision scheme instead of the old one [69]. The improvement of the new collision scheme results over the old collision scheme results was established by comparing to the results of the parton subdivision technique that agree with the theoretical results [69]. This comparison is very useful, but it would also be helpful to compare ZPC with an exact analytical solution of the RBE to have a more robust conclusion regarding how effectively ZPC models the entire time evolution of the QGP. While an analytical solution of the Boltzmann equation for a non-relativistic, non-expanding homogeneous gas has been known for decades [82], an exact analytical solution for a relativistic, isotropically expanding gas of massless particles was found only recently [77, 78]. Another key aspect of this research work that is presented in Ch. 4 is the assessment of parton transport in ZPC using this new analytical solution of the RBE as a benchmark.

1.5 Future Work in Parton Transport

Studying parton systems in a box with ZPC is in itself useful research, but more useful is studying the dynamics of the expanding matter produced in heavy ion collisions. Therefore,

any improvements that have been made to ZPC for box simulations are important in the sense that they should also make similar improvements for the more realistic conditions such as those that are used in the AMPT model [62]. While the new collision scheme described previously works quite well at reducing the artifacts from causality violation for box simulations [69], it does not do so for setups with three-dimensional expansion. This unexpected behavior is referred to as the 3D-problem and is discussed further in Ch. 5. Since parton collisions always occur in the two-parton CM frame, regardless of the geometrical setup being used, the 3D-problem is surprising. Initial results hint at an underlying issue in the random number generator (RNG) that causes some partons to be initialized inside the cross section of another parton. This behavior causes many collisions to occur at very early times, which is not expected. The need for a more modern RNG that does not suffer from the known problems of linear congruential pseudo-random generators is apparent [83]. Note that there is no indication as yet that ZPC itself or all parton cascades suffer from inherent problems; therefore, a rich variety of results using ZPC or the larger more wide-reaching AMPT are expected to be forthcoming.

The existence of the 3D-problem indicates that further work needs to be done before ZPC can be more accurate at high densities for simulating the partonic systems created by heavy ion collisions. One particularly interesting feature of a QGP is the probability distribution of the Mandelstam s that describes the CM energy for a pair of partons. Decades ago, an analytical distribution $f(s)$ was given [84] for a massless relativistic gas whose particles' energies follow a thermal distribution. For the reader's reference, a derivation of this and another $f(s)$ is presented in Appendix B.3. The $f(s)$ distribution is important for studying the QCD matter because its form determines the average collision energy $\langle\sqrt{s}\rangle$ of partons in the medium. Since s is related to the scattering angle that is also related to the differential cross section, one can imagine that different values of $\langle\sqrt{s}\rangle$ produce different behaviors in a simulated QGP. In Ch. 5, a comparison is made between $f(s)$ of Ref. [84] and the numerical result from ZPC. The two distributions agree incredibly well, which strengthens ones trust

that ZPC accurately models hot dense QCD matter.

The hypothesized CME [22] has recently garnered much attention from both theorists and experimentalists in the field of nuclear physics. Experiments performed by the STAR Collaboration [85] used isobar collisions $^{96}_{44}$Ru+$^{96}_{44}$Ru and $^{96}_{40}$Zr+$^{96}_{40}$Zr to subject the produced QCD matter to large electromagnetic fields. The magnetic fields generated by the receding protons in the nuclei would separate the differently charged quarks along the direction of the magnetic field. The observation of the CME would imply the existence of CP-violating regions and the approximate chiral symmetry restoration in the QGP [85]. Because the signal of the CME has a large background, its observation is technically difficult. Therefore, these isobar collisions are useful for reducing the background noise because the larger Z of Ruthenium nuclei would produce a notable increase of around 15% in the magnetic field, but the same A naïvely should produce very similar flow-related background [85]. While the existence of CP-violating regions in the QGP is an exciting prospect, a blind analysis of the high-statistical data sets indicates that no difference in the pre-defined CME signal is observed in the isobar collisions at RHIC [85]. Further research including the study of curved parton motion in ZPC is ongoing in the search for the CME. The cascade method lets the simulated partons follow their free-streaming trajectories between collisions; however, the strong electromagnetic fields that are produced in non-central A+A collisions would induce the medium's constituents to follow curved paths. Studying this phenomenon numerically using ZPC is useful because it would allow the generation of high statistical predictions regarding the kind and in what way certain experimental observables could be affected by the electromagnetic fields. A description of recent work implementing curved motion in ZPC is discussed in Ch. 5, and the initial results are promising.

Chapter 2

Developing a Semianalytical Model for the Initial Densities

A method to calculate the initial energy and net-conserved charge densities produced in heavy ion collisions that takes into account the finite nuclear thickness is presented here. The details of how this method includes both the finite longitudinal (z-) width and the finite duration time d_t of the initial parton production is discussed in Sec. 2.1. Section 2.2 contains a brief description of the data based parametrizations of the transverse mass and net-baryon density per unit rapidity that are used in the model, and a more detailed discussion can be found in Appendix A. Several qualitative behaviors and quantitative results for the initial energy density produced in central, Au+Au collisions are presented in Sec. 2.3. These include a discussion about an analytical upper bound of the maximum energy density and an approximate scaling relation that the model satisfies. Calculations of the net-conserved charge densities such as the net-baryon density are presented in Sec. 2.4, as well as the model's inherent assumptions regarding the net electric-charge and net strangeness densities. Finally, Sec. 2.5 contains an explanation of how the effect of transverse flow is incorporated into the model's semianalytical densities. The semianalytical model is useful for improving the initial densities of the matter produced by heavy ion collisions which is a vital part of the nuclear equation of state (EoS) and is also a key input for hydrodynamic simulations of the quark-gluon plasma. Because the EoS of the QGP is related to certain experimental observables, a better understanding of the initial produced densities will lead to better predictions of the location of the matter's trajectory in the QCD phase diagram.

2.1 The Finite Nuclear Thickness

The divergence of the initial energy density predicted by two previous analytical models [42, 43] motivates the development of a new model that cures these infinite energy densities [45]. The Bjorken energy density formula of Eq. (1.1) assumes that the initial state partons are produced at a z-coordinate $z_0 = 0$ and at a time $x = 0$, i.e., at the space-time point $(z_0, x) = (0, 0)$ [42]. An extension to this model assumes that they are also produced at $z_0 = 0$, but at any time $x \in [0, d_t]$ less than the crossing time d_t of the two nuclei [43]. The initial partons in this semianalytical model are assumed to be produced by the primary NN interactions at any space-time position (z_0, x) inside the overlap region of the two nuclei [45]. The effect of the transverse expansion of the overlap volume is initially neglected, but will be investigated later in Sec. 2.5. This semianalytical model also does not account for the slowing down of the participant nucleons due to the primary NN collisions; this treatment is the same as in the previous models [42, 43].

A key difference between this new model and that of the Bjorken energy density formula is that the overlapping and expanding stages cannot be clearly separated, but instead are mixed together [46]. The velocity along the z-direction of a produced parton is $v_z = (z - z_0)/(t - x)$ in the new semianalytical model, while it is $v_z = z/t$ in the Bjorken picture because all partons are produced at $(z_0, x) = (0, 0)$. On the other hand, the two models are similar in that all secondary parton interactions are ignored because analytically modelling this is too difficult. The primary benefit of this new semianalytical model is that it analytically accounts for the finite nuclear thickness of the overlap region for the initial parton production [45, 46]. The width of the overlap region comes from the thickness in the z-direction of the overlapping Lorentz-contracted spherical nuclei. Figure 2.1 shows a schematic representation of an A+A collision and the subsequent overlap of two identical relativistic nuclei traveling along the z-axis at a speed $\beta = \tanh(y_{\rm CM})$. As the nuclei pass through each other, the full z-width of the overlap region first increases from 0 at $t = 0$ to βd_t at $t = d_t/2$, and then decreases back to 0 at $t = d_t$ [45, 46]. The diamond in the $t - z$ plane is referred to as the production

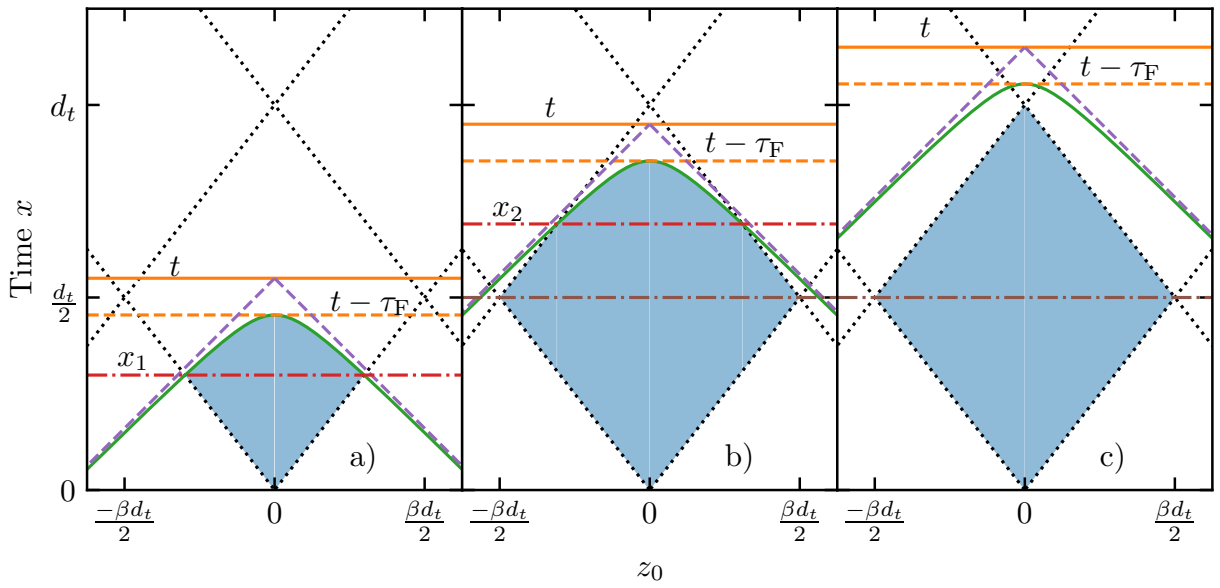

Figure 2.1: Schematic diagram of a central Au+Au collision for early (a), middle (b), and late (c) times. The dotted lines represent the boundaries of the overlap region S_0, and the dashed diagonal lines represent the light cone boundaries for partons that can reach $z \approx 0$ at time t. The hyperbola represents the boundary of these partons after considering the formation time $t_F = \tau_F \cosh(y)$. The dot-dashed lines divide the shaded production region for each time into different integration areas for the three pieces of the piecewise functions as described in Table 2.1.

region because it covers the area of primary NN collisions [86, 87]. The production region is the area surrounded by the four dotted lines in Fig. 2.1.

The goal of this semianalytical model is to estimate the initial energy or net conserved-charge in a narrow volume $z \in [-d, d]$ within the transverse overlap area A_T as a function of time t. It is assumed that the initial partons are produced at a z-coordinate z_0 and time x, i.e., at the space-time point (z_0, x), within the production area. Following its production, it is assumed that each parton propagates with its velocity until it is formed after a formation time t_F [45]. If a parton is produced at time x, its rapidity y must satisfy the following requirement in order to end up inside the narrow range $z \in [-d, d]$ at time t:

$$\frac{-d - z_0}{t - x} \leq \tanh(y) \leq \frac{d - z_0}{t - x}. \tag{2.1}$$

If one takes the limit $d \to 0$ the parton's rapidity and its allowed rapidity range become

$$y \to y_0 = \tanh^{-1}\left(\frac{-z_0}{t-x}\right), \tag{2.2}$$

$$\Delta y = \frac{2d\ \cosh^2 y}{t-x}. \tag{2.3}$$

Thus, the initial energy density at time t averaged over the full transverse overlap area is

$$\begin{aligned}\epsilon(t) &= \frac{1}{2dA_{\mathrm{T}}}\iint_S dxdz_0 \frac{d^3m_{\mathrm{T}}}{dxdz_0dy_0}\Delta y_0\ \cosh y_0 \\ &= \frac{1}{A_{\mathrm{T}}}\iint_S \frac{dxdz_0}{t-x}\frac{d^3m_{\mathrm{T}}}{dxdz_0dy_0}\cosh^3 y_0.\end{aligned} \tag{2.4}$$

Here, m_{T} is the transverse mass, and it is the same as the transverse energy E_{T} when the rapidity is $y = 0$. The notation for the transverse mass m_{T} in this semianalytical model is used to differentiate the data-based parametrizations described in Sec. 2.2 for dm_{T}/dy from dE_{T}/dy which was experimentally determined by the PHENIX Collaboration [44]. Note that the above integral converges for finite values of the parton formation time τ_{F} because the observation time t is larger than the maximum parton production time $x = t - \tau_{\mathrm{F}}$. In the case when $\tau_{\mathrm{F}} = 0$, an analytical upper bound for the maximum energy density $\epsilon^{\max}$ is derived in Sec. 2.3.2, which means that the above integral always converges.

One can test the validity of Eq. (2.4) by making some straightforward substitutions for the initial energy production which result from different physical pictures [45]. For example, if one neglects the finite time duration and longitudinal width of the initial energy production and uses the substitution $d^3m_{\mathrm{T}}/dx/dz_0/dy \to \delta(z_0)\delta(x)dm_{\mathrm{T}}/dy$, one recovers the Bjorken energy density formula of Eq. (1.1). On the other hand, if one considers the finite time duration, but neglects the finite longitudinal width and uses the substitution $d^3m_{\mathrm{T}}/dx/dz_0/dy \to \delta(z_0)d^2m_{\mathrm{T}}/dx/dy$, one recovers another previously known solution [43] of Eq. (1.2).

Note that the energy density of Eq. (2.4) is given by an integral over the production

region $S(t)$ which changes with time, so the integration limits depend on time t [45, 46]. For a given time t, the production region $S(t)$ can be defined as the set of all space-time points (z_0, x) which satisfy the following conditions. First, (z_0, x) must be inside the overlap region which is depicted in Fig. 2.1 as the diamond-shaped area surrounded by the four dotted lines. Second, (z_0, x) must be below the light cone boundaries that are shown as the two diagonal dashed lines in Fig. 2.1; this requirement ensures causality. Finally, (z_0, x) must also be below the formation time hyperbola which prevents a parton from contributing to the energy or net-conserved charge density at time t if the parton's finite formation time has not yet occurred. In the CM frame, the formation time of a parton is defined as:

$$t_F = \tau_{\rm F} \cosh(y). \tag{2.5}$$

In the above, $\tau_{\rm F}$ is a proper formation time, and it is multiplied by a time-dilation factor to account for each parton's rapidity y. If a parton is produced at (z_0, x) and would reach point the $(z_0 \approx 0, t)$ and contribute to the energy density of Eq. (2.4), its formation time would be $\tau_{\rm F} \cosh(y_0)$. Mathematically, the formation time curve is defined by the hyperbola

$$x_{\rm F} = t - \sqrt{z_0^2 + \tau_{\rm F}^2}. \tag{2.6}$$

This formation time hyperbola reduces to the light cone boundary for a proper formation time of $\tau_{\rm F} = 0$, while it is in general a more strict requirement than the light cone boundary for finite $\tau_{\rm F}$.

Since the integration limits of (z_0, x) in Eq. (2.4) depend on time, the energy and net-conserved charge densities are piecewise functions in time [45, 46]. The naïve picture of the crossing of two nuclei in Fig. 2.1 can be generalized by considering a starting time t_1 and an ending time t_2 for the initial production. The diamond production region S_0 is bounded by the lines $z_0 = \pm\beta(x - t_1)$ and $z_0 = \pm\beta(x - t_2)$ in this more general case. The integration limits for this more general case are summarized in Table 2.1, and it is emphasized that for

$t \in [0, t_1 + \tau_{\rm F})$, the energy or net-conserved charge densities are zero in the picture that this semianalytical model considers [45, 46]. Time t_a is the observation time when the formation time hyperbola of Eq. (2.6) intersects the two middle vertices of the production region where $(z_0, x) = (\pm\beta t_{21}/2, t_{\rm mid})$:

$$t_a = t_{\rm mid} + \sqrt{\tau_{\rm F}^2 + \left(\frac{\beta t_{21}}{2}\right)^2}. \tag{2.7}$$

Here, the following definitions are made for clarity:

$$t_{21} = t_2 - t_1, \quad t_{\rm mid} = (t_1 + t_2)/2. \tag{2.8}$$

In Table 2.1, the integration limits for each of the three pieces of the energy or net-baryon density are given. The first piece is defined when $t \in [t_1 + \tau_{\rm F}, t_a)$, i.e. early times at which the formation time hyperbola of Eq. (2.6) intersects the lower boundaries of the production region: $z_0 = \pm\beta(x - t_1)$. The time at which the formation time hyperbola intersects the lower or upper boundaries of the diamond-shaped production region are referred to as x_1 and x_2, respectively, which are given by

$$x_i = \frac{t - \beta^2 t_i - \sqrt{\beta^2\left[(t - t_i)^2 - \tau_{\rm F}^2\right] + \tau_{\rm F}^2}}{1 - \beta^2}, \text{with } i = 1, 2. \tag{2.9}$$

The first piece has two integration areas and can be seen in Fig. 2.1, or Table 2.1: the first area is triangular for times $x < x_1$ and the second area is for times $x_1 < x < x_{\rm F}$. The z_0-range of the second area is bounded by the z_0-coordinates of the formation time hyperbola of Eq. (2.6), where for a given time x, $z_{\rm F}(x)$ is given by:

$$z_F(x) = \sqrt{(t - x)^2 - \tau_{\rm F}^2}. \tag{2.10}$$

The second piece is defined when $t \in [t_a, t_2 + \tau_{\rm F})$, i.e. middle times when the formation time hyperbola of Eq. (2.6) intersects the upper boundaries of the diamond-shaped production region: $z_0 = \pm\beta(x - t_2)$. The second piece has three integration areas which are shown in

Piece	t-range	x-range	z_0-range
$\epsilon_{\rm I}(t)$ or $n_{\rm B,I}(t)$	$[t_1+\tau_{\rm F},\, t_a)$	$[t_1,\, x_1)$ $[x_1,\, t-\tau_{\rm F}]$	$[-\beta(x-t_1),\, \beta(x-t_1)]$ $[-z_{\rm F}(x),\, z_{\rm F}(x)]$
$\epsilon_{\rm II}(t)$ or $n_{\rm B,II}(t)$	$[t_a,\, t_2+\tau_{\rm F})$	$[t_1,\, t_{\rm mid})$ $[t_{\rm mid},\, x_2)$ $[x_2,\, t-\tau_{\rm F}]$	$[-\beta(x-t_1),\, \beta(x-t_1)]$ $[-\beta(t_2-x),\, \beta(t_2-x)]$ $[-z_{\rm F}(x),\, z_{\rm F}(x)]$
$\epsilon_{\rm III}(t)$ or $n_{\rm B,III}(t)$	$[t_2+\tau_{\rm F},\, \infty)$	$[t_1,\, t_{\rm mid})$ $[t_{\rm mid},\, x_2]$	$[-\beta(x-t_1),\, \beta(x-t_1)]$ $[-\beta(t_2-x),\, \beta(t_2-x)]$

Table 2.1: Piecewise solution of $\epsilon(t)$ and $n_{\rm B}(t)$ as functions of the observation time t, where the integration limits for each piece are written in the format $x \in [x^{\rm min}, x^{\rm max}]$ and $z_0 \in [z_0^{\rm min}, z_0^{\rm max}]$ for each part of the production area in the initial production time x and longitudinal position z_0 [45].

Ref. [45] or Table 2.1: the first is the triangular lower half of the diamond, the second is the trapezoidal upper half of the diamond below x_2, and the third is for $x_2 < x < x_{\rm F}$. The third and final piece is defined when $t \in [t_2+\tau_{\rm F}, \infty)$ and has two triangular integration areas which together form the entire diamond. Note that the energy or net-conserved charged density is higher for a smaller $\tau_{\rm F}$ when a given $\sqrt{s_{\rm NN}}$, A, and t are chosen because the integration area gets bigger, except for the late-time densities when $t > t_2 + \tau_{\rm F}$ that do not depend on $\tau_{\rm F}$.

Notably, the initial produced densities from this semianalytical model for late times ($t \geq t_2 + \tau_{\rm F}$) are independent of the parton formation time $\tau_{\rm F}$. This is understandable because the integration limits for (z_0, x) in Table 2.1 are independent of $\tau_{\rm F}$ for the third piece. Also, only partons with $y \approx 0$ will contribute to the densities at $z \approx 0$ for very late times because the velocity of partons in this semianalytical model is $v_z = (z - z_0)/(t - x)$. This fact is independent of the parton's space-time production point and implies that the results of this semianalytical model approach those of the Bjorken formula for very late times [46].

2.2 Data Based Parametrizations

To proceed further, only central Au+Au collisions will be considered and the function $d^3m_{\mathrm{T}}/dx/dz_0/dy$ in Eq. (2.4) will be specified. First, we assume that the initial transverse mass rapidity density of produced partons per production area can be written in the following factorized form:

$$\frac{d^3m_{\mathrm{T}}}{dxdz_0dy} = g(z_0, x)\frac{dm_{\mathrm{T}}}{dy}. \tag{2.11}$$

Here, the area density function $g(z_0, x)$ is normalized so that the volume between the three-dimensional surface $g(z_0, x)$ and the production region S_0 in the $t - z$ plane is equal to one:

$$\iint_{S_0} dxdz_0 \; g(z_0, x) = 1. \tag{2.12}$$

The above equation ensures that dm_{T}/dy represents the initial rapidity density of the transverse mass for all produced partons [45]. Next, the simplifying assumption of a uniform production of partons throughout the entire production region S_0 is assumed:

$$g(z_0, x) = \frac{2}{\beta t_{21}^2}. \tag{2.13}$$

With the assumptions of this semianalytical model, specifying the exact functional form of the transverse mass rapidity density allows the initial energy density of Eq. (2.4) to be written as

$$\epsilon(t) = \frac{2}{A_{\mathrm{T}}\beta t_{21}^2}\iint_S \frac{dxdz_0}{t-x}\frac{dm_{\mathrm{T}}}{dy_0}\cosh^3(y_0). \tag{2.14}$$

Apart from the parameters of this semianalytical model, the solution to Eq. (2.14) requires one to choose the shape of dm_{T}/dy. Unfortunately, the above integral cannot be solved analytically for the data-based parametrizations of dm_{T}/dy that are given in Appendix A.1 and A.2. However, in the late-time limit $t \to \infty$, one finds $y_0 \to 0$, and Eq. (2.14) recovers the Bjorken energy density formula of Eq. (1.1). Therefore, the results of this model are referred to as "semianalytical" because the analytical integral in Eq. (2.14) must be solved

numerically. With these assumptions on the factorization and uniform production, one only needs to choose a specific form for the transverse mass rapidity density dm_{T}/dy. Total energy conservation for the central Au+Au collisions, assuming all incoming nucleons are participants, leads to

$$\int \frac{dm_{\mathrm{T}}}{dy} \cosh(y) dy = A\sqrt{s_{\mathrm{NN}}}. \tag{2.15}$$

For the produced partons, dm_{T}/dy is assumed to have a Gaussian shape centered at $y = 0$ with a width σ found through the total energy conservation and with a height parametrized by results from the string melting version of the AMPT model [62]. For produced hadrons, dm_{T}/dy has two parts: one part is a single Gaussian for dE_{T}/dy, and the second is a sum of two symmetrically shifted Gaussian profiles for the net-baryon contribution to the energy $m_{\mathrm{N}}\ dN_{\mathrm{netB}}/dy$. The various parameters of the hadron dm_{T}/dy are calculated for each collision energy by ensuring the previously mentioned total energy conservation and the conservation of net-baryon number. For further details, the reader is invited to consult Appendix A.

2.3 Initial Energy Densities

In this semi-analytical model, the primary collisions between the two nuclei start at time t_1 and end at time t_2 [43, 45]. It is clear from Eq. (2.14) and Table 2.1 that the initial energy density for A+A collisions of a given energy $\sqrt{s_{\mathrm{NN}}}$ depends only on t_1, t_2, and τ_{F}. For now, the following choice for t_1 and t_2 is made

$$t_1 = 0.2d_t, \quad t_2 = 0.8d_t. \tag{2.16}$$

This choice ensures that the width of the production time distribution is similar to results from the string melting version of the AMPT model [62]. Because a boosted nucleus is shaped more like an ellipsoid instead of a uniform disk, the naïve choice of $t_1 = 0$ and $t_2 = d_t$

is less representative of the picture that is considered in this semianalytical model than is the choice of t_1 and t_2 of Eq. (2.16) [45].

In the following sections, several characteristics of the initial produced energy density from this semianalytical model are discussed with references to the previous models where applicable. First, a comparison between the energy densities $\epsilon_{\rm parton}$ and $\epsilon_{\rm hadron}$ is made in Sec. 2.3.1. Second, $\epsilon^{\rm max}_{\rm parton}$ at $\tau_{\rm F} = 0$ is shown to be finite through the derivation of an analytical upper bound in Sec. 2.3.2. Thereafter, $\epsilon_{\rm hadron}$ is referred to simply by ϵ. Third, ϵ is compared to $\epsilon_{\rm Bj}$ and $\epsilon(t)$ from Eq. (1.2) with a triangular time profile in Sec. 2.3.3. Finally, an approximate scaling and A-dependence of $\epsilon^{\rm max}$ is discussed in Sec. 2.3.4. An online web application that performs the semianalytical calculations for the initial energy density $\epsilon_{\rm hadron}$ when the user inputs the parameters of the collision system has been made [88].

2.3.1 Comparing $\epsilon_{\rm parton}$ and $\epsilon_{\rm hadron}$

The first set of calculations of the initial energy density with Eq. (2.14) is made using the transverse mass rapidity density $dm_{\rm T}/dy$ of the initial produced partons that is given in Appendix A.1. As is discussed there, the peak value of this distribution is parametrized according to results of the AMPT model [62, 43]. It is of interest to investigate the uncertainty of ϵ due to the choice of $dm_{\rm T}/dy$, which can be significantly different if the distribution is chosen for initial partons or final hadrons as shown in Fig. A.1. The hadron $dm_{\rm T}/dy$ is derived in Sec. A.2 and is shown by the dashed curves in Fig. A.1 for central Au+Au collisions at a range of collision energies. Note that both the parton and the hadron $dm_{\rm T}/dy$ satisfy the total energy conservation condition of Eq. (2.15).

Figure 2.2 shows the results of the initial energy density as a function of time for central Au+Au collisions at $\sqrt{s_{\rm NN}}$ = 3, 7.7, 39, and 200 GeV with two different $\tau_{\rm F}$ values. The energy density is zero for $t \leq t_1 + \tau_{\rm F}$ according to the semianalytical model, and increases smoothly with time until a maximum value is reached somewhere in the range $t_{\rm max} \in [t_{\rm mid} + \tau_{\rm F}, t_2 + \tau_{\rm F}]$ [45]. After the maximum value is reached, $\epsilon(t)$ then decreases with time, and the

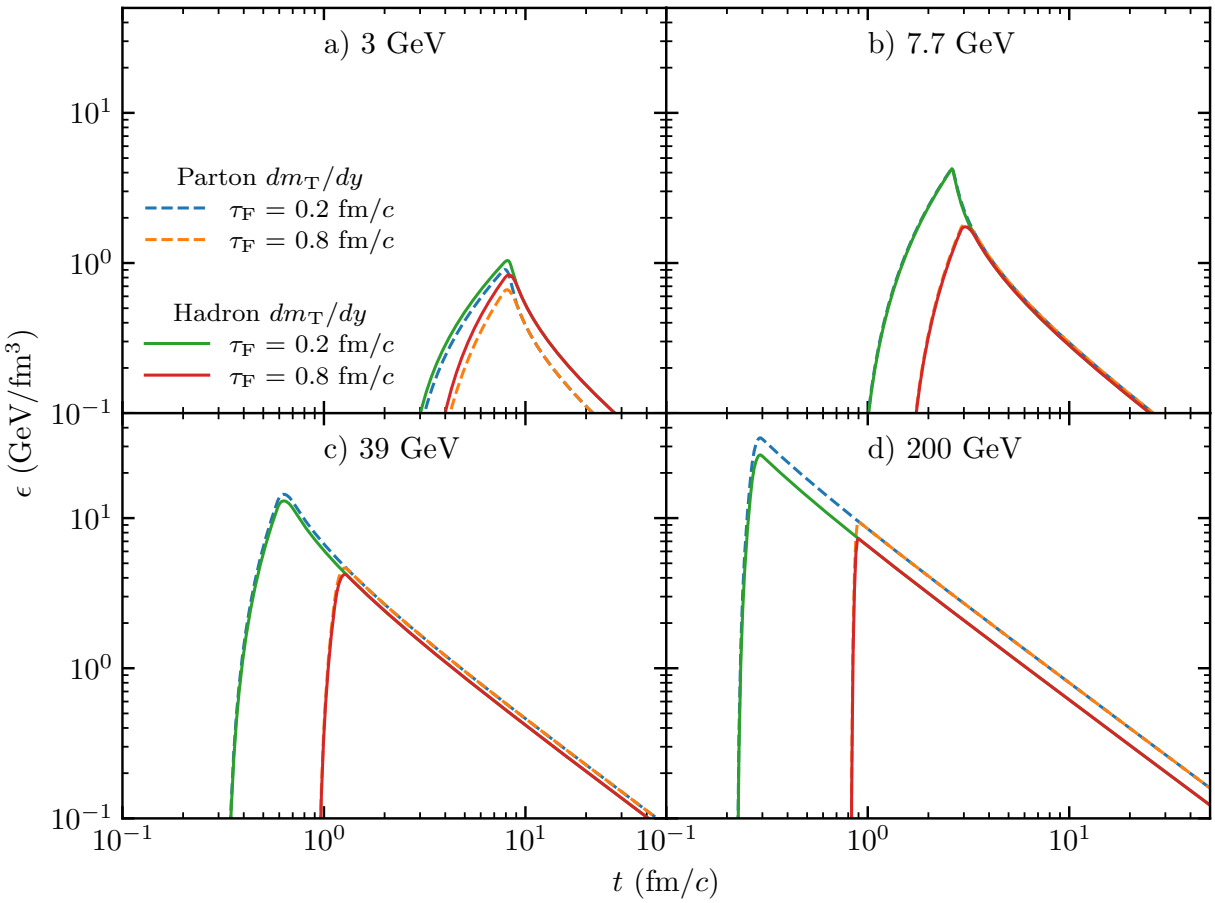

Figure 2.2: Energy density using the parton (dashed) or hadron (solid) dm_T/dy for central Au+Au collisions at $\sqrt{s_{NN}} = 3$, 7.7, 39, and 200 GeV with $\tau_F = 0.2$ and 0.8 fm/c.

late-time densities are the same for different τ_F values, for the same dm_T/dy profile. It is also clear from Fig. 2.2 that the maximum energy density ϵ^{max} increases as τ_F decreases, though the relative increase is smaller for smaller $\sqrt{s_{NN}}$. Additionally, ϵ^{max} at a given collision energy at a larger formation time lies on the decreasing part of the $\epsilon(t)$ curve for a smaller τ_F. The merging of the late time energy densities can be understood by considering the densities calculated from the uniform time profile in a previous study [43]. In that case, for times long after the maximum density is reached, the uniform time profile yields densities that are proportional to $\ln[(t-t_1)/(t-t_2)]$, which is independent of τ_F. As discussed in Sec. 2.1 with reference to Table 2.1, the late time behavior of this semianalytical model reproduces the same effect. Coincidentally, this is a characteristic of the semianalytical model, and it

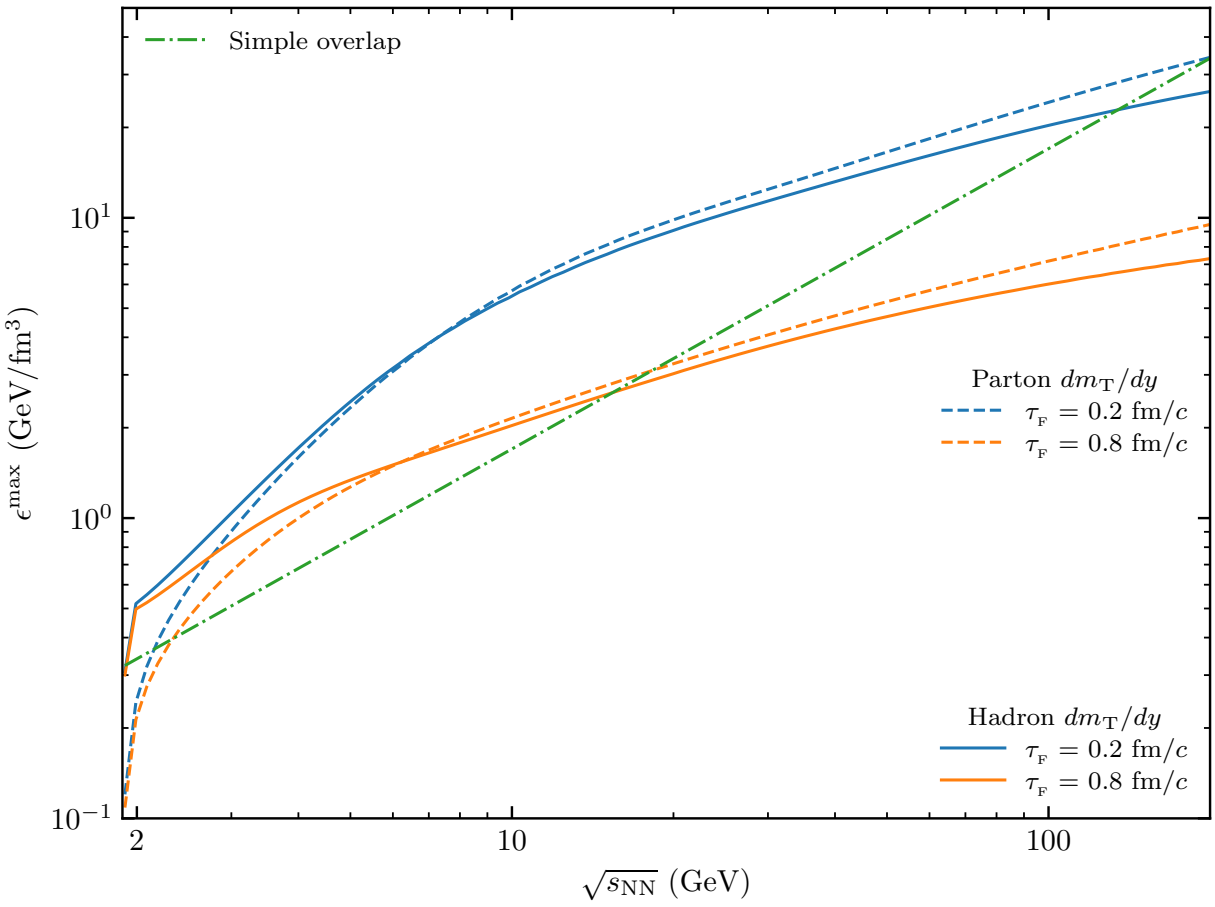

Figure 2.3: Maximum energy density $\epsilon^{\max}$ using the parton (dashed) or hadron (solid) dm_T/dy in central, Au+Au collisions as a function of $\sqrt{s_{NN}}$ with $\tau_F = 0.2$ and 0.8 fm/c. The naïve expectation of $\epsilon_{\text{overlap}}$ from Eq. (2.17) is also shown for reference.

applies also to the net-conserved charge densities that are calculated in Sec. 2.4.

The maximum values of the produced energy density $\epsilon^{\max}$ is shown in Figure 2.3 using the parton or hadron dm_T/dy in central, Au+Au collisions as a function of collision energy with two different τ_F values. For $\sqrt{s_{NN}} \in [3, 100]$ GeV, the maximum produced energy densities are similar for the two dm_T/dy distributions. At large collision energies, partons with $y \approx 0$ dominate the energy density near central space-time pseudorapidity $\eta_s \approx 0$ because the production area S_0 is small on the scale of the finite τ_F [45]. Thus, the $\epsilon^{\max}$ value for high $\sqrt{s_{NN}}$ should depend mostly on the mid-rapidity value $dm_T/dy(0)$ that can be seen in Fig. A.1. The end result is that the hadron $\epsilon^{\max}$ value is smaller than the parton

one at larger collision energies. On the other hand, for small $\sqrt{s_{\rm NN}}$, partons with non-zero rapidity may contribute to the energy density in the central spacetime-rapidity region [45]. Therefore, the energy density will also depend on the width of $dm_{\rm T}/dy$ for smaller $\sqrt{s_{\rm NN}}$. Figure A.1 shows that the height of the hadron $dm_{\rm T}/dy$ can be larger for lower $\sqrt{s_{\rm NN}}$, while the width of the profile is similar. Therefore, one expects the maximum energy density using the hadron $dm_{\rm T}/dy$ to be larger than using the parton $dm_{\rm T}/dy$ at lower $\sqrt{s_{\rm NN}}$.

A simple estimate for the energy density is also shown by the dot-dashed line in Fig. 2.3. This naïve estimate corresponds to the case when the two boosted nuclei would just overlap in volume, without interacting [45]. The energy density of this system according to the hard-sphere model of the nucleus is given by

$$\epsilon_{\rm overlap} = \frac{3\sqrt{s_{\rm NN}}}{4\pi r_{\rm N}^3}. \tag{2.17}$$

Here, $r_{\rm N} \approx 1.12$ fm is the nucleon radius. Clearly, Eq. (2.17) grows linearly with collision energy and is independent of the atomic number A of the colliding nuclei. The compression of the primary A+A collision should actually cause the maximum energy density in the central spacetime-rapidity region to be larger than $\epsilon_{\rm overlap}$ [45]. Figure 2.3 indeed shows this to be the case except at very small or very large $\sqrt{s_{\rm NN}}$. However, the maximum energy density using the hadron $dm_{\rm T}/dy$ is larger than $\epsilon_{\rm overlap}$ for collision energies near the threshold $\sqrt{s_{\rm NN}} = E_0 = 2m_{\rm N}$ GeV. The energy density using the parton $dm_{\rm T}/dy$ is smaller than the expectation of Eq. (2.17). Because the QGP is unlikely to be formed for collisions near the threshold energy, the hadron $dm_{\rm T}/dy$ should be more valid in that region [45]. On the other hand, the parton $dm_{\rm T}/dy$ is expected to be more applicable at very high $\sqrt{s_{\rm NN}}$, although the maximum energy density would be smaller than $\epsilon_{\rm overlap}$. This effect can be understood as being caused by the finite formation time: note that Fig. 2.5 shows that $\epsilon^{\rm max}$ for $\tau_{\rm F} = 0$ is always larger than the energy density of Eq. (2.17). In that figure, the $\tau_{\rm F} = 0$ result has a maximum energy density $\epsilon^{\rm max} \approx 300$ GeV/fm^3 when $\sqrt{s_{\rm NN}} = 50$ GeV, while $\epsilon_{\rm overlap} \approx 8.5$

GeV/fm^3 at the same collision energy.

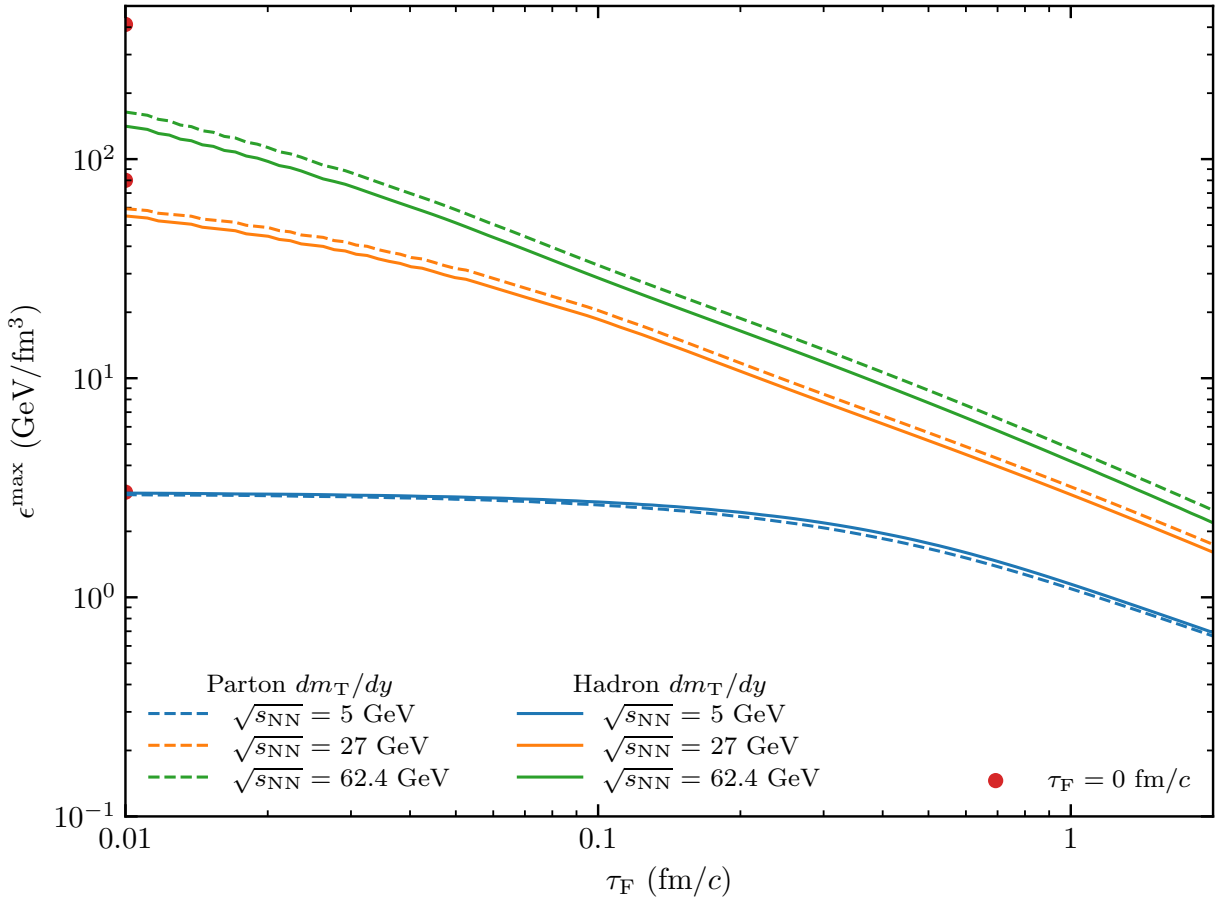

Figure 2.4: Maximum energy density $\epsilon^{\max}$ using the parton (dashed) or the hadron (solid) dm_T/dy in central, Au+Au collisions as a function of τ_F with $\sqrt{s_{NN}} = 5$, 27, and 62.4 GeV. The results using $\tau_F = 0$ fm/c are also shown for reference.

Figure 2.4 shows the formation time dependence of the maximum energy density using the parton or the hadron dm_T/dy for central, Au+Au collisions at $\sqrt{s_{NN}} = 5$, 27, and 62.4 GeV. There is a clear ordering of $\epsilon^{\max}$ for both dm_T/dy profiles, which can also be inferred from Fig. 2.3. At lower collision energies, the $\epsilon^{\max}$ from the parton dm_T/dy is slightly smaller than from the hadron dm_T/dy, and this deviation becomes smaller as τ_F decreases [45]. However, for $\sqrt{s_{NN}} \gtrsim 6$ GeV, the parton dm_T/dy yields maximum energy densities that are larger than from the hadron dm_T/dy, and this difference is roughly independent of τ_F as the formation time decreases below $\tau_F < 0.01$ fm/c. Notably, $\epsilon^{\max}$ from both dm_T/dy profiles becomes

mostly flat with $\tau_{\rm F}$ once a sufficiently small formation time is reached. In fact, the values at $\tau_{\rm F} = 0$ fm/c are also shown in Fig. 2.4 for reference. This fact represents a significant improvement over previous models which predicted diverging $\epsilon^{\rm max}$ as $\tau_{\rm F} \to 0$ [42, 43]. In the Bjorken energy density formula, the divergence goes like $1/\tau_{\rm F}$, while the more recent solution that considers only the finite duration time, but not the finite longitudinal width [43], goes like $\ln(1/\tau_{\rm F})$ for small formation times.

2.3.2 Finiteness of $\epsilon^{\rm max}$ at $\tau_{\rm F} = 0$

In Sec. 2.3.1, the numerical maximum energy density at $\tau_{\rm F} = 0$ fm/c for some collision energies was shown to be finite in this semianalytical model [45]. The symbols shown in Fig. 2.4 reflect these results and give an idea of how quickly $\epsilon^{\rm max}$ approaches these values as $\tau_{\rm F}$ decreases. Importantly, $\epsilon^{\rm max}(\tau_{\rm F} = 0)$ is finite for all collision energies, and the $\sqrt{s_{\rm NN}}$ dependence can be observed in Fig. 2.4 for the parton $dm_{\rm T}/dy$. For central Au+Au collisions at $\sqrt{s_{\rm NN}} \lesssim 7$ GeV, the maximum energy density value at $\tau_{\rm F} = 0$ fm/c is similar to the value at $\tau_{\rm F} = 0.1$ fm/c, i.e., they are within about 20% of each other. While these results are semianalytical in nature because Eq. (2.14) is not known to have an analytical solution, a proof for the finiteness of $\epsilon^{\rm max}(\tau_{\rm F} = 0)$ would substantiate the numerical results. To that end, an upper bound for $\epsilon^{\rm max}(\tau_{\rm F} = 0)$ is derived next.

In this semianalytical model, a parton's rapidity is given by Eq. (2.3), if it contributes to the density at mid-space-time pseudorapidity $\eta_s \approx 0$ [45]. This fact motivates the following change of variables to simplify the energy density of Eq. (2.14):

$$z_0 = -r_0 \sinh(y_0), \quad t - x = r_0 \cosh(y_0) \tag{2.18}$$

The subscript on the parton's rapidity is suppressed for clarity from now on, so Eq. (2.14)

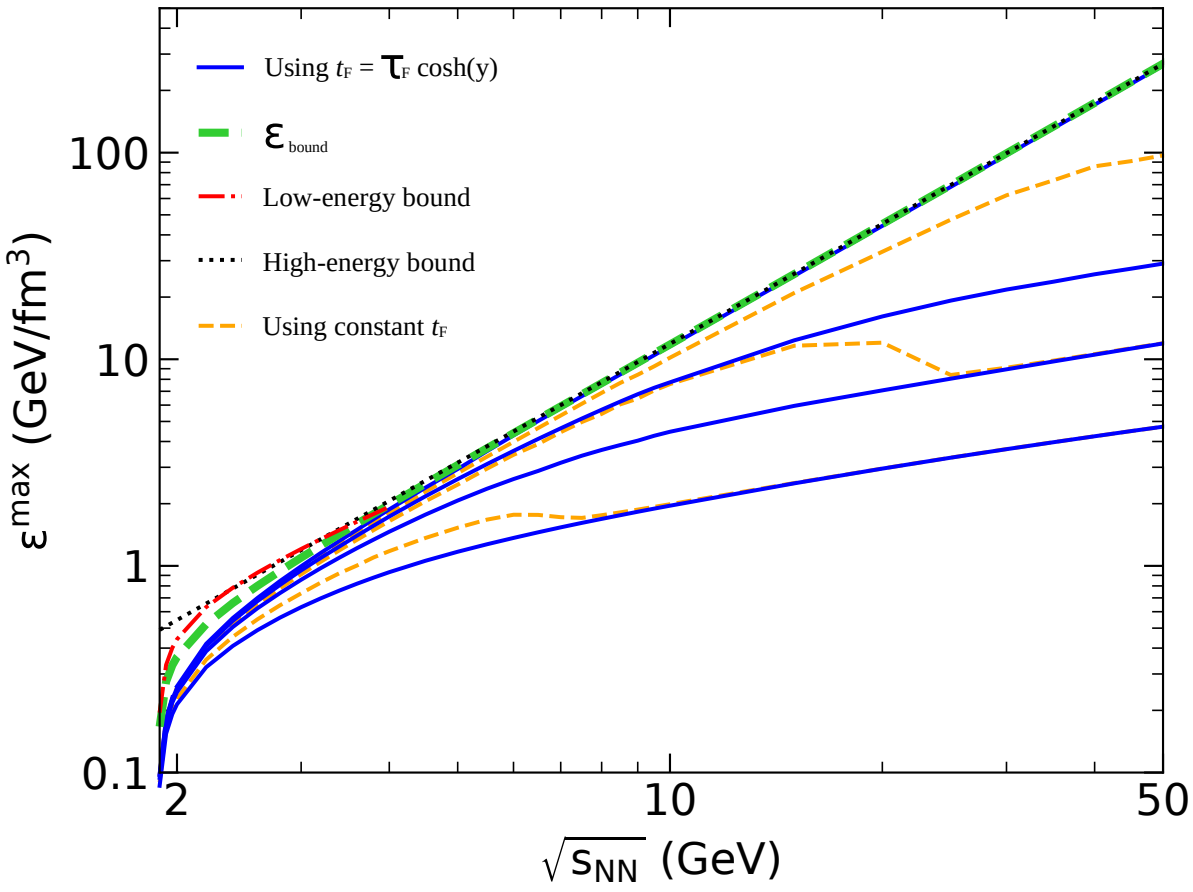

Figure 2.5: Maximum energy density for central Au+Au collisions as a function of collision energy at $\tau_F = 0, 0.1, 0.3$ and 0.9 fm/c in comparison with the upper bound of ϵ^{max} of Eq. (2.24), where the analytical low- and high-energy bounds are also shown. Dashed curves represent the ϵ^{max} results when using a constant formation time $t_F = 0.1, 0.3$, and 0.9 fm/c.

can be written as

$$\begin{aligned}\epsilon(t) &= \frac{2}{A_T \beta t_{21}^2} \iint_S \frac{dm_T}{dy} \cosh^2(y)\, dr_0 dy \\ &= \frac{2}{A_T \beta t_{21}^2} \int \frac{dm_T}{dy} \cosh^2(y) \Delta r_0(y) dy,\end{aligned} \tag{2.19}$$

where the definition $\Delta r_0(y) \equiv r_0^{\max}(y) - r_0^{min}(y)$ is also used for brevity [45].

Analysis of the generalized crossing diagram, which is similar to that shown in Fig. 2.1,

except using t_1 and t_2 instead of 0 and d_t, results in

$$r_0^{\min}(y) = 0, \quad r_0^{\max}(y) \leq r_1(y). \tag{2.20}$$

This result applies for times $t \leq t_2$, for a given parton rapidity y if the formation time is $\tau_{\rm F} = 0$ fm/c. Here, $r_1(y)$ is the r_0 value when a parton passing through the observation point $(0, t)$ with rapidity y intersects one of the $z_0 = \pm\beta(x - t_1)$ lines in the general crossing diagram:

$$r_1(y) = \frac{\beta(t - t_1)}{\beta\cosh(y) + |\sinh(y)|}. \tag{2.21}$$

Therefore, for times $t \leq t_2$, $\Delta r_0(y)$ is given by

$$\Delta r_0(y) \leq \frac{\beta t_{21}}{\beta\cosh(y) + |\sinh(y)|}, \tag{2.22}$$

whereas for times $t \geq t_2$, one obtains

$$\Delta r_0(y) = \frac{\beta\,\cosh(y)t_{21} - 2|\sinh(y)|(t - t_{\rm mid})}{\beta\cosh^2(y) - \sinh^2(y)/\beta}. \tag{2.23}$$

It is straightforward to show that this equation satisfies the inequality in Eq. (2.22). First, realize that $t - t_{\rm mid} \geq t_{21}/2$ since $t \geq t_2$ for this equation. Then, after the denominator is factored, the resulting term involving $\cosh(y) - |\sinh(y)|/\beta$ algebraically cancels with that in the numerator. These results can be combined with Eq. (2.19), which yields an upper bound on the produced energy density when $\tau_{\rm F} = 0$ fm/c and for the parton $dm_{\rm T}/dy$

$$\epsilon(t) \leq \frac{2}{A_{\rm T}t_{21}}\frac{dm_{\rm T}}{dy}(0)\int \frac{e^{-\frac{y^2}{2\sigma^2}}\,\cosh^2 y\; dy}{\beta\cosh y + |\sinh y|} \equiv \epsilon_{\rm bound}. \tag{2.24}$$

For central Au+Au collisions, this upper bound for the energy density is shown as a function of $\sqrt{s_{\rm NN}}$ in Fig. 2.5. At high collision energies, it approaches the $\epsilon^{\max}(\tau_{\rm F} = 0)$ value because the light cone boundaries overlap with the upper boundaries of the diamond

production region $z_0 = \pm\beta(x - t_2)$ as $\beta \to 1$. Therefore, the inequality of Eq. (2.22) becomes an equality for times $t \leq t_2$ but not for times $t > t_2$ [45]. The observation that $\epsilon_{\rm bound} \to \epsilon^{\rm max}(\tau_{\rm F} = 0)$ for large $\sqrt{s_{\rm NN}}$ suggests that the maximum energy density for $\tau_{\rm F} = 0$ fm/c is reached for a time $t \leq t_2$. In an earlier study, this was also the case for the triangular time profile where $\epsilon_{\rm tri}^{\rm max}$ occurs at a time $t_{\rm max} \in [t_{\rm mid} + \tau_{\rm F}, t_2 + \tau_{\rm F})$ [43]. There, the time at which the energy density attains its maximum value is $t_{\rm max} = t_{\rm mid} + \tau_{\rm F}/2 + \sqrt{\tau_{\rm F}}\sqrt{2t_{21} + \tau_{\rm F}}/2$.

An explicit analytical expression for the upper bound in Eq. (2.24) can be found using the following relation:

$$\frac{1}{\beta\cosh(y) + |\sinh(y)|} \leq \frac{e^{-|y|}}{\beta}. \tag{2.25}$$

Equation (A.3) then allows the upper bound in Eq. (2.24) to be simplified using the above inequality to the following:

$$\epsilon(t) \leq \frac{\mathrm{A}\sqrt{s_{\rm NN}}}{2A_{\rm T}\beta t_{21}}\left[2 + \mathrm{erfc}\left(\frac{\sigma}{\sqrt{2}}\right) + e^{4\sigma^2}\mathrm{erfc}\left(\frac{3\sigma}{\sqrt{2}}\right)\right]. \tag{2.26}$$

Here, $\mathrm{erfc}(x)$ refers to the well-known complementary error function. This result corresponds to the high energy limit of the upper bound and is shown in Fig. 2.5 where it agrees with $\epsilon_{\rm bound}$ when $\sqrt{s_{\rm NN}} \gtrsim 4$ GeV. However, the relation in Eq. (2.25) is not sufficiently restrictive for lower collision energies, so the high energy bound does not approach zero near the threshold energy, as one would expect [45].

For very low $\sqrt{s_{\rm NN}}$, where $\beta \ll 1$, the Gaussian width from Eq. (A.3) yields $\sigma < 0.707$ for $\sqrt{s_{\rm NN}} < 1.96$ GeV [45]. Because $\sigma < 1/\sqrt{2}$ implies that $\exp(-y^2/2/\sigma^2)\cosh^2(y) \leq 1$, the upper bound of Eq. (2.24) gives

$$\begin{aligned}\epsilon(t) &\leq \frac{2}{A_{\rm T}t_{21}}\frac{dm_{\rm T}}{dy}(0)\int\frac{dy}{\beta\cosh(y) + |\sinh(y)|} \\ &= \frac{8}{A_{\rm T}t_{21}\sqrt{1-\beta^2}}\frac{dm_{\rm T}}{dy}(0)\tanh^{-1}\left(\sqrt{\frac{1-\beta}{1+\beta}}\right).\end{aligned} \tag{2.27}$$

The above result can be considered as the low energy limit of the upper bound and is

also shown in Fig. 2.5. In that figure, the decrease of $\epsilon^{\max}(\tau_{\rm F} = 0)$ as $\sqrt{s_{\rm NN}} \to E_0$ is clearly recovered by Eq. (2.27), which visually verifies the analytical result. At very low collision energies near the threshold, Eq. (2.27) yields $\epsilon_{\rm bound} \propto \beta \ln(2/\beta)$ which approaches zero. Therefore, the maximum energy density $\epsilon^{\max}$ will also approach zero near the threshold collision energy even though the height of the initial transverse mass rapidity density $dm_{\rm T}/dy$ remains finite as is shown in Fig. A.5.

2.3.3 Comparing $\epsilon_{\rm hadron}$ to $\epsilon_{\rm Bj}$ and $\epsilon_{\rm tri}$

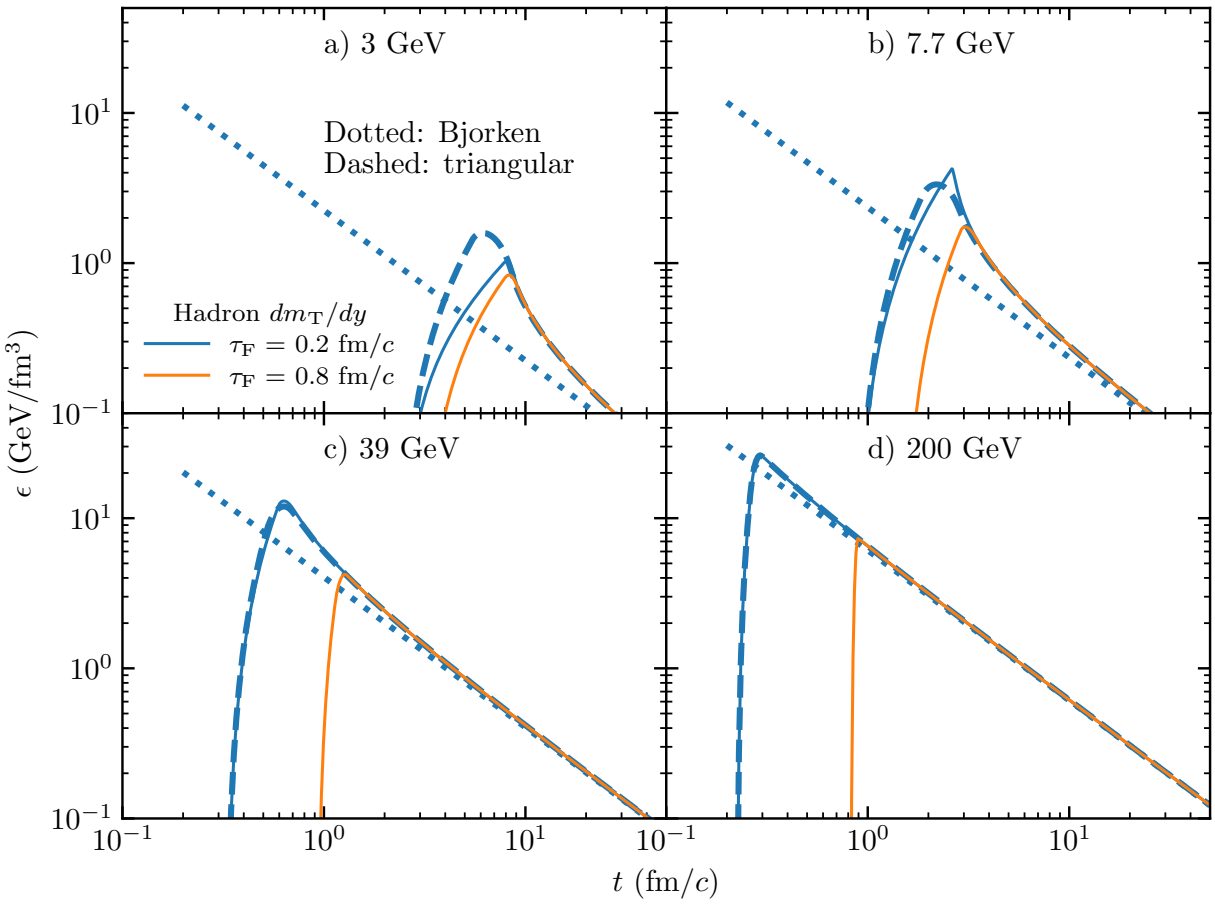

Figure 2.6: Energy density of produced hadrons in central Au+Au collisions at $\sqrt{s_{\rm NN}} = 3$, 7.7, 39, and 200 GeV for $\tau_{\rm F} = 0.2$ and 0.8 fm/c for the semianalytical model of Eq. (2.14), the Bjorken formula of Eq. (1.1), and the triangular solution of Eq. (2.28) for $\tau_{\rm F} = 0.2$ fm/c.

The differences between the $\epsilon_{\rm parton}$ and $\epsilon_{\rm hadron}$ and an analytical upper bound have been

discussed in Sec. 2.3.1 and Sec. 2.3.2, respectively. From now on, $\epsilon_{\rm hadron}$ will be used, unless otherwise specified, and the subscript will be excluded for clarity. This choice is made because the temperature T and chemical potentials μ can be extracted from a nuclear EoS if at least both the energy density and the net-baryon density are known [46]. Combining the results of $\epsilon_{\rm parton}(t)$ with $n_{\rm B}(t)$, which is calculated in Sec. 2.4, is incorrect because the $dm_{\rm T}/dy$ for initial partons is unrelated to the $dN_{\rm netB}/dy$ of Eq. (A.5). In the following section, ϵ from this semianalytical model [45] is compared with that of the Bjorken formula [42], and the more recent formula in Eq. (1.2) using a triangular time profile [43]. Note that $dm_{\rm T}/dy$ of Eq. (A.4) is substituted for the $dE_{\rm T}/dy$ term in Eqs. (1.1) and (1.2) in order to compare the results of the three models consistently.

Figure 2.6 shows the results of $\epsilon(t)$ in the central spacetime-rapidity region averaged over the full transverse overlap area for central Au+Au collisions at $\sqrt{s_{\rm NN}}$ = 3, 7.7, 39, and 200 GeV. The results are for $\tau_{\rm F}$ = 0.2 and 0.8 fm/c using the semianalytical model of Eq. (2.14), and $\tau_{\rm F}$ = 0.2 fm/c using the Bjorken formula of Eq. (1.1) and the triangular formula of Eq. (2.28). The large effect of including the finite nuclear thickness on the predicted energy densities is apparent from Fig. 2.6, especially at lower collision energies. Specifically, the time of maximum energy density occurs later when including the finite nuclear thickness effect [45]. This is similar to the effect of including the finite duration time d_t but not the finite z-width for parton production [43]. Because the Bjorken energy density formula of Eq. (1.1) diverges as $t \to 0$, the time of maximum energy density is $t_{\rm max} = \tau_{\rm F}$. For the triangular solution, $t_{\rm max}$ is given in Sec. 2.3.2 and can also be found in Ref. [43].

Also, the energy density of this semianalytical model can decrease more quickly for times just after $t_{\rm max}$ than the energy density of the Bjorken formula. This phenomenon is clearly seen in Fig. 2.6, and is especially evident at lower collision energies such as $\sqrt{s_{\rm NN}}$ = 3 or 7.7 GeV. The decrease of the energy density in Eq. (2.14) with time can be understood analytically since it behaves similarly to the results calculated using the uniform time profile of Ref. [43]. For that case, the energy density decreases as $\ln[(t-t_1)/(t-t_2)]$ for times

$t \geq t_2 + \tau_{\rm F}$ after $t_{\rm max}$ has been reached [46]. This means that for times t just after $t_2 + \tau_{\rm F}$, the energy density in this semianalytical model decreases as $\ln[1/(t - t_2)]$, which is faster than the $1/t$ rate of the Bjorken energy density for the same time t. Another way to interpret this phenomenon is in terms of a simple shift in time from t to $t - t_2$ on account of the finite nuclear thickness effect [46].

Compared to the triangular solution, the time of $\epsilon^{\rm max}$ for this semianalytical model occurs slightly later in time t, after $t_{\rm mid} + \tau_{\rm F}$ but earlier than $t_2 + \tau_{\rm F}$ [45] as shown in Fig. 2.6. This can be understood in terms of the decreasing rate at which the production region $S(t)$ grows for times $t \in [t_{\rm mid} + \tau_{\rm F}, t_2 + \tau_{\rm F}]$. Notably, the value of $\epsilon^{\rm max}$ in this semianalytical model is very close to the value of that in the triangular solution, for the same $\tau_{\rm F}$ and collision energy. Finally, for late times, $\epsilon_{\rm tri}(t)$ and $\epsilon(t)$ from the semianalytical model of Eq. (2.14) approach the Bjorken result [43, 45]. Note that the triangular solution is also a piecewise function of t [43]:

$$\begin{aligned}
\epsilon_{\rm tri}(t) &= \frac{4}{A_{\rm T} t_{21}^2} \frac{dm_{\rm T}}{dy}(0) \left[-t + t_1 + \tau_{\rm F} + (t - t_1) \ln\left(\frac{t - t_1}{\tau_{\rm F}} \right) \right], \text{ for } t \in [t_1 + \tau_{\rm F}, t_{\rm mid} + \tau_{\rm F}); \\
&= \frac{4}{A_{\rm T} t_{21}^2} \frac{dm_{\rm T}}{dy}(0) \left[t - t_2 - \tau_{\rm F} + (t - t_1) \ln\left(\frac{t - t_1}{t - t_{\rm mid}} \right) + (t_2 - t) \ln\left(\frac{t - t_{\rm mid}}{\tau_{\rm F}} \right) \right], \\
&\quad \text{for } t \in [t_{\rm mid} + \tau_{\rm F}, t_2 + \tau_{\rm F}); \\
&= \frac{4}{A_{\rm T} t_{21}^2} \frac{dm_{\rm T}}{dy}(0) \left[(t - t_1) \ln\left(\frac{t - t_1}{t - t_{\rm mid}} \right) + (t_2 - t) \ln\left(\frac{t - t_{\rm mid}}{t - t_2} \right) \right], \\
&\quad \text{for } t \in [t_2 + \tau_{\rm F}, \infty).
\end{aligned} \tag{2.28}$$

When the finite z-width of the initial parton production is ignored, only partons with $y \approx 0$ can enter the central spacetime-rapidity region of $\eta_s \approx 0$. Therefore, $dm_{\rm T}/dy(0)$ is present in the above triangular solution, because that solution only considers the finite duration time d_t for parton production [43].

As in Fig. 2.3, the maximum energy density $\epsilon^{\rm max}$ is extracted, and the values are plotted as functions of collision energy and formation time in Fig. 2.7 and Fig. 2.8, respectively. First,

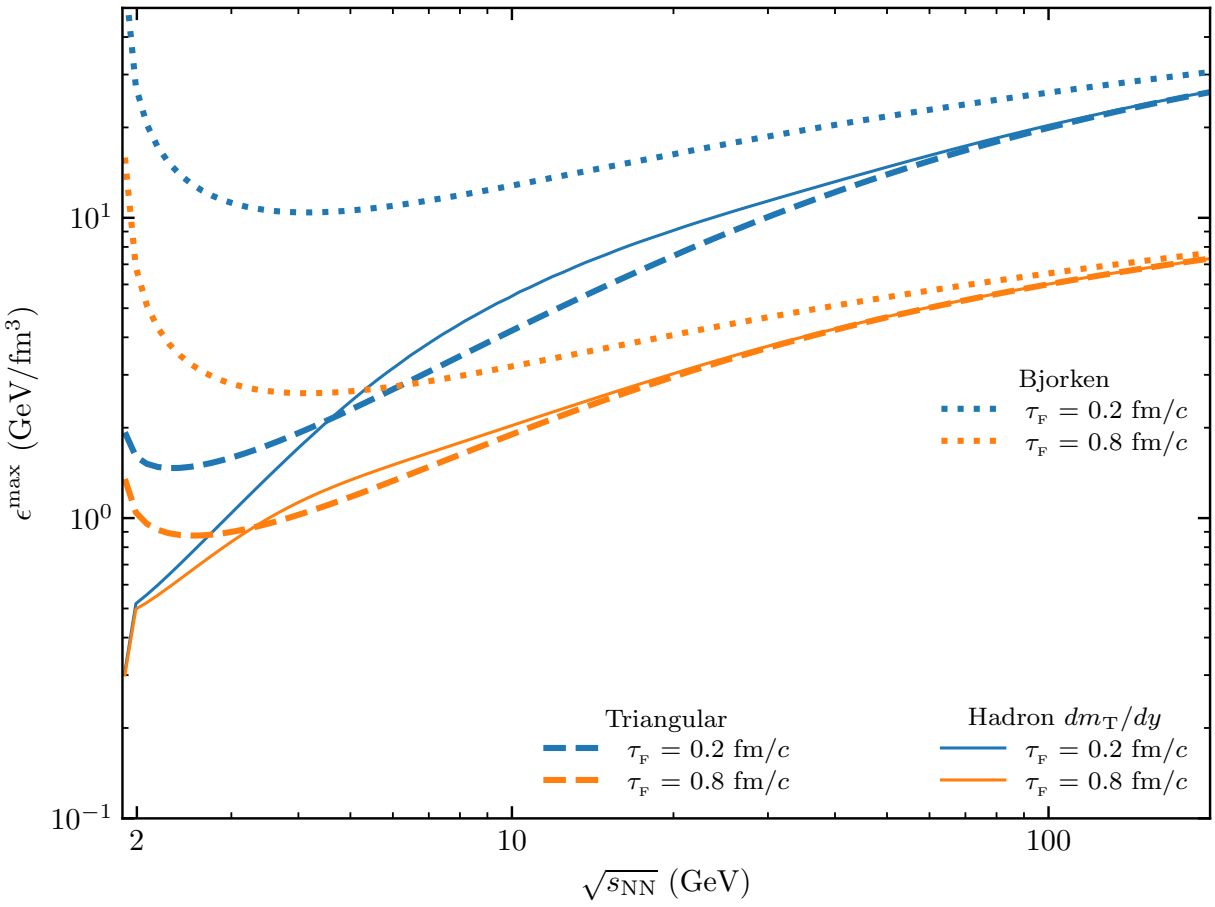

Figure 2.7: Maximum energy density using the hadron $dm_{\rm T}/dy$ in central Au+Au collisions as a function of $\sqrt{s_{\rm NN}}$ for $\tau_{\rm F} = 0.2$ and 0.8 fm/c for the semianalytical model of Eq. (2.14), the Bjorken formula of Eq. (1.1), and the triangular solution of Eq. (2.28).

the $\sqrt{s_{\rm NN}}$-dependence of $\epsilon^{\max}$ for Au+Au collisions with $\tau_{\rm F} = 0.2$ and 0.8 fm/c is shown in Fig. 2.7, in which the higher of the two curves corresponds to the smaller formation time for all three solutions. For large collision energies where $\tau_{\rm F} \gg d_t$, the semianalytical model results of Eq. (2.14) and the triangular solution of Eq. (2.28) approach the results of the Bjorken energy density formula [43, 45]. The naïve expectation that the semianalytical model results of Eq. (2.14) will differ significantly from the Bjorken $\epsilon^{\max}$ values when $\tau_{\rm F}/d_t \lesssim 1$ is depicted in Fig. 2.7. This limit can be thought of as the point at which the Bjorken energy density formula of Eq. (1.1) begins to break down [45].

In Fig. 2.8, the maximum energy density from Eq. (2.14) is compared to the Bjorken

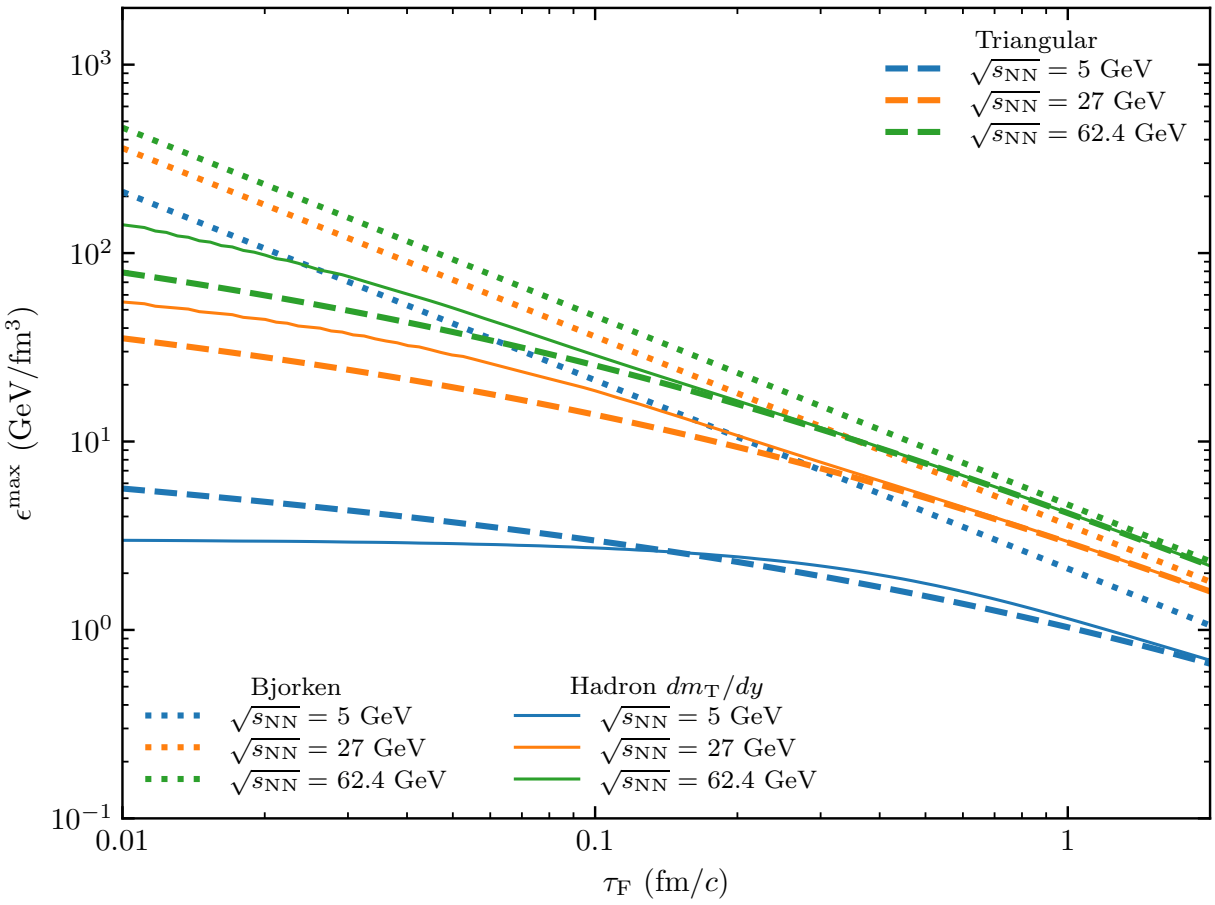

Figure 2.8: Maximum energy density using the hadron $dm_{\rm T}/dy$ in central Au+Au collisions as a function of $\tau_{\rm F}$ for $\sqrt{s_{\rm NN}} = 5$, 27, and 62.4 GeV for the semianalytical model of Eq. (2.14), the Bjorken formula of Eq. (1.1), and the triangular solution of Eq. (2.28).

and triangular solution $\epsilon^{\rm max}$ for central Au+Au collisions at $\sqrt{s_{\rm NN}} = 5$, 27, and 62.4 GeV as functions of $\tau_{\rm F}$. The flattening of $\epsilon^{\rm max}$ as $\tau_{\rm F} \to 0$ was also observed in Fig. 2.4 and is more apparent for lower collision energies. When $\tau_{\rm F}$ is not too small, the results of this semianalytical model [45] are quite close to the $\epsilon^{\rm max}$ of the triangular solution from Eq. (2.29). On the other hand, the $\epsilon^{\rm max}_{\rm Bj}$ is only sensitive to the value of $dm_{\rm T}/dy$ at mid-rapidity ($y = 0$), which grows for low collision energies as shown in Fig. A.1. Therefore, the Bjorken energy density formula of Eq. (1.1) predicts values that are much larger than the $\epsilon^{\rm max}$ of this model at low collision energies [45]. Note that this behavior also happens when the $\tau_{\rm F}$ value is sufficiently small, although for a real QGP, the difference may not matter since the parton

formation time is expected to be on the order $\tau_{\rm F} \approx 0.3$ - 1 fm/c.

The obvious difference between the two models is that there is a much weaker dependence on $\tau_{\rm F}$ for the $\epsilon^{\rm max}$ values of this semianalytical model, especially at lower collision energies [45]. The same qualitative features are displayed by the $\epsilon^{\rm max}$ from the triangular solution of Eq. (2.28), and this behavior was already found in the previous study [43]. When the $\epsilon^{\rm max}$ values of Eq. (2.14) are significantly different from those of the triangular solution, the ratio of the formation time to the duration time is found to be $\tau_{\rm F}/d_t \lesssim 0.2$. Sometimes, $\epsilon^{\rm max}$ from this semianalytical model can be larger than that of the triangular solution for some moderate collision energies; however, for small $\sqrt{s_{\rm NN}}$, the reverse is true [45]. The $\epsilon^{\rm max}$ according to the triangular time profile is given in Ref. [43] as:

$$\epsilon^{\rm max}_{\rm tri} = \frac{2}{A_{\rm T} t_{21}} \frac{dm_{\rm T}}{dy}(0) \left[-1 - \frac{\tau_{\rm F}}{t_{21}} + \sqrt{\frac{\tau_{\rm F}}{t_{21}}} \sqrt{2 + \frac{\tau_{\rm F}}{t_{21}}} + 2 \ln \left(\frac{1 + \sqrt{1 + 2t_{21}/\tau_{\rm F}}}{2} \right) \right] . \quad (2.29)$$

It is clear from the last term in the above definition that the triangular $\epsilon^{\rm max}$ diverges as $\ln(1/\tau_{\rm F})$ at low collision energies, but as $1/\tau_{\rm F}$ for high collision energies [43]. This is in contrast to the Bjorken formula which $\epsilon^{\rm max}$ diverges as $1/\tau_{\rm F}$ for all collision energies [42].

2.3.4 Scaling and A-dependence of $\epsilon^{\rm max}$

The initial produced energy density of Eq. (2.14) has an approximate scaling property [45]. In the hard sphere model of the nucleus, the z-width of the production region and the duration time d_t of the nuclear crossing are both proportional to $\rm A^{1/3}$. One also expects that the mid-rapidity value $dm_{\rm T}/dy(0)$ to be approximately proportional to the number of participant nucleons N_p [45]. In this semianalytical model, it is assumed that all 2A nucleons participate in the initial production of central A+A collisions; therefore, one also finds $dm_{\rm T}/dy(0) \propto$ A [45]. The PHENIX Collaboration also found this result in their parametrization of the final hadron $dE_{\rm T}/dy$ [44]. Equation (A.3) then implies that the Gaussian width of the $dm_{\rm T}/dy$ profile of produced partons must be independent of A. If this

were not the case, the proportionality of $dm_{\rm T}/dy(0)$ to A previously mentioned would break down for the central A+A collisions to which this semianalytical model applies [43, 45].

A scaled time t^s and scaled proper formation time $\tau_{\rm F}^s$ can be defined according to

$$t^s = \frac{t}{{\rm A}^{1/3}},\ \tau_{\rm F}^s = \frac{\tau_{\rm F}}{{\rm A}^{1/3}}. \tag{2.30}$$

The approximate conditions that the z-width and d_t of the production region are proportional to $A^{1/3}$ and $dm_{\rm T}/dy(0) \propto A$ implies the following facts [45]. First, for a given collision energy, $\epsilon(t)$ from Eq. (2.14) depends on the scaled t^s and $\tau_{\rm F}^s$ only, and second, $\epsilon^{\rm max}$ is only a function of $\tau_{\rm F}^s$. Therefore, one finds the following scaling relation of the maximum energy density for different collision systems (i.e., different A and $\tau_{\rm F}$):

$$\epsilon_{\rm AA}^{\rm max}(\tau_{\rm F}) = \epsilon_{\rm AuAu}^{\rm max}\left(\tau_{\rm F}^{\rm Au} = (197/{\rm A})^{1/3}\tau_{\rm F}\right). \tag{2.31}$$

Specifically, one can compare the maximum energy density for central O+O collisions with $\tau_{\rm F} = 0.30$ fm/c with those of central Au+Au collisions with $\tau_{\rm F} = 0.69$ fm/c at the same collision energy: $\epsilon_{\rm OO}^{\rm max}(\tau_{\rm F} = 0.30\ {\rm fm}/c) = \epsilon_{\rm AuAu}^{\rm max}(\tau_{\rm F} = 0.69\ {\rm fm}/c)$. Equation (2.31) also implies that $\epsilon_{\rm AA}^{\rm max}(\tau_{\rm F} = 0)$ is a function of collision energy only, not depending on A [45]. One can also apply the scaling relation of Eq. (2.31) to p + p collisions [70] even though collision systems with A = 1 are not technically within the scope of this semianalytical model [43, 45]. However, if one did use this scaling relationship in such a way, the result is $\epsilon_{\rm AA}^{\rm max}(\tau_{\rm F} = 0) = \epsilon_{\rm pp}^{\rm max}(\tau_{\rm F} = 0)$ for central AA collisions at the same $\sqrt{s_{\rm NN}}$.

The A-dependence of $\epsilon^{\rm max}$ for central collisions can be recovered from the $\tau_{\rm F}$-dependence of $\epsilon^{\rm max}$ at a given $\sqrt{s_{\rm NN}}$, such as from the results shown in Fig. 2.4, from the scaling relation of Eq. (2.31). Notably, this scaling is also satisfied by the previous Bjorken formula [42] of Eq. (1.1) and the triangular solution [43] of Eq. (2.28). Note that the A-dependences of the maximum energy density in these two previous models will be different from in this semianalytical model [45] because the $\tau_{\rm F}$-dependence is different as shown by Fig. 2.8. This

means that the $\epsilon^{\max}$ of this semianalytical model increases very slowly with A since the $\tau_{\rm F}$-dependence is almost flat. The maximum energy densities from the Bjorken formula of Eq. (1.1) grow quickly with A at small $\tau_{\rm F}$. However, for a finite $\tau_{\rm F}$, and high enough collision energy, our semianalytical model recovers the Bjorken $\epsilon^{\max}$ where $\epsilon^{\max} \propto {\rm A}^{1/3}$ for a fixed formation time. Finally, note that the upper bound $\epsilon_{\rm bound}$ of Eq. (2.24) would be independent of A if the same approximations on the z-width, duration time d_t, and $dm_{\rm T}/dy(0)$ are made [45].

2.4 Initial Net Conserved-Charge Densities

So far, the semianalytical model has been applied only to the initial energy densities for central Au+Au collisions. The net-baryon density $n_{\rm B}(t)$ can be calculated using the same method as outlined in the previous section for $\epsilon(t)$ [45]. One then obtains the following equation for the net-baryon density that is similar to Eq. (2.4):

$$n_{\rm B}(t) = \frac{1}{A_{\rm T}} \iint_S \frac{dx dz_0}{t-x} \frac{d^3 N_{\rm netB}}{dx dz_0 dy} \cosh^2(y). \tag{2.32}$$

Note that there is one fewer power of $\cosh y$ in this equation than in Eq. (2.14) because that equation involves $E = m_{\rm T}\cosh(y)$. The same assumptions regarding the factorization of $d^3 m_{\rm T}/dx/dz_0/dy$ and the uniform production of partons in Eq. (2.13) is applied to the above expression of $n_{\rm B}(t)$ [46]. One then obtains $d^3 N_{\rm netB}/dx/dz_0/dy = 2/(\beta t_{21}^2) dN_{\rm netB}/dy$. Therefore, the net-baryon density $n_{\rm B}(t)$ is also given by a piecewise solution of time t, as shown in Table 2.1.

The net-baryon density $n_{\rm B}(t)$ of Eq. (2.32) is plotted in Fig. 2.9 for central Au+Au collisions at $\sqrt{s_{\rm NN}}$ = 3, 7.7, 39, and 200 GeV with $\tau_{\rm F}$ = 0.2 and 0.8 fm/c. Similarly to the energy density $\epsilon(t)$ of Eq. (2.14), the net-baryon density starts at zero for $t \leq t_1 + \tau_{\rm F}$ and increases smoothly with time until $t_{\max}$. Note that the $t_{\max}$ for the maximum net-baryon density is the same as that for the maximum energy density in the semianalytical

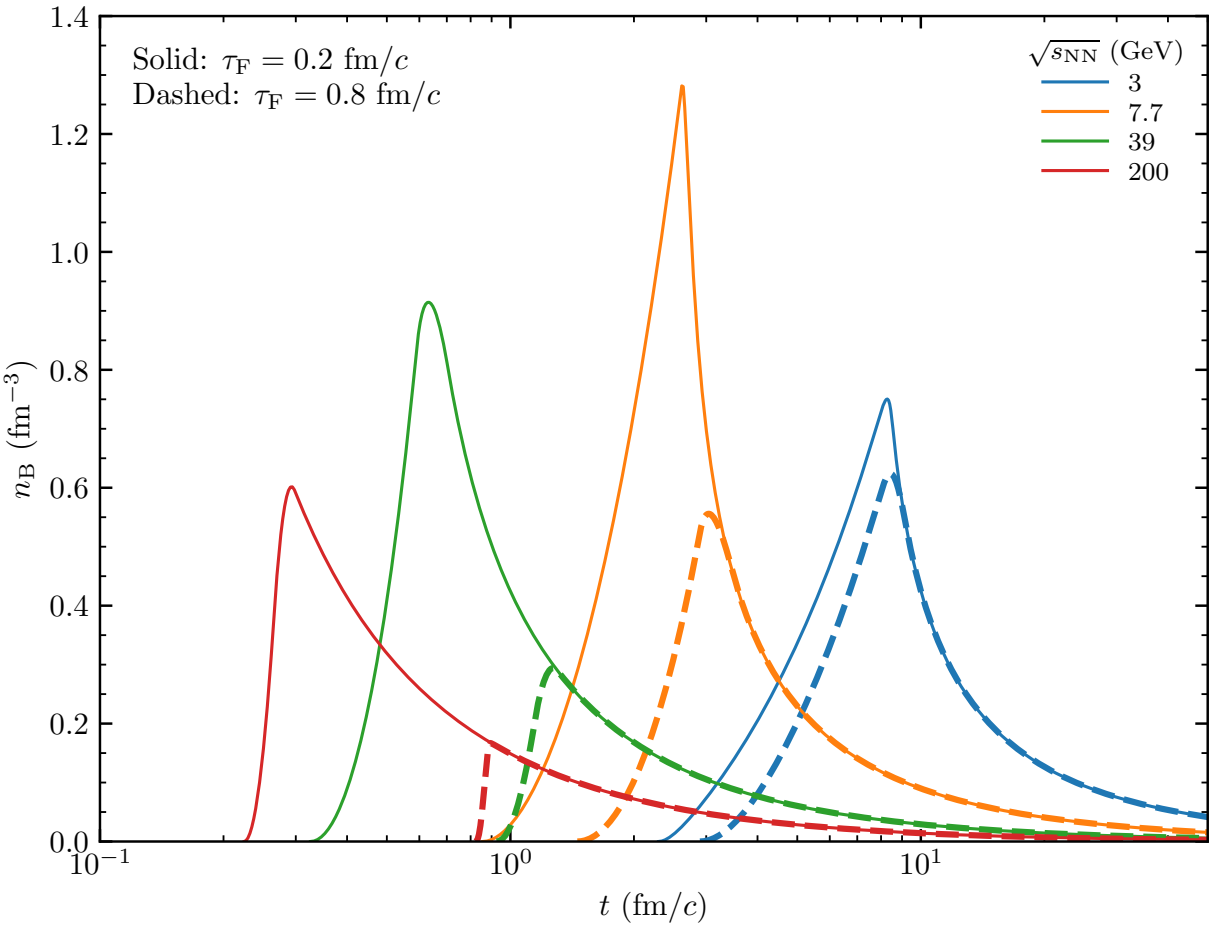

Figure 2.9: Net-baryon density $n_B(t)$ in central Au+Au collisions at $\sqrt{s_{NN}} = 3$, 7.7, 39, and 200 GeV for $\tau_F = 0.2$ and 0.8 fm/c. Note that these results are for $t_1 = 0.2d_t$ and $t_2 = 0.8d_t$.

model [46]. This is expected since the integration limits of Table 2.1 are the same for both produced densities. After t_{max}, the net-baryon density decreases and the late-time evolution is independent of the formation time. Interestingly, the maximum net-baryon density n_B^{max} decreases with increasing $\sqrt{s_{NN}}$ for most collision energies, except when it increases for some small to intermediate $\sqrt{s_{NN}}$ for a small enough τ_F [46].

If one would adapt the Bjorken energy density formula to calculate the net-baryon density by substituting dN_{netB}/dy for dm_T/dy, one would have

$$n_B^{Bj}(t) = \frac{1}{A_T}\frac{1}{t}\frac{dN_{netB}}{dy}. \tag{2.33}$$

It is clear from the t-dependence of the above equation that the same divergent behavior is expected in n_{B}^{Bj} as occurs in ϵ_{Bj}. Additionally, the late time evolution of the net-baryon density from Eq. (2.32) approaches the results of the Bjorken net-baryon formula of Eq. (2.33) for all formation times [46]. The approach to the Bjorken results also occurs earlier in time for larger $\sqrt{s_{\mathrm{NN}}}$ in the same way as does $\epsilon(t)$ from the semianalytical model. Finally, the maximum net-baryon density $n_{\mathrm{B}}^{\mathrm{max}}$ from the results of Eq. (2.32) are lower than the Bjorken ones at the same τ_{F}, but this difference decreases at higher collision energies [46].

While the net-electric charge Q is carried by the incoming protons, the net-baryon number B is carried by all the incoming nucleons. In this semianalytical model, it is assumed that the initial densities are produced by the primary NN collisions and are independent of the nucleon type [46]. This physically motivated assumption results in the net-electric charge density n_{Q} being strictly proportional to n_{B} for all times t throughout the evolution:

$$n_{\mathrm{Q}}(t) = n_{\mathrm{B}}(t)\frac{\mathrm{Z}}{\mathrm{A}}, \tag{2.34}$$

where Z and A are the atomic number and mass number of the colliding nuclei, respectively. Note that the semianalytical model for the initial production so far only applies to symmetric A+A collisions; however, future studies may warrant a generalization to non-symmetric and/or non-central collisions [46]. The above relationship for the net-electric charge density has also been used in other studies [89].

Finally, this semianalytical model is limited to considering nuclei which do not have valence-level strange s quarks. Therefore, the net-strangeness of the colliding nuclei is $S = 0$; and we assume that the production of s and $\bar{s}$ is symmetric [46]. This final assumption accounts for the phenomenologically relevant constraint of strangeness neutrality in the semianalytical model:

$$n_{\mathrm{S}}(t) = 0. \tag{2.35}$$

2.5 Transverse Expansion

Until now, the semianalytical model has been used to calculate the initial densities averaged over the entire transverse overlap area A_{T}. Unfortunately, this framework prevents the semianalytical model from being able to include the transverse flow phenomenon which has been observed at RHIC [1]. Therefore, the effect of transverse expansion on the produced densities of this semianalytical model is investigated by assuming that the radius of the transverse overlap area R_{T} in central A+A collisions increases with time [46] according to:

$$R_{\mathrm{T}}(t) = R_{\mathrm{A}} + \beta_{\mathrm{T}}(t)\,(t - t_1 - \tau_{\mathrm{F}})\,. \tag{2.36}$$

Here, the transverse flow velocity is modeled according to

$$\beta_{\mathrm{T}}(t) = \begin{cases} 0, & \text{for } t < t_1 + \tau_{\mathrm{F}} \\ \left[1 - e^{-(t-t_1-\tau_{\mathrm{F}})/t_{\mathrm{T}}}\right] \beta_{\mathrm{T,f}}, & \text{for } t \geq t_1 + \tau_{\mathrm{F}}. \end{cases} \tag{2.37}$$

The kinetic freezeout parameters, which were obtained by fitting the transverse momentum spectral shapes for central Au+Au collisions at 7.7 up to 200 GeV and Pb+Pb collisions at 2.76 TeV to a blast-wave model [70, 37, 17], have been used for this parametrization [46]. This data allows us to parametrize the final value of the transverse flow velocity $\beta_{\mathrm{T,f}}$ as

$$\beta_{\mathrm{T,f}} = \left[\frac{\ln\left(\sqrt{s_{\mathrm{NN}}}/E_0\right)}{64.7 + \ln\left(\sqrt{s_{\mathrm{NN}}}/E_0\right)}\right]^{0.202}. \tag{2.38}$$

We see that $\beta_{\mathrm{T,f}} \to 0$ as $\sqrt{s_{\mathrm{NN}}} \to E_0$. Note that the kinetic freezeout parameters reported in Ref. [37] contained various data [90, 91, 92, 93, 94, 95, 96, 97, 98, 99, 100, 101], which have also been used here.

After parametrizing $\beta_{\mathrm{T,f}}$, we assume that $t_{\mathrm{T}} \propto 1/n^{\max}$ to parametrize the timescale for the transverse flow development t_{T}, where $n^{\max}$ is taken as the parton number density at the time of $\epsilon^{\max}$. Here we assume that parton collisions lead to the transverse flow and that a

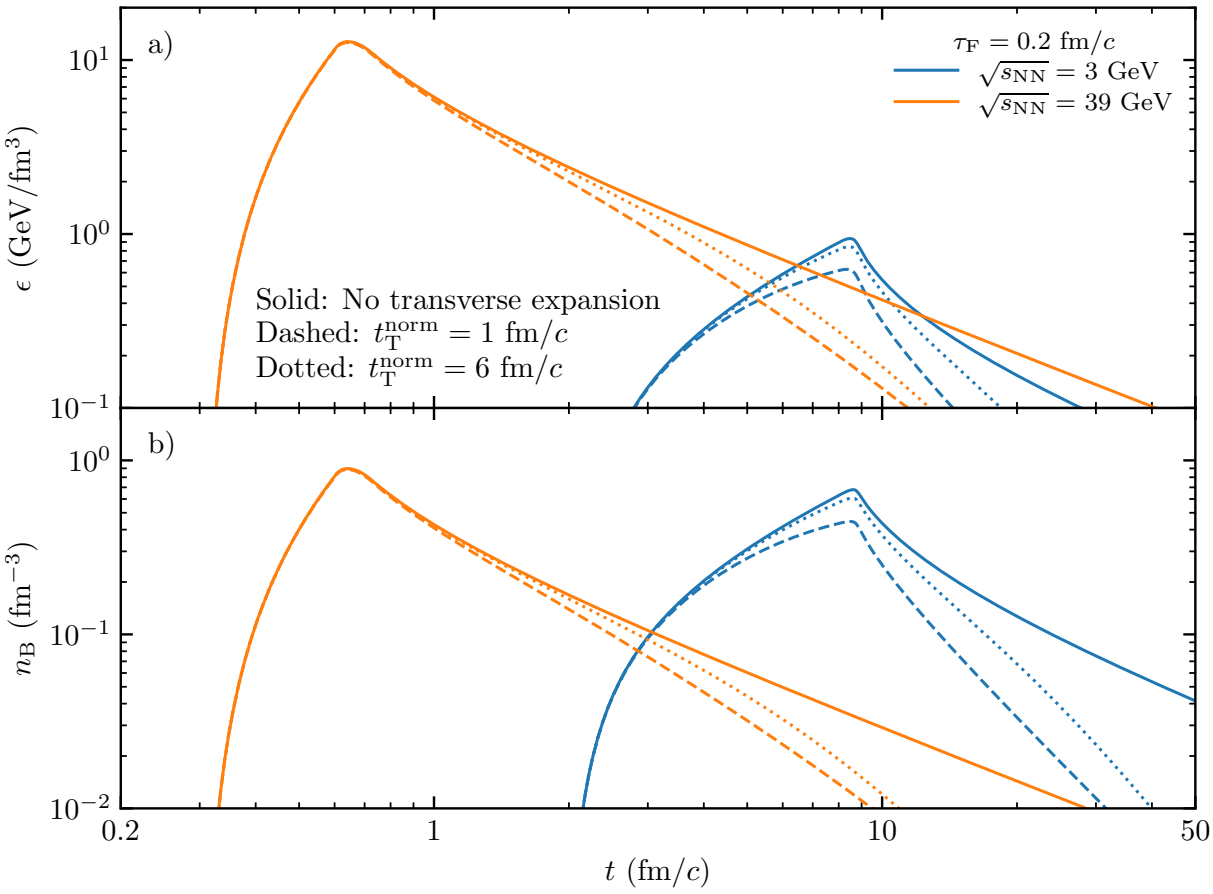

Figure 2.10: (a) Energy density $\epsilon(t)$ and (b) net-baryon density $n_B(t)$ for central Au+Au collisions at $\sqrt{s_{NN}} = 3$ and 39 GeV with $\tau_F = 0.2$ fm/c without transverse expansion and with transverse expansion with $t_T^{norm} = 1$ and 6 fm/c. Note that these results use the hadron dm_T/dy and $t_1 = d_t/6$ and $t_2 = 5d_t/6$.

parton's mean-free-path is inversely proportional to the parton number density [46]. Thus, a higher Using Boltzmann statistics, the simple relationship $n = \sqrt[4]{52\epsilon^3/27/\pi^2}$ is found for a massless QGP composed of gluons and three quark flavors, and the following maximum energy density that assumes a uniform production profile in time [43] is used:

$$\epsilon_{uni}^{max} = \frac{1}{\pi R_A^2 (t_2 - t_1)} \frac{dm_T}{dy}(0) \ln\left(1 + \frac{t_2 - t_1}{\tau_F}\right). \tag{2.39}$$

Note that $t_1 = 0.264 d_t$ and $t_2 = 0.736 d_t$ have been used in the above equation [46]. This choice ensures that the uniform time profile matches the mean and standard deviation of time

as the uniform $g(z_0, x)$ with $t_1 = d_t/6$ and $t_2 = 5d_t/6$. In this semianalytical model, choosing t_1 and t_2 in this manner ensures that $\epsilon^{\max} = 2\rho_0 m_{\rm N}$ and $n_{\rm B}^{\max} = 2\rho_0$ for the threshold collision energy $\sqrt{s_{\rm NN}} = E_0$ as one would naïvely expect. If the two colliding nuclei fully overlapped without interacting, the maximum densities would satisfy these conditions. Finally, $t_{\rm T}$ is normalized to a given value $t_{\rm T}^{\rm norm}$ for a collision energy $\sqrt{s_{\rm NN}} = 200$ GeV and parton proper formation time $\tau_{\rm F} = 0.3$ fm/c.

The effect on the initial densities when $t_{\rm T}^{\rm norm}$ is changed from 1 to 6 fm/c has also been investigated [46]. In Fig. 2.10, the energy density $\epsilon(t)$ and the net-baryon density $n_{\rm B}(t)$ for Au+Au collisions at $\sqrt{s_{\rm NN}} = 3$ and 39 GeV with $\tau_{\rm F} = 0.2$ fm/c are shown. Note that these results and all future results in this dissertation use $t_1 = d_t/6$ and $t_2 = 5d_t/6$ for the reason described above [46]. For early times before $t_{\max}$ is reached, the transverse expansion has essentially no effect on the produced energy density or net-baryon density. This is understandable since $t - t_1 - \tau_{\rm F}$ is still small compared to the value of $t_{\rm T}$. Once the maximum density is reached, the effect of transverse expansion becomes noticeable in that the peak value may be slightly smaller with transverse expansion than without [46]. This effect is more noticeable for lower collision energies and smaller values of $t_{\rm T}^{\rm norm}$. In fact, the case without transverse expansion may be considered as the limiting case of $t_{\rm T}^{\rm norm} \to \infty$ since this would delay the effect of transverse flow until far after the produced densities have reached zero. Finally, the late time evolution of the energy and net-baryon densities both behave in the same way after transverse expansion is considered. Namely, they decrease at a faster rate than their corresponding densities without transverse expansion and the relative change is the same for both quantities. This is because the transverse flow effect has been modeled with an expanding area [46] over which the corresponding energy or conserved charge is averaged over instead of including the effect inside the integrals of Eq. (2.14) or (2.32).

Chapter 3

Studying Trajectories in the QCD Phase Diagram

The thermodynamic properties and QCD phase diagram trajectories of the matter produced in central Au+Au collisions are presented and studied in this chapter. First, the equation of state (EoS) for a non-interacting, massless QGP is derived using Boltzmann or quantum statistics in Sec. 3.1. The temperature T and chemical potentials μ including their peak values are analyzed for a variety of different collision energies and parton formation times. Special attention is given to the location of a trajectory to the conjectured QCD critical point, the crossover line from FRG calculations, and certain constant energy density lines. The online web application has also been modified to perform the semianalytical calculations of the trajectories in the QCD phase diagram using the ideal gas EoS with either statistics [88]. Next, a more realistic lattice QCD-based EoS is presented in Sec. 3.2, and a similar analysis is done, especially comparing the more realistic trajectories to those from the conformal EoS. Then in Sec. 3.3, the strangeness neutrality in the lattice EoS is assessed, and interesting qualitative features are discussed relative to the functional renormalization group (FRG) calculations with $N_f = 2 + 1$. Finally, Sec. 3.4 gives a method to calculate the QGP lifetime for a given trajectory, and it is shown that the lattice EoS is unable to do so for collision energies below $\sqrt{s_{\mathrm{NN}}} \lesssim 7.7$ GeV. The QGP lifetime results from the ideal gas EoS indicate that the QGP formation depends on the EoS, the parton formation time, and the transverse expansion effect. However, recent results from the STAR Collaboration show that the matter formed by $\sqrt{s_{\mathrm{NN}}} = 3$ GeV Au+Au collisions is dominated by hadron degrees of freedom.

These results provide a useful tool for calculating the trajectory of the hot dense matter in the QCD phase diagram and should be useful for estimating the necessary collision energy for a trajectory to pass near the CEP. Until an improved realistic EoS is developed and can be used, the results of the ideal gas EoS seem to yield reasonably accurate results.

3.1 Trajectories of a Massless QGP for an Ideal Gas EoS

A previous study considered the thermodynamics of a QGP composed of gluons g and three quark flavors u, d, and s [61]. In that study, the authors used the current quark masses from the particle data group (PDG) [102] of $m_u = 2.16$ MeV/c^2, $m_d = 4.67$ MeV/c^2, and $m_s = 93$ MeV/c^2. It was also found that there is essentially no difference in the trajectories of the matter formed by relativistic heavy ion collisions if the quark masses are neglected [46, 61]. Therefore, a massless 3+1 flavor QGP is considered in the following results. The total energy, net-baryon, net-electric charge, and net-strangeness densities of such a system are found by summing over the individual partons' contributions [46, 61]:

$$\epsilon = \epsilon_g + \sum_q \left(\epsilon_q + \epsilon_{\bar{q}}\right), \qquad n_{\mathrm{B}} = \sum_q B_q \left(n_q - n_{\bar{q}}\right),$$
$$n_{\mathrm{Q}} = \sum_q Q_q \left(n_q - n_{\bar{q}}\right), \qquad n_{\mathrm{S}} = \sum_q S_q \left(n_q - n_{\bar{q}}\right). \tag{3.1}$$

Here, B_q, Q_q, and S_q refer to the baryon, electric charge, and strangeness numbers of quark flavor q, respectively. In general, the energy density ϵ_i and the number density n_i for a parton of flavor i are given by integrals over the momentum phase space with the phase-space density

and can be written as

$$\epsilon_i = \frac{1}{2\pi^2} \int_0^\infty dp\ p^2 \sqrt{p^2 + m_i^2}\ f_i(p),$$
$$n_i = \frac{1}{2\pi^2} \int_0^\infty dp\ p^2 f_i(p), \tag{3.2}$$

respectively, where m_i represents the parton mass. The single-particle distribution function $f_i(p)$ for a parton of flavor i in equilibrium is given by

$$f_i(p) = d_i \left[\exp\left(\frac{\sqrt{p^2 + m_i^2} - \mu_i}{T} \right) + K \right]^{-1}. \tag{3.3}$$

The degeneracy factor d_i in the above equation considers the number of unique spin and color states for each parton. Gluons have $d_i = 2 \times 8 = 16$ degenerate states, while quarks have $d_i = 2 \times 3 = 6$. Each parton has a chemical potential μ_i and the temperature T determines the phase space distribution of partons. The constant K is a factor which defines the statistics to be used: $K = 0$ for Boltzmann statistics, $K = 1$ for Fermi-Dirac statistics, and $K = -1$ for Bose-Einstein statistics [46]. The chemical potential for each parton flavor i is defined simply by the linear combination $\mu_i = B_i\mu_\mathrm{B} + Q_i\mu_\mathrm{Q} + S_i\mu_\mathrm{S}$, where μ_B, μ_Q, and μ_S are, respectively, the baryon, electric charge, and strangeness chemical potentials [46, 61].

3.1.1 The Ideal Gas EoS with Quantum Statistics

The gluons are bosons, having spin 1, while the quarks and anti-quarks are fermions, having spin 1/2. Thus, the massless QGP under consideration will use Bose-Einstein statistics for the gluons and Fermi-Dirac statistics for the quarks and antiquarks. For brevity, these two statistics will be combined under the term "quantum" statistics in all future discussions as was done in Ref. [46]. Next, the gluon chemical potential is $\mu_g = 0$ since it carries no baryon number, electric charge, or strangeness. Furthermore, the antiquark chemical potential is

related to the quark chemical potential if the two share the same flavor q according to $\mu_q + \mu_{\bar{q}} = 0$. With these definitions, one can straightforwardly write down the total energy density and net-number density of a quark-antiquark pair in quantum statistics as

$$\begin{aligned} \epsilon_q + \epsilon_{\bar{q}} &= -\frac{18T^4}{\pi^2}\left[Li_4\left(-e^{-\mu_q/T}\right) + Li_4\left(-e^{\mu_q/T}\right)\right] = \frac{7\pi^2}{20}T^4 + \frac{3\mu_q^2}{2}T^2 + \frac{3\mu_q^4}{4\pi^2}, \\ n_q - n_{\bar{q}} &= \frac{6T^3}{\pi^2}\left[Li_3\left(-e^{-\mu_q/T}\right) - Li_3\left(-e^{\mu_q/T}\right)\right] = \mu_q T^2 + \frac{\mu_q^3}{\pi^2}. \end{aligned} \tag{3.4}$$

Here, the polylogarithm function of order n, $Li_{\mathrm{n}}(z)$, is used in the same manner as Ref. [103]. The right-hand sides of both lines in the equations above are obtained from the corresponding sum or difference of polylogarithm functions using the following relationship for the Bernoulli polynomials $B_n(x)$:

$$Li_{\mathrm{n}}(z) = (-1)^{n-1}Li_{\mathrm{n}}\left(\frac{1}{z}\right) - \frac{(2\pi i)^n}{n!}B_n\left(\frac{\ln(-z)}{2\pi i} + \frac{1}{2}\right). \tag{3.5}$$

Note that the above relationship is valid when z is not in the range $(0, 1)$ and for strictly positive natural numbers $n \in \mathbb{N}^+$.

On substituting these expressions into the definitions of the total energy and net-conserved charge densities of Eq. (3.1), one obtains

$$\begin{aligned} \epsilon = {} & \frac{19\pi^2}{12}T^4 + \frac{(\mu_{\mathrm{B}} + 2\mu_{\mathrm{Q}})^2 + (\mu_{\mathrm{B}} - \mu_{\mathrm{Q}})^2 + (\mu_{\mathrm{B}} - \mu_{\mathrm{Q}} - 3\mu_{\mathrm{S}})^2}{6}T^2 \\ & + \frac{(\mu_{\mathrm{B}} + 2\mu_{\mathrm{Q}})^4 + (\mu_{\mathrm{B}} - \mu_{\mathrm{Q}})^4 + (\mu_{\mathrm{B}} - \mu_{\mathrm{Q}} - 3\mu_{\mathrm{S}})^4}{108\pi^2}, \end{aligned} \tag{3.6}$$

$$n_{\mathrm{B}} = \frac{\mu_{\mathrm{B}} - \mu_{\mathrm{S}}}{3}T^2 + \frac{(\mu_{\mathrm{B}} + 2\mu_{\mathrm{Q}})^3 + (\mu_{\mathrm{B}} - \mu_{\mathrm{Q}})^3 + (\mu_{\mathrm{B}} - \mu_{\mathrm{Q}} - 3\mu_{\mathrm{S}})^3}{81\pi^2}, \tag{3.7}$$

$$n_{\mathrm{Q}} = \frac{2\mu_{\mathrm{Q}} + \mu_{\mathrm{S}}}{3}T^2 + \frac{2(\mu_{\mathrm{B}} + 2\mu_{\mathrm{Q}})^3 - (\mu_{\mathrm{B}} - \mu_{\mathrm{Q}})^3 - (\mu_{\mathrm{B}} - \mu_{\mathrm{Q}} - 3\mu_{\mathrm{S}})^3}{81\pi^2}, \tag{3.8}$$

$$n_{\mathrm{S}} = -\frac{\mu_{\mathrm{B}} - \mu_{\mathrm{Q}} - 3\mu_{\mathrm{S}}}{3}T^2 - \frac{(\mu_{\mathrm{B}} - \mu_{\mathrm{Q}} - 3\mu_{\mathrm{S}})^3}{27\pi^2}. \tag{3.9}$$

Combining the result of Eq. (3.9) with the net-strangeness density $n_{\mathrm{S}} = 0$ from the semianalytical model in Sec. 2.4 yields the following relationship for the EoS of an ideal gas with

quantum statistics [46]

$$\mu_{\rm B} - \mu_{\rm Q} - 3\mu_{\rm S} = 0. \tag{3.10}$$

The above result corresponds to the strange quark chemical potential $\mu_s = 0$ and means that the three chemical potentials are not mutually independent [46]. Therefore, the system of equations in Eqs. (3.6) - (3.8) may be simplified to the following set of equations:

$$\epsilon = \frac{19\pi^2}{12}T^4 + 3\frac{(\mu_{\rm B} - 2\mu_{\rm S})^2 + \mu_{\rm S}^2}{2}T^2 + 3\frac{(\mu_{\rm B} - 2\mu_{\rm S})^4 + \mu_{\rm S}^4}{4\pi^2}, \tag{3.11}$$

$$n_{\rm B} = \frac{\mu_{\rm B} - \mu_{\rm S}}{3}T^2 + \frac{(\mu_{\rm B} - 2\mu_{\rm S})^3 + \mu_{\rm S}^3}{3\pi^2}, \tag{3.12}$$

$$n_{\rm Q} = \frac{2\mu_{\rm B} - 5\mu_{\rm S}}{3}T^2 + \frac{2(\mu_{\rm B} - 2\mu_{\rm S})^3 - \mu_{\rm S}^3}{3\pi^2}. \tag{3.13}$$

The T, $\mu_{\rm B}$, $\mu_{\rm Q}$, and $\mu_{\rm S}$ values which are extracted from ϵ, $n_{\rm B}$, and $n_{\rm Q}$ using Eqs. (3.10) - (3.13) are referred to as the "full solution" of the conformal quantum EoS [46].

One may further simplify the resulting relations of the ideal gas EoS with quantum statistics by setting one or both of the $\mu_{\rm Q}$, $\mu_{\rm S}$ to zero [46, 61]. For example, if the electric charge is ignored by setting $\mu_{\rm Q} = 0$ in Eq. (3.10), the strangeness chemical potential is proportional to the net-baryon chemical potential: $\mu_{\rm S} = \mu_{\rm B}/3$. Under the assumption of a vanishing $\mu_{\rm Q}$, one find the simplified equations

$$\epsilon_1 = \frac{19\pi^2}{12}T^4 + \frac{\mu_{\rm B}^2}{3}T^2 + \frac{\mu_{\rm B}^4}{54\pi^2}, \tag{3.14}$$

$$n_{\rm B,1} = \frac{2\mu_{\rm B}}{9}T^2 + \frac{2\mu_{\rm B}^3}{81\pi^2}. \tag{3.15}$$

The above relations are referred to as the "partial-1" solution of the quantum EoS because only one chemical potential $\mu_{\rm Q}$ was neglected [46]. In this approximation, the net-electric charge density of Eq. (3.13) would give $n_{\rm Q} = n_{\rm B}/2 \neq n_{\rm B}Z/A$, and is therefore inconsistent with the semianalytical model result in Sec. 2.4. Note that for the Au+Au collisions that are considered in this work, the ratio $Z/A \approx 0.4$ is reasonably close to 1/2, so the partial-1 solution of the quantum EoS may be expected to approximate the full solution results

reasonably well [46]. This discrepancy is a consequence of the choice of μ_{Q} and also happens if one considers Boltzmann statistics as in Sec. 3.1.2.

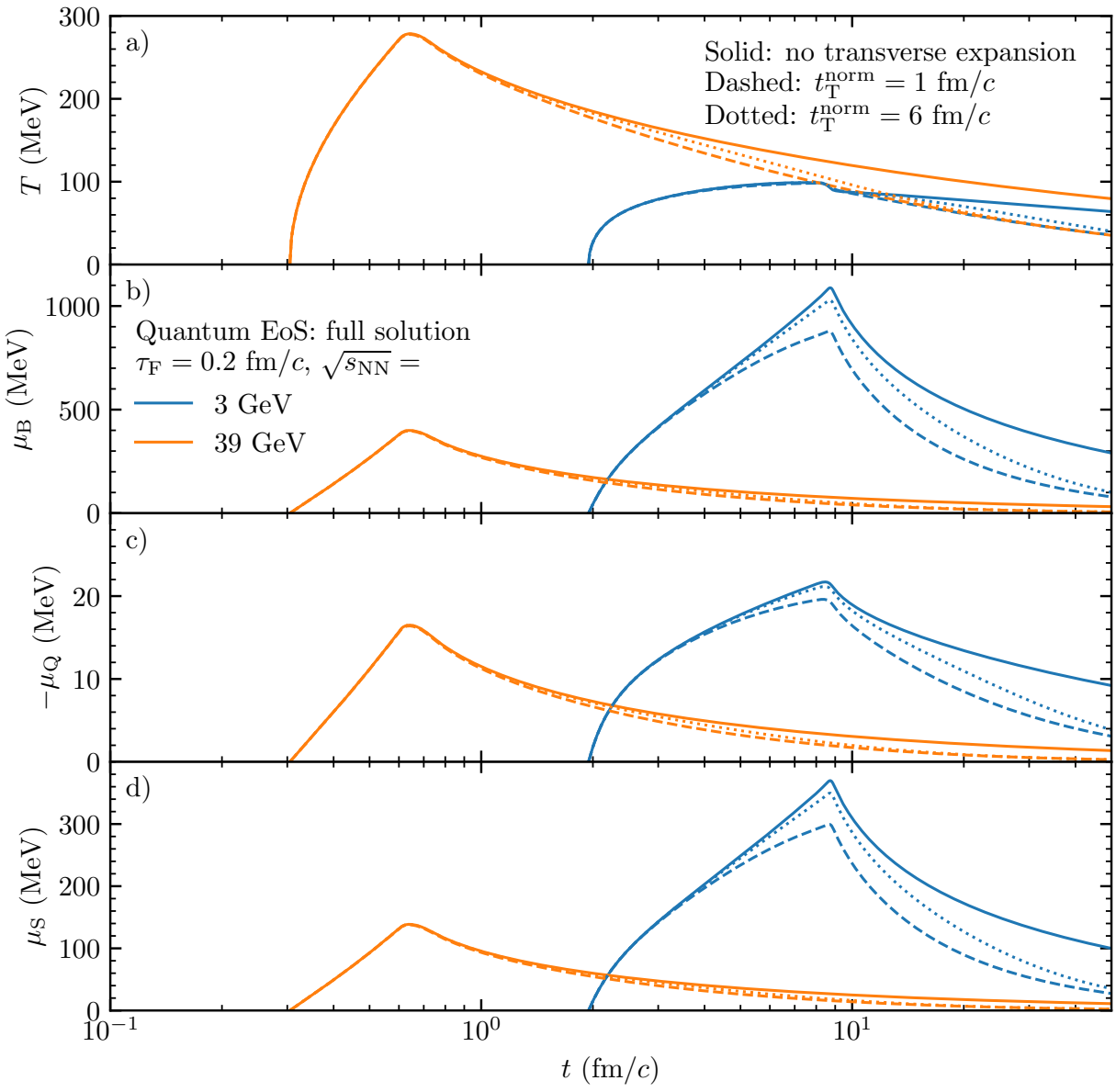

Figure 3.1: (a) $T(t)$, (b) $\mu_{\mathrm{B}}(t)$, (c) $-\mu_{\mathrm{Q}}(t)$, and (d) $\mu_{\mathrm{S}}(t)$ of a massless QGP from the full solution of the quantum EoS with no transverse expansion (solid), and transverse expansion with $t_{\mathrm{T}}^{\mathrm{norm}} = 1$ (dashed) and 6 (dotted) fm/c for central Au+Au collisions at $\sqrt{s_{\mathrm{NN}}} = 3$ and 39 GeV with $\tau_{\mathrm{F}} = 0.2$ fm/c. Note that these results use $t_1 = d_t/6$ and $t_2 = 5d_t/6$.

One may also ignore both the electric charge and the strangeness by setting $\mu_{\mathrm{Q}} = \mu_{\mathrm{S}} = 0$ in Eq. (3.10). In this case, one finds the following simplified system of equations which is

similar to that of Eqs. (3.14) - (3.15):

$$\epsilon_2 = \frac{19\pi^2}{12}T^4 + \frac{\mu_{\rm B}^2}{2}T^2 + \frac{\mu_{\rm B}^4}{36\pi^2}, \tag{3.16}$$

$$n_{\rm B,2} = \frac{\mu_{\rm B}}{3}T^2 + \frac{\mu_{\rm B}^3}{27\pi^2}. \tag{3.17}$$

Since both of $\mu_{\rm Q}$ and $\mu_{\rm S}$ were set equal to zero, we refer to Eqs. (3.16) - (3.17) as the "partial-2" solution of the quantum EoS [46]. Note that the the above assumption would violate Eq. (3.10) from the semianalytical model. In addition, the partial-2 solution of the quantum EoS yields $n_{\rm Q} = 0$ and $n_{\rm S} = -n_{\rm B}$ which is inconsistent with the results of the semianalytical model in Sec. 2.4. The same problems are found by considering Boltzmann statistics in Sec. 3.1.2. Note that the results of the semianalytical model [46] agree qualitatively with those of the AMPT model [61].

Figure 3.1 shows the T and μ results that are extracted using the full solution of the quantum EoS for central Au+Au collisions at $\sqrt{s_{\rm NN}} = 3$ and 39 GeV with $\tau_{\rm F} = 0.2$ fm/c, where the starting and ending times of parton production are $t_1 = d_t/6$ and $t_2 = 5d_t/6$ as described in Sec. 2.4. Results without transverse expansion are compared to those with transverse expansion for $t_{\rm T}^{\rm norm} = 1$ and 6 fm/c. It is clear that the maximum temperature $T^{\rm max}$ increases with collision energy and the maximum net-baryon chemical potential $\mu_{\rm B}^{\rm max}$ decreases with $\sqrt{s_{\rm NN}}$. The decrease of $\mu_{\rm B}^{\rm max}$ actually happens from $\sqrt{s_{\rm NN}} = 5$ GeV, while there is slight increase for lower collision energies [46]. Additionally, the maximum magnitude of the electric charge chemical potential is $|\mu_{\rm Q}|^{\rm max} \lesssim 30$ MeV, which is on the order of 10% of $T^{\rm max}$, while the strangeness chemical potential $\mu_{\rm S}$ appears to be $\mu_{\rm S} \approx \mu_{\rm B}/3$. These results for $\mu_{\rm Q}$ and $\mu_{\rm S}$ from the full solution of the quantum EoS indicate that the approximations which led to the partial-1 solution in Eqs. (3.14) - (3.15) are reasonable for an ideal gas of massless partons [46]. Note that the recent numerical results from the AMPT model for the ideal gas EoS [61] also show $\mu_{\rm Q} \approx 0$ and $\mu_{\rm S} \approx \mu_{\rm B}/3$.

The smaller duration time d_t at higher collision energies causes the peak values of T

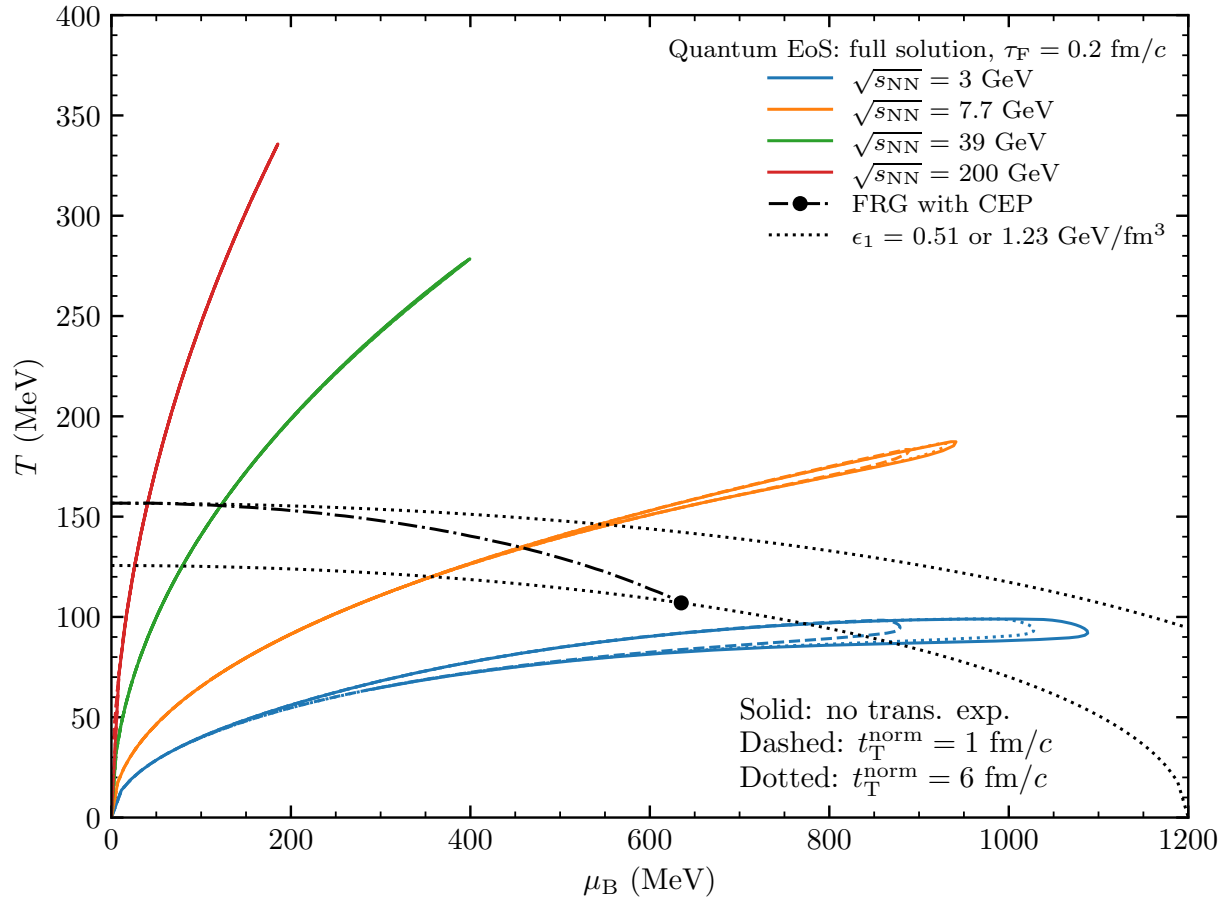

Figure 3.2: $T - \mu_B$ trajectories of a massless QGP from the full solution of the quantum EoS for central Au+Au collisions at $\sqrt{s_{NN}} = 3$, 7.7, 39, and 200 GeV with $\tau_F = 0.2$ fm/c with no transverse expansion (solid) or transverse expansion with $t_T^{norm} = 1$ (dashed) and 6 (dotted) fm/c. Also shown are two lines of constant $\epsilon_1 = 0.51$ and 1.23 GeV/fm^3 as calculated from Eq. (3.14). Note that these results use $t_1 = d_t/6$ and $t_2 = 5d_t/6$.

and μ to occur earlier in time in Fig. 3.1. Note that the maximum values occur at t_{max} which is the time when the densities of the semianalytical model are maximum [46]. Apart from the behavior of the maximum values of T and μ with $\sqrt{s_{NN}}$, the time evolution of the T and μ matches the evolution of the densities from the semianalytical model [46]. The behavior of T^{max} and μ_B^{max} with $\sqrt{s_{NN}}$ is the same for results including transverse expansion or not. This behavior is expected because the transverse expansion effect of Sec. 2.5 affects the energy density $\epsilon(t)$ and net-baryon density $n_B(t)$ in the same way. Figure 3.1 shows that this implementation of transverse expansion changes the T and μ values in the same way as

it changes the densities of the semianalytical model [46].

The $T-\mu_{\rm B}$ QCD phase diagram trajectories of a massless QGP from the full solution of the quantum EoS without transverse expansion and with $t_{\rm T}^{\rm norm}=1$ and 6 fm/c for central Au+Au collisions at $\sqrt{s_{\rm NN}}=3$, 7.7, 39, and 200 GeV with $\tau_{\rm F}=0.2$ fm/c are shown in Fig. 3.2. For very early times $t\in[0,t_1+\tau_{\rm F})$ when the system has densities $(\epsilon,n_{\rm B})=(0,0)$, the net-baryon chemical potential and temperature are at $(\mu_{\rm B},T)=(0,0)$ because of the vanishing quark masses [46]. While the $\sqrt{s_{\rm NN}}=3$ GeV trajectory does not pass through the crossover curve from the FRG calculations with $N_F=2+1$[104], the $\sqrt{s_{\rm NN}}=7.7$ GeV one does. In fact, we have shown that the trajectories for collision energies $\sqrt{s_{\rm NN}}\gtrsim 4$ GeV pass through the FRG crossover curve [46].

Each trajectory in Fig. 3.2 reaches its endpoint at the time when both $\epsilon^{\rm max}$ and $n_{\rm B}^{\rm max}$ are reached, and turns clockwise then returns toward the origin. For very high collision energies, the outgoing and returning parts of the trajectory are quite close to each other and appear to overlap at this scale [46]. However, for lower collision energies such as $\sqrt{s_{\rm NN}}=3$ GeV, the two parts are clearly distinguishable. One can understand this behavior in terms of the uniform time profile for density production from Ref. [43] in which both the energy $\epsilon(t)$ and net-baryon density $n_{\rm B}(t)$ have the same evolution up to a proportionality constant [46]. This means that the time evolution of the semianalytical densities from Ch. 2 should be quite close for all times. Therefore, the returning of a trajectory should overlap with the outgoing part because for two points (one on the increasing part and the other on the decreasing part) in a trajectory with the same energy density, the net-baryon densities will also be very similar [46]. We have found in Ref. [46] that for $\sqrt{s_{\rm NN}}\gtrsim 4.4$ GeV, both the outgoing and returning parts of the trajectory intersect the FRG crossover curve [104]; however, neither part does so if $\sqrt{s_{\rm NN}}\lesssim 3.6$ GeV. Two lines of constant ϵ which intersect the endpoints of the FRG crossover curve have also been calculated using Eq. (3.14) from the partial-1 solution of the quantum EoS [46]. These constant energy density curves correspond to $\epsilon=0.51$ and 1.23 GeV/fm^3, and are shown in Fig. 3.2.

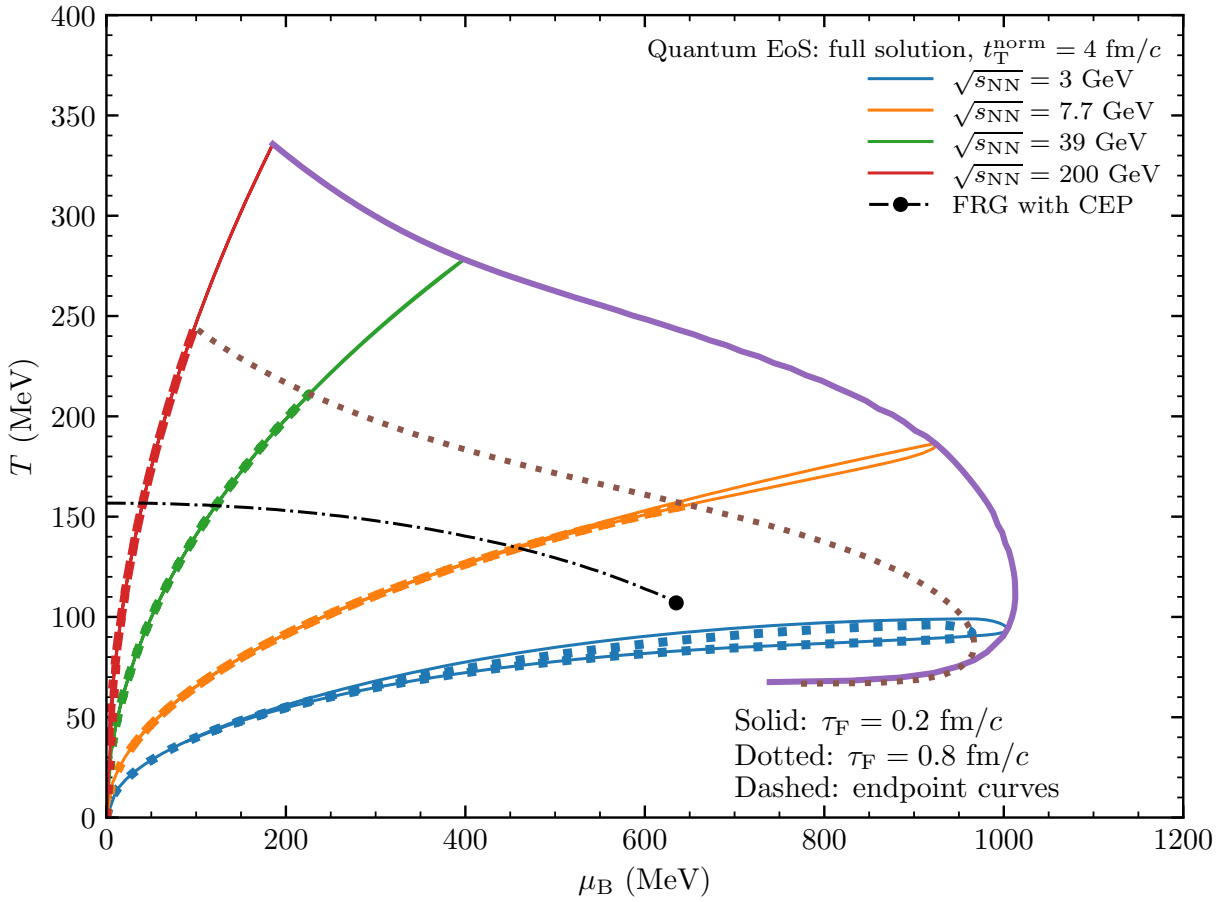

Figure 3.3: $T - \mu_{\rm B}$ trajectories of a massless QGP from the full solution of the quantum EoS for central Au+Au collisions at $\sqrt{s_{\rm NN}} = 3$, 7.7, 39, and 200 GeV and $\tau_{\rm F} = 0.2$ and 0.8 fm/c. These results are for transverse expansion with $t_{\rm T}^{\rm norm} = 4$ fm/c.

Figure 3.2 also shows the relatively small effect of transverse expansion on the resulting trajectories, and this can be understood in the following way [46]. The implementation of transverse expansion in the semianalytical model occurs via a time-dependent transverse area $A_{\rm T}(t)$ which increases according to a timescale $t_{\rm T}$ as is described in Sec. 2.5. For very early times when $t - t_1 - \tau_{\rm F} < t_{\rm T}$, transverse flow has not yet significantly developed, so the transverse expansion should have a very small effect on the densities. Therefore, the outgoing part of the trajectory which corresponds to early times will be affected only slightly [46]. For later times when $t - t_1 - \tau_{\rm F} > t_{\rm T}$, the transverse expansion decreases the energy density and net-baryon density by the same factor because it occurs outside the

integrals of Eqs. (2.14) and (2.32). However, the late time evolution of the semianalytical model's densities approaches the Bjorken densities and goes like $1/t$. Therefore, the late time densities and corresponding point of the trajectory with transverse expansion at time t is the same as those without transverse expansion at some later time $t' > t$ [46]. The final effect of transverse expansion then is only in changing the turning point or endpoint of a trajectory because the returning part of a trajectory with transverse expansion will overlap with one without transverse expansion. Note that the rate at which the matter follows the trajectory will be faster with transverse expansion than without as is discussed in Sec. 3.3.

The results of the semianalytical model [45, 46] depend on the parton proper formation time. Figure 3.3 shows how the $T - \mu_{\rm B}$ trajectories from the full solution of the quantum EoS depend on $\tau_{\rm F}$. For a given collision energy, the trajectory at a smaller formation time is long with the endpoint being farther away from the origin than for a trajectory with a larger formation time. Specifically, as $\tau_{\rm F}$ decreases, the trajectory endpoint moves to a larger $\mu_{\rm B}$ and a higher T except at very low energies where the temperature at the endpoint may decrease [46]. For moderate to high $\sqrt{s_{\rm NN}}$, the trajectory endpoint corresponds to both $\epsilon^{\rm max}$ and $n_{\rm B}^{\rm max}$, but this is not always the case at low collision energies. The outgoing parts of a trajectory with a given $\sqrt{s_{\rm NN}}$ and different formation times sometimes do not overlap perfectly, this behavior is consistent with the significant dependence of $\epsilon(t)$ and $n_{\rm B}(t)$ on $\tau_{\rm F}$ for early times as depicted in Fig. 2.6. This same feature does not occur on the returning parts of a trajectory for a given collision energy because the densities of the semianalytical model are insensitive to $\tau_{\rm F}$ at late times [46].

Also shown in Fig. 3.3 is the dependence on $\sqrt{s_{\rm NN}}$ of the endpoint of a trajectory for a given $\tau_{\rm F}$. There is a clear separation between the endpoint curves for different $\tau_{\rm F}$ values at high collision energies; however this separation decreases [43, 45] and disappears for $\sqrt{s_{\rm NN}} \lesssim 3$ GeV. The sensitivity of the trajectory endpoint to the formation time can be understood in terms of the simpler uniform time profile [43], which has maximum values proportional to $\ln\left(1 + t_{21}/\tau_{\rm F}\right)$ [46]. Recall that the energy and net-baryon densities are both maximal at the

location of the endpoint of a trajectory. It was shown in Ref. [46] that the maximum densities are inversely proportional to $\tau_{\rm F}$ because $\ln(1+t_{21}/\tau_F) \sim t_{21}/\tau_F$ as long as the collision energy is large enough to ensure that $t_{21}/\tau_F \ll 1$. Thus, trajectories at high $\sqrt{s_{\rm NN}}$ are quite sensitive to the value of $\tau_{\rm F}$. However, when $t_{21}/\tau_F \gg 1$ for lower $\sqrt{s_{\rm NN}}$, the maximum densities scale approximately as $\ln(t_{21}/\tau_F)$, so they are not as sensitive to the formation time. Together, these two facts imply that the endpoint is more sensitive to $\tau_{\rm F}$ at high collision energies than at low collision energies [46].

For the threshold collision energy E_0, the endpoint curves for different formation time values converge to the same endpoint point [46]. In Ref. [46] when transverse expansion is neglected, that point is located at $(\mu_{\rm B}, T) \sim (900\,{\rm MeV},\ 60\,{\rm MeV})$. Figure 3.3 shows that the point is now located at $(\mu_{\rm B}, T) \sim (720\,{\rm MeV},\ 60\,{\rm MeV})$ after transverse expansion with $t_{\rm T}^{\rm norm} = 4$ fm/c is taken into account. The CEP from the FRG calculations [104] located at $(\mu_{\rm B}, T) = (635\,{\rm MeV},\ 107\,{\rm MeV})$ is well within the endpoint curve with $\tau_{\rm F} = 0.8$ fm/c. Thus, central Au+Au collisions should be able to produce matter which can access this CEP location [46]. It was also shown that the region below the $\sqrt{s_{\rm NN}} = 2$ GeV trajectory is essentially inaccessible to the central Au+Au collisions according to this semianalytical model [46]. This is understandable since $\epsilon < m_{\rm N} n_{\rm B}$ is physically inaccessible, but the ideal gas EoS with quantum statistics has $\epsilon < m_{\rm N} n_{\rm B}$ in the region of the QCD phase diagram below the $\sqrt{s_{\rm NN}} = 2$ GeV trajectory.

Note that the semianalytical model of Sec. 2.1 should break down for very low collision energies because the primary collisions would not form a state of matter with partonic degrees of freedom [46]. The semianalytical model predicts that the trajectories from the ideal gas EoS start at the origin in the QCD phase diagram and return toward it precisely because the system is assumed to always be in the parton phase. Additionally, future work is needed to improve the model to include the energy loss of the participant nucleons and the interactions between secondary particles, which is currently beyond the scope of the model [46]. Note that the choice to neglect the secondary particle interactions is made so

that the resulting equations may be analytically solved while still producing a reasonably accurate trajectory; however, these effects are considered in the AMPT model calculations of the collision trajectories [61]. Since, the AMPT model results and those of this semianalytical model share many of the same qualitative features for the trajectories from the ideal gas EoS, one expects the effect of secondary particle interactions to be relatively small [46].

The semianalytical model gives $\epsilon^{\max} = 2\rho_0 m_{\rm N}$ and $n_{\rm B}^{\max} = 2\rho_0$ for the threshold collision energy $\sqrt{s_{\rm NN}} = E_0$ which is the naïve expectation [46]. Therefore, the densities of the Sec. 2.2 and Sec. 2.4 should be accurate for very low collision energies. On the other hand, the system is expected to freeze out from a parton matter into hadrons, whose behavior can be described by a hadron resonance gas model. This means that the treatment of the system as a massless QGP below the phase transition is unreliable. Thus, the trajectories from the ideal gas EoS that are far below the FRG crossover curve (or the first-order phase transition line beyond the CEP) should not be trusted [46].

3.1.2 The Ideal Gas EoS with Boltzmann Statistics

The results of Sec. 3.1.1 used quantum statistics in the treatment of a massless QGP with an ideal gas EoS. Now, the Maxwell-Boltzmann statistics will be used to describe the thermodynamics of the same massless QGP. Note that the following equations are simpler than the equivalent equations that include the finite quark masses [61].

$$\epsilon = \frac{12}{\pi^2} T^4 \left[4 + 3\cosh\left(\frac{\mu_{\rm B} + 2\mu_{\rm Q}}{3T}\right) + 3\cosh\left(\frac{\mu_{\rm B} - \mu_{\rm Q}}{3T}\right) + 3\cosh\left(\frac{\mu_{\rm B} - \mu_{\rm Q} - 3\mu_{\rm S}}{3T}\right)\right], \tag{3.18}$$

$$n_{\rm B} = \frac{4}{\pi^2} T^3 \left[\sinh\left(\frac{\mu_{\rm B} + 2\mu_{\rm Q}}{3T}\right) + \sinh\left(\frac{\mu_{\rm B} - \mu_{\rm Q}}{3T}\right) + \sinh\left(\frac{\mu_{\rm B} - \mu_{\rm Q} - 3\mu_{\rm S}}{3T}\right)\right], \tag{3.19}$$

$$n_{\rm Q} = \frac{4}{\pi^2} T^3 \left[2\sinh\left(\frac{\mu_{\rm B} + 2\mu_{\rm Q}}{3T}\right) - \sinh\left(\frac{\mu_{\rm B} - \mu_{\rm Q}}{3T}\right) - \sinh\left(\frac{\mu_{\rm B} - \mu_{\rm Q} - 3\mu_{\rm S}}{3T}\right)\right], \tag{3.20}$$

$$n_{\rm S} = -\frac{12}{\pi^2} T^3 \sinh\left(\frac{\mu_{\rm B} - \mu_{\rm Q} - 3\mu_{\rm S}}{3T}\right). \tag{3.21}$$

It is clear that the above equation for the net-strangeness density also yields Eq. (3.10) when one enforces the strangeness neutrality condition of the semianalytical model as discussed in Sec. 2.5. The above set of equations may be further simplified using Eq. (3.10) and written as:

$$\epsilon = \frac{12}{\pi^2} T^4 \left[7 + 3\cosh\left(\frac{\mu_{\rm B} - 2\mu_{\rm S}}{T}\right) + 3\cosh\left(\frac{\mu_{\rm S}}{T}\right)\right], \tag{3.22}$$

$$n_{\rm B} = \frac{4}{\pi^2} T^3 \left[\sinh\left(\frac{\mu_{\rm B} - 2\mu_{\rm S}}{T}\right) + \sinh\left(\frac{\mu_{\rm S}}{T}\right)\right], \tag{3.23}$$

$$n_{\rm Q} = \frac{4}{\pi^2} T^3 \left[2\sinh\left(\frac{\mu_{\rm B} - 2\mu_{\rm S}}{T}\right) - \sinh\left(\frac{\mu_{\rm S}}{T}\right)\right]. \tag{3.24}$$

The above equations are referred to as the full solution of the Boltzmann EoS [46].

While Eqs (3.22) - (3.24) are straightforwardly stated, one is also free to simplify them by ignoring one or both of the electric charge and strangeness chemical potentials. If the electric charge is ignored by setting $\mu_{\rm Q} = 0$ in Eq. (3.10), one discovers the following partial-1 solution of the Boltzmann EoS:

$$\epsilon_1 = \frac{12}{\pi^2} T^4 \left[7 + 6\cosh\left(\frac{\mu_{\rm B}}{3T}\right)\right], \tag{3.25}$$

$$n_{\rm B,1} = \frac{8}{\pi^2} T^3 \sinh\left(\frac{\mu_{\rm B}}{3T}\right). \tag{3.26}$$

On the other hand, one may ignore both electric charge and strangeness by using $\mu_{\rm Q} = \mu_{\rm S} = 0$ and find the partial-2 solution of the Boltzmann EoS:

$$\epsilon_2 = \frac{12}{\pi^2} T^4 \left[4 + 9\cosh\left(\frac{\mu_{\rm B}}{3T}\right)\right], \tag{3.27}$$

$$n_{\rm B,2} = \frac{12}{\pi^2} T^3 \sinh\left(\frac{\mu_{\rm B}}{3T}\right). \tag{3.28}$$

Figure 3.4 shows the time evolutions of the T and μ extracted using the full solution, the partial-1 solution, and the partial-2 solution of the Boltzmann ideal gas EoS for a massless

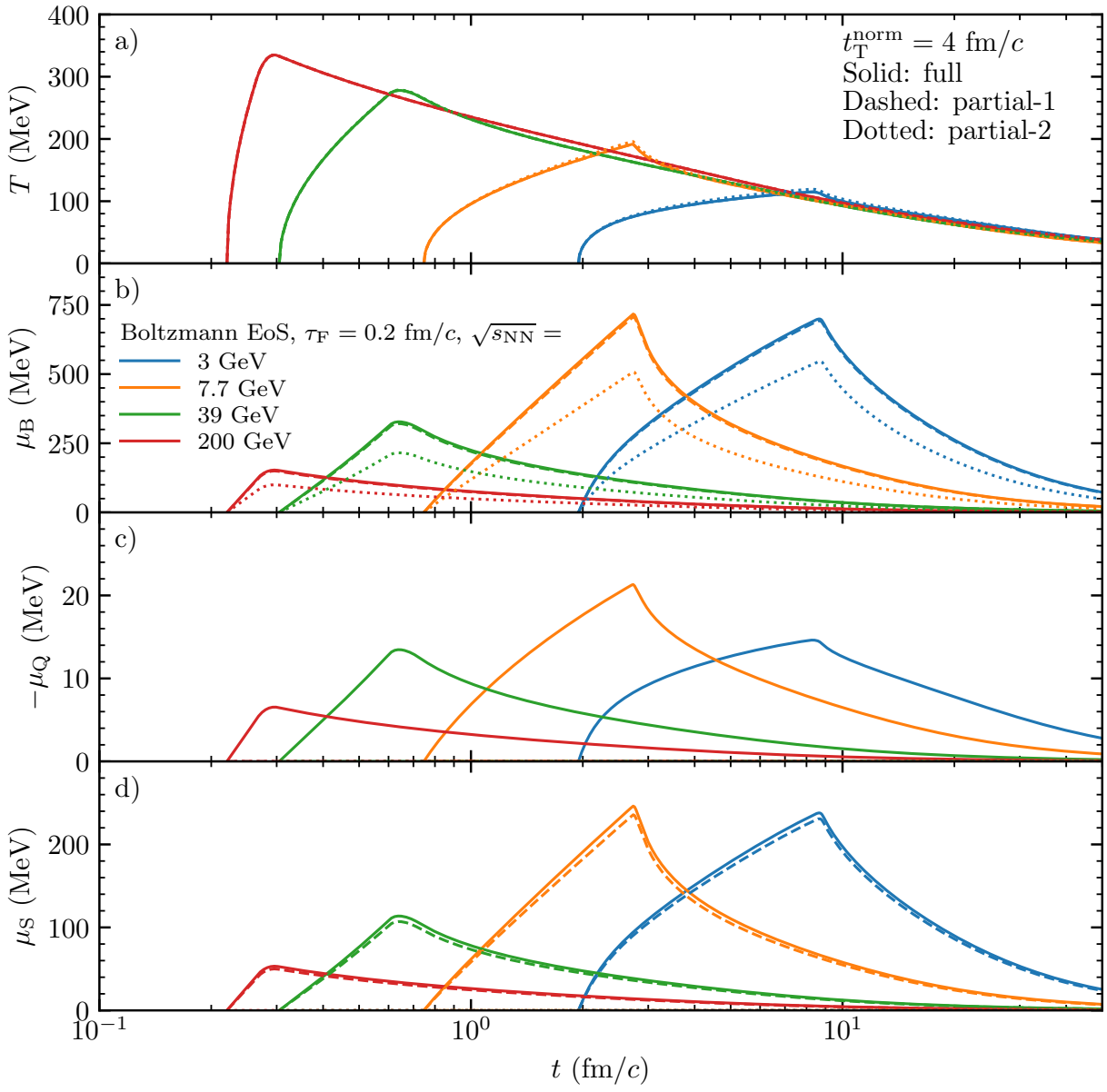

Figure 3.4: (a) $T(t)$, (b) $\mu_{\rm B}(t)$, (c) $-\mu_{\rm Q}(t)$, and (d) $\mu_{\rm S}(t)$ of a massless QGP from the full (solid), partial-1 (dashed), and partial-2 (dotted) solutions of the Boltzmann EoS for central Au+Au collisions at $\sqrt{s_{\rm NN}} = 3$, 7.7, 39, and 200 GeV with $\tau_{\rm F} = 0.2$ fm/c and $t_{\rm T}^{\rm norm} = 4$ fm/c. Note that these results use $t_1 = d_t/6$ and $t_2 = 5d_t/6$.

QGP from central Au+Au collisions at $\sqrt{s_{\rm NN}} = 3$, 7.7, 39, and 200 GeV with $\tau_{\rm F} = 0.2$ fm/c. These results are similar to those shown in Fig. 3.1 for the quantum ideal gas EoS, except that here only the case of transverse expansion with $t_{\rm T}^{\rm norm} = 4$ fm/c is considered since the effect of transverse expansion on the resulting trajectories was shown to be rather

small there [46]. Notably, the results for the partial-1 solution which makes the simplifying assumption of $\mu_{\rm Q} = 0$ and consequently, $\mu_{\rm S} = \mu_{\rm B}/3$, are very similar to the full solution results. There is essentially no difference in the time evolution of the temperature for all collision energies, while there are only very minor deviations in the net-baryon chemical potential [46]. In fact, the time evolution of $\mu_{\rm S}$ shows that the net-strangeness density in the partial-1 solution is similar to the full solution one. This fact further supports the validity of the assumptions that lead to the partial-1 solutions of Eqs. (3.25) - (3.26) for Boltzmann statistics or Eqs. (3.14) - (3.15) for quantum statistics. On the other hand, the results from the partial-2 solution have essentially the same $T(t)$, but significantly smaller $\mu_{\rm B}(t)$ values. Additionally, the magnitude of $\mu_{\rm Q}$ from the full solution of the Boltzmann EoS is slightly smaller than that of the quantum EoS full solution.

Figure 3.5 shows how the $T - \mu_{\rm B}$ trajectories of a massless QGP depend on the different solutions of the Boltzmann EoS for central Au+Au collisions at $\sqrt{s_{\rm NN}} = 3$, 7.7, 39, and 200 GeV with $\tau_{\rm F} = 0.2$ fm/c and $t_{\rm T}^{\rm norm} = 4$ fm/c. It is clear that the trajectories from the partial-1 solution of the Boltzmann EoS match almost perfectly those of the full solution, and this behavior is also found for the quantum EoS [46]. Two lines of constant energy density as calculated from the partial-1 solution of the Boltzmann EoS in Eq. (3.25), which pass through the endpoints of the FRG crossover curve, are shown. In contrast to similar curves from the quantum EoS in Fig. 3.2, these exhibit a half-loop structure such that the lower half of a given constant-ϵ_1 line goes toward the origin instead of high $\mu_{\rm B}$ [46]. This behavior can be understood by considering the total differential of Eq. (3.25): $d\epsilon_1 = \partial_T \epsilon_1 dT + \partial_{\mu_{\rm B}} \epsilon_1 d\mu_{\rm B}$. For a constant energy density, the total change in ϵ_1 is $d\epsilon_1 = 0$, and this naturally leads to the following relation:

$$\frac{d\mu_{\rm B}}{dT} = -\frac{\partial_T \epsilon_1}{\partial_{\mu_{\rm B}} \epsilon_1}. \tag{3.29}$$

In the above equation, the numerator on the right-hand-side is zero if $\mu_{\rm B}/(3T) \approx 4.15$, and this criterion corresponds to the turning point of the constant ϵ_1 line for the Boltzmann EoS [46]. Thus, if one traces a constant ϵ_1 line from the high T side at zero net-baryon

chemical potential where $\epsilon \gg m_{\rm N} n_{\rm B}$, eventually one will reach a point near the turning point beyond which $\epsilon < m_{\rm N} n_{\rm B}$. It is not natural for nuclear matter such as the QGP to have an energy density smaller than $m_{\rm N} n_{\rm B}$ because the baryon number is closely related to the baryon mass. Therefore, the $(\mu_{\rm B}, T)$ points on the lower part of the constant ϵ_1 lines of the Boltzmann EoS do not represent a physical QGP system [46].

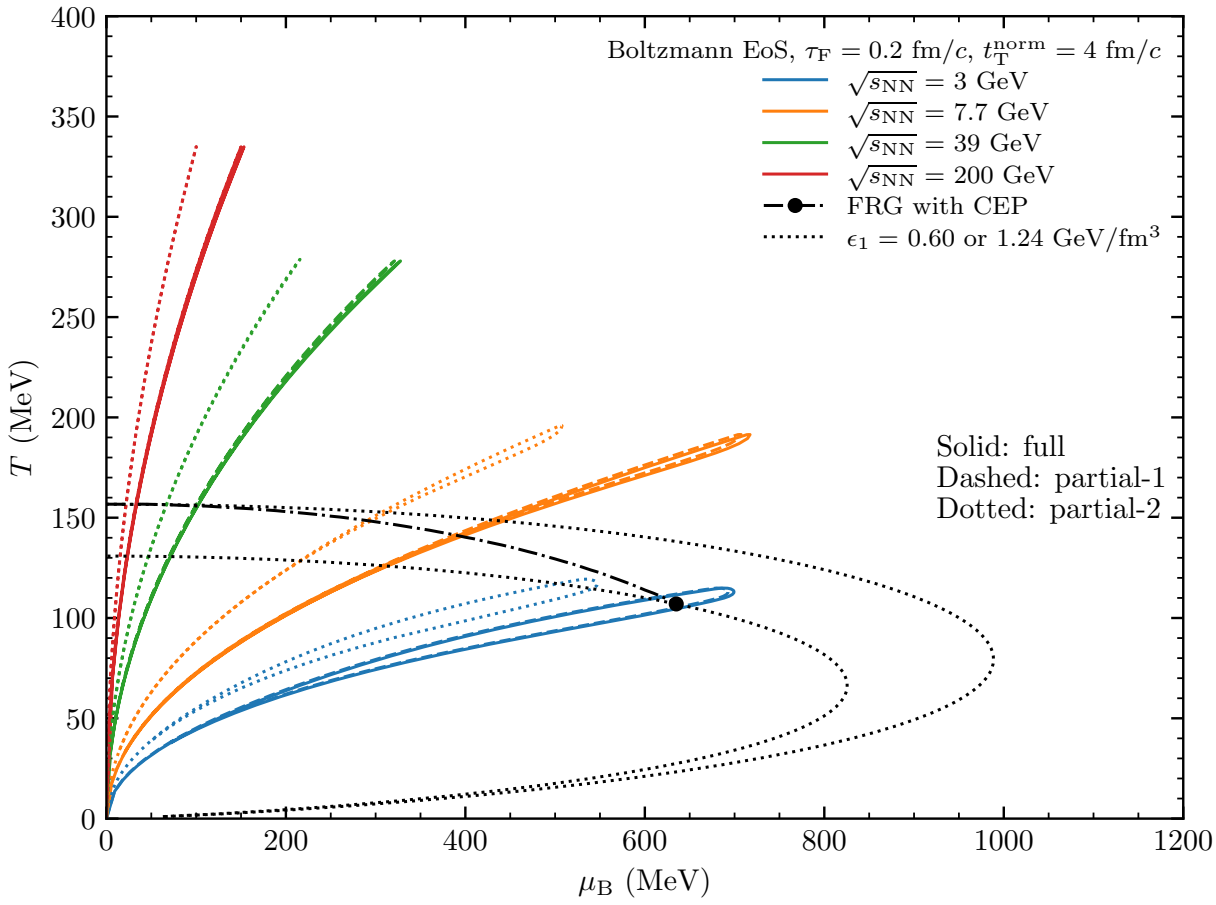

Figure 3.5: $T-\mu_{\rm B}$ trajectories of a massless QGP from the full (solid), partial-1 (dashed), and partial-2 (dotted) solutions of the Boltzmann EoS for central Au+Au collisions at $\sqrt{s_{\rm NN}} =$ 3, 7.7, 39, and 200 GeV with $\tau_{\rm F} = 0.2$ fm/c and $t_{rmT}^{rmnorm} = 4$ fm/c. The FRG crossover curve with the CEP and two lines of constant $\epsilon_1 = 0.60$ and 1.24 GeV/fm^3 as calculated with Eq. (3.25) are also shown for reference.

In Fig. 3.6, the $T - \mu_{\rm B}$ trajectories from the semianalytical model are compared to those extracted from the Bjorken energy density formula [42] of Eq. (1.1) and net-baryon density formula [46] of Eq. (2.33). For high collision energies, the trajectories from the Bjorken

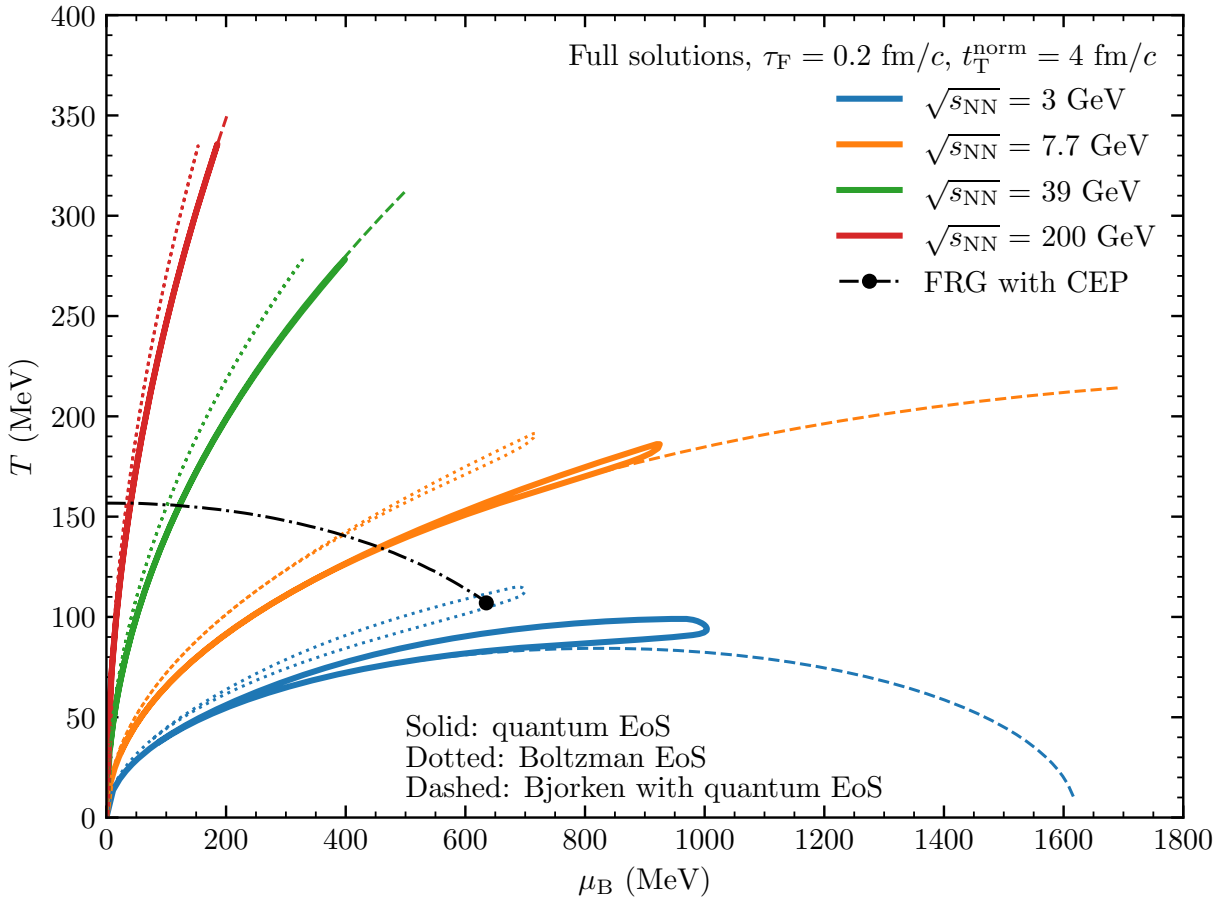

Figure 3.6: $T-\mu_B$ trajectories of a massless QGP from the full solutions of the ideal gas EoS with the semianalytical model densities and the quantum EoS with the Bjorken densities for central Au+Au collisions at $\sqrt{s_{NN}} = 3$, 7.7, 39, and 200 GeV with $\tau_F = 0.2$ fm/c and $t_T^{norm} = 4$ fm/c. The FRG crossover curve with the CEP is also shown for reference.

densities are quite close to those extracted from the semianalytical model that includes the finite nuclear thickness when the same EoS is used. This behavior is expected because the semianalytical model [45, 46] approaches the Bjorken results at large $\sqrt{s_{NN}}$ where $d_t/\tau_F \ll 1$. However, for lower collision energies the μ_B^{max} of the Bjorken trajectories is much larger than the semianalytical model trajectories, and there is only a "returning" part of the trajectory. These features of the Bjorken trajectories are caused by the maximum energy and net-baryon densities occurring at the earliest time ($t = \tau_F$). On the other hand, the densities from the semianalytical model peak at a later time somewhere in the range $t \in [t_a, t_2 + \tau_F)$ [45]. Also, note that the late time portion of the Bjorken trajectories overlaps with the returning part of

the trajectories from the semianalytical model. This behavior is also expected since the two methods of calculating the produced densities agree at late times [43, 45], and this behavior is also shown in Fig. 2.6.

At low collision energies, we found a problem in the extraction of the trajectory when using the Bjorken densities and the quantum EoS [46]; namely, sometimes no solution for the $T-\mu_{\rm B}$ trajectory exists for early times. For example, for $\sqrt{s_{\rm NN}}=2$ GeV and $\tau_{\rm F}=0.3$ fm/c, no solution could be found before $t\approx 8$ fm/c when $\mu_{\rm B}^{\rm max}\approx 1300$ MeV and $T\approx 0$ MeV [46]. For times just after this, the temperature starts to rise from zero and the net-baryon chemical potential decreases leading to the trajectory extracted from the semianalytical model's densities. It was found that the problem occurs primarily for low energies and/or small formation times, such that it was not found to occur for $\sqrt{s_{\rm NN}}\gtrsim 5$ GeV when $\tau_{\rm F}=0.3$ fm/c [46]. Interestingly, the problem does not occur for the Boltzmann EoS [105]. The problem can be understood using the partial-1 solution of the quantum EoS in Eqs. (3.14) - (3.15). Those two equations give $\epsilon^{1/4}/n_{\rm B}^{1/3}\geq (2187\pi^2/128)^{1/12}\simeq 1.533$ where equality corresponds to the solution at $T=0$ MeV [46]. However, the maximum Bjorken energy and net-baryon densities both depend on the formation time like $1/\tau_{\rm F}$, which means $\epsilon^{1/4}/n_{\rm B}^{1/3}\propto \tau_{\rm F}^{1/12}$ decreases to the previously mentioned value of 1.533 for finite formation times. If $\tau_{\rm F}$ were to decrease further, no $(\mu_{\rm B},T)$ solution can exist [46]. These results only occur because the forms of the Bjorken energy density and net-baryon density formulas are different from the ones in the Bjorken hydrodynamic flow picture [42], which has $n\propto 1/\tau_{\rm F}$ and $\epsilon\propto 1/\tau_{\rm F}^{4/3}$.

Figure 3.6 also shows that the magnitude of the net-baryon chemical potential can be larger than $m_{\rm N}$ [46]. It is straightforward to show analytically that using the Bjorken densities and the partial-1 solution of the quantum EoS in Eqs. (3.14) - (3.15), the net-baryon chemical does not have an upper limit for the parton phase [46]. For example, consider the peak Bjorken densities at $\tau_{\rm F}=0.2$ fm/c and $\sqrt{s_{\rm NN}}=7.7$ GeV, which correspond to the endpoint of the dashed orange curve in Fig. 3.6. It is easy to see from Eqs. (3.14) - (3.15) that decreasing $\tau_{\rm F}$ will cause the endpoint to move to the right, reaching a larger $\mu_{\rm B}$, while the

$T/\mu_{\rm B}$ ratio decreases [46]. Thus, the maximum net-baryon chemical potential $\mu_{\rm B}^{\rm max}$ for a Bjorken trajectory at a given collision energy is reached when $T = 0$ MeV if one considers all formation times. In that case, the partial-1 solution of the quantum EoS yields

$$\frac{\epsilon}{n_{\rm B}} = \frac{3}{4}\mu_{\rm B}^{\rm max}. \tag{3.30}$$

However, the Bjorken energy and net-baryon density satisfy the inequality

$$\frac{\epsilon}{n_{\rm B}} = m_{\rm N} + \frac{dE_{\rm T}/dy}{dN_{\rm netB}/dy} \geq m_{\rm N} \tag{3.31}$$

if one uses the definition of the hadron $dm_{\rm T}/dy$ from Sec. A.2. It is easy to see that combining these two relations gives

$$\mu_{\rm B}^{\rm max} \geq \frac{4m_{\rm N}}{3} \simeq 1.25 \text{ GeV}. \tag{3.32}$$

In Ref. [46], it was shown that the 2 GeV Bjorken trajectory reaches the $T = 0$ axis when $\mu_{\rm B} \approx 1.25$ GeV; in Fig. 3.6, the 3 GeV Bjorken trajectory reaches the $T = 0$ axis near $\mu_{\rm B} \approx 1.6$ GeV. This is consistent with the expectation that the $\mu_{\rm B}^{\rm max}$ value at $T = 0$ increases with $\sqrt{s_{\rm NN}}$ for the Bjorken trajectories of the quantum EoS [46].

The two ideal gas EoS are also compared in Fig. 3.6. Specifically, the value of the maximum temperature $T^{\rm max}$ are quite similar for the same collision energy, except for very low $\sqrt{s_{\rm NN}}$ when the Boltzmann EoS predicts larger values than the quantum EoS [46]. These results are the same as those from the numerical AMPT model calculations [61], and the Pauli exclusion principle in quantum statistics accounts for this behavior. One may also wish to understand this analytically, and this can be accomplished by examining the leading terms of the Taylor expansion of Eq. (3.26):

$$n_{\rm B,1} \simeq 8\frac{\mu_{\rm B}T^2}{3\pi^2} + 4\frac{\mu_{\rm B}^3}{81\pi^2}. \tag{3.33}$$

Because the coefficient of each term in the above equation is larger than the corresponding

coefficient in Eq. (3.15) for the quantum EoS, $\mu_{\rm B}$ for the quantum EoS will be larger than for the Boltzmann EoS for the same $n_{\rm B}$ and when the T values are similar[46].

3.2 Trajectories of a Massless QGP for a Lattice QCD-Based EoS

The $T-\mu_{\rm B}$ trajectories extracted from an ideal gas EoS for a massless QGP in Sec. 3.1 do not account for interactions among the partons; therefore, they are not accurate if the temperature of the system is low enough [46]. For lower temperatures, the system is expected to behave like a hadron-resonance gas [67]. However, when the T of the system is larger enough and parton degrees of freedom should dominate the matter, other models are needed. A lattice QCD-based EoS [67, 106] provides another way to relate the energy density ϵ and net conserved-charge densities n to the temperature T and net-conserved charge chemical potentials μ. The pressure P in this EoS is first written as a Taylor series expansion in the three scaled chemical potentials μ/T up to a total power of $i+j+k \leq 4$ [67]:

$$\frac{P}{T^4} = \sum_{i,j,k} \frac{1}{i!j!k!} \chi^{BQS}_{ijk} \left(\frac{\mu_{\rm B}}{T}\right)^i \left(\frac{\mu_{\rm Q}}{T}\right)^j \left(\frac{\mu_{\rm S}}{T}\right)^k . \tag{3.34}$$

Since all the χ^{BQS}_{ijk} coefficients were calculated on a $48^3 \times 12$ lattice for temperatures in the range $T \in [135, 220]$ MeV, the pressure and all quantities derivable from it using standard thermodynamic relations are approximately known [106]. Unfortunately, this temperature range is not nearly wide enough to encompass the complete evolution of the matter which is produced during relativistic heavy-ion collisions [46]. Therefore, a more complete EoS was constructed [67] by smoothly merging each of the χ^{BQS}_{ijk} coefficients to the corresponding results from the hadron resonance gas model [107]. Merging the lattice-QCD results to the HRG model ones constrains the low T behavior of the EoS. In the high temperature limit, the new EoS is also constrained because each coefficient is forced to smoothly approach the

Boltzmann value [67]. The coefficients (except for χ_{200}^{BQS}) were fitted to ratios of ninth-degree polynomials in inverse powers of the scaled temperature $T_1 = T/(154\text{MeV})$ according to:

$$\chi_{ijk}^{BQS} = \frac{\sum_n a_n^{ijk}/T_1^n}{\sum_n b_n^{ijk}/T_1^n} + c_0^{ijk}. \tag{3.35}$$

It was found that χ_{200}^{BQS} had a different function form:

$$\chi_{200}^{BQS} = e^{-h_1/T_2 - h_2/T_2^2} f_3 \left[1 + \tanh\left(f_4 T_2 + f_5\right)\right]. \tag{3.36}$$

In the above equation, $T_2 = T/(200\text{MeV})$ is another scaled temperature [67]. All the constant coefficients a_n, b_n, c_0, h_1, h_2, f_3, and f_4 in Eqs. (3.35) - (3.36) were published in Ref. [67].

The pressure p above only depends on the parametrizations of the χ_{ijk}^{BQS} with T; therefore, the textbook thermodynamic relations can be used to find the densities including the entropy density s as functions of T and μ:

$$\begin{aligned}
&\frac{\epsilon}{T^4} = \frac{s}{T^3} - \frac{P}{T^4} + \frac{\mu_\text{B}}{T}\frac{n_\text{B}}{T^3} + \frac{\mu_\text{Q}}{T}\frac{n_\text{Q}}{T^3} + \frac{\mu_\text{S}}{T}\frac{n_\text{S}}{T^3}, \quad \frac{n_\text{B}}{T^3} = \frac{1}{T^3}\frac{\partial P}{\partial \mu_\text{B}}\bigg|_{T,\mu_\text{Q},\mu_\text{S}}, \\
&\frac{n_\text{Q}}{T^3} = \frac{1}{T^3}\frac{\partial P}{\partial \mu_\text{Q}}\bigg|_{T,\mu_\text{B},\mu_\text{S}}, \frac{n_\text{S}}{T^3} = \frac{1}{T^3}\frac{\partial P}{\partial \mu_\text{S}}\bigg|_{T,\mu_\text{B},\mu_\text{Q}}, \frac{s}{T^3} = \frac{1}{T^3}\frac{\partial P}{\partial T}\bigg|_{\mu_\text{B},\mu_\text{Q},\mu_\text{S}}.
\end{aligned} \tag{3.37}$$

The above set of equations is referred to from now on as the lattice EoS, and several conditions that are relevant to heavy-ion collision may be implemented. Specifically, the conditions of the semianalytical model [43, 45] of Eqs. (2.34) - (2.35) in Sec. 2.5 may be implemented. Then the energy density and net-conserved charge densities of the semianalytical model may be used as inputs in the lattice EoS above in order to extract the T and μ values of the full solution of the lattice EoS.

In considering the full solutions of the ideal gas EoS of Sec. 3.1, the resulting equations for ϵ and n_B are relatively easy to comprehend, which makes the numerical extraction of trajectories a straightforward process [46]. However, the lattice EoS described above does

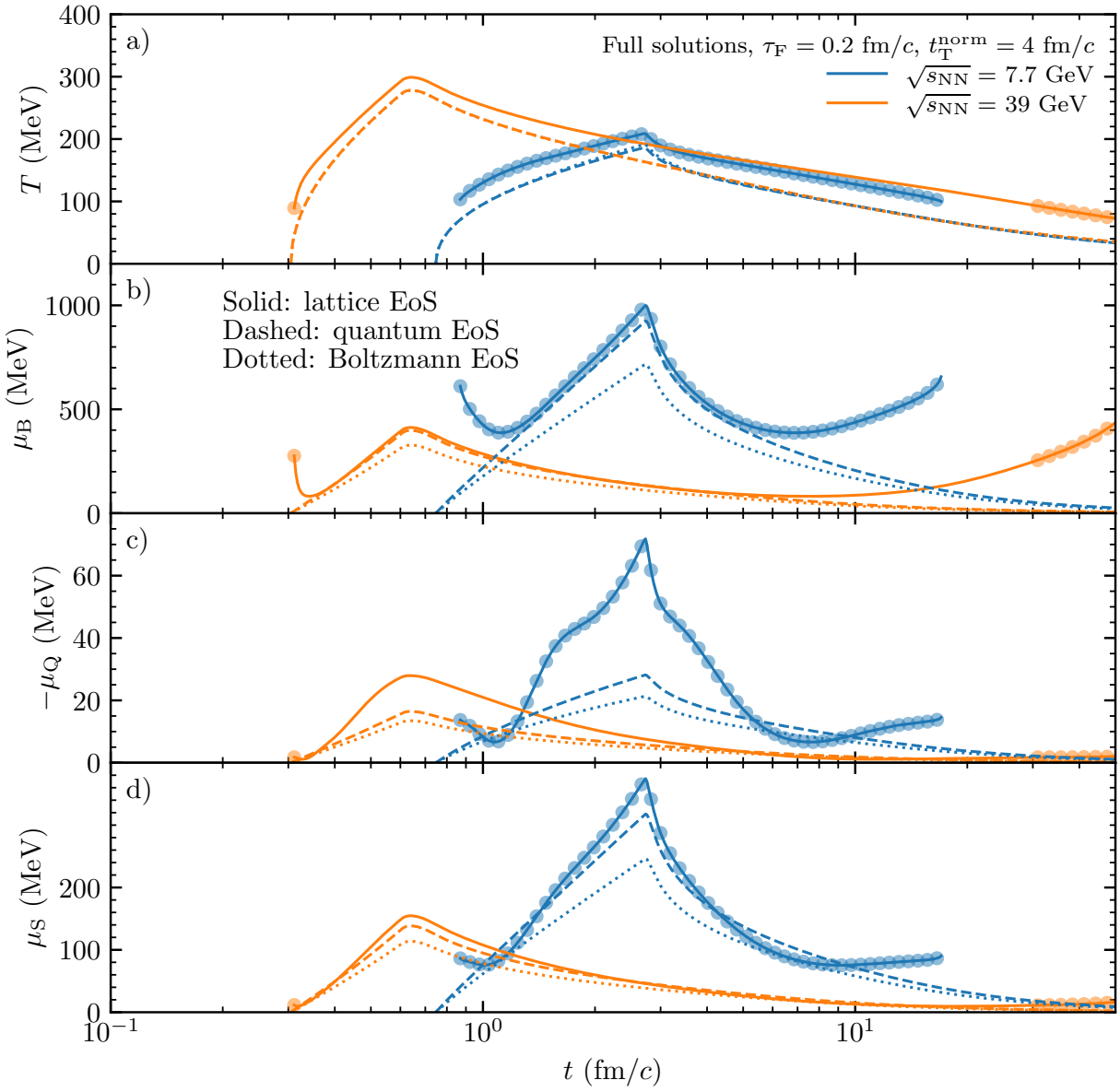

Figure 3.7: $T(t)$, $\mu_B(t)$, $-\mu_Q(t)$, and $\mu_S(t)$ of a QGP from the full solution of the lattice (solid), quantum (dashed), and Boltzmann (dotted) EoS for central Au+Au collisions at $\sqrt{s_{NN}} = 7.7$ and 39 GeV with $\tau_F = 0.2$ fm/c and $t_T^{norm} = 4$ fm/c. Circles represent times when $\mu_B/T > 2.5$ for the lattice EoS.

not lend itself to such simple extractions of the T and μ values due to the complicated behavior of the χ_{ijk}^{BQS} coefficients [67]. Therefore, a new method of extracting the T and μ values for a given input of ϵ and n is necessary. This method involves calculating the intersections of constant ϵ and n_B contours (for a given time t in the evolution) in the

$T-\mu_{\rm B}$ phase diagram [46]. First, all solutions with a temperature $T < 70$ MeV are rejected because the energy density of Eq. (3.37) can be negative there, which is unphysical [46]. Additionally, the lattice EoS often yields multiple simultaneous solutions for a given (ϵ, n) input, which further complicates matters. Specifically, one branch of solutions could occur at an unexpectedly large value of the net-baryon chemical potential at $\mu_{\rm B} \gtrsim 2$ GeV with also a large temperature $T \gtrsim 500$ MeV [46]. This branch is also neglected since the lattice QCD calculations have been shown to be invalid at large $\mu_{\rm B}/T$ values [67]. For low $\sqrt{s_{\rm NN}}$, the trajectories from the lattice EoS may also form two branches: one with an expected behavior, and the other with a smaller T and larger $\mu_{\rm B}$. The second branch is also rejected on account of its larger $\mu_{\rm B}/T$ value, and it may also be located at or below $T \approx 135$ MeV where the lattice QCD calculations of this EoS terminate [106]. These restrictions on the solutions of the lattice EoS have the consequence that some very low collision energies have no T and μ solutions whatsoever, while low to intermediate $\sqrt{s_{\rm NN}}$ may only have partial solutions throughout the entire evolution [46]. For example, no T and μ solutions were found when the densities of $\sqrt{s_{\rm NN}} = 2$ GeV were used as inputs in the lattice EoS. Similarly, near $\sqrt{s_{\rm NN}} \simeq 4$ GeV, only partial trajectories may be extracted when the densities are in the vicinity of the $\epsilon^{\rm max}$.

Figure 3.7 shows the time evolution of T, $\mu_{\rm B}$, $-\mu_{\rm Q}$, and $\mu_{\rm S}$ of a QGP from the full solution of the lattice, quantum and Boltzmann EoS for central Au+Au collisions at $\sqrt{s_{\rm NN}} = 7.7$ and 39 GeV with $\tau_{\rm F} = 0.2$ fm/c and $t_{\rm T}^{\rm norm} = 4$ fm/c. The temperatures from the lattice EoS are slightly larger than that from the ideal gas EoS, which leads to a much longer QGP lifetime [46]. For low collision energies, no $T-\mu$ solution from the lattice EoS can be found, this is why the 7.7 GeV lattice (T, μ) do not have a complete time evolution. Specifically, the early times and late times in the 7.7 GeV evolution have no solutions when using the lattice EoS [46]. Solutions that have $\mu_{\rm B}/T > 2.5$ are also indicated in Fig. 3.7 and represent times when the lattice EoS is expected to break down [67, 108]. Specifically, the entire evolution of the $\sqrt{s_{\rm NN}} = 7.7$ GeV results have $\mu_{\rm B}/T > 2.5$, but only the very early and late times

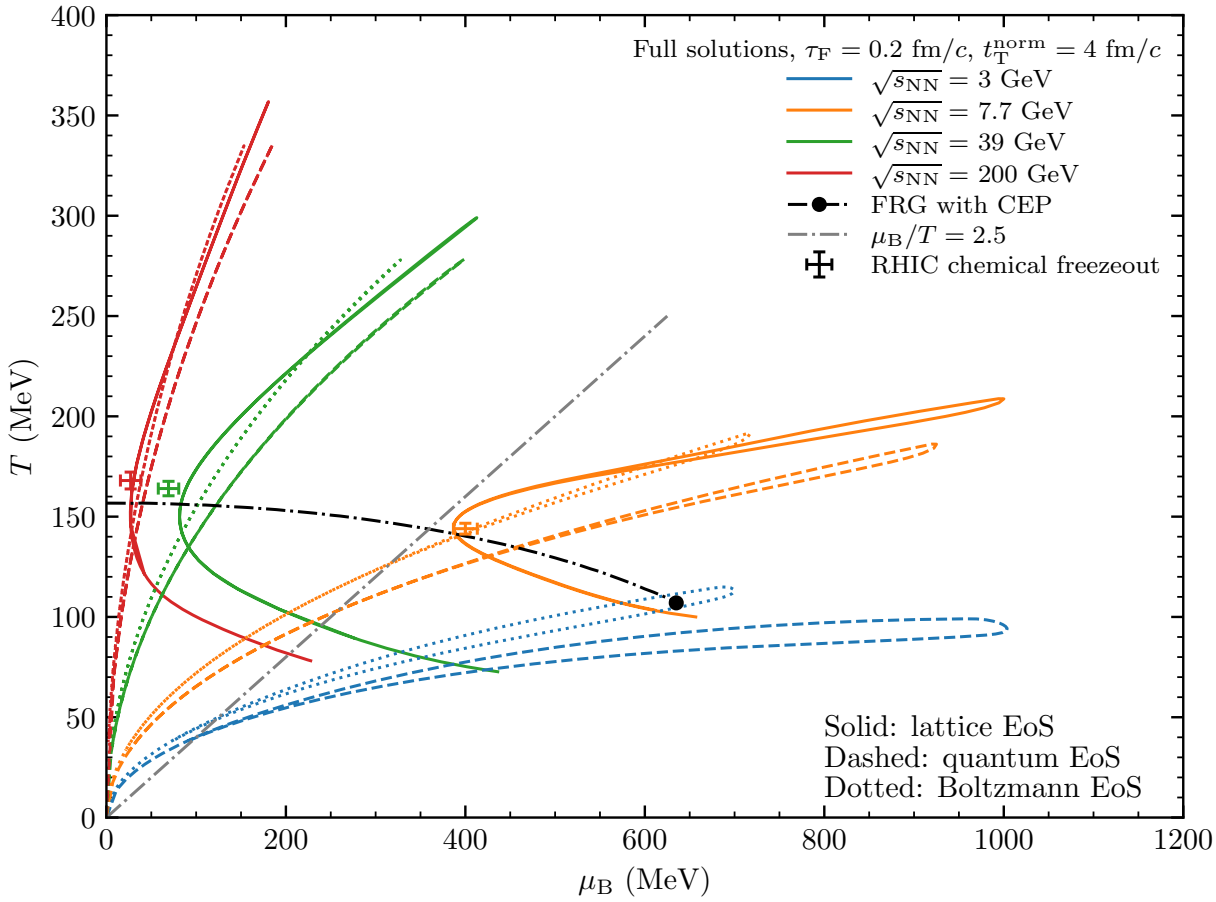

Figure 3.8: $T - \mu_B$ trajectories of a massless QGP from the full solution of the lattice (solid), quantum (dashed), and Boltzmann (dotted) EoS for central Au+Au collisions at $\sqrt{s_{NN}} = 3$, 7.7, 39, and 200 GeV with $\tau_F = 0.2$ fm/c and $t_T^{norm} = 4$ fm/c. RHIC chemical freezeout data (error bar markers) and the FRG crossover curve with the CEP and the $\mu_B/T = 2.5$ line are also shown for reference.

of the $\sqrt{s_{NN}} = 39$ GeV results do. Also, it is noteworthy is that μ_B can decrease at early times in the lattice EoS because the trajectories typically start at a finite (μ_B, T). This is in contrast to the trajectories from the ideal gas EoS which always start at the origin due to the massless partons [46]. The μ_S value from the lattice EoS is reasonably close to the quantum EoS, but the value of μ_Q in the lattice EoS is significantly larger than that of the quantum EoS.

The trajectories extracted from the full solution of the lattice EoS and both ideal gas EoS for central Au+Au collisions at $\sqrt{s_{NN}} = 3$, 7.7, 39, and 200 GeV for $\tau_F = 0.2$ fm/c and

$t_{\rm T}^{\rm norm} = 4$ fm/c are compared in Fig. 3.8. Compared with the quantum EoS, the $T^{\rm max}$ from the lattice EoS is larger for all collision energies, but the $\mu_{\rm B}^{\rm max}$ may be slightly smaller at high $\sqrt{s_{\rm NN}}$ and significantly larger at low $\sqrt{s_{\rm NN}}$. In comparing with the Boltzmann EoS, the same behavior of $T^{\rm max}$ is displayed, but the $\mu_{\rm B}^{\rm max}$ is larger for all collision energies. Additionally, the point at which the $T - \mu_{\rm B}$ trajectory intersects the FRG crossover curves is at a slightly smaller $\mu_{\rm B}$, and the shift is less noticeable at higher collision energies [46]. More important is the fact that lattice EoS trajectories bend when they fall below the FRG crossover curve because of the smooth transition of the lattice EoS to the hadron resonance gas model at small T.

Chemical freezeout data [37] extracted from grand canonical fits to the particle yields are also shown in Fig. 3.8. The chemical freezeout points are quite close to the intersection points of the lattice EoS trajectories with the FRG crossover curve [46]. It was also found that the trajectories and intersection points depend on the parametrization of $dN_{\rm netB}/dy$. In a previous parametrization of $dN_{\rm netB}/dy$, the trajectories appeared to be closer to the RHIC chemical freezeout data than using the updated $dN_{\rm netB}/dy$ [46]. For moderate to high collision energies, which roughly correspond to the region with small $\mu_{\rm B}/T$, the lattice EoS trajectories are expected to be much more realistic than the ideal gas ones. However, for large $\mu_{\rm B}/T$, the lattice EoS breaks down [67], and the trajectories from it should not be trusted. For example, we have shown [46] that the lattice EoS trajectory at $\sqrt{s_{\rm NN}} = 5$ GeV has no part below the FRG crossover curve, and it only occurs beyond $\mu_{\rm B}/T > 2.5$. Therefore, alternatives such as the ideal gas EoS should be used to calculate trajectories for the collision energies where the lattice EoS breaks down [46].

3.3 Strangeness Neutrality

The full solutions of the ideal gas equation of state with both quantum and Boltzmann statistics has $\mu_{\rm Q} \simeq 0$ as shown in Figs. 3.1 and 3.4. The approximate equality of the net-

electric charge chemical potential with zero causes the partial-1 solution that assumes $\mu_{\rm Q} = 0$ to have nearly the same $T - \mu_{\rm B}$ trajectories as the full solutions for either EoS [46]. This fact leads one naturally to ask why $\mu_{\rm Q}$ has such a small value. Answering this question begins by recalling that the semianalytical model has the strangeness neutrality condition $n_{\rm S}(t) = 0$ built in as shown in Sec. 2.4. The model [46] also predicts that the net-electric charge density would be half the net-baryon density $n_{\rm Q}(t) = n_{\rm B}(t)/2$ if both colliding nuclei have $Z = A/2$. It is straightforward to verify that these conditions of $n_{\rm S} = 0$ and $n_{\rm Q} = n_{\rm B}/2$ result in $\mu_{\rm Q} = 0$ for the ideal gas EoS with either statistics [46]. This implies that the full solution of the ideal gas EoS should have $\mu_{\rm Q} \simeq 0$ because most nuclei have $Z \sim A/2$. Recent results from the AMPT model also have shown that the net-electric charge chemical potential has $\mu_{\rm Q} \approx 0$ [61]. Notably, this result seems to be independent of the $s - \bar{s}$ symmetry of the initial production and $n_{\rm S}(t) = 0$, both of which the AMPT model does not assume [62]. On the other hand, the $\mu_{\rm Q}$ values extracted from the full solution of the lattice EoS are often significantly larger than those of the ideal gas EoS as is shown in Fig. 3.7.

Figure 3.9 depicts the strangeness neutrality in the full solution of the lattice EoS by plotting the dependence of the net-strangeness chemical potential $\mu_{\rm S}$ and the net-electric charge chemical potential $\mu_{\rm Q}$ on the net-baryon chemical potential $\mu_{\rm B}$ for a range of temperatures. The results of Fig. 3.9 are for the (Z, A) values of Au nuclei under the conditions of Eqs. (2.34) and (2.35). The figure shows that $\mu_{\rm S} \simeq \mu_{\rm B}/3$ if the temperature is greater than $T \gtrsim 160$ MeV; but the approximation does not describe the lattice results well for lower temperatures. The results of the FRG calculations [109] also showed very similar results to those of Fig. 3.9 except that the FRG method results have a strict ordering of $\mu_{\rm S}(\mu_{\rm B})$ with T [109]. Specifically, the FRG results at higher T approach the $\mu_{\rm S} = \mu_{\rm B}/3$ line, which indicates that approximation of the partial-1 solution is applicable to those calculations as well [46]. On the other hand, the results from the full solution of the lattice EoS in Fig. 3.9 reproduce this ordering of $\mu_{\rm S}$ for low temperatures below $T \lesssim 180$ MeV. However, no clear ordering exists for higher temperatures for either $\mu_{\rm S}$ or $\mu_{\rm Q}$. It is also worth nothing that

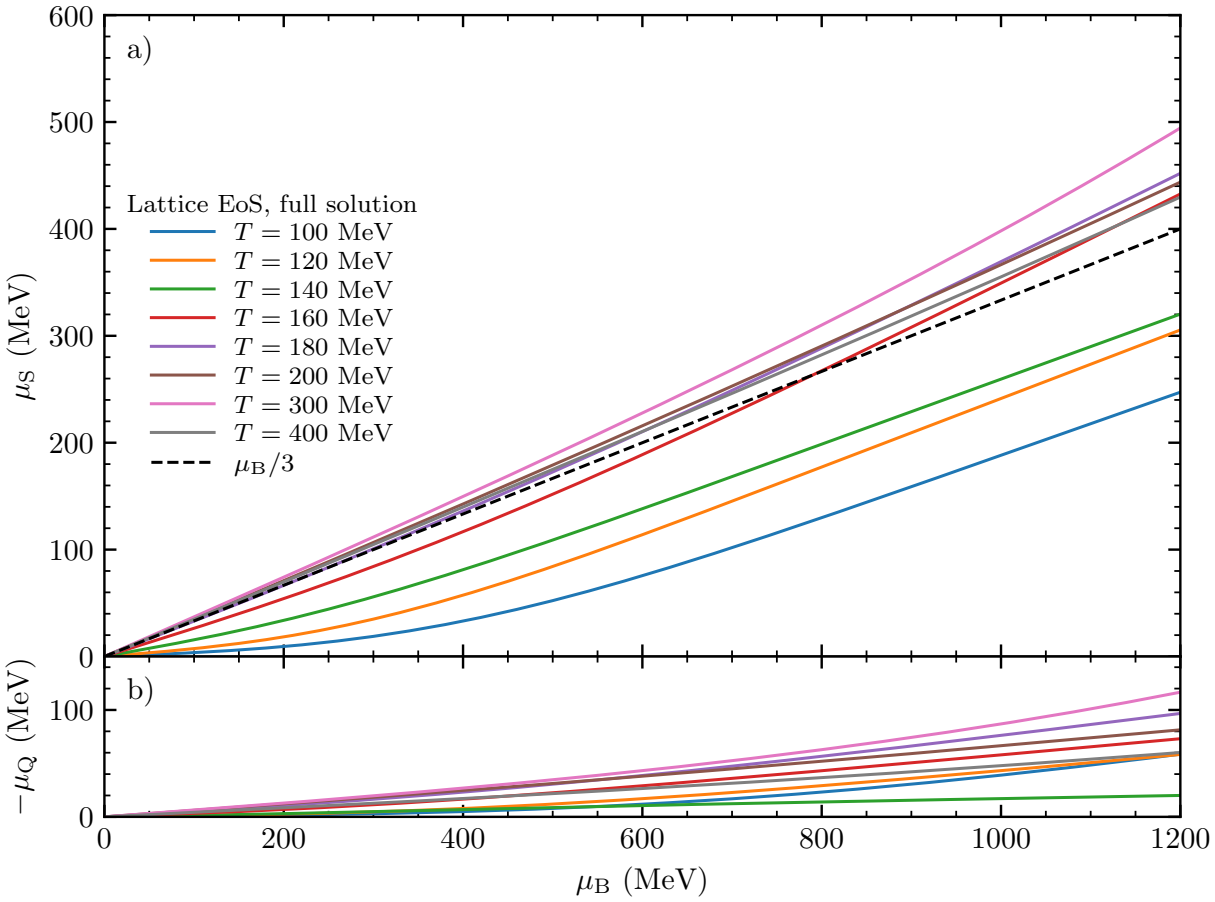

Figure 3.9: Net-strangeness chemical potential μ_S (a) and net-electric charge chemical potential $-\mu_Q$ (b) as functions of the net-baryon chemical potential μ_B at various temperatures for the full solution of the lattice EoS under the condition $n_Q = n_B Z/A$ (for Au) and $n_S = 0$. The line $\mu_S = \mu_B/3$ is also shown for reference.

the magnitude of μ_Q is small in the lattice EoS when $\mu_B/T < 2.5$ in Fig. 3.9, in fact the magnitude is not larger than ≈ 60 MeV. Clearly, the assumptions of the partial-1 solution $\mu_Q = 0$ and $\mu_S = \mu_B/3$ do not work nearly as well in the lattice EoS as they do in the ideal gas EoS [46]. This fact results in the $T - \mu_B$ trajectories of the lattice EoS having temperatures that differ by $\approx 2\%$ and net-baryon chemical potentials that differ by $\approx 16\%$ from the corresponding trajectories of the ideal gas EoS[46]. However, the QGP lifetime which is discussed next does not change much.

3.4 The Lifetime of a QGP

It is possible to calculate the time when the matter enters the parton phase, the time when it exits the parton phase, and the QGP lifetime. Together, these are referred to as $t_{\rm start}$, $t_{\rm end}$, and $t_{\rm QGP} = t_{\rm end} - t_{\rm start}$, respectively [46]. This is accomplished by calculating the first and last times when a $T - \mu_{\rm B}$ trajectory intersects the FRG crossover curve [104] if the collision energy is not too low. For very low collision energies where the trajectory does not intersect the FRG crossover curve, $t_{\rm start}$ and $t_{\rm end}$ are calculated by finding the times when the trajectory intersects the line of constant energy density $\epsilon = 0.51$ GeV/fm^3 that is shown in Fig. 3.2 [45]. The starting time and lifetime of the QGP phase are shown in Fig. 3.10 from the full solutions of the quantum, Boltzmann, and lattice equations of state for central Au+Au collisions as functions of $\sqrt{s_{\rm NN}}$ for $\tau_{\rm F} = 0.2$ fm/c and $t_{\rm T}^{\rm norm} = 4$ fm/c. While the results in Fig. 3.10 are only for one value of $\tau_{\rm F}$, we have shown [45] that $t_{\rm start}$ at a given energy is larger for a larger $\tau_{\rm F}$ as expected and $t_{\rm start}$ is significantly larger at lower energies mostly due to the longer crossing time d_t. The results without transverse expansion in Ref. [45] show that the QGP lifetime is shorter for a larger $\tau_{\rm F}$ because $t_{\rm end}$ and the late-time trajectory are essentially independent of $\tau_{\rm F}$ without transverse expansion. Figure 3.10 shows that the QGP lifetimes from the lattice EoS are larger than those from the ideal gas EoS with either statistics. This happens primarily because the late-time temperatures in the lattice EoS are much larger than in the ideal gas EoS, which is shown in Fig. 3.7.

Figure 3.10 shows that transverse expansion has a significant effect on the QGP lifetimes, especially for large collision energies. Specifically, transverse expansion with $t_{\rm T}^{\rm norm} = 4$ fm/c decreases $t_{\rm QGP}$ by more than a factor of 2 for the lattice EoS at $\sqrt{s_{\rm NN}} = 200$ GeV with $\tau_{\rm F} = 0.2$ fm/c. In Ref. [46], several values of $t_{\rm T}^{\rm norm}$ were considered, and it was found that larger values of $t_{\rm T}^{\rm norm}$ increases the QGP lifetime because the transverse flow develops more slowly. Note that the $t_{\rm start}$ values are essentially unaffected by the transverse expansion effect because transverse expansion takes some time to develop and does not affect the early densities (and hence the trajectories) very much [46]. Including transverse expansion

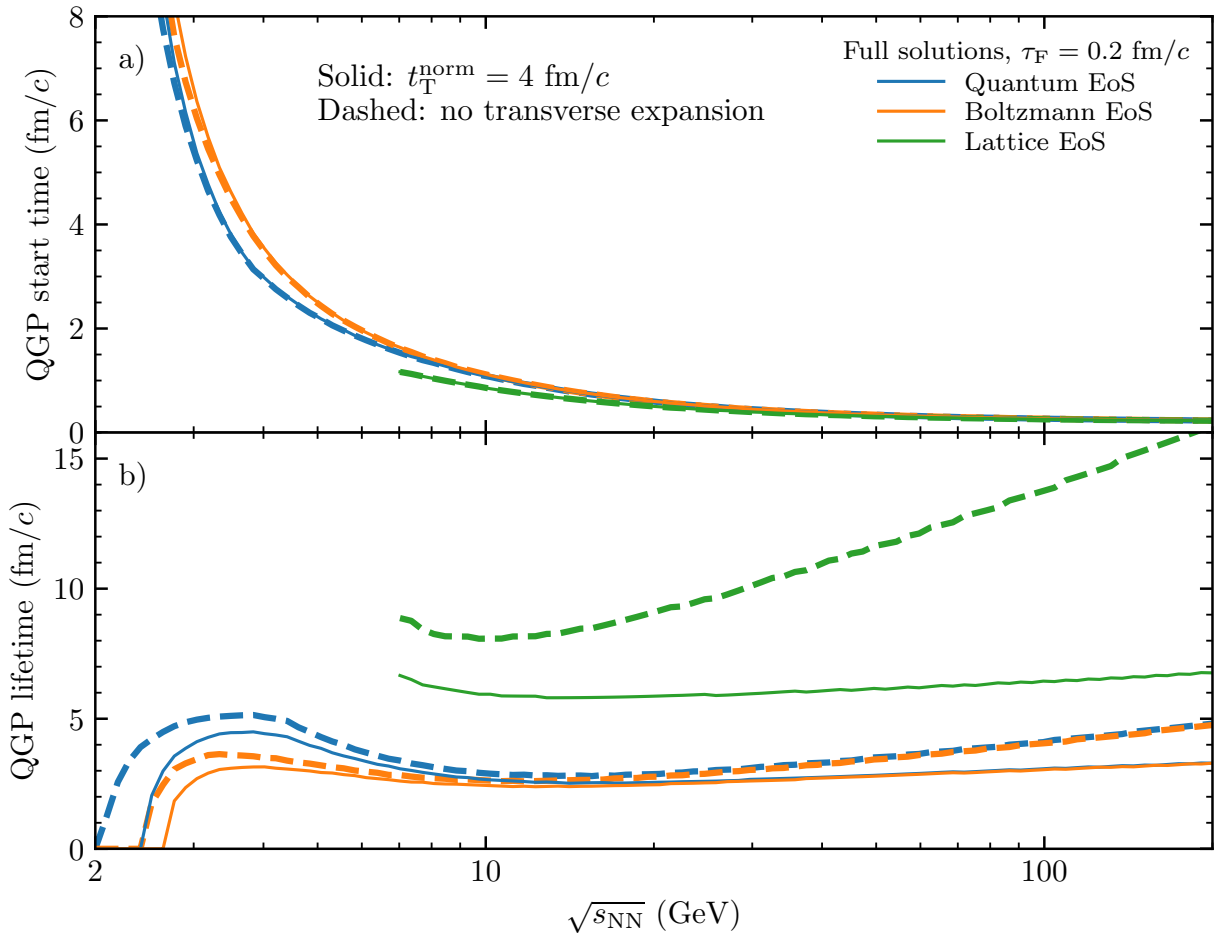

Figure 3.10: The starting time and lifetime of the QGP phase from the full solutions of the quantum EoS, Boltzmann EoS, and lattice EoS for central Au+Au collisions as functions of $\sqrt{s_{\mathrm{NN}}}$ for $\tau_{\mathrm{F}} = 0.2$ fm/c without transverse expansion and with $t_{\mathrm{T}}^{\mathrm{norm}} = 4$ fm/c.

results in smaller densities at late times, so the t_{end} and the QGP lifetime will decrease. Therefore, the QGP lifetime depends significantly on the transverse expansion at all collision energies [46]. Interestingly, the path of a collision trajectory including its position relative to the CEP does not change much for $\sqrt{s_{\mathrm{NN}}} \gtrsim 7.7$ GeV [46]. We have also shown that t_{QGP} may be shorter for a smaller τ_{F} with transverse expansion if $\sqrt{s_{\mathrm{NN}}}$ is large enough. [46]. This counterintuitive behavior is more obvious lattice EoS results, and it is actually a consequence of smaller formation times leading to higher densities and faster rates of transverse expansion. This causes the t_{end} value to be smaller and the QGP lifetime to be shorter.

From Fig. 3.10, it is clear that the QGP lifetime does not increase monotonically with the

collision energy, as one would naïvely expect. For low collision energies between $\sqrt{s_{\rm NN}} \in [3, 5]$ GeV, the results from the ideal gas EoS show that $t_{\rm QGP}$ may have a local maximum [46]. However, more work is needed since the lattice results cannot reach very low collision energies due to the large $\mu_{\rm B}/T$ value there. Still, the lattice EoS results do suggest a slight increase in $t_{\rm QGP}$ once the collision energy decreases below $\sqrt{s_{\rm NN}} \lesssim 11.5$ GeV [46]. Interestingly, numerical results from the AMPT model calculations have also observed a similar non-monotonic dependence on $\sqrt{s_{\rm NN}}$ of $t_{\rm QGP}$ when using the Boltzmann EoS [61]. For the ideal gas EoS results, the QGP lifetime decreases after it reaches the local maximum, before it starts to increase with $\sqrt{s_{\rm NN}}$. The increases of $t_{\rm QGP}$ for high collision energies may be rather slow for the lattice EoS results which include transverse expansion [46]. Recently, the STAR Collaboration showed that the matter produced in Au+Au collisions at $\sqrt{s_{\rm NN}} = 3$ GeV is most likely dominated by hadronic interactions instead of partonic ones [48]. However, the results of Figs. 3.10(a)-(b) indicate that the QGP formation in such collisions depends on more parameters than just the collision energy [46]. For instance, the formation time, the chosen equation of state, and the rate of transverse expansion have all been shown to affect the calculated value of $t_{\rm QGP}$ for $\sqrt{s_{\rm NN}} = 3$ GeV collisions. Interestingly, our work has also shown that the QGP would be formed regardless of these parameters for $\sqrt{s_{\rm NN}} = 4$ GeV central Au+Au collisions.

Chapter 4

Assessing the Accuracy of the ZPC Parton Transport Model

A recent exact analytical solution of the relativistic Boltzmann equation (RBE) provides a much-needed theoretical result against which numerical studies can be compared. Section 4.1 discusses the exact solution paying special attention to its approach to equilibrium and the initial condition. The solution is defined for a massless, isotropically expanding gas, but it is also valid for a non-expanding system. Therefore, we implement the initial condition in ZPC, and the numerical momentum distributions are compared to the theoretical result in Sec. 4.2. Several collision schemes are analyzed and found to give varying levels of accuracy relative to the exact solution. Notably, the universality of the opacity χ is observed such that results at different temperatures but the same χ are statistically the same. This χ-universality motivates the parametrization of two generalized collision schemes in Sec. 4.3 that have a mean deviation from the theoretical result of less than 0.3%. The unexpected excellent agreement between ZPC and the exact solution at high opacities, where the parton cascade usually suffers from causality violation, is a good sign for future works using ZPC for parton transport and kinetic theory calculations. Numerical studies of heavy ion collisions using AMPT will benefit from the knowing that ZPC is robust, after having successfully passed a wide gamut of tests.

4.1 An Exact Analytical Solution of the Relativistic Boltzmann Equation

Recently, an exact analytical solution of the RBE was found for a massless gas under two-body isotropic scatterings in a Friedman-Lemaître-Robertson-Walker (FLRW) metric [77, 78]. The exact solution gives the time evolution of the single particle distribution function as

$$f(p,\tau) = \lambda \exp\left(-\frac{u\cdot p}{T(\tau)\kappa(\tau)}\right)\left[\frac{4\kappa(\tau)-3}{\kappa^4(\tau)} + \frac{u\cdot p}{T(\tau)}\frac{1-\kappa(\tau)}{\kappa^5(\tau)}\right]. \tag{4.1}$$

In Eq. (4.1), λ is the fugacity, $u^\mu = (1,0,0,0)$ is the four-velocity of the co-moving frame, and p^μ is the four-momentum. The temperature depends on the time-dependent scale factor $a(t)$ according to $T(t) = T(0)/a(t)$, where $a(t)$ controls the spatial expansion and $T(0)$ refers to the initial temperature. The simplest FLRW metric may be expressed as

$$ds^2 = dt^2 - a^2(t)\left(dx^2 + dy^2 + dz^2\right). \tag{4.2}$$

There is also a scaled time variable

$$\tau = \int_{\hat{t}_0}^{\hat{t}} \frac{dt'}{a^3(t')} \tag{4.3}$$

in Eq. (4.1) which accounts for the spatial expansion by scaling the time t by the time-dependent mean-free path [77]. The expression for τ above uses the definitions $\hat{t} = t\sigma n_0$ and $\hat{t}_0 = t_0\sigma n_0$, for a constant two-parton cross section σ and initial particle number density n_0. The function $\kappa(\tau) = 1 - \exp\left(-\tau/6\right)/4$ originates in the analytic solution for the evolution of the moments [77].

The FLRW metric defined in Eq. (4.2) is homogeneous, and the single particle distribution function is independent of the spatial coordinates and spherically symmetric in momentum space [77, 78]. Notationally, it will be written as $f(x^\mu, p^\mu, t) \to f(p,t)$ for the remainder of

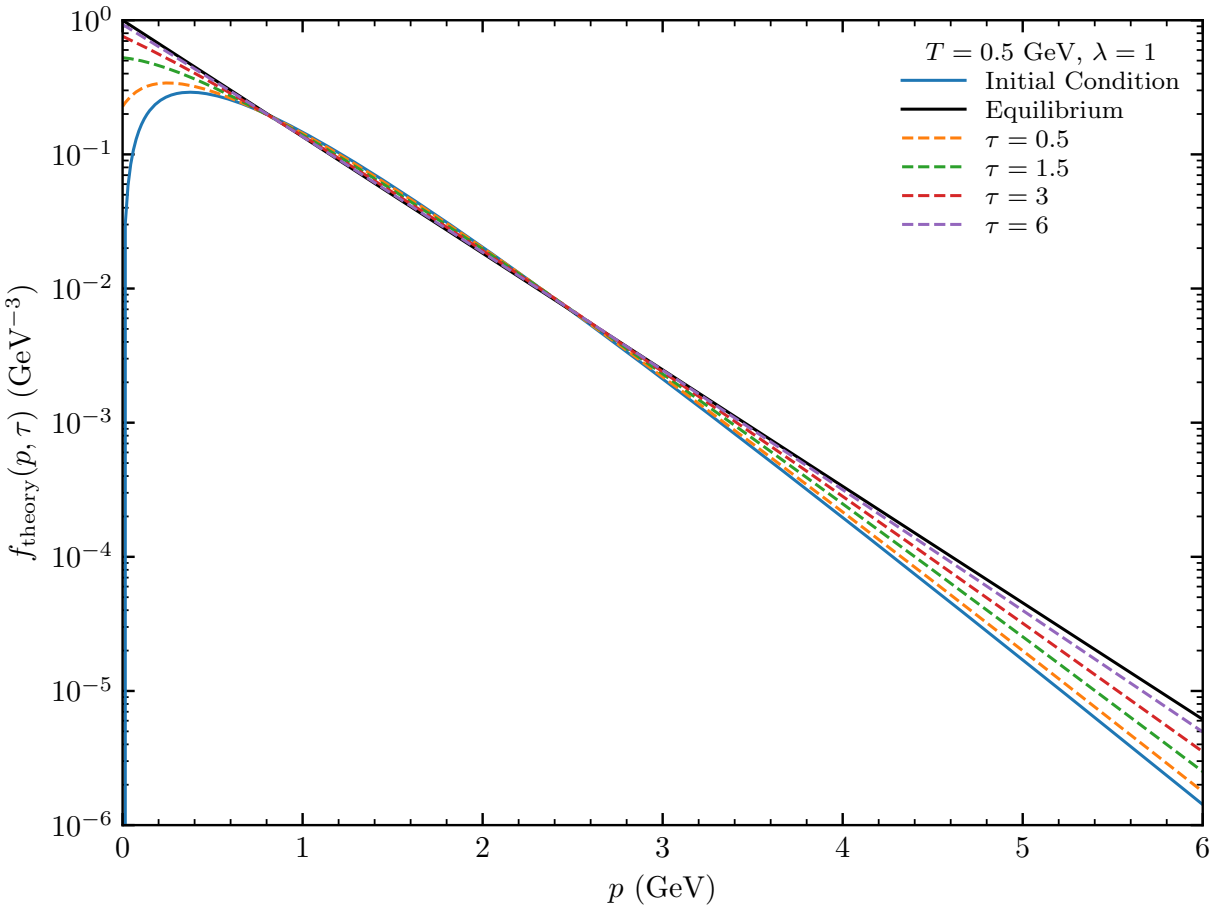

Figure 4.1: Time evolution of $f_{\text{theory}}(p, \tau)$ (dashed) for a non-expanding massless gas from the initial condition (blue) to the equilibrium distribution (black) at $T = 0.5$ GeV with a fugacity of $\lambda = 1$.

this chapter. It is straightforward to find the initial condition of Eq. (4.1) by taking $\tau = 0$ and writing $T(0) = T_0$:

$$f(p, \tau = 0) = \lambda \frac{256}{243} \frac{p}{T_0} \exp\left(-\frac{4p}{3T_0}\right). \tag{4.4}$$

One may also easily show that the exact solution of Eq. (4.6) approaches a thermal distribution for very late times when $\tau \to \infty$ (when this limit can be reached):

$$f_{\text{eq}}(p) \equiv f(p, \tau \to \infty) = \lambda \exp\left(-\frac{p}{T}\right). \tag{4.5}$$

The hadron transport program SMASH [110] was recently compared to the exact solution of

Eq. (4.1) and was found to agree with the approach to equilibrium of the exact solution [111].

Given that the hadron cascade solution of the RBE has been shown to agree with the exact solution, a logical research goal is to answer the question if the ZPC parton cascade [64] also agrees with the exact solution of Eq. (4.1), especially at the high densities expected for a parton matter. Answering this question is a worthwhile pursuit partly because the AMPT model [62] results depend on the accuracy of the ZPC parton cascade. Therefore, we have implemented the initial condition of Eq. (4.4) in ZPC for a system of 16000 massless gluons. Note that the exact solution is also valid when the time-dependent scale factor is a constant $a(t) = 1$ [77]. In this case, one may use the standard ZPC simulations in a box with periodic boundary conditions and isotropic scattering [64] and compare the numerical results to the analytical ones. The choice of a non-expanding system means that the temperature remains constant $T(\tau) = T_0$. From now on, the subscript for the initial temperature will be omitted for clarity, thus Eq. (4.1) may be written in the form:

$$f_{\text{theory}}(p,\tau) = \exp\left(-\frac{p}{T\kappa(\tau)}\right)\left[\frac{4\kappa(\tau)-3}{\kappa^4(\tau)} + \frac{p}{T}\frac{1-\kappa(\tau)}{\kappa^5(\tau)}\right]. \tag{4.6}$$

In the above definition, $\tau = \hat{t} = t\sigma n_0$ because $a(t) = 1$ and $\hat{t}_0 = 0$ in Eq. (4.3).

Figure 4.1 depicts the initial condition of Eq. (4.4), the equilibrium distribution of Eq. (4.5), and the exact solution of Eq. (4.6) for several values of τ for a massless homogeneous gas at $T = 0.5$ GeV with a fugacity of $\lambda = 1$ as a function of the momentum p. At the initial time $\tau = 0$, the initial condition starts at zero when $p = 0$. It steeply rises until a maximum value is reached at $p_{\max} = 0.375$ GeV, and then it decreases. The decrease of the initial distribution with p is at first slower than an exponential function, but eventually it becomes faster than the thermal distribution that is also shown in Fig. 4.1. One can also easily observe the time evolution of the exact solution's approach to equilibrium, which is characterized by an increase in the low-p region and the high-p tail of the distribution with τ. Additionally, the middle momentum region is characterized by a slight decrease with τ

of the distribution from the initial condition to the equilibrium value. Note that there are two stationary points in the exact solution, which give the same value of f regardless of the value of τ.

4.2 Numerical Results from ZPC

The time evolution of a massless gas of gluons in ZPC depends on the temperature T and the cross section σ. Equilibrium is reached at different times depending not on these values separately, but upon a specific combination of these quantities such as the opacity χ [69]. One simple definition of the opacity is the ratio of the interaction length d_{int} to the mean free path l:

$$\chi = \frac{d_{\text{int}}}{l} = \frac{\sqrt{\sigma/\pi}}{1/(\sigma n)}. \tag{4.7}$$

If one assumes that such a gluon system may be described by Boltzmann statistics, then the opacity is given by

$$\chi = \frac{16}{\pi^2} T^3 \sqrt{\frac{\sigma^3}{\pi}}. \tag{4.8}$$

Here, the number density of gluons under Boltzmann statistics is $16T^3/\pi^2$, and the term in the square root originates from the ratio of the interaction length $\sqrt{\sigma/\pi}$ to the mean free path $1/(n\sigma)$ for a density n [79]. Because the parton collision rate depends on the system density, ZPC simulations reach equilibrium at different times depending on χ. Therefore, it will be useful to understand how the time in simulations with one opacity relate to the time evolution of systems with different opacity. Note that the global time t in ZPC is related to τ of the exact solution by χ and T only:

$$\tau = t \sqrt[3]{\frac{16\chi^2}{\pi}} T. \tag{4.9}$$

The scaled time τ thus provides a useful way to relate the evolution of systems at different opacities to one another. For example, with $T = 0.5$ GeV, $t = 9.18$ fm/c and $t = 1.98$ fm/c

correspond to $\tau = 40$ for $\chi = 1$ and $\chi = 10$, respectively. The rest of the results in this chapter uses a cutoff time for the ZPC simulations which corresponds to $\tau = 60$ since this time is long enough for the simulations at each opacity to reach equilibrium. Note that the following results use a constant parton number of $N_{\text{parton}} = 16000$ per event and statistical significance is ensured by using 1000 events for any given configuration.

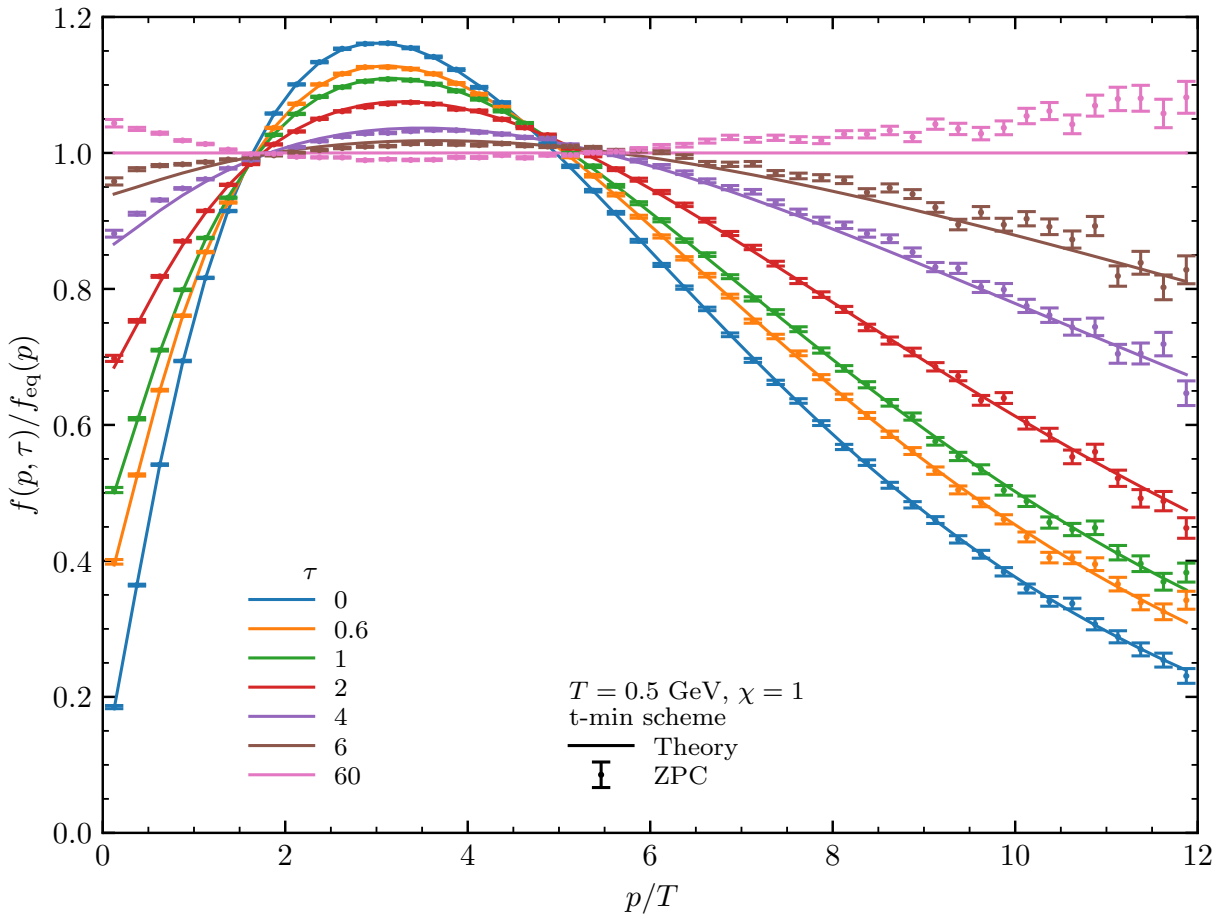

Figure 4.2: Ratio of the bin-averaged $f(p,\tau)/f_{\text{eq}}(p)$ from the exact solution and ZPC using the t-minimum scheme for several τ with $T = 0.5$ GeV and $\chi = 1$ versus p/T.

One key aspect of the ZPC parton cascade is the ability of the user to specify a scattering prescription [64]. To that end, a generic form for the collision scheme is defined using a single parameter r, which allows one to smoothly interpolate between the new collision scheme [69] and the old one [64]. Recall that the parton collision times $t_{c,1}$ and $t_{c,2}$ are in general different,

so there is freedom in assigning a time t_c when the collision will actually occur in ZPC.

$$t_c = \min(t_{c,1}, t_{c,2}) + r|t_{c,1} - t_{c,2}| \tag{4.10}$$

Note that the new collision scheme [69] corresponds to $r = 0$, and the old scheme [64] corresponds to $r = 0.5$ in Eq. (4.10). From now on the new collision scheme will be referred to as the t-minimum scheme since it uses the minimum of the two parton collision times as the real collision time in ZPC. Similarly, the old collision scheme will be referred to as the t-average scheme because it uses the average of the two parton collision times. In Sec. 4.3, two generalized collision schemes will be introduced, which parametrize r as a function of χ; they will be called the t-general-1(2) schemes.

The ratio $f(p,\tau)/f_{\rm eq}(p)$ for $f_{\rm theory}(p,\tau)$ and $f_{\rm ZPC}(p,\tau)$ using the t-minimum scheme [69] for $\chi = 1$ and $T = 0.5$ GeV as a function of p/T is plotted in Fig. 4.2. Note that the bin-averaged values are actually plotted, and these are calculated using

$$f(p_i,\tau) = \int_a^b f(p_i,\tau) d^3p \Big/ \int_a^b d^3p. \tag{4.11}$$

Then, each bin-averaged value $f(p_i,\tau)$ is plotted at the midpoint $(a+b)/2$ for each momentum bin where a constant bin width is used. The initial momentum distribution with $\tau = 0$ from the exact solution is larger than the equilibrium distribution for p/T approximately in the range $\in [1.5, 5]$. However, for $p/T \lesssim 1.5$ and $p/T \gtrsim 5$, the exact solution has a significantly lower occupation compared with the equilibrium distribution when $\tau = 0$. This behavior is also shown in Fig. 4.1. For the initial distribution, $f_{\rm ZPC}(p,0)$ agrees almost perfectly with $f_{\rm theory}(p,0)$, and this agreement is expected since the initial momentum distribution in ZPC is sampled directly from the initial condition of Eq. (4.4). As τ increases, parton collisions cause the system to approach equilibrium, and the exact solution reproduces this behavior as expected; by $\tau = 60$, there is essentially no difference between $f_{\rm theory}(p)$ and

$f_{\rm eq}(p)$. Figure 4.2 shows that the ZPC results agree with the exact solution for early times, but start to differ at late τ. For example, the exact solution reaches equilibrium near $\tau = 60$, but the ZPC model results at this time have an overpopulation of partons with $p/T \lesssim 1.5$ and $p/T \gtrsim 5$ and a slight underpopulation for the central range of p/T in approximately $[1.5, 5]$.

The mean deviation MD between the bin-averaged $f_{\rm theory}(p,\tau)$ and numerical $f_{\rm ZPC}(p,\tau)$ is calculated to quantify the agreement of ZPC with the exact solution according to

$$\mathrm{MD}(\tau) = \frac{\sqrt{\sum_i \left[N_{\rm ZPC}(p_i,\tau) - N_{\rm theory}(p_i,\tau)\right]^2}}{\sum_i N_{\rm theory}(p_i,\tau)}. \tag{4.12}$$

This specific measure of the accuracy is chosen because it ensures that the deviation would be $\mathrm{MD} = 1/\sqrt{N}$ if it were due only to a Gaussian fluctuation. For the ZPC results presented in this work, the total parton number for all events in a dataset is $N = 1.6 * 10^7$. Thus, the lower bound on the MD is $1/4000 = 0.025\%$, and this corresponds to only statistical deviations between the ZPC results and the exact solution.

The τ-evolution of the MD is plotted in Fig. 4.3 for several χ with $T = 0.5$ GeV using the t-minimum collision scheme. At early times in the evolution when $\tau < 1$, the ZPC model results agree almost perfectly with the exact solution results for all opacities. The agreement indicates that the deviations between the two models are consistent with Gaussian fluctuations. Figure 4.3 shows that, at finite χ, the mean deviation increases for later times when $\tau > 1$ until it reaches a saturation value at approximately $\tau = 60$. For $\chi = 0.1$ and the subdivision results, there is no noticeable increase with τ, and the MD remains consistent with statistical fluctuations throughout the entire evolution. This result is in agreement with previous results which have shown that ZPC does not suffer from causality violation at low opacities or in the dilute limit [69]. Interestingly, the increase and saturation of MD depends non-monotonically on χ, which is similar to the behavior of the ratio of the $\mathrm{var}(p_{\rm T})$ to the theoretical value in the Boltzmann limit as shown in Ref. [69]. At saturation, the MD

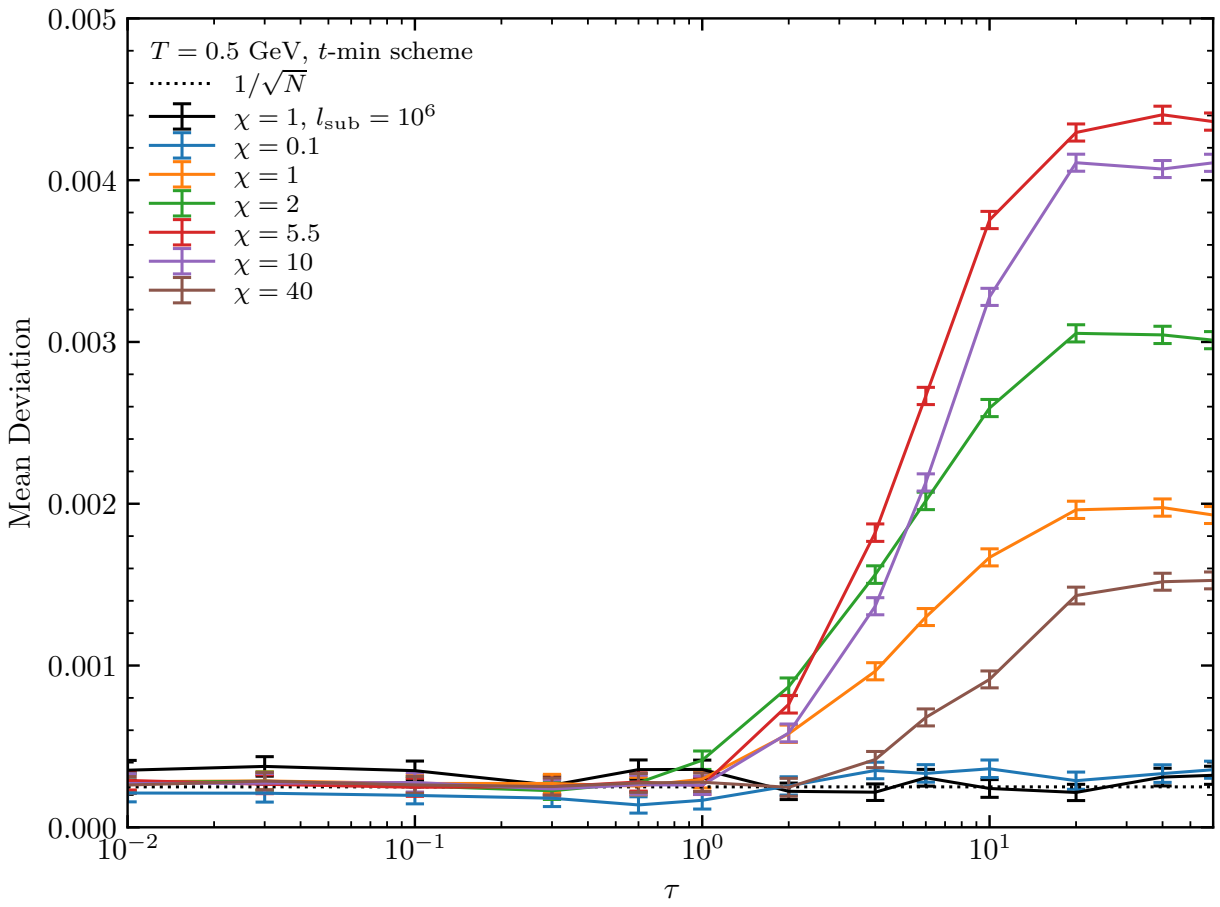

Figure 4.3: The τ-evolution of MD for several χ with $T = 0.5$ GeV using the t-minimum collision scheme. The subdivision result for $l_{\rm sub} = 10^6$ which reduces the effective opacity to $\chi_{\rm eff} = 0.001$ and the lower bound of $1/\sqrt{N}$ are also shown for reference.

increases from the lowest χ, reaches a maximum value at $\chi = 5.5$, and decreases for $\chi > 5.5$. Specifically, for $\chi = 0.1$, MD $\approx 0.04\%$, while for $\chi = 5.5$, MD $\approx 0.44\%$ at $\tau = 60$. The maximum MD at equilibrium is unexpectedly small at a reasonably large χ since a parton cascade must suffer from the causality violation when it is not in the dilute limit [69, 79]. Note that the error bars on the MD results of Fig. 4.3 are calculated using the standard error analysis procedures according to

$$\delta\mathrm{MD}(\tau) = \frac{1}{\sum_i N_{i,\mathrm{ZPC}}(\tau)} \sqrt{\frac{\sum_i \left[N_{i,\mathrm{ZPC}}(\tau) - N_{i,\mathrm{theory}}(\tau)\right]^2 \delta N_i^2}{\sum_i \left[N_{i,\mathrm{ZPC}}(\tau) - N_{i,\mathrm{theory}}(\tau)\right]^2}}. \tag{4.13}$$

For brevity in Eq. (4.13), the total number of partons in the i^{th} momentum bin is written as $N_{i,\text{ZPC}}$ for the ZPC results and $N_{i,\text{theory}}$ for the exact solution results. Additionally, the uncertainty of N_i is assumed to be $\delta N_i = \sqrt{N_{i,\text{theory}}}$, though only very small differences occur if one would use $\delta N_i = \sqrt{N_{i,\text{ZPC}}}$.

4.3 Generalized Collision Schemes to Further Improve Accuracy

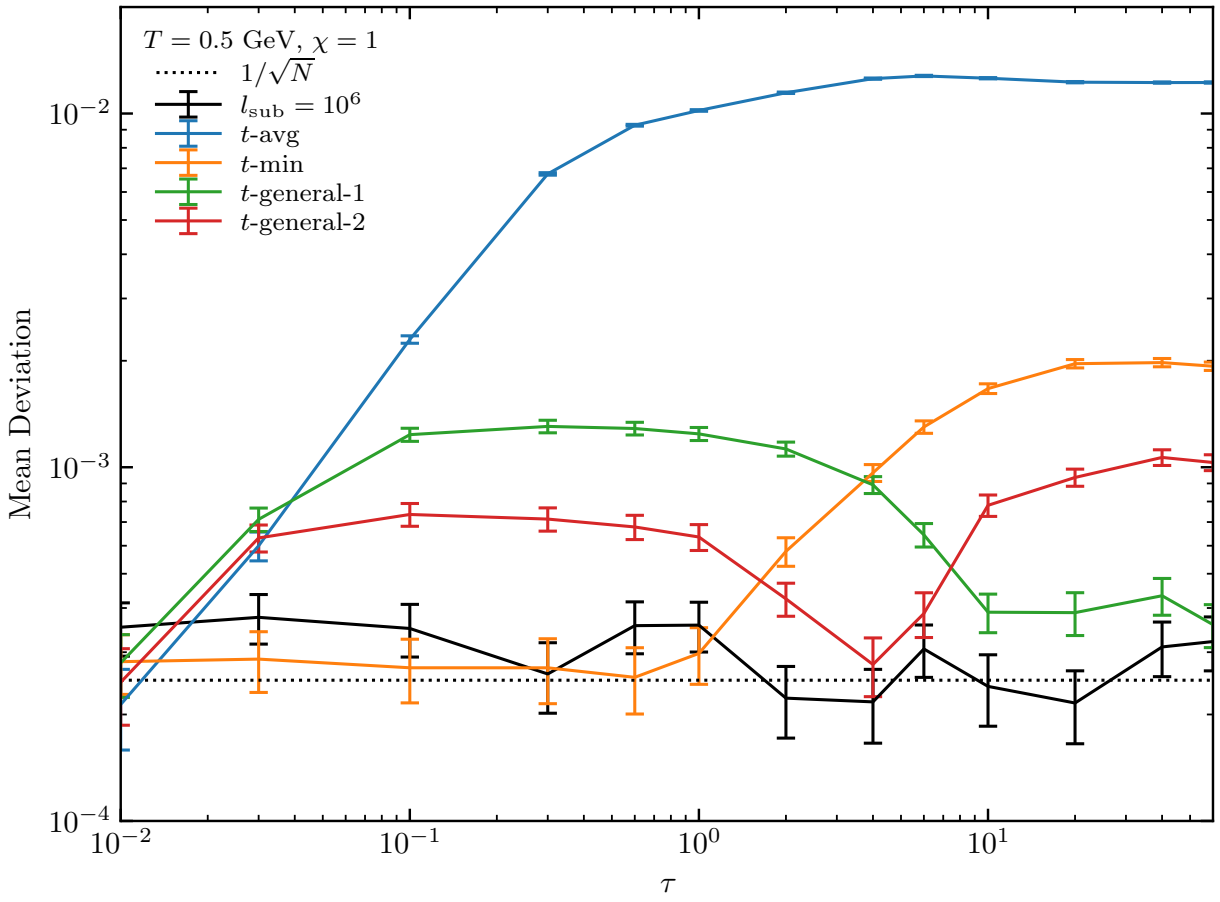

Figure 4.4: The τ-evolution of MD for the t-average (blue), t-minimum (orange), the t-general-1 (green) and the t-general-2 (red) collision schemes with $T = 0.5$ GeV and $\chi = 1$. The results for parton subdivision with $l_{\text{sub}} = 10^6$ (black) and the theoretical expectation for Gaussian fluctuations are also shown for reference.

The mean deviation between the ZPC $f_{\text{ZPC}}(p, \tau)$ and that of the exact solution was shown

to be unexpectedly small at a relatively large opacity of $\chi = 5.5$ in Sec. 4.2. Therefore, one may ask whether the agreement between the ZPC results and the exact solution can be improved using a different collision scheme. To that end, two generalized collision schemes are found with the goal of improving the MD maximally for each opacity. This goal is accomplished by testing different values of r in Eq. (4.10) at a given χ in order to find the optimal r_{optimal} that minimizes the MD in one of two ways. The t-general-1 collision scheme minimizes the equilibrium value of the MD at each χ separately, then parametrizes the resulting r_{optimal} values as a function of χ. On the other hand, the t-general-2 collision scheme minimizes the maximum MD overall all τ in the evolution and parametrizes those r_{optimal} values.

Figure 4.4 shows the τ-evolution of the mean deviation for the t-average, t-minimum, and both t-general collision schemes for $\chi = 1$ with $T = 0.5$ GeV. The results for the parton subdivision method with $l_{\text{sub}} = 10^6$ are also shown, and they appear to have no dependence on τ and remain mostly consistent with the lower bound of $1/\sqrt{N}$ where the MD is caused by only statistical fluctuations. Note that the faster subdivision scheme for box calculations is utilized here in which the volume is reduced by $V \to V/l_{\text{sub}}$ instead of the original subdivision scheme which increases the parton number. [69]. For the t-average collision scheme [64], the MD reaches an equilibrium value of $\approx 1.2\%$ which is a factor of ≈ 6.3 times the value for the t-minimum scheme [69]. It is also clear that fine-tuning of the r parameter in Eq. (4.10) may further reduce the equilibrium value of the MD. Note that the MD for the t-general-1 scheme has a value of $\approx 0.04\%$ at equilibrium which is quite close to the expectation of statistical fluctuations, though the earlier τ results are much worse than those of the t-minimum scheme. The t-general-2 scheme also yields a lower value of the equilibrium MD, but does not show quite the same improvement at equilibrium as does the t-general-1 scheme. On the other hand, the maximum value of the MD in the t-general-2 scheme is lower than the maximum MD of the t-general-1 scheme, which may be a desirable feature. Unfortunately, adjusting the value of r often causes the early-τ results to be much

worse than when using the t-minimum collision scheme. This behavior has been observed for a variety of collision schemes.

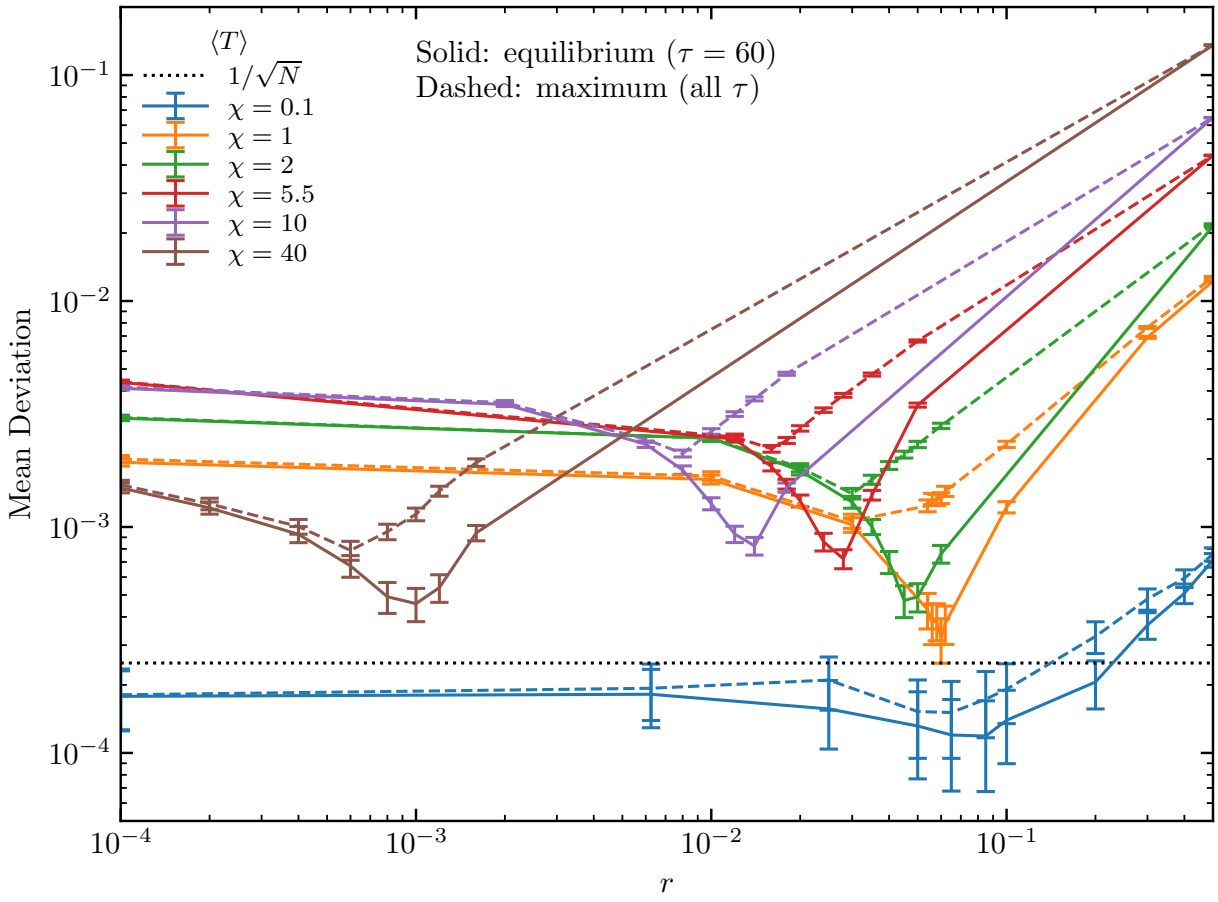

Figure 4.5: The equilibrium (solid) and maximum (dashed) values of the T-averaged MD versus r for several χ. The theoretical expectation for Gaussian fluctuations is also shown for reference.

Another unexpected feature of the ZPC results is an apparent lack of dependence on the temperature of the MD for a given χ, which we refer to as the χ-universality. The lack of significant differences between the entire τ-evolutions of the MD for $T = 0.2$ GeV and $T = 0.5$ GeV motivates the choice to average the MD over the two temperatures. For the remainder of this section, this T-averaged MD is presented instead of for each temperature separately. Figure 4.5 shows the dependence of the equilibrium (at $\tau = 60$) and the maximum (over all τ) value of the MD averaged over T on the r parameter of the collision scheme in

Eq. (4.10) for several χ. Note that the $r = 0$ values for the t-minimum scheme [69] are plotted at the position $r = 10^{-4}$, and the same non-monotonic behavior of MD with χ is also observed in Fig. 4.3. As r increases from zero, both the equilibrium and maximum MD decrease until they reach a minimum value at some optimal r_{optimal}, and the optimal r is larger for the equilibrium MD results. Initially when r increases from zero, the decrease of MD may be rather small until r approaches about a factor of 10 times lower than the r_{optimal}. In this region of slow descent, the MD at equilibrium and its maximum value over all τ have exactly the same behavior. Then the maximum MD reaches its minimum value with r at about 60% the r_{optimal} value for the equilibrium MD. Beyond r_{optimal}, both the equilibrium and maximum values of the MD increase until attaining the same maximum value at $r = 0.5$ for the t-average collision scheme [64].

It is also apparent from Fig. 4.5 that the value of r_{optimal} increases as χ decreases for either the equilibrium or maximum values of the T-averaged MD. The previously observed χ-universality of the MD motivates the parametrizing of r_{optimal} for both the equilibrium and the maximum MD values as a function of χ only. The uncertainty in r_{optimal} for each χ is estimated by calculating the full-width of the MD(r) curve at 125% the value of MD(r_{optimal}). These data are then used in an iterative fitting procedure to obtain a smoothly decreasing function $r(\chi)$: this is referred to as the t-general-1 or -2 collision scheme. In the iterative procedure, first a function with three unknown coefficients is fit to the individual $r_{\text{optimal}}(\chi)$ values of either the equilibrium or maximum MD. Two of the three coefficients are found to be quite close for the parametrizations of both MD, therefore their average is taken and used in a second fitting function. The closeness of the two coefficients is assessed by way of the covariance matrix of the three parameters in each fit which diagonal elements quantify the square of the uncertainty in each free parameter. The second stage of the fitting process involves a function with only one free parameter, these are the constant coefficients

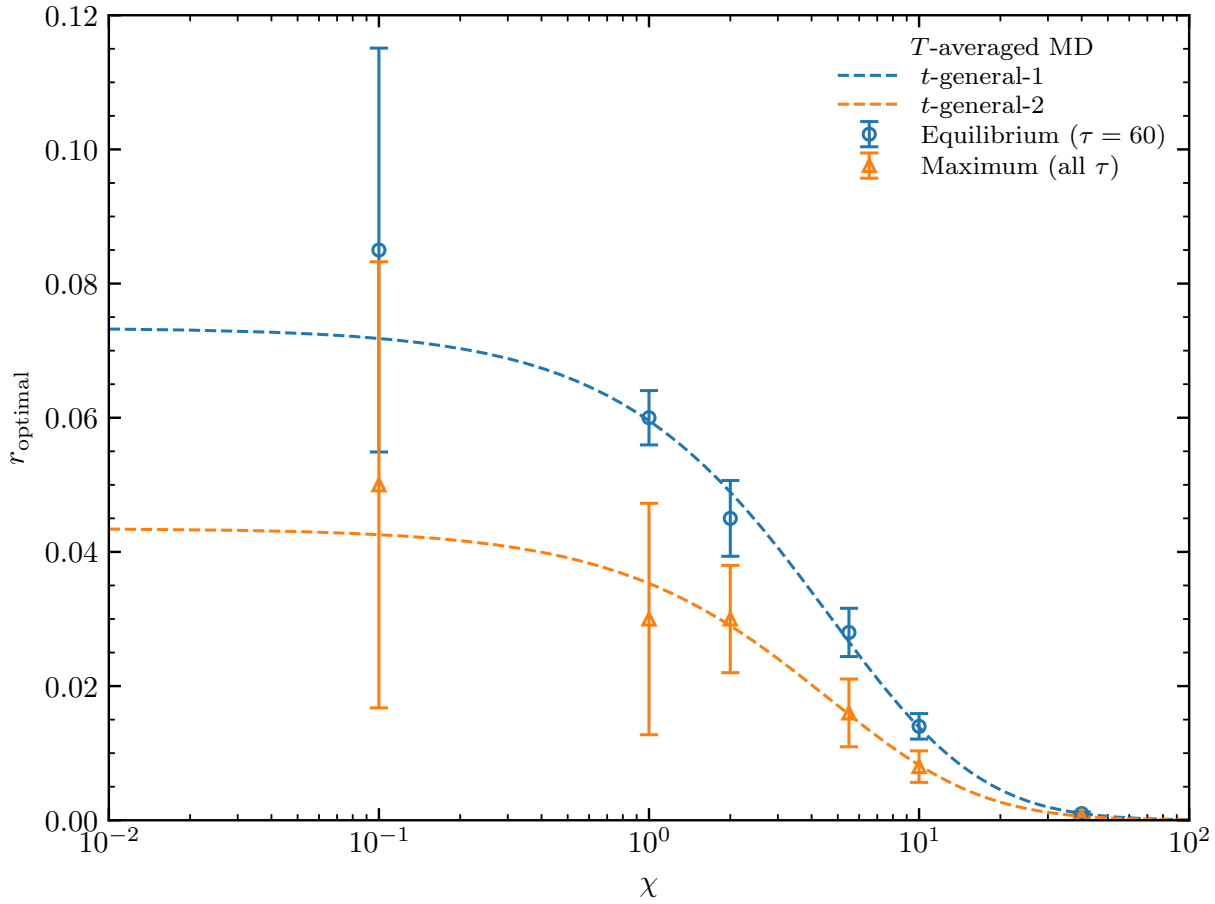

Figure 4.6: The individual T-averaged r_{optimal} values (markers with error bars) and their parametrizations (dashed) for the equilibrium (blue) and maximum (orange) MD versus χ.

in Eq. (4.14). The parametrizations of $r(\chi)$ for both t-general collision schemes are given by

$$\begin{aligned} r_1(\chi) &= 873\,(15.8+\chi)^{-3.40}, \quad t\text{-general-1 for the equilibrium MD} \\ r_2(\chi) &= 518\,(15.8+\chi)^{-3.40}, \quad t\text{-general-2 for the maximum MD.} \end{aligned} \tag{4.14}$$

The specific functional form of $r(\chi)$ in Eq. (4.14) ensures that $r \to 0$ as $\chi \to \infty$, which is a trend observed in Fig. 4.5. Equation (4.14) also results in r being always less than one, which must happen since otherwise Eq. (4.10) would give negative collision times for $r > 1$, which would be undesirable.

In Fig. 4.6, the r_{optimal} values for both the equilibrium value and the maximum value of

the MD are plotted together with their estimated uncertainties for each opacity and their parametrizations $r_i(\chi)$ for the two datasets. The two generalized collision schemes defined with these parametrizations are given in Eq. (4.14) above. The t-general-1 scheme has a value of $r_1(0) \approx 0.044$, while the t-general-2 scheme has $r_2(0) \approx 0.073$. The uncertainties for each r_{optimal} value increases as χ decreases, and this trend may be viewed in Fig. 4.5 where the width of each $r(\chi)$ curve at 125% of the value of the minimum deviation increases as χ decreases. This behavior also agrees with the expectation that the collision scheme does not matter much at low opacity, where the parton cascade method should be accurate and free from causality violation [69, 79]. In the high-opacity limit, both parametrizations decrease as a power of χ, and this means that $r \approx 0$ will yield the best results in ZPC [69] in the limit of dense systems.

The ratio of $f_{\text{ZPC}}(p,\tau)$ to the bin-averaged $f_{\text{theory}}(p,\tau)$ at equilibrium ($\tau = 60$) is shown in Fig. 4.7 for several opacities with $T = 0.5$ GeV. The results using the t-minimum collision scheme [69] are compared to those of the t-general-1 collision scheme of Eq. (4.14). When using the t-minimum scheme, $f_{\text{ZPC}}(p,\tau) > f_{\text{theory}}(p)$ at $p/T \lesssim 1.5$ and $p/T \gtrsim 5$, but the reverse is true for p/T approximately in the range $[1.5, 5]$ at all χ. On the other hand, the t-general-1 scheme decreases the ratio of the ZPC results to the exact solution $f_{\text{theory}}(p,\tau)$ for the same low and high momenta ranges, while it increases the ratio for the middle momenta. The result is an almost perfectly flat curve consistent with unity for most of the p-range. Large statistical fluctuations are expected at high momenta since there are far fewer partons with $p \gg T$. Notably, the $f_{\text{ZPC}}(p,\tau)$ from the t-general-1 collision scheme are underpopulated relative to $f_{\text{theory}}(p,\tau)$ for $p/T \lesssim 1$, and this behavior is not due to statistical fluctuations.

In Fig. 4.8, the T-averaged MD as a function of χ is plotted and the accuracies of various collision schemes are compared relative to the exact solution [77, 78]. The t-minimum scheme [69] significantly reduces the error between $f_{\text{ZPC}}(p,\tau)$ and $f_{\text{theory}}(p,\tau)$ at equilibrium when compared with the t-average scheme [64]. Interestingly, a non-monotonic behavior in χ of the equilibrium MD also appears when using the t-minimum scheme, whereas the

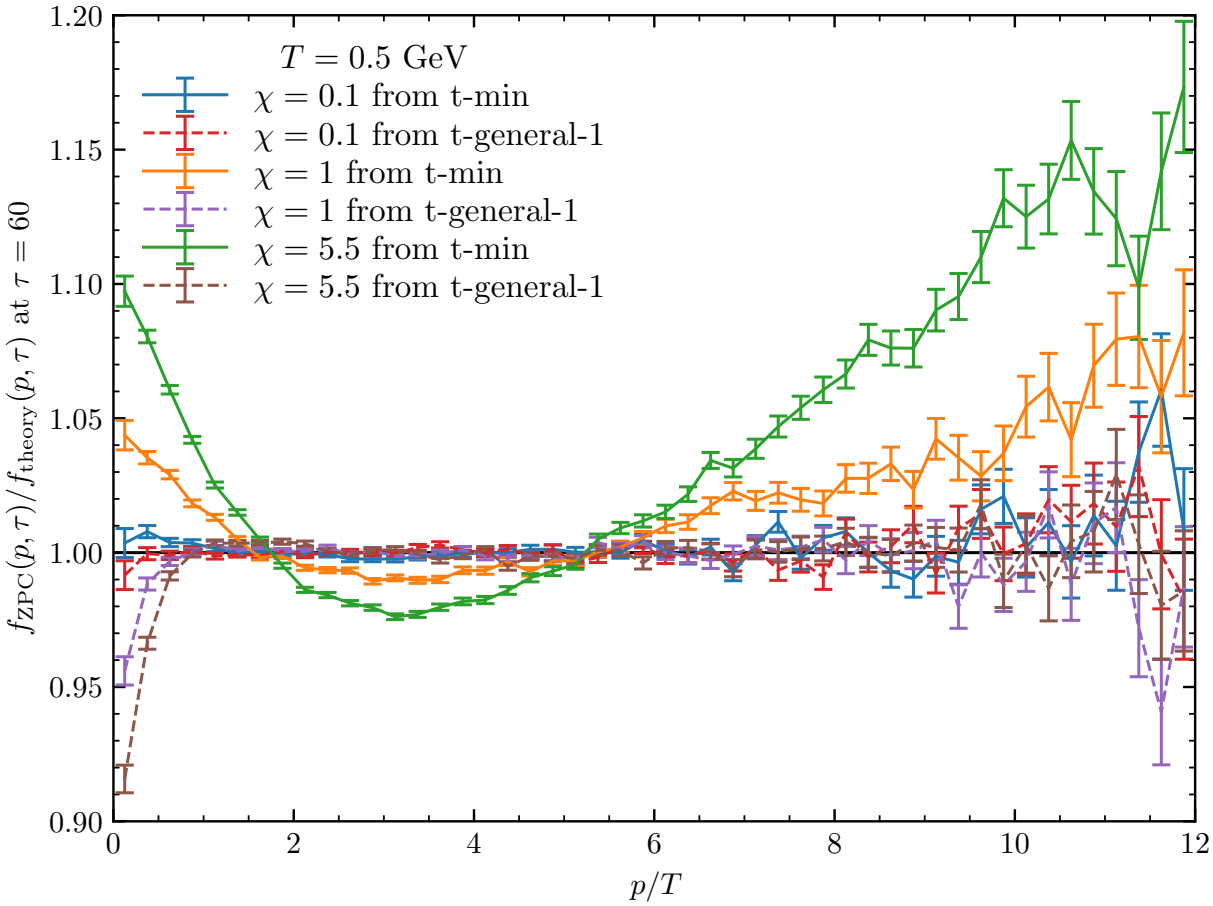

Figure 4.7: The ratio $f_{\mathrm{ZPC}}(p,\tau)/f_{\mathrm{theory}}(p,\tau)$ versus momentum p at $\tau = 60$ using the t-minimum (solid) and t-general-1 (dashed) collision schemes for several χ with $T = 0.5$ GeV.

t-average scheme increases monotonically within $\chi \in [0.1, 40]$. A further improvement in the value of the MD when compared with the t-minimum scheme is obtained when using either of the two t-general schemes of Eq. (4.14). Except at low χ, where the collision scheme is not expected to significantly alter the numerical results, both t-general schemes decreases the value of MD for $\chi \geq 1$ significantly. The t-general-1 scheme reduces the MD by a factor up to 5; the t-general-2 scheme by a factor up to 2. Both t-general schemes also display a similar non-monotonic dependence of the MD on χ. Notably, in the dilute limit when $\chi \ll 1$, all collision scheme appear to converge to the same value near the lower bound of $1/\sqrt{N}$ which is consistent with previous results [69]. Also, when using either of the t-general collision

schemes, at no point does the error between the ZPC results and the exact solution exceed 0.25%, which is an unexpectedly good agreement for large χ. Given that the initial condition of Eq. (4.4) is far away from equilibrium as shown by Fig. 4.1, the agreement between the ZPC model results and the exact solution is a non-trivial verification of the ZPC parton transport model.

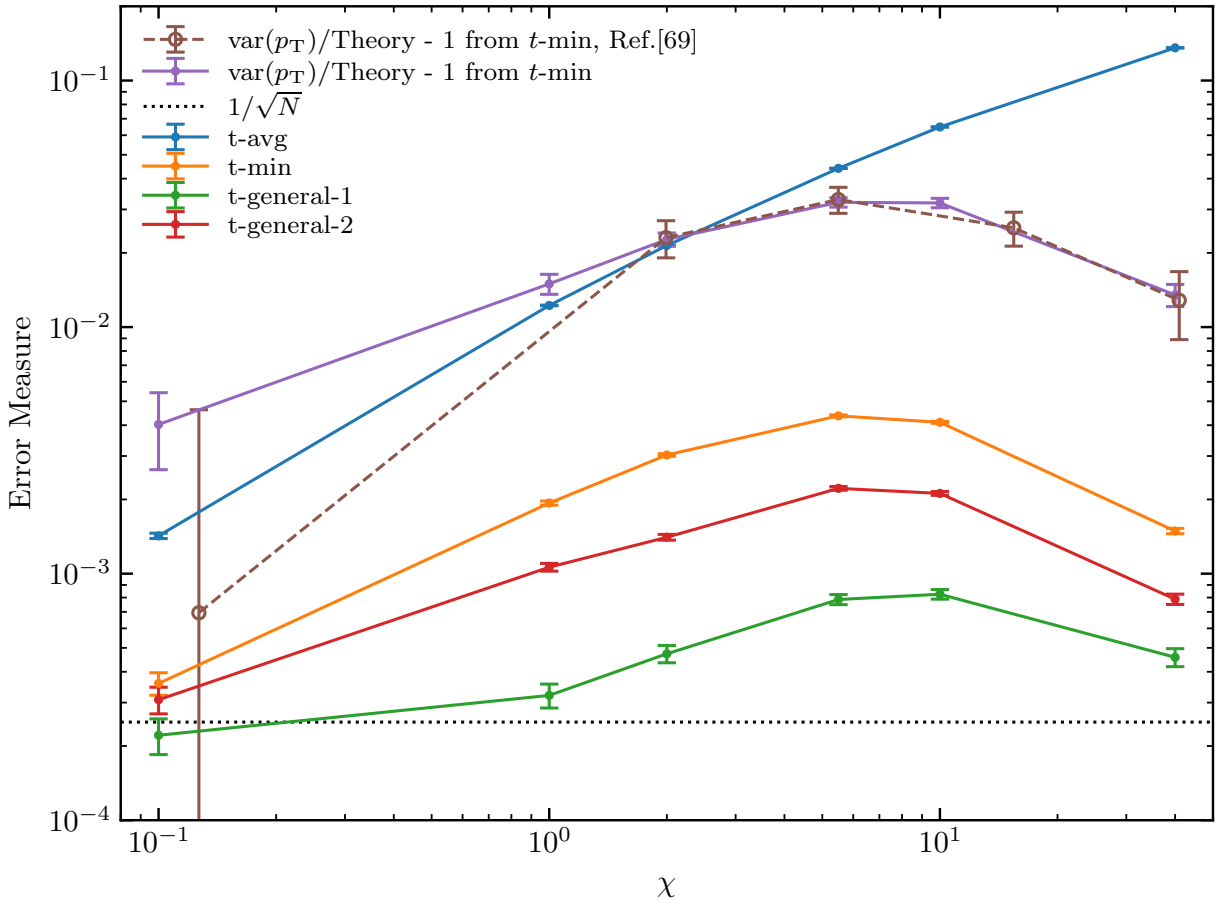

Figure 4.8: The MD averaged over T for the t-average, the t-minimum, both t-general collision schemes, and the var(p_T) /Theory $-$ 1 compared to that of Ref. [69] versus χ. The theoretical expectation of Gaussian fluctuations (dotted) is also shown for reference.

Figure 4.8 also shows the same non-monotonic behavior of the error between the var(p_T) and the theoretical thermal equilibrium value for the Boltzmann distribution [69]. Here, the variance of the p_T distribution is defined by $\mathrm{var}(p_T) = \langle p_T^2 \rangle - \langle p_T \rangle^2$, and the theoretical value for the massless parton system under consideration is $\mathrm{var}(p_T) = (8 - 9\pi^2/16)T^2$. Note that

the general forms of the $\langle p_{\mathrm{T}} \rangle$ and $\langle p_{\mathrm{T}}^2 \rangle$ for massive partons are derived in Appendix B.1, while the theoretical value quoted just now corresponds to the limit $m \to 0$ in Eqs. (B.15) and (B.16). Note that using the var(p_{T}) as a measure of the agreement between the numerical momentum distribution and the theoretical expectation is rather limiting because two different functions can have very different shapes but the same var(p_{T}). For completeness however, we have calculated the var(p_{T}) at equilibrium and compared to the previous results [69]. A good agreement for $\chi > 1$ has been observed within statistical errors. In the low opacity region, the uncertainty of the previous results [69] are expected to be larger than that of our results by a factor $\approx 2\sqrt{2}$. This expectation is based on the fact that the results in this chapter use four times the number of partons and the same number of events. Because our error bars of the var(p_{T}) in Fig. 4.8 represent the T-averaged results, this implies that they account for eight times the number of simulated partons than do the previous results. Under this simple assumption, even the low χ var(p_{T}) results would be consistent with each other. In fact, both results have been found to be consistent with the subdivision results. Overall, the MD of Eq. (4.12) should be a more robust measure of the accuracy of the ZPC model than the previous var(p_{T}) measure because the MD evaluates the full momentum distribution.

Chapter 5

Working on Unsolved Problems in Parton Transport

In Ch. 4, parton transport in ZPC was assessed with an exact solution of the relativistic Boltzmann equation and was found to reproduce almost exactly the theoretical results. This chapter maintains the focus on parton transport in ZPC, but addresses work that has been done on open problems. The 3D problem, or why a new collision scheme works very well in box simulations but not in simulations with 3D expansion, is discussed in Sec. 5.1. The solution to this problem has direct implications on future numerical studies of heavy ion collisions because ZPC is used to calculate the partonic interactions in the AMPT model. Therefore, answering whether a new collision scheme can be used to remove the causality violation in ZPC instead of resorting to the parton subdivision method will mean accurate results in AMPT can be obtained without altering event-by-event fluctuations and paying a massive computational overhead. A problem is found in the default random number generator (RNG) of ZPC for a spherical initial condition with 3D expansion, and using a more modern RNG removes the problem. Unfortunately, the same issue still occurs in the default initial condition with 3D expansion. Section 5.2 presents the agreement of numerical probability density functions of the total CM energy squared s for parton collisions. These distributions are derived in Appendix B.3, and the agreement ZPC has with them is excellent. Reproducing theoretical $f(s)$ distributions implies that ZPC correctly models the distribution of scattering processes that occur in the medium produced by heavy ion collisions. More work is still needed to understand why one of these distributions should describe

the $f(s)$ for collisions of approaching partons. Finally, a method of implementing the effect of external fields on the partons in ZPC is discussed in Sec. 5.3. Allowing partons' trajectories to curve between collisions would enable one to numerically study the chiral magnetic effect that has recently generated quite a stir in the field of nuclear physics [22, 85, 112].

5.1 The 3D Problem

5.1.1 The Default Initial Condition

Equation (4.10) defines the generic collision scheme for two-to-two parton scattering in ZPC via the single parameter $r \in [0, 1]$. With this definition, the original scattering prescription [64] in ZPC corresponds to $r = 0.5$, while the new collision scheme [69] corresponds to $r = 0$. Note that the results in this section use the differential cross section with forward-angle scatterings. In Sec. 4.2, the old and new scattering schemes are named as the t-average and t-minimum schemes, respectively. The t-minimum collision scheme has recently been used to significantly improve the ZPC results for box simulations [69] by reproducing the exact subdivision answers for a large factor $l_{\rm sub} = 10^6$. Reference [69] utilized the new subdivision transformation which reduces the box volume by $V \to V/l_{\rm sub}$ instead of increasing the parton number by $N \to N \times l_{\rm sub}$. This newer subdivision method, which only works for simulations with a fixed volume, decreases the computational cost and makes large subdivision factors feasible. Unfortunately, the t-minimum collision scheme does not work well at improving the ZPC results for simulations with three-dimensional expansion, which is unexpected. This failure of the t-minimum scheme for 3D expansion simulations is referred to as the 3D problem.

Figure 5.1 shows the ratios of the final $dN/dp_{\rm T}$ for the t-average and t-minimum collision schemes to the subdivision results for the built-in 3D expansion initial condition with $N_{\rm parton} = 500$, $T = 0.5$ GeV, $\sigma = 2.6$ mb, and an initial opacity at mid-pseudorapidity of $\chi(\eta \approx 0) = 0.48$ for 1000 events. Here, the gluon number density in the default initial

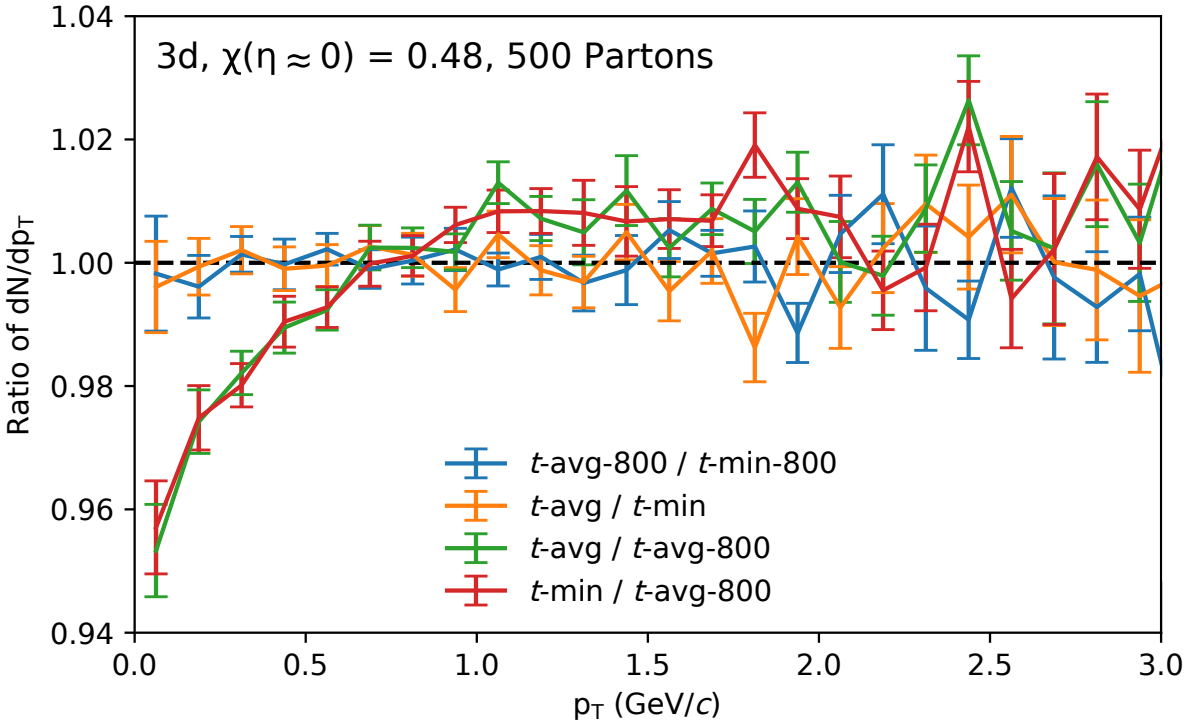

Figure 5.1: The ratios of dN/dp_{T} at freezeout for the 3D expansion initial condition for 500 partons per event at $T = 0.5$ GeV, $\sigma = 2.6$ mb, and an initial opacity at mid-pseudorapidity of $\chi(\eta \approx 0) = 0.48$ for the t-average and t-minimum collision schemes. Note that "-800" represents the subdivision results at $l_{\mathrm{sub}} = 800$.

condition of ZPC depends on the pseudorapidity η according to

$$n(\eta = 0) = \frac{N}{\pi R_{\mathrm{T}}^2 \tau_0 \Delta\eta}, \tag{5.1}$$

where R_{T} is the transverse area, τ_0 is the parton formation time, and $\Delta\eta = 10$ is the total spread in pseudorapidity of the initial partons [64]. Note that the t-average collision scheme is labelled by "i11", and the t-minimum collision scheme is labelled by "i20" in the ZPC program, this is an older notation that refers to the user-defined value of $IORD\_SCH$ that sets the collision scheme in ZPC [64]. The ratio of dN/dp_{T} with a subdivision factor of $l_{\mathrm{sub}} = 800$ for the two collision schemes is consistent with unity over a wide range of p_{T}. This behavior is consistent with the fact that the collision scheme does not affect the final results

in ZPC, when the opacity is small enough (after parton subdivision) [79]. Both collision schemes without subdivision have the same p_{T}-distributions, and their ratio in Fig. 5.1 is also essentially equal to one over the same range. The ratios of dN/dp_{T} for each non-subdivision result to the subdivision result is lower by approximately 5% for the smallest p_{T}-bin. As p_{T} increases, the ratio increases toward one for both collision schemes, and reaches unity near $p_{\mathrm{T}} \approx 0.8$ GeV/c. For higher transverse momentum bins, the non-subdivision results have a slightly higher population than the subdivision results, although the statistical uncertainties are large enough to almost be consistent with unity. Currently, there is some uncertainty on whether $l_{\mathrm{sub}} = 800$ is a large enough subdivision factor to guarantee the results are exact, so more work is needed to investigate this question. However, if the subdivision results with $l_{\mathrm{sub}} = 800$ can be trusted and yield the exact answer, then Fig. 5.1 clearly shows that the t-average and t-minimum collision schemes produce almost the same (albeit inaccurate) results for the default 3D expansion initial condition; this seems to contradict the finding from the previous ZPC box calculations [69].

For comparison, the results shown in Fig. 5.2 are the same as those of Fig. 5.1 except that the box initial condition is used with a constant opacity of $\chi = 0.48$, and the simulation is stopped after $t = 24$ fm/c. The size of the box is chosen such that its volume equals that of a system of 500 gluons at $T = 0.5$ GeV when using Maxwell-Boltzmann statistics, and this choice ensures that the system will reach equilibrium if the simulation runs for long enough. The blue line of Fig. 5.2 shows that the t-average and t-minimum collision schemes with subdivision produce the same p_{T} spectra. Note that the subdivision factor is significantly larger ($l_{\mathrm{sub}} = 10^6$) because the box simulations of ZPC can take advantage of the new parton subdivision method [69]. The results of the two collision schemes without subdivision are significantly different across the same p_{T}-range, with the t-average scheme about 13% smaller than the t-minimum scheme at the lowest p_{T}-bin. As p_{T} increases, this ratio increases toward one and surpasses unity around $p_{\mathrm{T}} \approx 0.6$ GeV/c before it reaches a maximum value of approximately 1.04 around $p_{\mathrm{T}} \approx 1.3$ GeV/c. The t-average to t-minimum

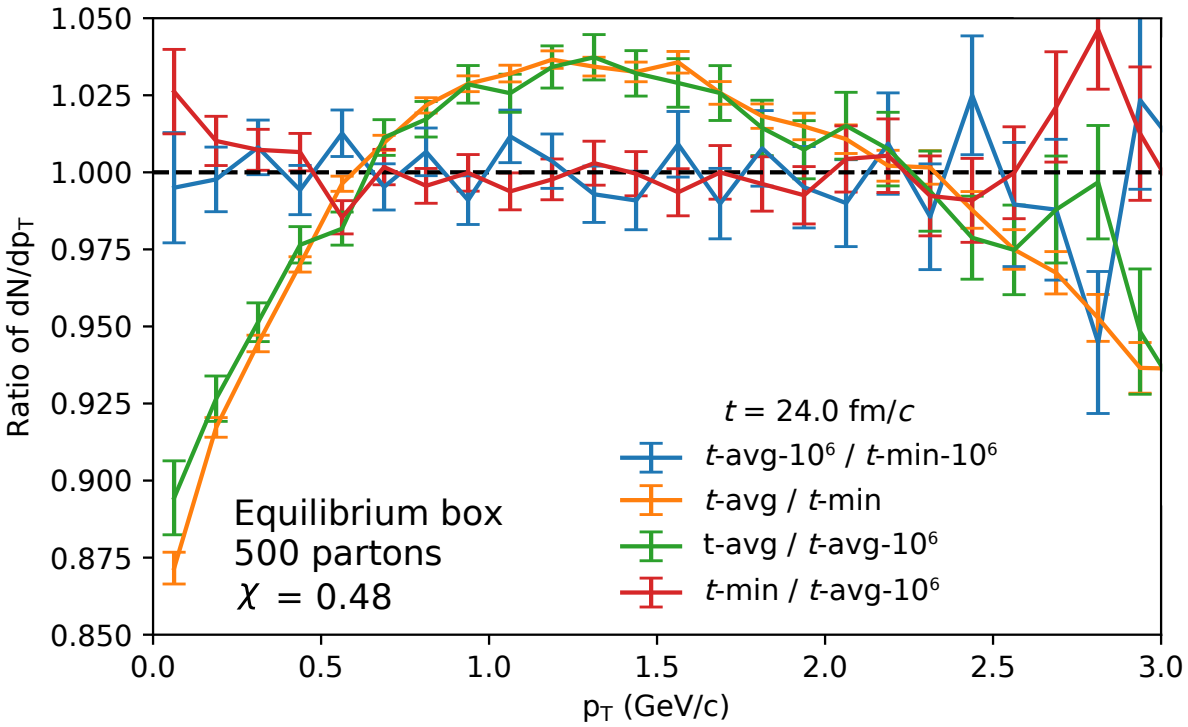

Figure 5.2: The ratios of dN/dp_{T} at $t = 24$ fm/c for the box initial condition with 500 partons per event at $T = 0.5$ GeV and an opacity of $\chi = 0.48$ for the t-average and t-minimum collision schemes. Note that "-10^6" represents the subdivision results at $l_{\mathrm{sub}} = 10^6$.

dN/dp_{T} ratio then decreases with p_{T} and falls below one around $p_{\mathrm{T}} \approx 2.2$ GeV/c. This behavior is clearly quite different from the corresponding result of Fig. 5.1, which shows the failure of the t-minimum collision scheme to reduce the causality violation problem for the 3D expansion initial condition. The ratios of the results for both collision schemes without subdivision to the subdivision results are also shown in Fig. 5.2, and it is clear that the t-minimum scheme produces a final transverse momentum spectrum that is quite close to the subdivision answer. This is further evidence to support the fact that the t-minimum scheme is useful for getting much closer to the exact answer for box simulations in ZPC [69].

Since there is not an immediately obvious reason why the t-minimum collision scheme should fail to reduce the causality violation for ZPC simulations using the 3D expansion initial condition, one may ask if there is a previously unknown problem with the subroutines

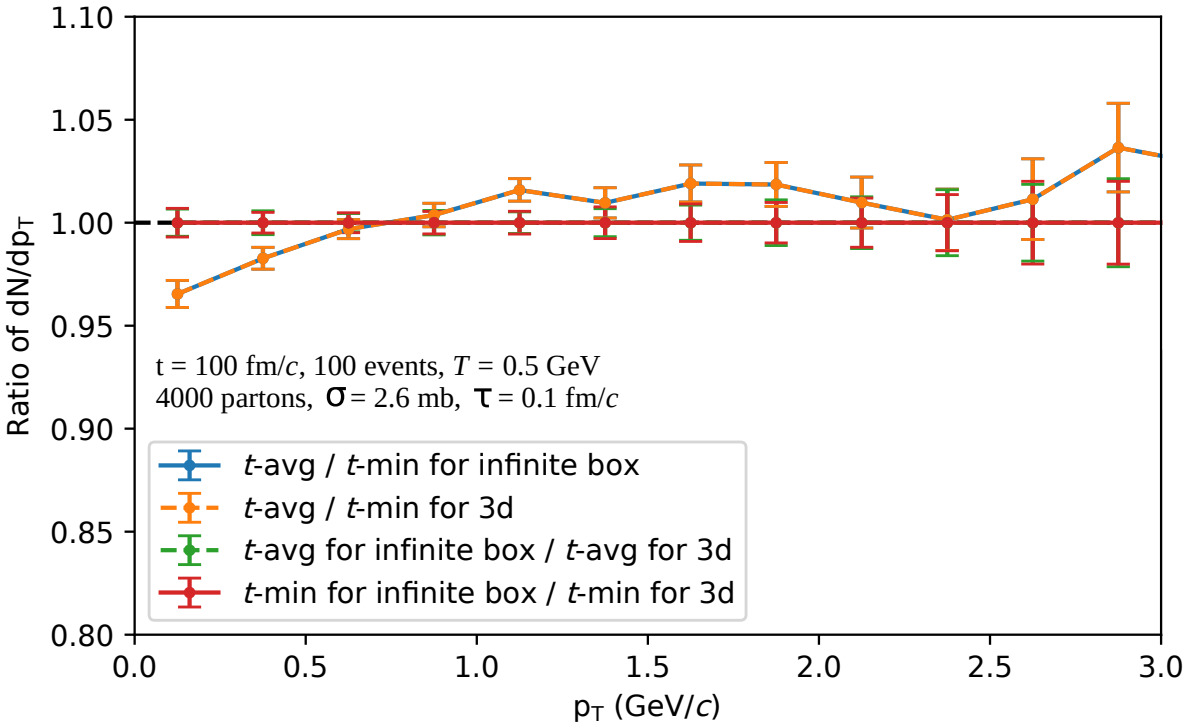

Figure 5.3: The ratios of dN/dp_{T} at $t = 100$ fm/c for the 3D expansion initial condition with or without an effectively infinite box for 4000 partons at $T = 0.5$ GeV and an initial opacity at mid-pseudorapidity of $\chi(\eta \approx 0) = 0.48$ for the t-average and t-minimum collision schemes.

which are used for the 3D expansion simulations. One easy way to test this question is to use the 3D expansion initial condition inside an effectively "infinite" box and compare the results to the normal 3D expansion results. For the purposes of this test, the side length of the box is set to $10 * 10^8 = 10^9$ fm, and the normal 3D expansion simulations are allowed to run until $t = 10^6$ fm/c. These choices ensure that no parton will encounter the edge of the box before the ending time since the 3D expansion initial condition has a maximum transverse radius of $r_{\mathrm{T}} = 5$ fm/c and a maximum z-position of $z \approx 7.4$ fm/c when a parton formation time of $\tau_0 = 0.1$ fm/c is chosen. The result of this test is depicted in Fig. 5.3 which shows the ratios of dN/dp_{T} for the two cases just mentioned for both the t-average and t-minimum collision schemes. The ratio of dN/dp_{T} for either collision scheme from the 3D expansion

initial condition inside the infinite box to the one without the infinite box is equal to one over a wide range of p_{T}. Also, the ratios of dN/dp_{T} between the two collision schemes from either the 3D expansion initial condition inside an infinite box or without an infinite box are the same. These two facts indicate that there is not a problem with the subroutines in ZPC which are used for simulations with 3D expansion, since if such problems did exist, one would expect to observe the ratios of the p_{T} spectra in Fig. 5.3 not being equal to one. Note that these results with 4000 partons are inconsistent with the orange curve in Fig 5.1 for 500 partons and need further investigation.

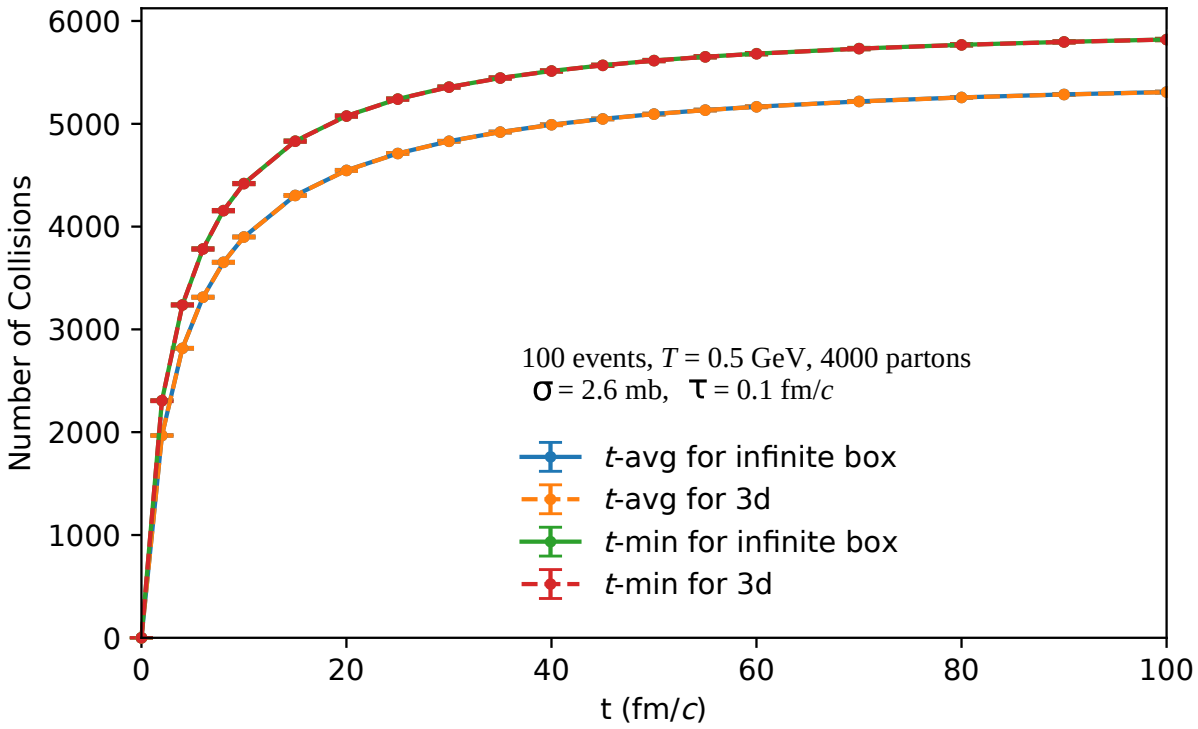

Figure 5.4: The collision number per event for the 3D expansion initial condition with or without an effectively infinite box for 4000 partons at $T = 0.5$ GeV and an initial opacity at mid-pseudorapidity of $\chi(\eta \approx 0) = 0.48$ for the t-average and t-minimum collision schemes versus time t.

Figure 5.4 shows the time-evolution of the collision number per event for the 3D expansion initial condition with or without the infinite box for 4000 partons at $T = 0.5$ GeV and an

initial opacity at mid-pseudorapidity rapidity of $\chi(\eta \approx 0) = 0.48$ for the t-average and t-minimum collision schemes. The collision number per event increases very quickly from $t = 0$ fm/c in all cases, but the rate of increase slows gradually until it becomes almost flat around $t = 100$ fm/c. The results for the t-average collision scheme [64] increase less quickly than for the t-minimum collision scheme since the collision time is taken as the average of the two parton collision times $t_{c,1}$ and $t_{c,2}$ instead of as the minimum [69]. Clearly the minimum of two positive values is smaller than the average of two, and this means that the t-minimum scheme will result in more collisions occurring earlier in time than the t-average scheme. There is no difference between the collision number per event for either the t-average or the t-minimum collision schemes for the 3D expansion initial condition with or without an infinite box. This further supports the idea that a problem with the 3D expansion subroutines in ZPC does not exist because otherwise one would expect the results inside the infinite box to differ from the normal 3D expansion results. Since no difference is observed, in fact the two sets of results are almost identical, we conclude that some aspect of the 3D expansion initial condition itself must contribute to the 3D problem. These results lack information for times at and just after the parton formation time τ_0, which motivates the investigation of the early collisions in ZPC simulations using the 3D expansion initial condition.

In Fig. 5.5, the collision rate divided by the value of the subdivision factor for ZPC simulations using the default 3D expansion initial condition for 500 partons at $T = 0.5$ GeV and an initial opacity at mid-pseudorapidity $\chi(\eta \approx 0) = 0.02$ is shown as a function of time for the t-average and t-minimum collision schemes. The parton formation time is $\tau_0 = 0.1$ fm/c, so the collision rate must be zero before this time, since no partons will have been formed. The collision rate apparently increases quite quickly for times just after the parton formation time, and reaches a peak value around $t \approx 0.15$ fm/c for all cases in Fig. 5.5. Note that the initial zero collision rate at $t = 0$ fm/c is plotted at $t = 0.01$ fm/c. After reaching its peak value, the collision rate decreases smoothly with time and eventually reaches zero after about ≈ 80 fm/c for all cases. It is also clear that the simulations which use the t-average

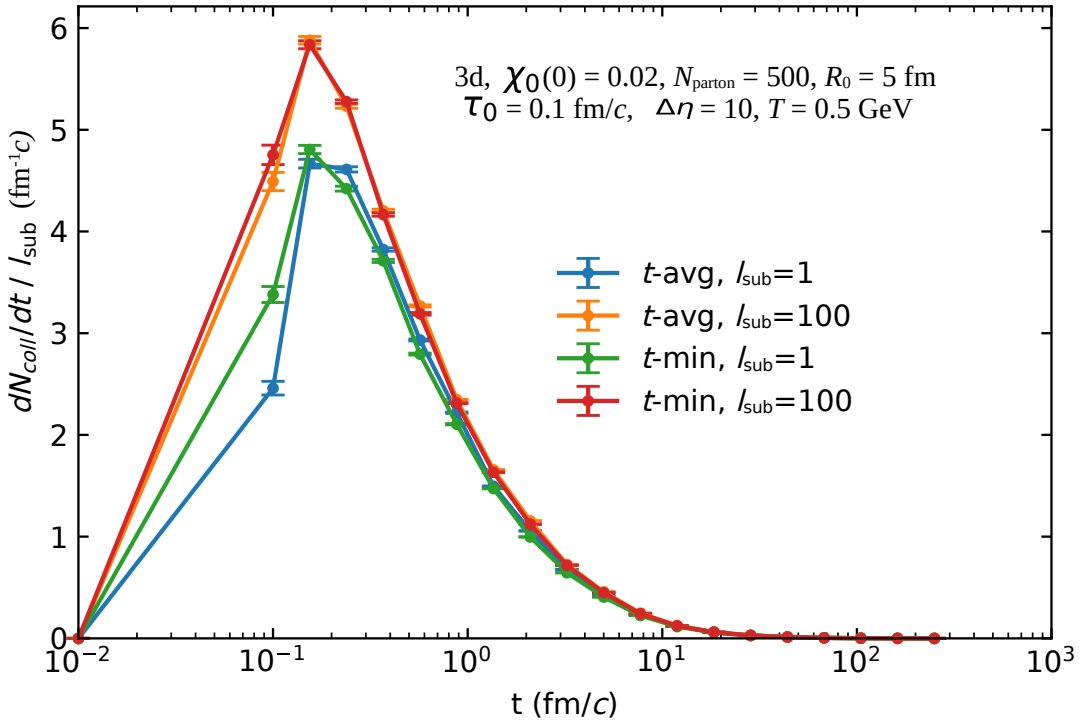

Figure 5.5: The collision rate divided by the subdivision factor $dN_{\text{coll}}/dt/l_{\text{sub}}$ without and with subdivision ($l_{\text{sub}} = 100$) using the default 3D expansion initial condition for 500 partons at $T = 0.5$ GeV and $\chi(\eta \approx 0) = 0.02$ for the t-average and t-minimum collision schemes versus time t.

scheme have a lower collision rate just after the parton formation time than the t-minimum results. This agrees with the expectation that the t-minimum scheme should yield more collisions earlier in time. The initial opacity was chosen to be rather small (already near the dilute limit of $\chi \ll 1$) to ensure that the results without subdivision are expected to be almost exactly correct. Figure 5.5 shows that after using the subdivision method with $l_{\text{sub}} = 100$, the collision rate at $t = 0.1$ fm/c is nearly double that of the same results without subdivision (labelled as $l_{\text{sub}} = 1$). Since one would expect an almost exact agreement between the non-subdivision and subdivision results (regardless of the collision scheme) at this small opacity, these results indicate that there is likely a problem with the implementation of the parton subdivision method for 3D expansion cases in ZPC. To test this hypothesis, a new initial condition for ZPC simulations with 3D expansion that uniformly distributes the same

number of partons inside a sphere is used.

5.1.2 A Spherical Initial Condition

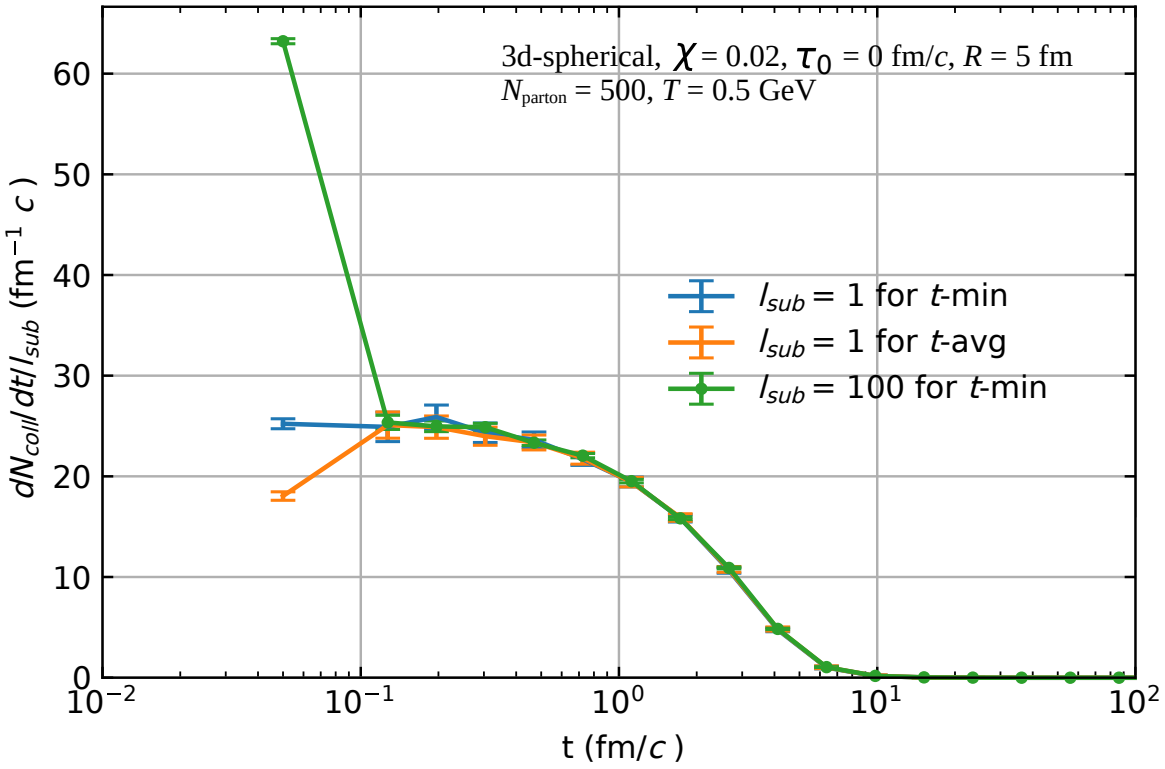

Figure 5.6: The collision rate divided by the subdivision factor $dN_{\mathrm{coll}}/dt/l_{\mathrm{sub}}$ without and with subdivision ($l_{\mathrm{sub}} = 100$) using the spherical 3D expansion initial condition for 500 partons at $T = 0.5$ GeV and $\chi = 0.02$ for the t-average and t-minimum collision schemes versus time t.

The initial radius of the new spherical initial condition for 3D expansion simulations is chosen to be the same as the initial transverse radius of the default initial condition: namely $R = 5$ fm. Inside the sphere, the partons are distributed uniformly in space and the initial formation time is set to $\tau_0 = 0$ fm/c for the spherical initial condition. Figure 5.6 shows the same results as the previous figure, except using the spherical initial condition. Again, the collision rate for the t-average scheme is smaller than that of the t-minimum scheme for the simulations without subdivision at the earliest time. The results that use $l_{\mathrm{sub}} = 100$

are much larger than those without subdivision by a factor of ≈ 2.5 for the t-minimum scheme. For times later than $t \gtrsim 0.15$ fm/c, all cases have the same value of $dN_{\rm coll}/dt/l_{\rm sub}$ within the statistical uncertainties. When taken together, Figs. 5.5 - 5.6 indicate that the subdivision method for simulations with 3D expansion may have some problem. Because both the default and the spherical initial conditions produce higher collision rates at very early times for simulations with subdivision, it would be useful to further investigate this unexpected behavior.

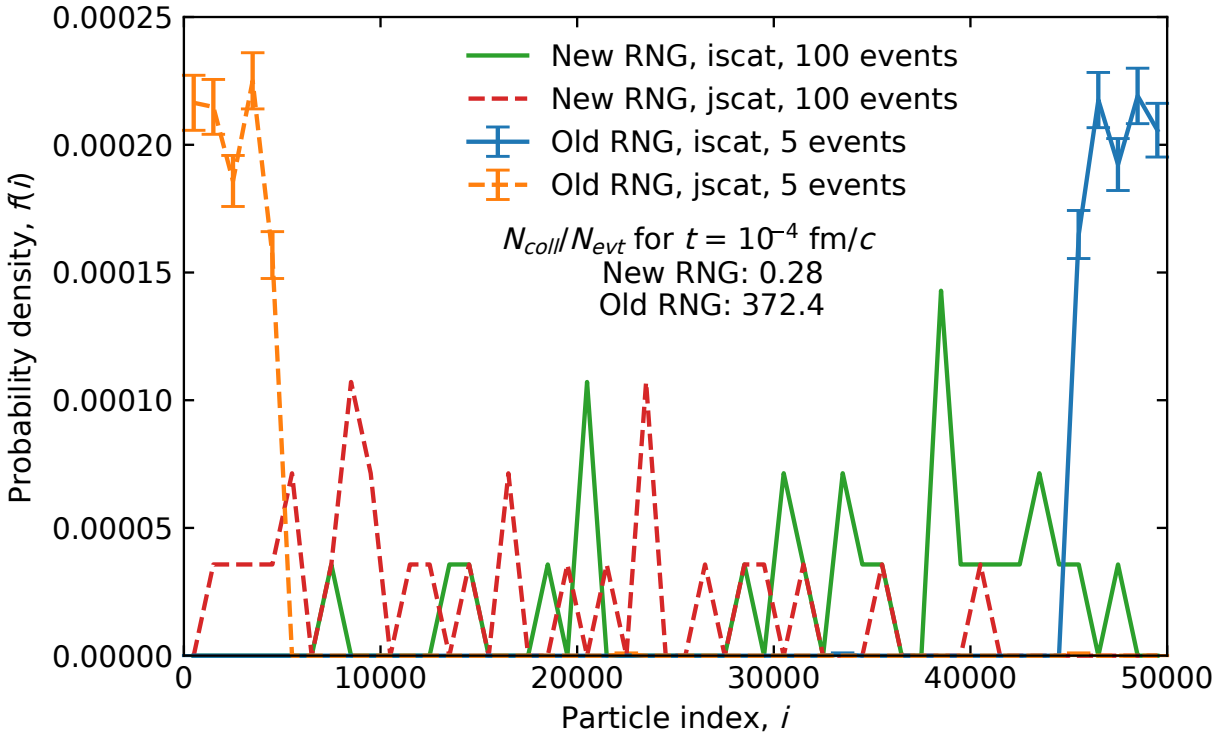

Figure 5.7: The probability density of indices for colliding partons before $t = 10^{-4}$ fm/c using the default random number generator and a newer built-in one for the spherical initial condition with 500 partons at $T = 0.5$ GeV and $l_{\rm sub} = 100$.

Using the spherical initial condition with 500 partons and a temperature of $T = 0.5$ GeV for a subdivision factor of $l_{\rm sub} = 100$, all the particle record of one event was recorded for those partons that collide before $t = 10^{-4}$ fm/c. Such early collisions should be statistically unlikely if the partons are distributed uniformly throughout the physical space. A strange correlation between the indices of the partons that collide unexpectedly early is depicted in

Fig. 5.7 for the simulations using the old random number generator that is provided in ZPC by default [64]. The probability density of parton indices for collisions that occur earlier than $t = 10^{-4}$ fm/c shows that virtually all of these partons have an index of iscat $\gtrsim 44000$ or jscat $\lesssim 6000$ where iscat and jscat are the parton indices. This result is strange since one would expect a uniform distribution of parton indices involved in collisions, assuming the spatial distribution of partons is actually uniform. In order for a collision to occur so early in time, the positions of the colliding partons must be quite close (already smaller than the interaction length $\sqrt{\sigma/\pi}$). Since the initial position of partons is determined by randomly sampling some distribution (which is assumed to be uniform), the result of Fig. 5.7 indicate that the random numbers that correspond to the initial positions should be nearly the same for partons which differ in index by approximately 45000. These random numbers were recorded for all such partons involved in early collisions, and it was observed that the partons' spatial positions are calculated using random numbers which are always 259200 places apart in the generated sequence of random numbers. This fact indicates that the original random number generator of ZPC suffers from a pseudo period; in fact the value of 259200 is exactly one of the parameters used by the linear congruential random number generator [83, 113].

The discovery of this problem motivates the use of a newer random number generator for ZPC that does not suffer from the same pseudo period problem. Fortunately, such modern random number generators are quite common and easy to implement. Figure 5.7 shows that the correlation between the indices of colliding partons for collisions earlier than $t = 10^{-4}$ fm/c disappears when using the newer random number generator. In fact, the event averaged collision number for these early collisions was reduced by a factor of more than 1300. Therefore, the new random number generator essentially removes the occurrence of unexpectedly early collisions.

After implementing the new random number generator in ZPC, the collision number per event at very early times is reduced dramatically as shown by Fig. 5.8. When using the old

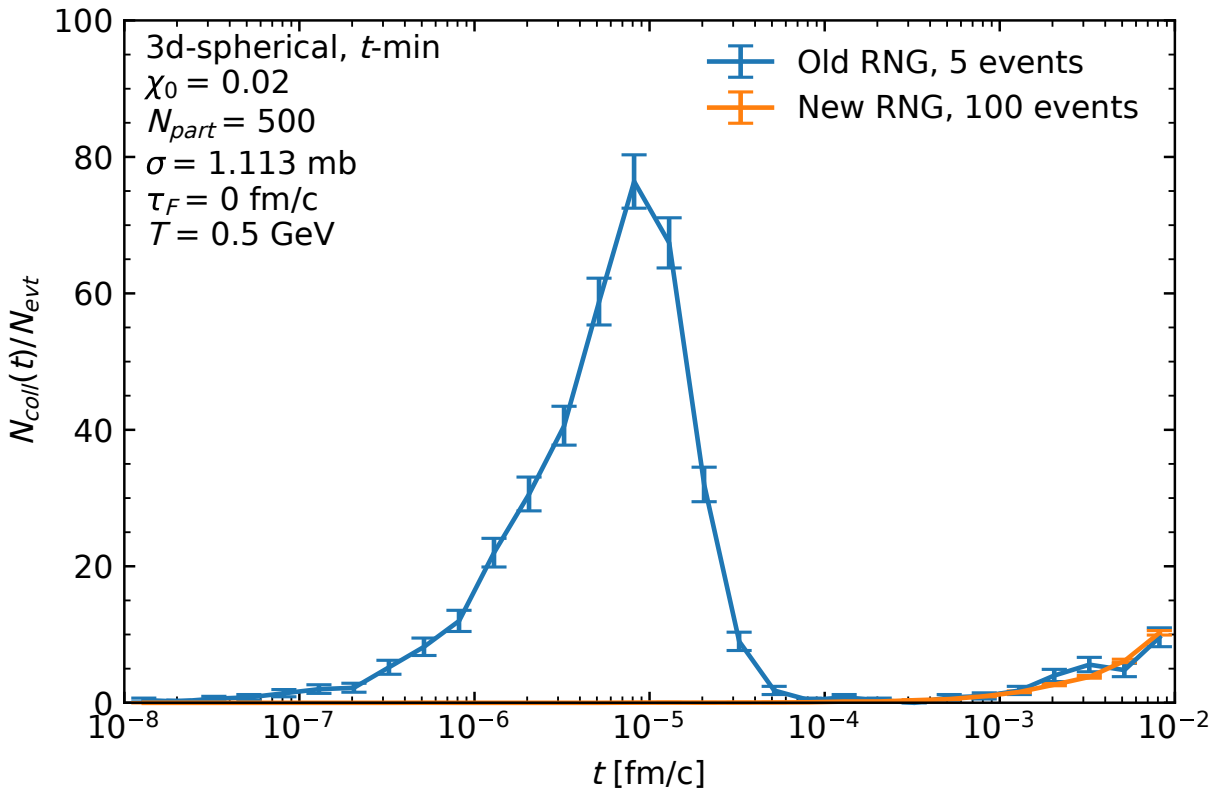

Figure 5.8: The collision number per event for the spherical initial condition of ZPC simulations with 3D expansion for 500 partons at $T = 0.5$ GeV and an initial opacity of $\chi = 0.02$ using the old and a modern random number generator for the t-minimum collision scheme versus time t.

random number generator, a peak in the collision number per event occurs near $t = 10^{-5}$ fm/c, but does not exist for the results using the new random number generator. These results are for the spherical initial condition using subdivision, but must also occur for the default initial condition with subdivision because the problem originates when generating many pseudo random numbers and is independent of the initial condition. Note that after a time of about $t \approx 10^{-3}$ fm/c, the event average collision number begins to rise for the simulations regardless of which random number generator is used. These collisions are interpreted as "correct" in the sense that they are the earliest collisions that take place not as a result of problems in the random number generator.

After implementing the new random number generator that does not suffer from the

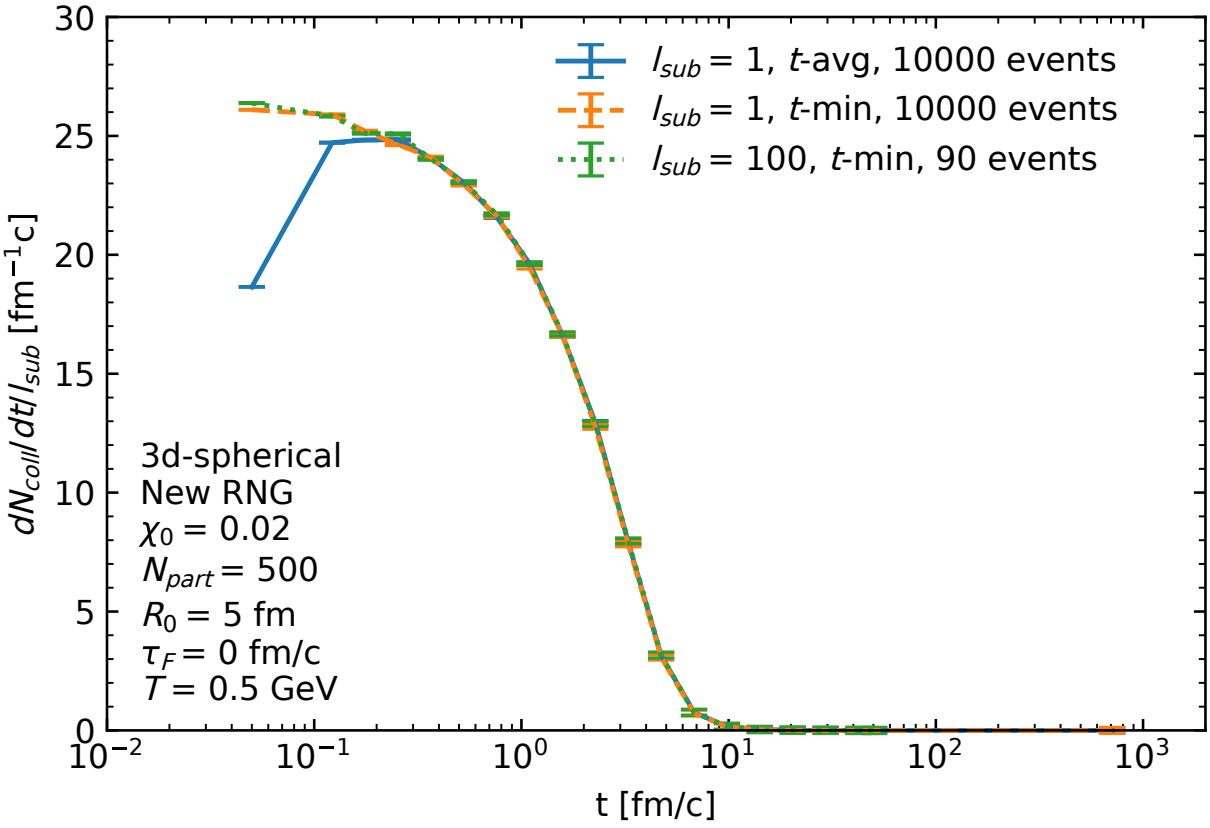

Figure 5.9: The collision rate divided by the subdivision factor $dN_{\text{coll}}/dt/l_{\text{sub}}$ using the new random number generator for the spherical 3D expansion initial condition for 500 partons at $T = 0.5$ GeV and $\chi = 0.02$ without subdivision for the t-average and t-minimum and with subdivision for the t-minimum scheme time t.

pseudo period, the collision rate divided by l_{sub} for the simulations using parton subdivision with $l_{\text{sub}} = 100$ do not exhibit the uncharacteristically large values. Figure 5.9 shows that the t-minimum collision scheme now agrees quite well with the subdivision results at the early times. Again, the earliest collisions happen at a slower rate for the t-average collision scheme because the collision time for that scheme is larger on average than for the t-minimum scheme. Notably, the collision rate at late times for all schemes agree with each other and reach zero around $t = 10$ fm/c.

Figure 5.10 shows the results of using the new random number generator on the time evolution of the collision rate scaled by the subdivision factor for the t-average and t-minimum collision schemes without subdivision and with subdivision for the t-minimum scheme for

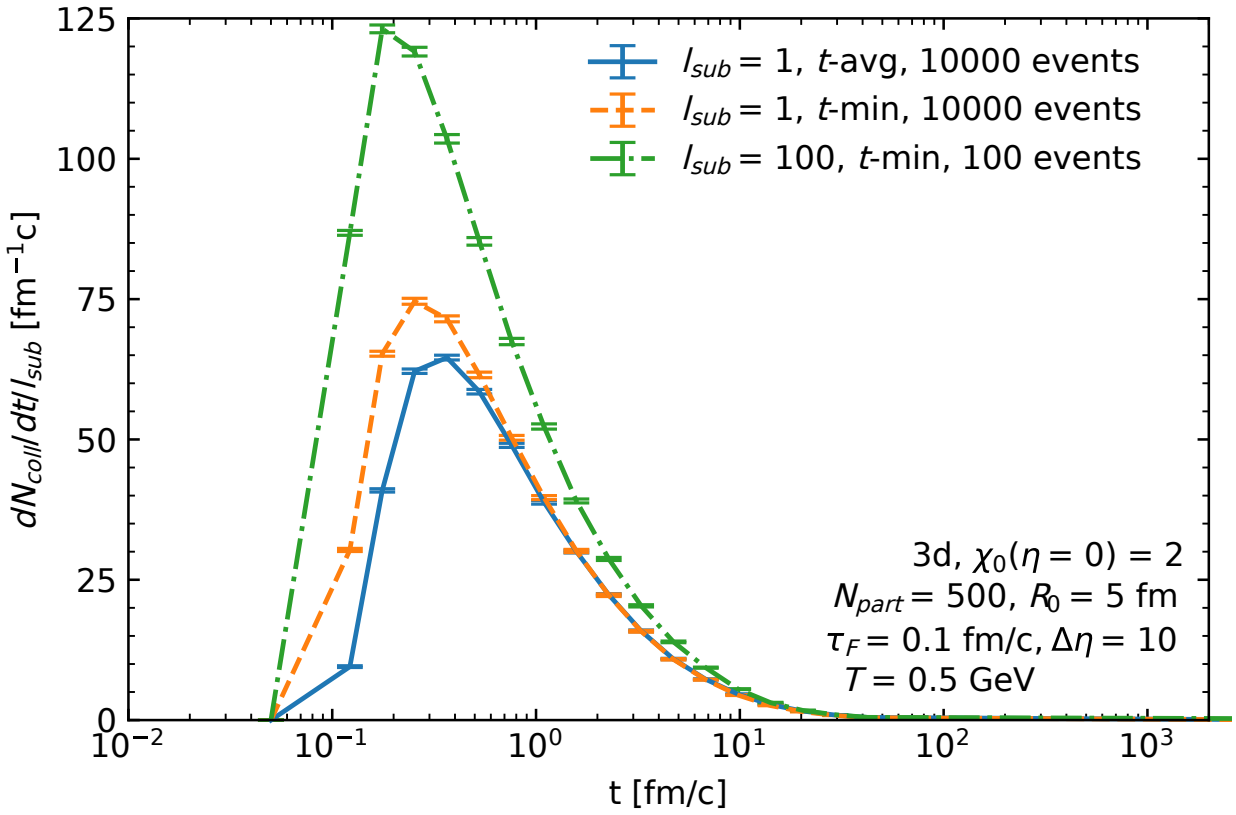

Figure 5.10: The collision rate divided by the subdivision factor $dN_{\rm coll}/dt/l_{\rm sub}$ using the new random number generator for the default 3D expansion initial condition for 500 partons at $T = 0.5$ GeV with an initial opacity at mid-pseudorapidity of $\chi(\eta = 0) = 2$ without subdivision for the t-average and t-minimum schemes and with subdivision for the t-minimum scheme time t.

the default initial condition. The default initial condition has been selected to have the same opacity at mid-pseudorapidity as the results shown in Fig. 5.9 so that the simulations can be as similar as possible. Note that the opacity decreases as pseudorapidity increases, so the collisions that occur in those regions should be even more free of causality violation than the region at $\eta \approx 0$. While using the new random number generator improves the early collision rate problem for the spherical initial condition, it fails to do so for the default initial condition because the rate with subdivision is still too high according to Fig. 5.9. These results use the moderately high initial opacity at mid-pseudorapidity $\chi(\eta = 0) = 2$, so they likely also suffer from the causality violation. Therefore, a better test will be to use the new

RNG for low opacity calculations in the default initial condition for 3D expansion to extract the early collision rates. After that, the ratio of the p_{T} spectrum to the subdivision result should also be checked and compared to the calculations using the old RNG. Unfortunately, this means that the 3D problem is still unsolved for the default initial condition.

5.2 Comparing $f(s)$ in ZPC to Analytical Distributions

In Sec. B.3.1, the probability density function for any pair of massless particles whose energies follow a thermal distribution is derived by considering the thermal average of the cross section $\langle\sigma\rangle$. That result also relies on the cross section for two such particles depending only on the Mandelstam $\hat{s}$ of those particles ($\sigma(\hat{s})$), and was given in Ref. [84]. To improve the readability, $\hat{s}$ is written as s, i.e., the "hat" symbol is suppressed throughout this section. For clarity, the final result of the derivation in the Appendix is written here

$$f(s) = \frac{1}{64T^2}\left[\left(\frac{\sqrt{s}}{T}\right)^3 K_1\left(\frac{\sqrt{s}}{T}\right) + 2\left(\frac{\sqrt{s}}{T}\right)^2 K_2\left(\frac{\sqrt{s}}{T}\right)\right], \tag{5.2}$$

The special functions $K_i(x)$ in Eq. (5.2) above are modified Bessel functions of the second kind. While the derivation of the above result is a useful exercise, a more important task is comparing Eq. (5.2) to the numerical $f(s)$ for parton pairs in ZPC. The comparison is made using a system of 4000 massless gluons in a box whose energies follow a Maxwell-Boltzmann distribution for two different temperatures. The opacity of the system is chosen to be $\chi = 1$, and a subdivision factor of $l_{\mathrm{sub}} = 10^4$ is used to ensure that the final results do not suffer from causality violation. Recall that the subdivision factor decreases the system's effective opacity by $\chi \to \chi/\sqrt{l_{\mathrm{sub}}}$. For this test, the effective opacity $\chi = 0.01 \ll 1$ is quite near the dilute limit.

Figure 5.11(a) shows the comparison of the numerical $f(s)$ for the setup described above to the analytical result of Eq. (5.2) for $T = 0.2$ and 0.5 GeV. Note that the theory results are the bin-averaged values for the same discrete s-bins in the ZPC results. The ratio of

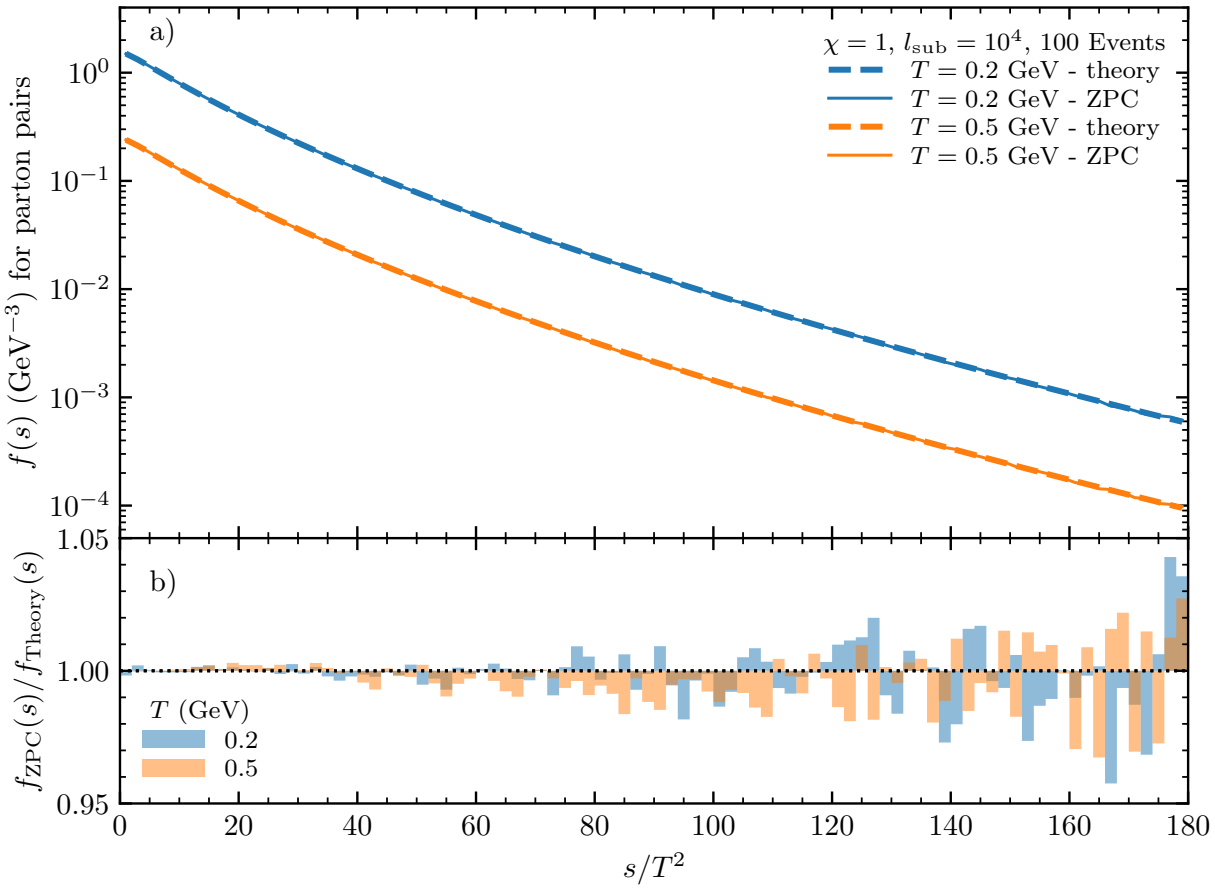

Figure 5.11: (a) The probability density function $f(s)$ for all parton pairs in ZPC for 4000 partons in a box with an opacity of $\chi = 1$ and a subdivision factor of $l_{\rm sub} = 10^4$ compared to $f(s)$ from the calculation of $\langle\sigma\rangle$ for massless particles with Maxwell-Boltzmann statistics, and (b) the ratio $f_{\rm ZPC}(s)/f_{\rm theory}(s)$ for two temperatures versus s/T^2.

the two bin-averaged results is plotted in Fig. 5.11(b), and the numerical results differ by less than 5% from the analytical result in any s bin. In fact, the deviation between the two results is far less than 1% for s bins near the average of $\langle s\rangle = 18T^2$ for both temperatures. The larger deviations of the numerical result relative to the analytical one at large s are a limitation of the finite statistics in the ZPC result. This agreement indicates that the ZPC parton cascade correctly reproduces the expected analytical result of the probability density function of s.

Table 5.1 shows the results of comparing $\langle s\rangle$ and $\langle\sqrt{s}\rangle/T$ for the parton pairs, which have the distributions plotted in Fig. 5.11. The deviations in these measures are small since

T (GeV)	N_{pairs}	$\langle s \rangle / T^2$	Dev. (%)	$\langle \sqrt{s} \rangle / T$	Dev. (%)
0.2	21907025	17.997	0.015	3.681	0.006
0.5	21900993	17.977	0.125	3.680	0.042

Table 5.1: Comparison of the numerical $\langle s \rangle$ and $\langle \sqrt{s} \rangle$ for pairs of massless gluons in a box whose energies follow a Maxwell-Boltzmann statistics with an opacity of $\chi = 1$ and a subdivision factor of $l_{\text{sub}} = 10^4$ at two temperatures to the corresponding analytical results for $f(s)$ from Eq. (5.2).

the ratio of the numerical result to the analytical one in panel (b) of that figure fluctuates around unity. For both temperatures, the s values for nearly 2.2×10^7 parton pairs were recorded, and the deviations expressed as a percentage from the analytical mean values is presented. The mean s for both temperatures is quite close to the analytical result of $18T^2$, and the percent deviations are far below 1% in both cases. Note that the analytical result of $\langle \sqrt{s} \rangle = 75\pi T/64 \approx 3.682T$, and the percent deviations of the numerical result to this value are even smaller than 0.1% in both cases. The results of Fig. 5.11 and Table 5.1 indicate that the $f(s)$ distribution that is found by calculating the thermal average of the cross section $\langle \sigma(s) \rangle$ represents the probability density of s for parton pairs. On the other hand, it would also be useful to know the distribution of s for pairs of partons which actually collide in ZPC.

Another probability density function for the Mandelstam s is derived using the thermal average of the cross section multiplied by the relative velocity between two partons $\langle \sigma v_{rel} \rangle$ as in Ref. [114, 115]. Here, the relative velocity is defined as

$$v_{rel} = \sqrt{s\,(s - 4m^2)}/(2E_a E_b), \tag{5.3}$$

where m is the particle mass, and E_i are the particle energies. For the massless partons under consideration here, this reduces to $v_{rel} = s/(2p_a p_b)$ where p_i are the magnitude of the particle three-momenta. This definition of v_{rel} is the same as in Ref. [114, 116], but the authors of Ref. [115] use twice this value instead. Again, for clarity, the final result in

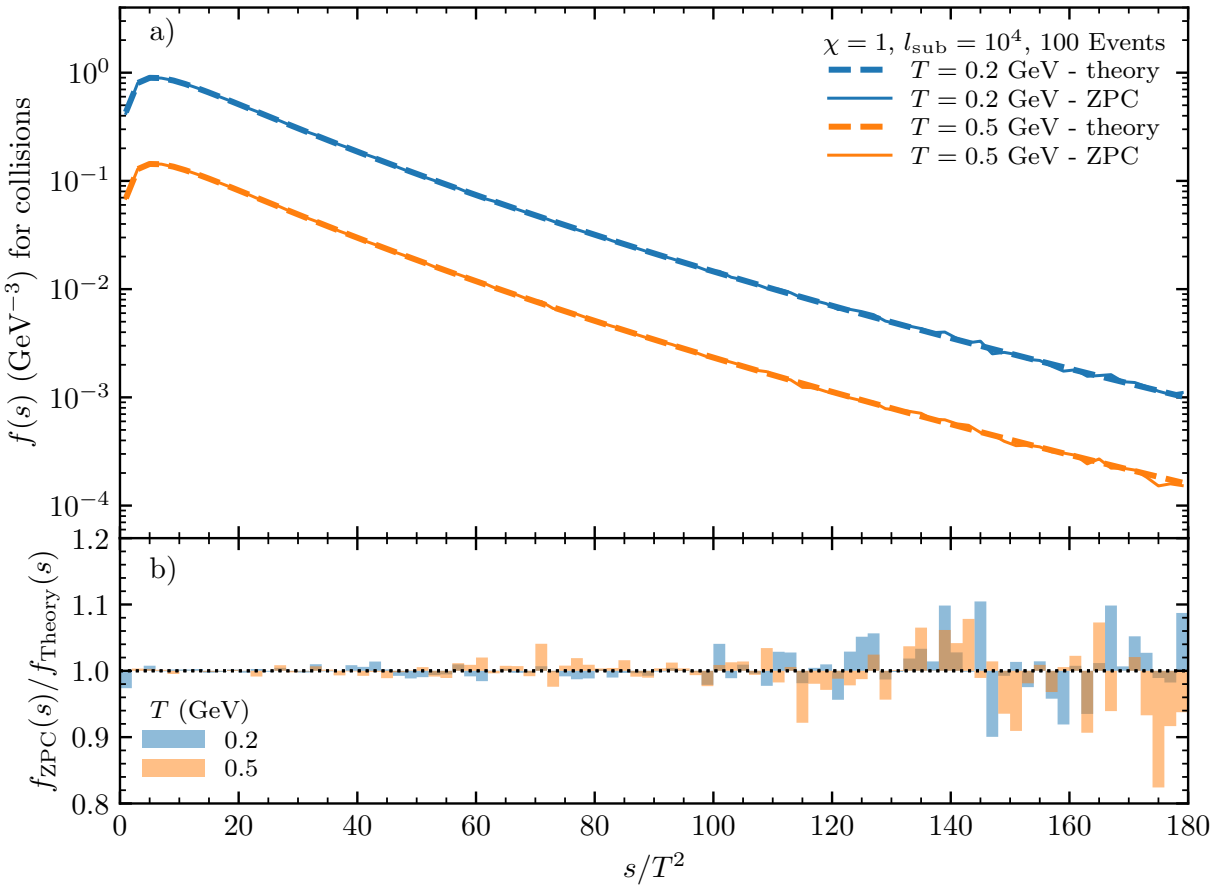

Figure 5.12: (a) The probability density function $f(s)$ for colliding partons in ZPC for 4000 partons in a box with an opacity of $\chi = 1$ and a subdivision factor of $l_{\rm sub} = 10^4$ compared to $f(s)$ from the calculation of $\langle \sigma v_{rel} \rangle$ for massless particles with Maxwell-Boltzmann statistics, and (b) the ratio $f_{\rm ZPC}(s)/f_{\rm theory}(s)$ for two temperatures versus s/T^2.

Eq. (B.32) from the derivation in the Appendix is written here

$$f_{\rm coll}(s) = \frac{1}{32T^2}\left(\frac{\sqrt{s}}{T}\right)^3 K_1\left(\frac{\sqrt{s}}{T}\right) \tag{5.4}$$

Figure 5.11(a) shows the comparison of the numerical $f(s)$ for colliding partons in ZPC to the analytical result of Eq. (5.4) for $T = 0.2$ and 0.5 GeV. Again, the comparison has been made to the bin-averaged analytical results to have a fair comparison to the discrete s-bins in the ZPC results. The ratio of the two bin-averaged results is plotted in Fig. 5.12(b), and the numerical results differ by less than 20% from the analytical result in any s bin. In

T (GeV)	$N_{\rm col}$	$\langle s \rangle / T^2$	%-Error	$\langle \sqrt{s} \rangle / T$	%-Error
0.2	1996602	24.015	0.061	4.420	0.058
0.5	2001404	24.001	0.003	4.418	0.005

Table 5.2: Comparison of the numerical $\langle s \rangle$ and $\langle \sqrt{s} \rangle$ for colliding massless gluons in a box whose energies follow a Maxwell-Boltzmann statistics with an opacity of $\chi = 1$ and a subdivision factor of $l_{\rm sub} = 10^4$ at two temperatures to the corresponding analytical results for $f_{\rm coll}(s)$ from Eq. (5.4).

fact, the deviation between the two results is less than about 2% for s bins near the average of $\langle s \rangle = 24T^2$ for both temperatures. The deviations between the numerical result and the analytical one at large s are still mostly less than 10% for all s bins, while the total number of collisions is about a factor of ten smaller than the recorded number of parton pairs for the same events. Again, an excellent agreement between the two independent results indicates that ZPC correctly reproduces the analytical result of the probability density function of s as derived from $\langle \sigma v_{rel} \rangle$.

Table 5.2 shows the results of comparing $\langle s \rangle$ and $\langle \sqrt{s} \rangle / T$ for the colliding partons which have the distributions plotted in Fig. 5.12. For both temperatures, the s of nearly 2.0×10^6 collisions was recorded, and the deviations expressed as a percentage from the analytical mean values is presented. The mean s for both temperatures is quite close to the analytical result of $24T^2$, and the percent deviations are far below 0.1% in both cases. Note that the analytical result of $\langle \sqrt{s} \rangle = 45\pi T/32 \approx 4.418T$, and the percent deviations of the numerical result to this value are even smaller than 0.06% in both cases. The results of Fig. 5.12 and Table 5.2 indicate that the $f(s)$ distribution that is found by calculating the thermal average of the cross section $\langle \sigma v_{rel} \rangle$ represents the probability density of s for colliding partons. However, a direct proof of this relationship has not yet been obtained.

5.3 Curved Parton Motion

The method of the ZPC parton cascade is different from that of a typical simulation of many particles in which all the particles' positions are updated at each time step [64]. Instead,

in ZPC, the simulation moves forward in time from collision to collision, and the particles are assumed to travel along their individual free-streaming trajectories between successive collisions. All future collisions are predicted by searching for intersections between these straight-line paths, and an interaction list is constantly updated as collisions occur. The default method of ZPC uses this algorithm of the parton cascade; however, allowing partons to follow curved trajectories would enable one to study the effect of external fields on a parton system [117, 118]. These include the electromagnetic effects that are important during the early stages of heavy ion collisions and are related to the chiral magnetic effect [119, 112, 22]. With this in mind, we have modified ZPC to allow partons to follow curved motion under the influence of external fields. This modification is first described below and then a comparison of the typical program structure and the modified one is made. Initial tests have demonstrated that the modified ZPC program gives the same final results such as the collision number and p_{T} spectrum, which indicates that the new method should correctly model curved parton motion.

Including curved parton motion in ZPC is no small task since the program has been built to simulate free streaming particles only [64]. However, we devised a method to implement curved motion, which uses many of the same tools that are already present in the current ZPC code. First, a new parameter in the initialization file called *icurve* has been introduced, and the new subroutine called *recalc_intlist* may be utilized by setting $icurve = 1$. Because ZPC progresses through the simulation from collision to collision instead of at regular time steps, there is an added difficulty in implementing curved parton motion. The main idea behind this implementation of curved parton motion is to let the program progress until a time when the partons' trajectories should curve enough under the influence of the selected external fields. Thus, an array of time steps called *tstep* is introduced which contains the times at which to apply the external fields to change some or all of the parton's spacetime four-vectors and four-momenta. Currently, there are 100 elements in the *tstep* array, and the user is free to choose whether *tstep* should be linearly spaced or logarithmically spaced in

time from a starting time *tstart* and a stop time *tstop*. The stop time of the external fields effect is currently chosen as $t_{\rm end}/2$, where $t_{\rm end}$ is the ending time of the individual simulation and depends on the scaled time τ of Eq. (4.9). Of course, one is free to choose the last time in *tstep* to be equal to the program ending time, in which case the partons will always be affected by the external fields.

Before describing the new *recalc_intlist* subroutine further, the main steps of the ZPC program that are located in the *zpc_run* subroutine are described first. Note that the term "particle record" refers to the following information for each parton: the type, the space-time four vector x^μ, the four momentum p^μ, the mass m, the pseudorapidity η, the rapidity y, and the proper time τ. The space-time four vector x^μ contains the last interaction time and the position at that time for each parton. Also, an "operation" refers to either a parton formation or a collision, either between partons or between a parton and a wall.

---

1. The particle records of the partons from the previous collision are saved, this enables fixed time analysis.

2. The type, time, and particle indices of the next operation are determined by the time of the earliest interaction in the interaction list.

3. The freezeout condition is checked; if it is met the event terminates.

4. The global time t is updated, and the next operation is performed as follows.

   (a) For a parton formation: the parton to be formed is assigned to a cell based on its position.

   (b) For a collision with a wall: the involved parton's current cell is updated, and the lists of partons in each cell are updated.

   (c) For a two-parton collision: both partons' positions are updated, and the and new parton four-momenta are determined.

5. The interaction list is updated for the particles involved in the current operation.

In the outline that follows, t_{op} refers to the time of the next operation to be performed and t_{istep} refers to the next time when the external fields will be applied. Note that the steps outlined below are inserted between steps 2. and 3. in the normal ZPC code as outlined above.

---

1. If $t_{op} < t_{istep}$: the external fields are not applied, and the program continues normally.
2. If $t_{op} \geq t_{istep}$: the external fields are applied, and the program diverts its normal procedure as follows.
   (a) Set $t = t_{istep}$.
   (b) Reset the entire interaction list.
   (c) Apply the external fields to each formed parton and propagate each parton forward in time from its last interaction time to t.
   (d) Reassign each formed parton to a cell.
   (e) Recalculate a new interaction list using the updated particle records.
3. Return to step 2. in the normal procedure.

The entire interaction list is reset and recalculated at each time t_{istep} in the *tstep* array. Therefore, before one can test whether the *recalc_intlist* subroutine is implemented correctly, it is first necessary to study the effect of the new subroutine on the collision history without letting the partons experience curved motion. This is accomplished by setting the behavior of the external fields to propagate each formed parton forward in time to t_{istep} along its free-streaming trajectory. In this way, the distribution of energy and momenta is unchanged and the interaction list will be exactly the same. Recall that the external fields are applied only when the next collision in the normal ZPC procedure would occur after t_{istep}; thus, no collisions will be skipped.

icurve	T (GeV)	χ	$l_{\rm sub}$	$\langle N_{\rm coll}\rangle$	$\sigma_{N_{\rm coll}}/\sqrt{N_{\rm event}}$
0	0.5	1	1	41174.78	22.11
1	0.5	1	1	41135.67	22.25
0	0.5	1	10^4	40042.54	21.13
1	0.5	1	10^4	39974.95	17.85
0	0.7	40	1	126927.65	38.33
1	0.7	40	1	126960.27	36.33

Table 5.3: Event averaged collision number and standard errors for 100 events of ZPC simulations using the t-minimum collision scheme without ($icurve = 0$) and with ($icurve = 1$) the *recalc_intlist* subroutine for 4000 partons at $T = 0.5$ GeV with $\chi = 1$ and $l_{\rm sub} = 1$ or 10^4 and for 13000 partons at $T = 0.7$ GeV with $\chi = 40$ and $l_{\rm sub} = 1$.

As a first test of the *recalc_intlist* subroutine described above, the collision history is compared for the ZPC results without and with the new subroutine. Specifically, the event averaged collision number $\langle N_{\rm coll}\rangle$ is compared for several scenarios without and with the *recalc_intlist* subroutine enabled. These results have used $\tau = 20$ as the ending time for all simulations in a box, and the last time when the particle records are updated is at $\tau = 10$ for 100 events of each case. Table 5.3 presents the results for simulations using 4000 partons with $T = 0.5$ GeV and an opacity of $\chi = 1$ without and with a parton subdivision factor of $l_{\rm sub} = 10^4$. The results without subdivision ($l_{\rm sub} = 1$) show that the event averaged collision number for the simulations with $icurve = 1$ are statistically the same as for $icurve = 0$. In fact, the standard errors of the mean have also been calculated and show that the two sets of results are completely consistent with each other. When the parton subdivision method is used, the effective opacity becomes $\chi \to 1/\sqrt{l_{\rm sub}} = 0.01$, and the results are also almost exactly the same. Now however, the results are a little farther apart, having a deviation less than 2σ where σ here refers to the standard error. These deviations are still quite small, especially considering the low number of events, therefore it is expected that the two datasets are consistent in the limit of many events. Finally, the results of 13000 partons with $T = 0.7$ GeV and $\chi = 40$ are also completely consistent with each other when the collision list is recalculated using the new subroutine or not.

Note that the method of including external fields takes longer to run than the default

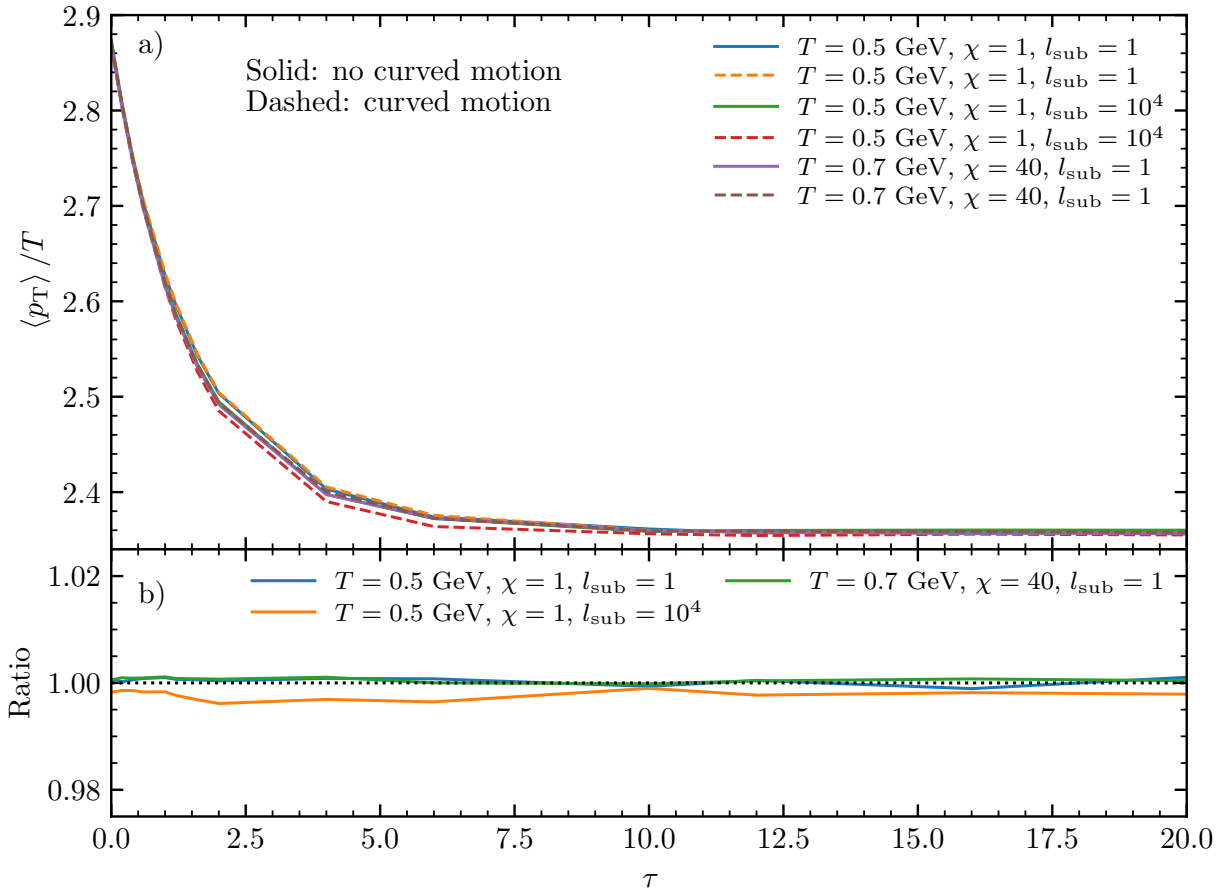

Figure 5.13: (a) The time-evolution of the $\langle p_{\rm T} \rangle / T$ for ZPC simulations in a box without or with calling the external field routine and (b) the ratio of the $\langle p_{\rm T} \rangle$ for scenarios without to those with calling the external field routine 100 events of 4000 partons at $T = 0.5$ GeV and an opacity $\chi = 1$ without or with subdivision at $l_{\rm sub} = 10^4$ and for 13000 partons at $T = 0.7$ GeV and $\chi = 40$ without subdivision.

ZPC simulations because the collision list needs to be recalculated many times. For the results presented in Table 5.3, the running time increases by at most a factor of ≈ 4, which is not too large. Also, an interesting threshold in the collision number has been observed such that if the collision number per event is lower than ≈ 16700, then exactly the same number of collisions occurs independent of the value of *icurve*. This can be understood in terms of the calculation of a two-parton scattering event in which the new positions and momenta are calculated based on the previous particle record information. Without updating the particle records in the new subroutine, the new momenta are calculated using the position of the

particle at its last collision time. However, if the particle records are updated periodically, the partons' locations will be slightly different and the finite precision inherent in any numerical calculation gives a fluctuation on the level of $\approx 10^{-9}$. These small deviations in the new positions compound when the number of collisions per event exceeds a threshold and lead to the discrepancies in the collision history. However, this change of history does not change the statistical behavior of the ZPC evolution.

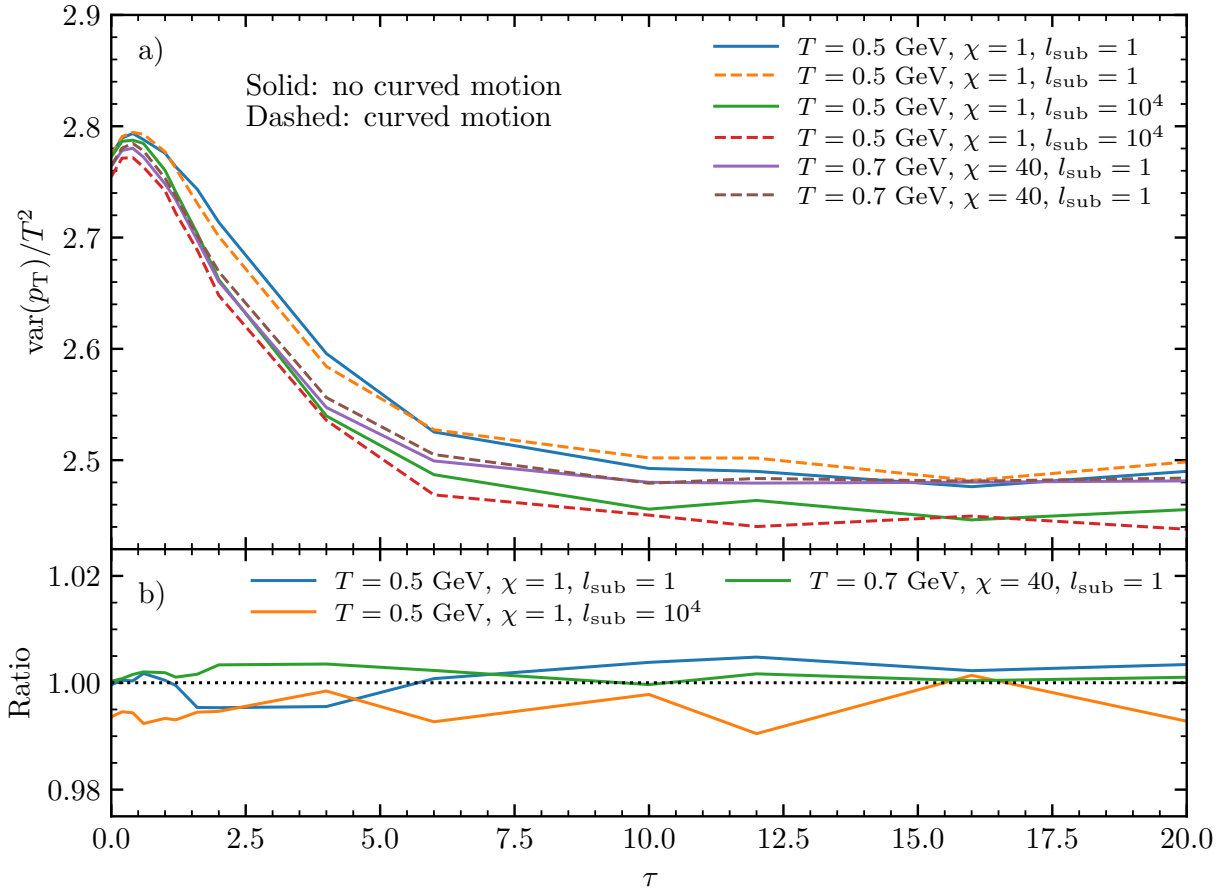

Figure 5.14: (a) The time-evolution of the var($p_{\rm T}$) /T^2 for ZPC simulations in a box without or with calling the external field routine and (b) the ratio of the var($p_{\rm T}$) for scenarios without to those with calling the external field routine for 100 events of 4000 partons at $T = 0.5$ GeV and an opacity $\chi = 1$ without or with subdivision at $l_{\rm sub} = 10^4$ and for 13000 partons at $T = 0.7$ GeV and $\chi = 40$ without subdivision.

While the first test of the collision number per event is successful, it will be more beneficial to compare the time evolution of the $p_{\rm T}$ distribution between the two cases. To that end, the

τ-evolution of the $\langle p_{\mathrm{T}} \rangle$ for the same simulations of Table 5.3 is shown in Fig. 5.13. Note that the time τ here is the same scaled time as discussed in Eq. (4.9) of Sec. 4.2. For $T = 0.5$ and 0.7 GeV, the ending times are $t_{\mathrm{end}} \approx 4.6$ and 0.3 fm/c, respectively. Figure 5.13(a) shows that there is essentially no difference between the $\langle p_{\mathrm{T}} \rangle$ for either case of *icurve* across a wide range of opacities. This result is expected after considering the success of the previous test of the collision number per event. Importantly, the ratios of the $icurve = 1$ to $icurve = 0$ results for the three effective χ cases are all much smaller than 1% and have been plotted in Fig. 5.13(b). Especially considering that only 100 events were used, this result is an excellent indication that recalculating the partons' spatial coordinates and the collision list does not change the behavior of the ZPC. This is important evidence that including curved parton motion via real external fields that affect the parton momenta and spatial coordinates will not be incorrect in this implementation.

Figure 5.14 shows the time evolution of the variance of the p_{T} spectrum scaled by the square of the temperature from the same simulations described above, whose results were presented in Table 5.3 and Fig. 5.13. Whereas the statistical deviations between the simulations with $icurve = 1$ and those with $icurve = 0$ were far smaller than 0.5% when measured by the $\langle p_{\mathrm{T}} \rangle$, the var($p_{\mathrm{T}}$) has deviations around 1% on average. Note that these results are obtained using an off-equilibrium initial condition [69] in order to make the approach to equilibrium observable. The results using the *recalc_intlist* subroutine are completely consistent with the entire time-evolution of the var(p_{T}) from the simulations with $icurve = 0$. For each opacity, the var(p_{T}) are statistically the same for both cases of *icurve*, but the differences between the two results are noticeable over the entire τ-evolution. This is most likely caused by the small event number and may be expected because statistical fluctuations in the var(p_{T}) will be larger than in the $\langle p_{\mathrm{T}} \rangle$ when the same number of events is used. This is because the variance depends on the square of the deviations from the mean.

Overall, a new subroutine that allows one to implement the effect of external fields on the partons in ZPC has been created, and future study of curved parton motion in

ZPC is now possible. The subroutine has been tested using a simple case in which all the partons positions are updated to the position along their free-streaming trajectories at specific points in time. This alters the fundamental behavior of ZPC and means that the interaction list has to be recalculated at each time step. The results using the periodically recalculated interaction list are shown to be the same as the previous default ZPC results within statistical uncertainties. The effect of recalculating the collision list on the transverse momentum spectrum has been shown to be negligible from the dilute limit to high opacities, which is good evidence that the new subroutine will work as expected for all opacities when curved parton motion is implemented. While these initial results for the implementation of external fields in ZPC are promising regarding the eventual goal of studying curved parton motion, more benchmarks are needed. Before continuing further, the results in this section will be made more robust by increasing the number of events in each case, and possibly by adding a few more χ cases. Future test will include implementing a uniform external field that curves the partons' trajectories where the final results are known analytically. Eventually, external electromagnetic fields [117] that are generated by the receding protons in a heavy ion collision will be used to study the effect of electromagnetic fields on the dense parton system.

Chapter 6

Summary and Future Work

The purpose of this research is to use semianalytical and numerical methods to study relativistic heavy ion collisions so that the properties of the hot dense QCD matter they produce can be better understood. While the field of nuclear physics encompasses a broad range of fascinating topics, the many experimental and theoretical studies of the QGP are particularly exciting. Not only do the properties of the QGP have implications for our knowledge of the very early universe just microseconds after the Big Bang, but they might also determine the physics of extreme astrophysical objects such as neutron stars. Therefore, advancements in cosmology, astrophysics, the Standard Model, and perhaps even beyond are expected natural consequences of improving our understanding of heavy ion collisions and the quark-gluon plasma. The results presented in this dissertation represent some recent developments in semianalytical and numerical calculations of the characteristics of the QGP such as how its initial energy density or time evolution contribute to its trajectory in the QCD phase diagram.

First, a semianalytical model of the produced initial energy and net conserved-charge densities is developed in Ch. 2. By considering the finite width of the overlap region along the beam axis of the colliding nuclei, a new formula is derived for the initial energy density as a function of time. Analytically, the result involves calculating an integral over the production area for a given observation time; however, the chosen form of the initial transverse energy production per unit rapidity prevents closed form solutions so far. Therefore, the model is referred to as semianalytical because the previously mentioned definite integral must be numerically calculated at every time throughout the evolution. In spite of the analytical

limitations, the semianalytical results have been shown to improve the estimates of the initial energy densities produced during central Au+Au collisions. Whereas previous models suffered from divergent maximum energy densities at zero parton formation time at all collision energies, the improved semianalytical model has an analytical upper bound for the maximum energy density. The existence of this upper bound proves that including the finite nuclear thickness for the parton production is necessary if one wants to accurately predict the initial energy densities in heavy ion collisions. This becomes especially important for the search for the conjectured critical endpoint in the QCD phase diagram. The maximum energy density of this semianalytical model also has an approximate scaling relation with the nuclear mass number. This implies that the maximum energy density for a nucleus with mass number different from that of gold and one parton formation time is exactly equal to the maximum energy density for a gold nucleus and a different formation time at the same collision energy.

The semianalytical model may also be applied to calculate the initial produced net conserved-charge densities such as the net-baryon density. Predicting the time evolution of the net-baryon density is important for understanding the properties of the dense matter created in heavy ion collisions. The net-strangeness density is identically zero in the semianalytical model because the colliding nuclei carry no net strangeness when strange quark and strange antiquark productions are assumed to be symmetric. Some studies have used the choice of setting the strangeness chemical potential to zero, but this choice is inaccurate and violates the strangeness neutrality in heavy ion collisions. Finally, a transverse flow effect is included in the semianalytical densities by way of a transverse overlap area that expands with time. Reasonable parametrizations of the final transverse flow velocity are made based on RHIC experimental data. Together, these allow the calculation of the energy density averaged over a growing transverse area and primarily affects the late time densities, though it also sometimes decreases the maximum values. One example of a future extension to this semianalytical model is the following. It is assumed that parton production occurs uniformly

throughout the entire overlap region, which simplifies the integral in Eq. (2.4) considerably. The same assumption is also used in the calculation of the net-baryon density. This assumption removes complicated dependence on the spatial and temporal parton production from the integrand, making the equations far more tractable. However, future work could be devoted to incorporating a non-uniform function for the parton production because this is a more general picture.

Second, the thermodynamic variables and QCD phase diagram trajectories of a QGP are extracted from several nuclear equations of state using the semianalytical densities as inputs in Ch. 3. Assuming a QGP that has densities given by the results of the semianalytical model, the temperature and chemical potential are extracted first from an ideal gas equation of state assuming massless partons with either Boltzmann or quantum statistics [46]. The maximum temperature and net-baryon chemical potential are found to depend significantly on the collision energy and parton formation time. Their dependence on key parameters of the semianalytical model has implications on how close a given trajectory passes to the QCD critical endpoint. Then, a more realistic EoS is used based on lattice QCD results, which accounts for the low energy expectation that the matter is dominated by hadron degrees of freedom [67]. The lattice EoS is not accurate for $\mu_{\mathrm{B}}/T > 2.5$, and it was found that the thermodynamic variables cannot be extracted for low energy collisions that have large net-baryon densities. Therefore, the QGP lifetime can only be calculated for low energy collisions using the less accurate ideal gas EoS [46]. The strangeness neutrality in the lattice EoS is found to be different from the FRG calculations [109] that have a strict ordering with T of the μ_{B} dependence of μ_{S}. The lattice EoS shows a similar ordering, but only for low T, while in the high T limit it does not converge to $\mu_{\mathrm{S}} \approx \mu_{\mathrm{B}}/3$, which is expected from the FRG results and the ideal gas EoS for massless partons.

There are several relevant directions in which this work can be continued. First, the lattice QCD based equation of state [67] has some limitations such as not being valid at high baryon chemical potentials or low temperatures. Recently, a new lattice equation of state has

been found by re-summing the terms in the Taylor expansion of the pressure and is notably improved over the previous version [120]. It would be good to use this newer lattice equation of state to extract the thermodynamic properties from the densities of the semianalytical model and assess any changes to the trajectories. In particular, the re-summed lattice EoS might make it possible to extract trajectories at lower collision energies than is currently possible. This could improve the estimation of the QGP lifetime at these low collision energies and also check the recent findings of the STAR Collaboration that the QGP is not formed at 3 GeV Au+Au collisions [48]. Second, the ideal gas equations of state with either Boltzmann or quantum statistics predict that the trajectories start at and for late times approach the origin in the QCD phase diagram [46]. This prediction is obviously incorrect since the normal nuclear matter exists at the finite baryon chemical potential $\mu_{\mathrm{B}} \approx m_{\mathrm{N}}$ when $T = 0$. This behavior in the ideal gas EoS is caused by taking the quark masses to be zero; however, a similar behavior also occurs when including the quark current masses [61]. Since the matter should behave as a hadron resonance gas below the phase transition line, a useful extension to the current work would be to use a hadron equation of state when the temperature is small enough. The main difficulty in doing this will be in smoothly merging the QGP equation of state for high T with the hadron one near the phase transition.

Third, parton transport in ZPC [64] is assessed using an exact analytical solution of the relativistic Boltzmann equation in Ch. 4. The exact solution [77, 78] for a massless parton gas under isotropic scatterings gives the time evolution of the momentum distribution $f(\mathbf{p}, t)$ for a given initial condition. Using a new parton collision scheme [69], ZPC is found to reproduce the exact solution results with an unexpectedly high degree of accuracy throughout the evolution even at high densities. Then, calculating the mean deviation between the numerical and theoretical distribution functions enables the optimal collision scheme to be found for each opacity. These results are combined into two generalized collision schemes, and they produce an even better agreement with the exact solution, having a mean deviation not worse than 0.25%. The interesting observation of the universal dependence of the ZPC

results on the opacity χ rather than on T is also discussed. Overall, improvements to parton transport in ZPC are useful for numerical studies of the QGP with transport models such as the AMPT model [62].

Finally, the initial results from work done to address several open questions related to parton transport in ZPC [64] are discussed in Ch. 5. The new collision scheme [69] that works well for simulations in a box unexpectedly does not work well for simulations with 3D expansion. The origin of this problem may be related to an unexpectedly large collision rate per parton at very early times, just after the initial parton formation time. A new spherical initial condition is introduced to more easily understand the spatial distribution of partons, and a clear peak in the collision number is shown to result from a pseudo-period in the default random number generator (RNG) of ZPC that is based on the linear congruential method [83]. The poor behavior of the RNG manifests itself when generating many random numbers for the partons' positions and momenta; the pseudo-period causes partons with indices a fixed distance apart to be initialized at almost exactly the same spatial coordinates. After implementing a modern RNG, the unexpectedly high early collision rate vanishes for the spherical initial condition, but it does not for the default initial conditions with 3D expansion evolution. Therefore, further work is needed to improve the ZPC accuracy in 3D expansion calculations. Second, two analytical distributions [84, 114] for the Mandelstam s variable are derived in Appendix B.3 assuming the massless partons follow a Boltzmann distribution. ZPC successfully reproduces both of these distributions; the first by calculating $f(s)$ of all parton pairs, and the second by calculating $f(s)$ for actual colliding parton pairs. The agreement of both the numerical $\langle s \rangle$ and $\langle \sqrt{s} \rangle$ has an error of less than 0.125%, and the distributions themselves also have a small deviation from the theoretical results.

Third, ZPC uses the cascade method to simulate the collisions of many particles that are assumed to be free-streaming between collisions [64]. The large magnetic fields that are generated by the receding protons in heavy ion collisions would influence the generated medium, e.g., leading to the chiral magnetic effect [22]. Thus, a new method for letting

partons' trajectories curve under the influence of external fields is implemented in ZPC. If a parton's trajectory were to change, the entire collision list would need to be recalculated, and this would need to occur for many times throughout the evolution when the external fields are active. Therefore, a new subroutine has been included in ZPC that allows the partons to change their positions under the influence of a user-defined external field. Currently, a specific external field is not implemented, so each parton propagates forward in time along its straight line path, but the collision list is recalculated at each time step. Initial results that compare the collision number in ZPC calculations without the new subroutine and with the new subroutine indicate that the program models the same dynamical system across the full range of opacities. A similar result is obtained from analyzing the differences between the time evolution of the $\langle p_{\mathrm{T}} \rangle$ and $\mathrm{var}(p_{\mathrm{T}})$ for both cases. Because the new subroutine produces the same statistical behavior for many effective opacities, it is expected that the results that incorporate a field and consequently the curved motion will also be accurate.

Future studies of parton transport with ZPC [64] could focus on answering several questions. First, the cause of the 3D problem in simulations using the default initial condition must be discovered. Solving this problem will mean that a proper collision scheme can be used to reduce the causality violation instead of using the computationally-expensive and fluctuation-altering parton subdivision method [79]. Second, a proof is needed for why the $f(s)$ distribution for colliding parton pairs in ZPC is apparently exactly given by the theoretical distribution of Appendix B.3. Specifically, it is necessary to understand why the distribution derived using the thermal average of the cross section and a relative velocity should give the $f(s)$ of colliding parton pairs in ZPC. Third, more tests are needed to verify the correct behavior of the new curved motion subroutine in ZPC. Some initial tests should involve changing the partons' momenta in a simple way so that the system's behavior can be analytically known and compared to the numerical results. Following this verification, realistic electromagnetic fields [117] can be used to subject the partons to the expected fields in heavy ion collisions to study related effects such as CME signals [112].

It is the author's earnest wish that the research presented in this dissertation is useful to the field of relativistic heavy ion physics. The semianalytical and numerical studies of heavy ion collisions presented herein represent only a small fraction of the ongoing work in nuclear physics. Finally, the author would like to acknowledge the use of the Numpy [121], Scipy [122], and Matplotlib [123] packages in the Python programming language. The numerical analyses and data presentation in this work could not have been possible without these valuable open-source tools or the innumerable tutorials that are freely available.

References

[1] STAR Collaboration, J. Adams *et al.*, Nucl. Phys. A **757**, 102 (2005).

[2] PHENIX Collaboration, K. Adcox *et al.*, Nucl. Phys. A **757**, 184 (2005).

[3] ALICE Collaboration, J. Schukraft, J. Phys. G **38**, 124003 (2011).

[4] BRAHMS Collaboration, I. Arsene *et al.*, Nucl. Phys. A **757**, 1 (2005).

[5] PHOBOS Collaboration, B. B. Back *et al.*, Nucl. Phys. A **757**, 28 (2005).

[6] BRAHMS Collaboration, I. G. Bearden *et al.*, Phys. Rev. Lett. **88**, 202301 (2002).

[7] CMS Collaboration, V. Khachatryan *et al.*, JHEP **04**, 039 (2017).

[8] ATLAS Collaboration, M. Aaboud *et al.*, Nature Phys. **13**, 852 (2017).

[9] M. Gyulassy and L. McLerran, Nuclear Physics A **750**, 30 (2005).

[10] R. B. Clare and D. Strottman, Phys. Rept. **141**, 177 (1986).

[11] S. A. Bass *et al.*, Prog. Part. Nucl. Phys. **41**, 255 (1998).

[12] F. Karsch, Nucl. Phys. A **698**, 199 (2002).

[13] HotQCD Collaboration, A. Bazavov *et al.*, Phys. Rev. D **90**, 094503 (2014).

[14] J. I. Kapusta, Landolt-Bornstein **23**, 563 (2010).

[15] A. Andronic, F. Beutler, P. Braun-Munzinger, K. Redlich, and J. Stachel, Phys. Lett. B **675**, 312 (2009).

[16] Y. Mehtar-Tani and G. Wolschin, Phys. Rev. Lett. **102**, 182301 (2009).

[17] ALICE Collaboration, B. Abelev *et al.*, Phys. Rev. C **88**, 044910 (2013).

[18] PHENIX Collaboration, A. Adare *et al.*, Phys. Rev. Lett. **101**, 232301 (2008).

[19] JET Collaboration, K. M. Burke *et al.*, Phys. Rev. C **90**, 014909 (2014).

[20] P. Braun-Munzinger and J. Stachel, Phys. Lett. B **490**, 196 (2000).

[21] ALICE Collaboration, J. Adam *et al.*, JHEP **03**, 081 (2016).

[22] K. Fukushima, D. E. Kharzeev, and H. J. Warringa, Phys. Rev. D **78**, 074033 (2008).

[23] CMS Collaboration, V. Khachatryan *et al.*, JHEP **09**, 091 (2010).

[24] CMS Collaboration, V. Khachatryan *et al.*, Phys. Lett. B **742**, 200 (2015).

[25] A. Dumitru *et al.*, Phys. Lett. B **697**, 21 (2011).

[26] A. M. Poskanzer and S. A. Voloshin, Phys. Rev. C **58**, 1671 (1998).

[27] P. Huovinen, P. F. Kolb, U. W. Heinz, P. V. Ruuskanen, and S. A. Voloshin, Phys. Lett. B **503**, 58 (2001).

[28] A. Bilandzic, C. H. Christensen, K. Gulbrandsen, A. Hansen, and Y. Zhou, Phys. Rev. C **89**, 064904 (2014).

[29] M. Asakawa, U. W. Heinz, and B. Muller, Phys. Rev. Lett. **85**, 2072 (2000).

[30] M. A. Stephanov, K. Rajagopal, and E. V. Shuryak, Phys. Rev. D **60**, 114028 (1999).

[31] K. Fukushima and T. Hatsuda, Rept. Prog. Phys. **74**, 014001 (2011).

[32] M. A. Stephanov, Phys. Rev. Lett. **107**, 052301 (2011).

[33] A. Bzdak *et al.*, Phys. Rept. **853**, 1 (2020).

[34] Z. Li, K. Xu, X. Wang, and M. Huang, Eur. Phys. J. C **79**, 245 (2019).

[35] STAR Collaboration, B. Mohanty, J. Phys. G **38**, 124023 (2011).

[36] X. Luo and N. Xu, Nucl. Sci. Tech. **28**, 112 (2017).

[37] STAR Collaboration, L. Adamczyk *et al.*, Phys. Rev. C **96**, 044904 (2017).

[38] D. Keane, J. Phys. Conf. Ser. **878**, 012015 (2017).

[39] M. Okai, K. Kawaguchi, Y. Tachibana, and T. Hirano, Phys. Rev. C **95**, 054914 (2017).

[40] C. Shen *et al.*, Nucl. Phys. A **967**, 796 (2017).

[41] L. Du, U. Heinz, and G. Vujanovic, Nucl. Phys. A **982**, 407 (2019).

[42] J. D. Bjorken, Phys. Rev. D **27**, 140 (1983).

[43] Z.-W. Lin, Phys. Rev. C **98**, 034908 (2018).

[44] PHENIX Collaboration, S. S. Adler *et al.*, Phys. Rev. C **71**, 034908 (2005), [Erratum: Phys.Rev.C 71, 049901 (2005)].

[45] T. Mendenhall and Z.-W. Lin, Phys. Rev. C **103**, 024907 (2021).

[46] T. Mendenhall and Z.-W. Lin, Phys. Rev. C **107**, 034909 (2023).

[47] STAR Collaboration, J. Adam *et al.*, Phys. Rev. Lett. **126**, 092301 (2021).

[48] STAR Collaboration, M. S. Abdallah *et al.*, Phys. Lett. B **827**, 137003 (2022).

[49] Z. Xu and C. Greiner, Phys. Rev. C **71**, 064901 (2005).

[50] Z.-W. Lin, Phys. Rev. C **90**, 014904 (2014).

[51] P. Jacobs and X.-N. Wang, Prog. Part. Nucl. Phys. **54**, 443 (2005).

[52] Y. Aoki, G. Endrodi, Z. Fodor, S. D. Katz, and K. K. Szabo, Nature **443**, 675 (2006).

[53] R. Bellwied *et al.*, Phys. Lett. B **751**, 559 (2015).

[54] HotQCD Collaboration, A. Bazavov *et al.*, Phys. Lett. B **795**, 15 (2019).

[55] R. V. Gavai and S. Gupta, Phys. Rev. D **68**, 034506 (2003).

[56] STAR Collaboration, M. M. Aggarwal *et al.*, Phys. Rev. Lett. **105**, 022302 (2010).

[57] STAR Collaboration, L. Adamczyk *et al.*, Phys. Rev. Lett. **113**, 092301 (2014).

[58] V. Koch, A. Majumder, and J. Randrup, Phys. Rev. Lett. **95**, 182301 (2005).

[59] B. Zhang, L.-W. Chen, and C. M. Ko, J. Phys. G **35**, 065103 (2008).

[60] C. Shen and L. Yan, Nucl. Sci. Tech. **31**, 122 (2020).

[61] H.-S. Wang, G.-L. Ma, Z.-W. Lin, and W.-J. Fu, Phys. Rev. C **105**, 034912 (2022).

[62] Z.-W. Lin, C. M. Ko, B.-A. Li, B. Zhang, and S. Pal, Phys. Rev. C **72**, 064901 (2005).

[63] X.-N. Wang and M. Gyulassy, Phys. Rev. D **44**, 3501 (1991).

[64] B. Zhang, Comput. Phys. Commun. **109**, 193 (1998).

[65] Y. He and Z.-W. Lin, Phys. Rev. C **96**, 014910 (2017).

[66] B.-A. Li and C. M. Ko, Phys. Rev. C **52**, 2037 (1995).

[67] J. Noronha-Hostler, P. Parotto, C. Ratti, and J. M. Stafford, Phys. Rev. C **100**, 064910 (2019).

[68] P. Alba *et al.*, Phys. Rev. D **96**, 034517 (2017).

[69] X.-L. Zhao, G.-L. Ma, Y.-G. Ma, and Z.-W. Lin, Phys. Rev. C **102**, 024904 (2020).

[70] STAR Collaboration, B. I. Abelev *et al.*, Phys. Rev. C **79**, 034909 (2009).

[71] H.-T. Janka, K. Langanke, A. Marek, G. Martinez-Pinedo, and B. Mueller, Phys. Rept. **442**, 38 (2007).

[72] C.-P. Ma and E. Bertschinger, Astrophys. J. **455**, 7 (1995).

[73] P. L. Bhatnagar, E. P. Gross, and M. Krook, Phys. Rev. **94**, 511 (1954).

[74] W. Florkowski, R. Ryblewski, and M. Strickland, Nucl. Phys. A **916**, 249 (2013).

[75] G. S. Denicol, U. W. Heinz, M. Martinez, J. Noronha, and M. Strickland, Phys. Rev. Lett. **113**, 202301 (2014).

[76] G. S. Denicol, U. W. Heinz, M. Martinez, J. Noronha, and M. Strickland, Phys. Rev. D **90**, 125026 (2014).

[77] D. Bazow, G. S. Denicol, U. Heinz, M. Martinez, and J. Noronha, Phys. Rev. Lett. **116**, 022301 (2016).

[78] D. Bazow, G. S. Denicol, U. Heinz, M. Martinez, and J. Noronha, Phys. Rev. D **94**, 125006 (2016).

[79] B. Zhang, M. Gyulassy, and Y. Pang, Phys. Rev. C **58**, 1175 (1998).

[80] D. Molnar and M. Gyulassy, Phys. Rev. C **62**, 054907 (2000).

[81] G. Kortemeyer, W. Bauer, K. Haglin, J. Murray, and S. Pratt, Phys. Rev. C **52**, 2714 (1995).

[82] M. Krook and T. T. Wu, Phys. Rev. Lett. **36**, 1107 (1976).

[83] G. Ossola and A. D. Sokal, Phys. Rev. E **70**, 027701 (2004).

[84] E. W. Kolb and S. Raby, Phys. Rev. D **27**, 2990 (1983).

[85] STAR Collaboration, M. Abdallah *et al.*, Phys. Rev. C **105**, 014901 (2022).

[86] K. Kajantie, R. Raitio, and P. V. Ruuskanen, Nucl. Phys. B **222**, 152 (1983).

[87] C. Spieles *et al.*, Phys. Rev. C **60**, 054901 (1999).

[88] A web interface that performs the semianalytical calculation of the collision trajectory of central A+A collisions for selected equations of state is available at https://myweb.ecu.edu/linz/densities/ (2022).

[89] A. Monnai, B. Schenke, and C. Shen, Int. J. Mod. Phys. A **36**, 2130007 (2021).

[90] E802 Collaboration, Y. Akiba *et al.*, Nucl. Phys. A **610**, 139C (1996).

[91] E802 Collaboration, L. Ahle *et al.*, Phys. Rev. C **57**, R466 (1998).

[92] E866 and E917 Collaborations, L. Ahle *et al.*, Phys. Lett. B **476**, 1 (2000).

[93] E877 Collaboration, J. Barrette *et al.*, Phys. Rev. C **62**, 024901 (2000).

[94] E802 Collaboration, L. Ahle *et al.*, Phys. Rev. C **60**, 064901 (1999).

[95] E802 and E866 Collaborations, L. Ahle *et al.*, Phys. Rev. C **60**, 044904 (1999).

[96] E866 and E917 Collaborations, L. Ahle *et al.*, Phys. Lett. B **490**, 53 (2000).

[97] E895 Collaboration, J. L. Klay *et al.*, Phys. Rev. Lett. **88**, 102301 (2002).

[98] NA49 Collaboration, C. Alt *et al.*, Phys. Rev. C **77**, 024903 (2008).

[99] NA49 Collaboration, C. Alt *et al.*, Phys. Rev. C **73**, 044910 (2006).

[100] NA49 Collaboration, T. Anticic *et al.*, Phys. Rev. C **69**, 024902 (2004).

[101] NA49 Collaboration, S. V. Afanasiev *et al.*, Phys. Rev. C **66**, 054902 (2002).

[102] Particle Data Group, K. A. Olive *et al.*, Chin. Phys. C **38**, 090001 (2014).

[103] S. A. Chin, Phys. Lett. B **78**, 552 (1978).

[104] W.-J. Fu, J. M. Pawlowski, and F. Rennecke, Phys. Rev. D **101**, 054032 (2020).

[105] Z.-W. Lin and T. Mendenhall, Rev. Mex. Fis. Suppl. **3**, 040920 (2022).

[106] S. Borsanyi *et al.*, JHEP **10**, 205 (2018).

[107] P. Huovinen and P. Petreczky, Phys. Lett. B **777**, 125 (2018).

[108] T. Mendenhall and Z.-W. Lin, EPJ Web Conf. **276**, 01012 (2023).

[109] W.-J. Fu, J. M. Pawlowski, and F. Rennecke, Phys. Rev. D **100**, 111501 (2019).

[110] J. Weil *et al.*, Phys. Rev. C **94**, 054905 (2016).

[111] J. Tindall, J. M. Torres-Rincon, J. B. Rose, and H. Petersen, Phys. Lett. B **770**, 532 (2017).

[112] X.-L. Zhao and G.-L. Ma, Phys. Rev. C **106**, 034909 (2022).

[113] A. Sibidanov, Comput. Phys. Commun. **221**, 299 (2017).

[114] P. Gondolo and G. Gelmini, Nucl. Phys. B **360**, 145 (1991).

[115] P. Koch, B. Muller, and J. Rafelski, Phys. Rept. **142**, 167 (1986).

[116] N. M. MacKay and Z.-W. Lin, Eur. Phys. J. C **82**, 918 (2022).

[117] X.-L. Zhao, Y.-G. Ma, and G.-L. Ma, Phys. Rev. C **97**, 024910 (2018).

[118] X.-L. Zhao, G.-L. Ma, and Y.-G. Ma, Phys. Lett. B **792**, 413 (2019).

[119] X.-L. Zhao, G.-L. Ma, and Y.-G. Ma, Phys. Rev. C **99**, 034903 (2019).

[120] S. Borsanyi *et al.*, Phys. Rev. D **105**, 114504 (2022).

[121] C. R. Harris *et al.*, Nature **585**, 357 (2020).

[122] P. Virtanen *et al.*, Nature Methods **17**, 261 (2020).

[123] J. D. Hunter, Computing in Science & Engineering **9**, 90 (2007).

[124] M. Gyulassy and X.-N. Wang, Comput. Phys. Commun. **83**, 307 (1994).

[125] NA49 Collaboration, T. Anticic *et al.*, Phys. Rev. Lett. **93**, 022302 (2004).

[126] E917 Collaboration, B. B. Back *et al.*, Phys. Rev. Lett. **86**, 1970 (2001).

[127] NA49 Collaboration, T. Anticic *et al.*, Phys. Rev. C **83**, 014901 (2011).

[128] NA49 Collaboration, H. Appelshauser *et al.*, Phys. Rev. Lett. **82**, 2471 (1999).

[129] BRAHMS Collaboration, I. C. Arsene *et al.*, Phys. Lett. B **677**, 267 (2009).

[130] BRAHMS Collaboration, I. G. Bearden *et al.*, Phys. Rev. Lett. **93**, 102301 (2004).

Appendix A: Constructing Data-Based Parametrizations of Initial Energy

A.1 dm_{T}/dy of Initially Produced Partons

The initial dm_{T}/dy of produced partons is parametrized as a Gaussian function of rapidity y:

$$\frac{dm_{\mathrm{T}}}{dy} = \frac{dm_{\mathrm{T}}}{dy}(0)e^{-\frac{y^2}{2\sigma^2}}, \tag{A.1}$$

where the notation $F(0)$ is used to represent the value of the function $F(y)$ at $y = 0$ [45]. The peak value of dm_{T}/dy at different collision energies is then taken from a parametrization of the results from the string melting version of the AMPT model [43]:

$$\frac{dm_{\mathrm{T}}}{dy}(0) = 168\left(\frac{\sqrt{s_{\mathrm{NN}}}}{\mathrm{GeV}} - 0.930\right)^{0.348}\mathrm{GeV}. \tag{A.2}$$

The requirement of total energy conservation from Eq. (2.15) allows one to determine the Gaussian width σ:

$$\sigma = \sqrt{W_0(r^2)},\ \text{with}\ r = \frac{\mathrm{A}\sqrt{s_{\mathrm{NN}}}}{\sqrt{2\pi}\frac{dm_{\mathrm{T}}}{dy}(0)}, \tag{A.3}$$

where $W_0(x)$ is the $k = 0$ branch of the Lambert W function (or the omega function) $W_k(x)$.

Figure A.1 shows the dm_{T}/dy of initial partons as given by Eq. (A.1) for central Au+Au collisions at several collision energies (solid curves). A monotonic increase of the peak value and the Gaussian width with the collision energy $\sqrt{s_{\mathrm{NN}}}$ is observed. Symbols represent the results of initially produced partons from the string melting version of the AMPT model [43],

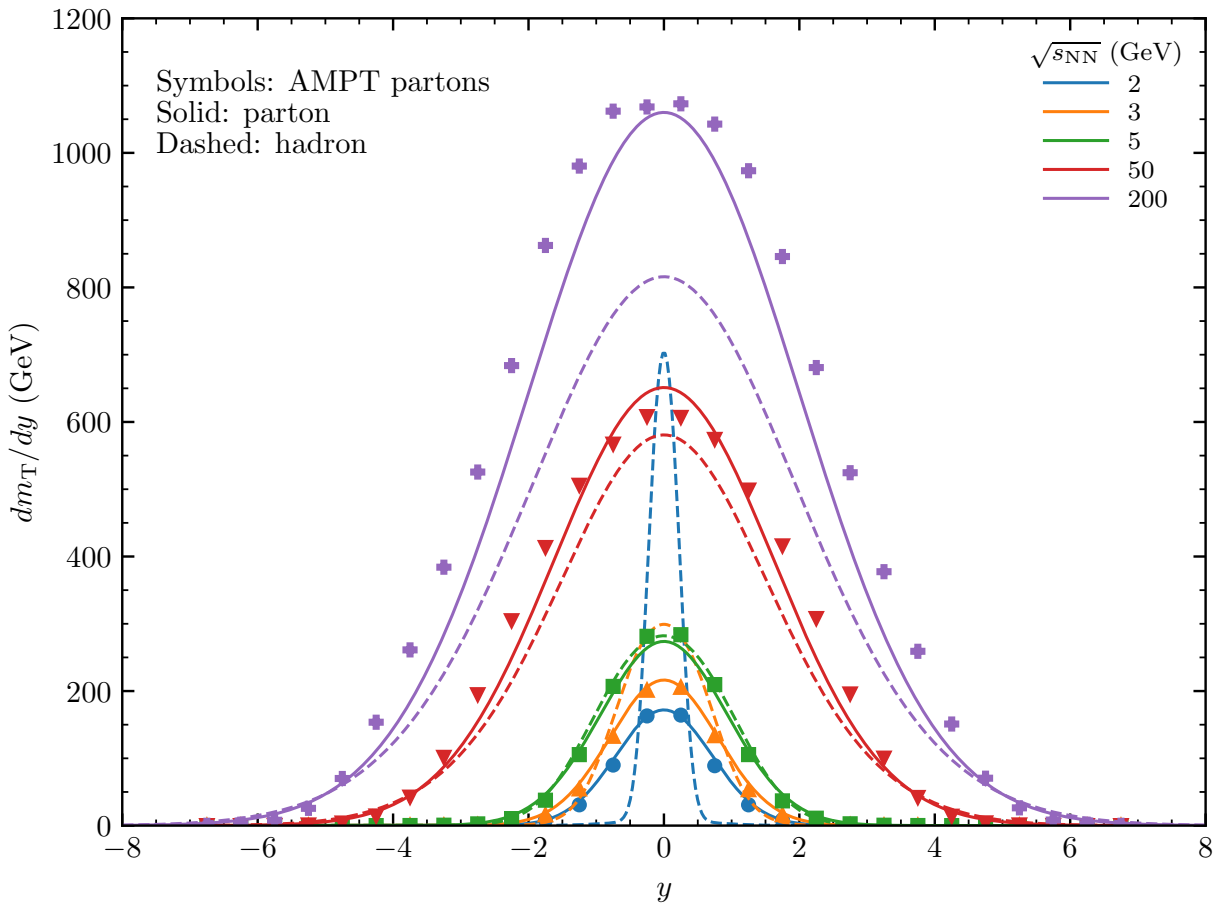

Figure A.1: Transverse mass per unit rapidity for produced initial state partons (solid) and final state hadrons (dashed) for central Au+Au collisions at $\sqrt{s_{\rm NN}}$ = 2, 3, 5, 50, and 200 GeV. Symbols represent the initial parton results from the string melting version of the AMPT model [43].

which show the same qualitative features. Note that in more realistic calculations such as those from the HIJING model [63, 124] or the AMPT model [62], a small fraction of the incoming nucleons are spectators in central collisions. The $dm_{\rm T}/dy$ of final state hadrons is also shown in Fig. A.1. At $\sqrt{s_{\rm NN}}$ = 2 GeV, there is a clear difference between the parton $dm_{\rm T}/dy$ and the hadron $dm_{\rm T}/dy$ in that a non-monotonic behavior of $dm_{\rm T}/dy(0)$ appears for the hadron distribution. This is understandable from the net-baryon term in the definition of the hadron $dm_{\rm T}/dy$ of Eq. (A.4) and the corresponding curve in Fig. A.5. While the hadron $dm_{\rm T}/dy(0)$ is larger than the parton one at low collision energies, it is smaller for $\sqrt{s_{\rm NN}} \gtrsim 6$ GeV. In Fig. A.1, the hadron $dm_{\rm T}/dy$ and parton $dm_{\rm T}/dy$ are shown to have similar values

for collision energies between ≈ 3 and 50 GeV. One can also note the obvious difference in the widths of the parton and hadron $dm_{\rm T}/dy$ distributions in Fig. A.1. At 2 GeV near the threshold energy, the hadron $dm_{\rm T}/dy$ has a much higher peak and is much narrower than the parton $dm_{\rm T}/dy$ because of the slow baryons, while the hadron $dm_{\rm T}/dy$ has a lower peak at the top RHIC energy consistent with the effect of strong secondary interactions.

A.2 $dm_{\rm T}/dy$ Based on Data of Final State Hadrons

In the PHENIX Collaboration's data-based parametrization of the transverse energy pseudo-rapidity density near the central spacetime-rapidity region ($\eta = 0$), they define the "transverse energy" $E_{\rm T}$ as $E_{\rm T} = \sum_i E_i \sin\theta_i$ [44]. Here, θ_i is the polar angle of particle i and E_i is defined as $E_i^{tot} - m_{\rm N}$ for baryons, $E_i^{tot} + m_{\rm N}$ for antibaryons, and E_i^{tot} for all other particles [44]. Note that E_i^{tot} is the total energy of the particle and $m_{\rm N}$ is the nucleon mass.

As a result of the $E_{\rm T}$ definition above, the total transverse energy of hadrons at $y = 0$ is given by

$$\frac{dm_{\rm T}}{dy} = \frac{dE_{\rm T}}{dy} + m_{\rm N}\frac{dN_{\rm netB}}{dy}, \tag{A.4}$$

where $N_{\rm netB}$ represents the net-baryon number. The hadron $dm_{\rm T}/dy$ function for calculating the energy density via Eq. (2.14) is determined by assuming that $dE_{\rm T}/dy$ is a single Gaussian and that $dN_{\rm netB}/dy$ is described by a double-Gaussian [16, 125]:

$$\begin{aligned} \frac{dE_{\rm T}}{dy} &= \frac{dE_{\rm T}}{dy}(0)\exp\left(-\frac{y^2}{2\sigma_1^2}\right), \\ \frac{dN_{\rm netB}}{dy} &= C\left\{\exp\left[-\frac{(y+y_B)^2}{2\sigma_2^2}\right] + \exp\left[-\frac{(y-y_B)^2}{2\sigma_2^2}\right]\right\}. \end{aligned} \tag{A.5}$$

First, regarding $dE_{\rm T}/dy(0)$, the PHENIX Collaboration [44] has parametrized the mid-

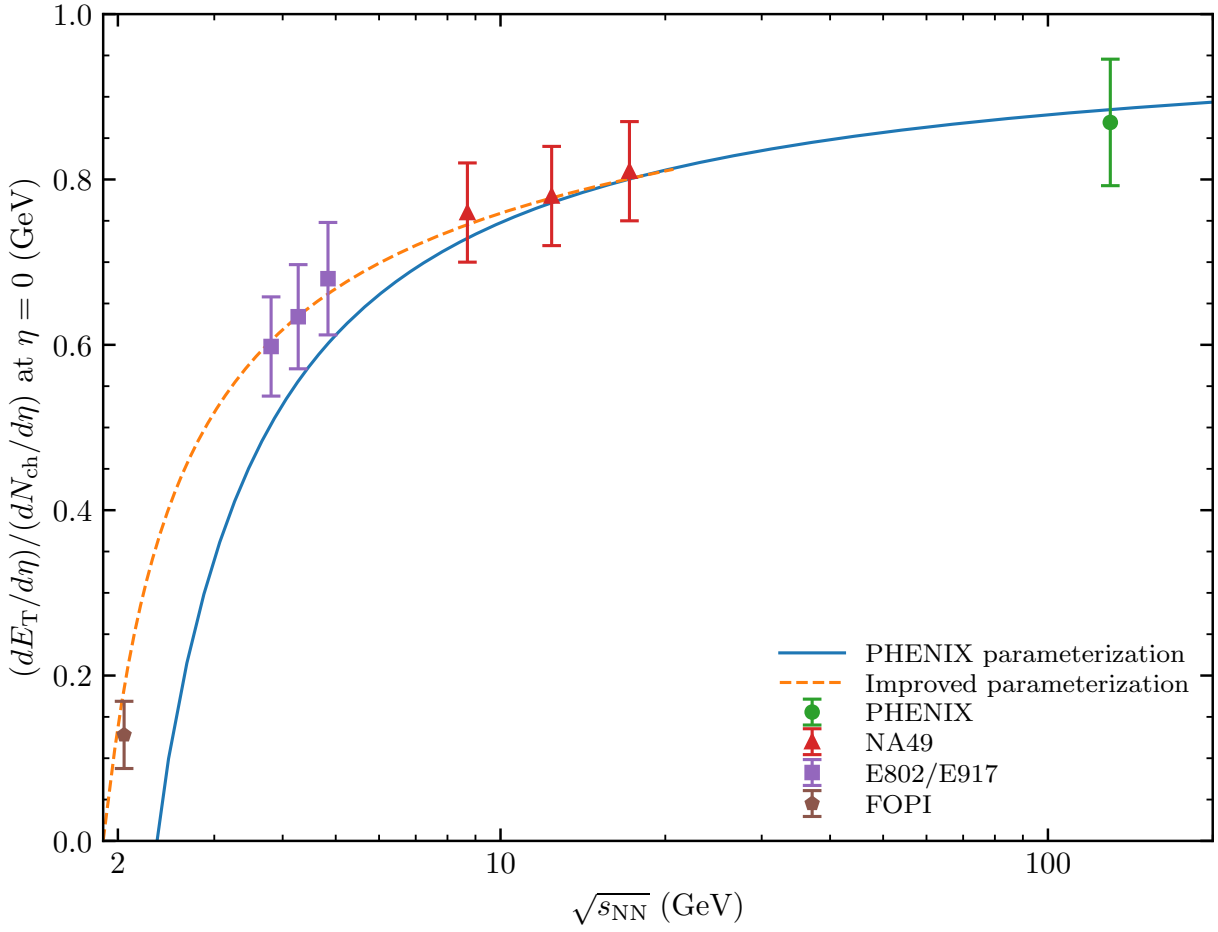

Figure A.2: $(dE_T/d\eta)/(dN_{ch}/d\eta)$ data at $\eta = 0$ compared with the improved parametrization for collision energies below $\sqrt{s_{NN}} < 20.7$ GeV and the older parametrization from the PHENIX Collaboration [44].

pseudorapidity data as

$$\begin{aligned} \frac{dN_{ch}}{d\eta}(0) &= 0.37 N_p \ln\left(\frac{\sqrt{s_{NN}}}{1.48\text{GeV}}\right), \\ \frac{dE_T}{d\eta}(0) &= 0.365 N_p \ln\left(\frac{\sqrt{s_{NN}}}{2.35\text{GeV}}\right) \text{ GeV}, \end{aligned} \tag{A.6}$$

where N_p is the number of participant nucleons that is taken as 2A for the central collisions considered by the semianalytical model [45] of Ch. 2. It was found that the $dE_T/d\eta(0)$ parametrization underestimates the $(dE_T/d\eta)/(dN_{ch}/d\eta)$ ratio for collision energies less than $\sqrt{s_{NN}} \approx 10$ GeV [44, 45], and this fact is displayed in Fig. A.2. Since the effect of finite nuclear

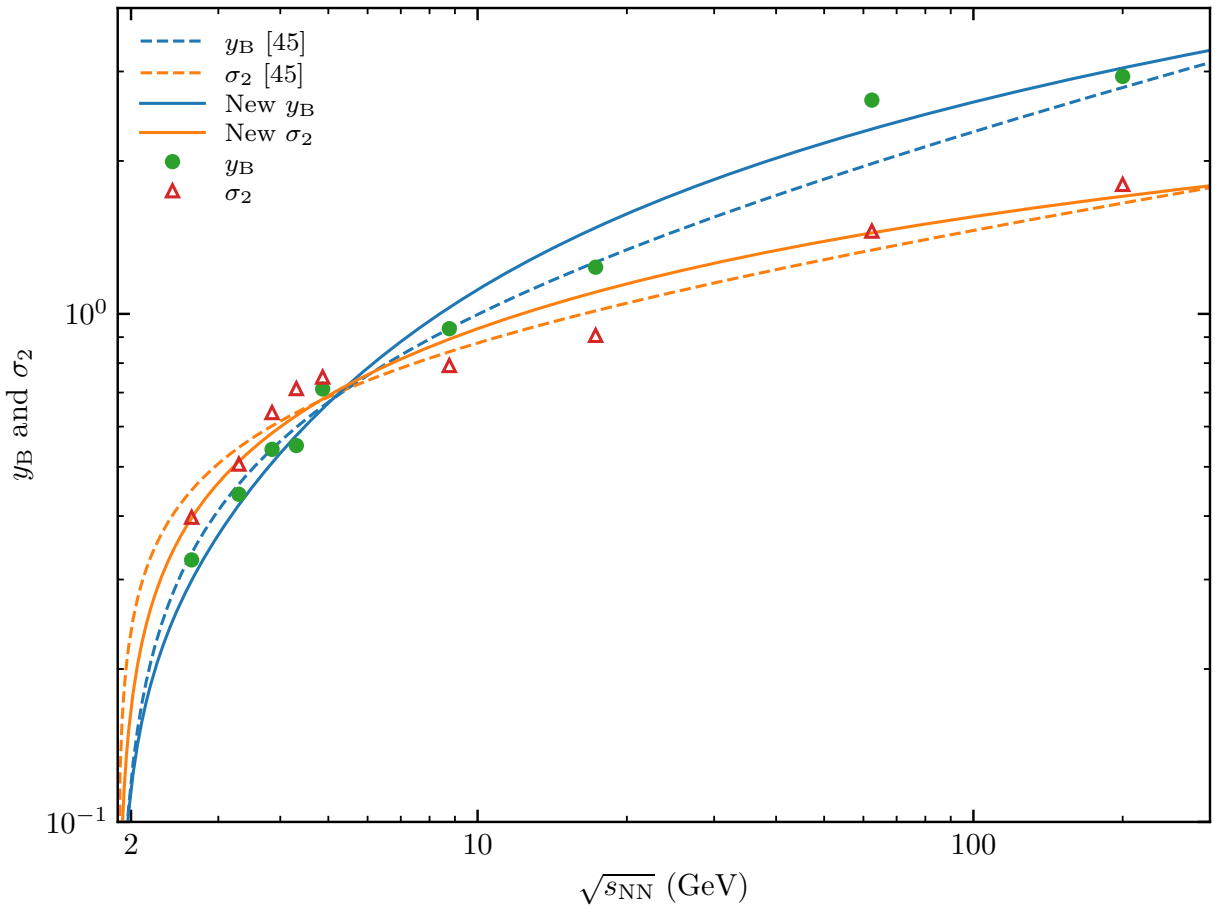

Figure A.3: Individual fit values of y_B (circles) and σ_2 (triangles), their previous parametrizations [45] (dashed), and their updated parametrizations in Eq. (A.8) (solid).

thickness is more important at lower collision energies and the PHENIX Collaboration's parametrization of $dN_{ch}/d\eta(0)$ is accurate down to lower energies than that of $dE_T/d\eta(0)$, we have improved the $dE_T/d\eta(0)$ parametrization [45]. Specifically, the same $dN_{ch}/d\eta(0)$ parametrization is chosen as in Ref. [44], but the $(dE_T/d\eta)/(dN_{ch}/d\eta)$ function is refit to the experimental data at low energies. The result of this improved parametrization is

$$\frac{dE_T}{d\eta}(0) = 0.308 N_p \ln^{1.08}\left(\frac{\sqrt{s_{NN}}}{E_0}\right) \text{ GeV}, \tag{A.7}$$

for $\sqrt{s_{NN}} \leq 20.7$ GeV, where $E_0 = 2m_N$ is the threshold collision energy [45, 46]. As is shown in Fig. A.2, this improved low energy parametrization intersects the PHENIX

parametrization at $\sqrt{s_{\rm NN}} \approx 20.7$ GeV, above which the PHENIX $dE_{\rm T}/d\eta(0)$ parametrization is used. Next, the transverse energy rapidity density is related to the transverse energy pseudorapidity density [44] as $dE_{\rm T}/dy(0) = 1.25\ dE_{\rm T}/d\eta(0)$.

Second, the following parametrizations for the double Gaussian parameters $y_{\rm B}$ and σ_2 for the net-baryon rapidity density profile are taken:

$$\begin{aligned} y_{\rm B} &= 0.599 \left[1 - \frac{1}{2.18 + \ln^{1.86}\left(\frac{\sqrt{s_{\rm NN}}}{E_0}\right)} \right] y_{\rm CM}, \\ \sigma_2 &= 0.838 \left[1 - \frac{1}{5.01 + \ln^{1.61}\left(\frac{\sqrt{s_{\rm NN}}}{E_0}\right)} \right] \sqrt{\ln\left(\frac{\sqrt{s_{\rm NN}}}{E_0}\right)}. \end{aligned} \tag{A.8}$$

Recall that $E_0 = 2m_{\rm N}$ is the threshold collision energy [46]. These parametrizations have been obtained using the proton dN/dy data at $\sqrt{s_{\rm NN}} = 2.65$, 3.30, 3.85, and 4.31 GeV [97] and the net-proton dN/dy data at $\sqrt{s_{\rm NN}} = 4.87$ [94, 126], 8.77 [127], 17.3 [128], 62.4 [129] and 200 GeV [130] in central Au+Au collisions (with the exception that central Pb+Pb data are used at 8.77 and 17.3 GeV).

Note that the parametrizations for $y_{\rm B}$ and σ_2 of Eq. (A.8) for $dN_{\rm netB}/dy$ are updated from those given in Ref. [45]. This change was made for two reasons [46]. First, the previous parametrizations [45] contain a positive power of the collision energy $\sqrt{s_{\rm NN}}$. For example, $y_{\rm B} \propto (\sqrt{s_{\rm NN}} - E_0)^{0.196} \ln^{0.392}(\sqrt{s_{\rm NN}})$ was used previously. This functional form will break down above a certain high energy because $y_{\rm B} > y_{\rm CM}$ will eventually cause the energy in the $dN_{\rm netB}/dy$ term of Eq. (A.4) to exceed the total energy, which would be unphysical. Thus, the new forms in Eq. (A.8) are used without positive powers of $\sqrt{s_{\rm NN}}$ to remedy this problem [46]. Second, we have corrected the collision energies for the low energy proton dN/dy data [97]. Before, the values $\sqrt{s_{\rm NN}} = 2.4$, 3.1, 3.6, and 4.1 GeV were used [45], and these have been updated to $\sqrt{s_{\rm NN}} = 2.65$, 3.31, 3.85, and 4.31 GeV, respectively. The updated values are the actual beam kinetic energies after correcting for the energy loss before reaching the target [97]. We also realized that the net-proton dN/dy data at $\sqrt{s_{\rm NN}} \approx 5$ GeV

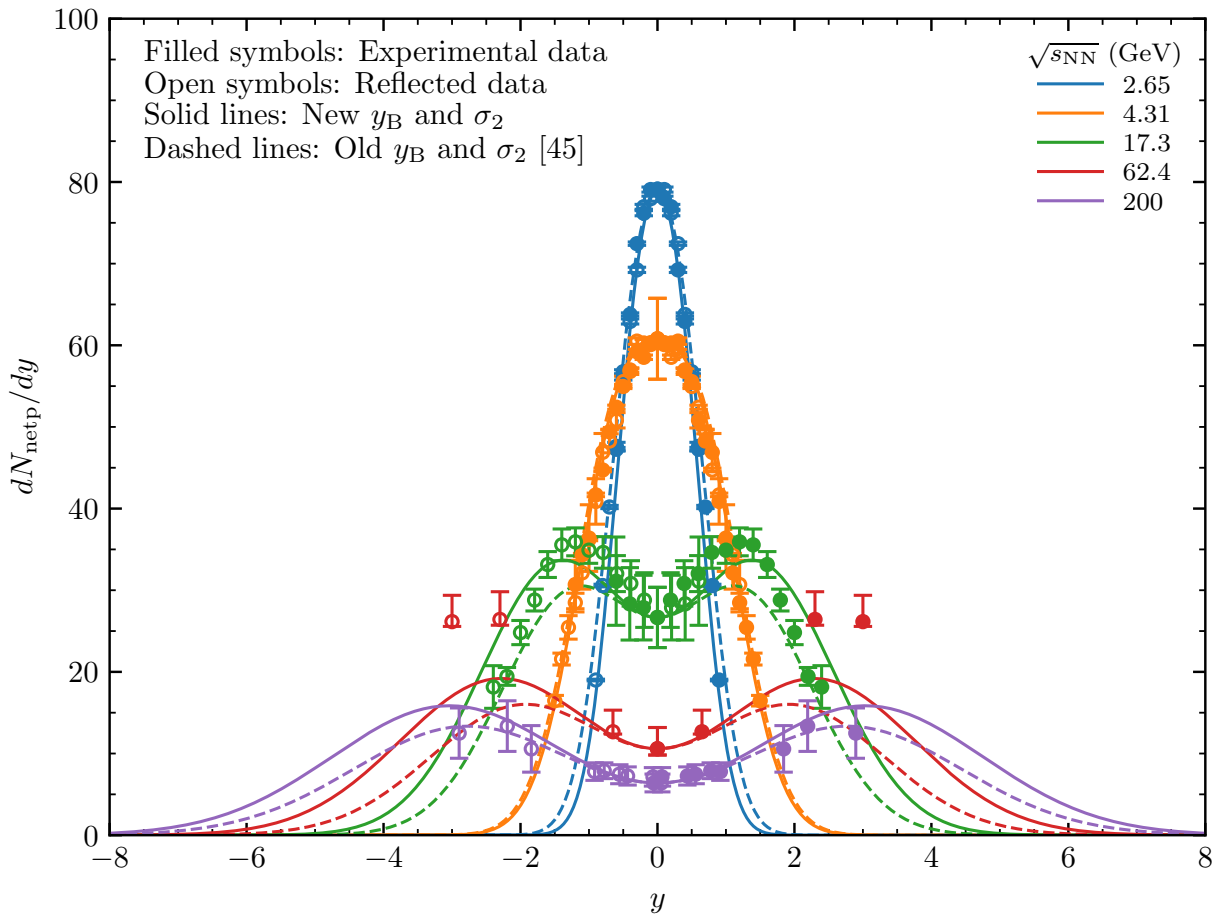

Figure A.4: Net-proton dN/dy data (circles) for central Au+Au (Pb+Pb) at $\sqrt{s_{NN}} = 2.65$, 4.31, (17.3), 62.4, and 200 GeV in comparison with the scaled net-baryon parametrizations (curves) using the old y_B and σ_2 from Ref. [45] (dashed) or the new y_B and σ_2 in Eq. (A.8) (solid). Filled circles represent actual data and open circles are reflected data across $y = 0$.

actually contains data for $\sqrt{s_{NN}} = 4.70$ [93], 4.86 [94], and 4.88 GeV [126]. Therefore, we combined the data at 4.86 GeV and 4.88 GeV into one data set at $\sqrt{s_{NN}} = 4.87$ GeV. In addition, the net-proton data at $\sqrt{s_{NN}} = 8.77$ [127] and 62.4 GeV [129] are also used for the updated parametrizations of Eq. A.8.

In Fig. A.3, the updated individual fit values for y_B and σ_2 are shown in comparison with their previous parametrizations [45] and the new parametrizations [46]. For collision energies $\sqrt{s_{NN}} < 4$ GeV, the new parametrizations for y_B and σ_2 match the individual fit values quite well [46]. On the other hand, the individual fit values for larger collision energies

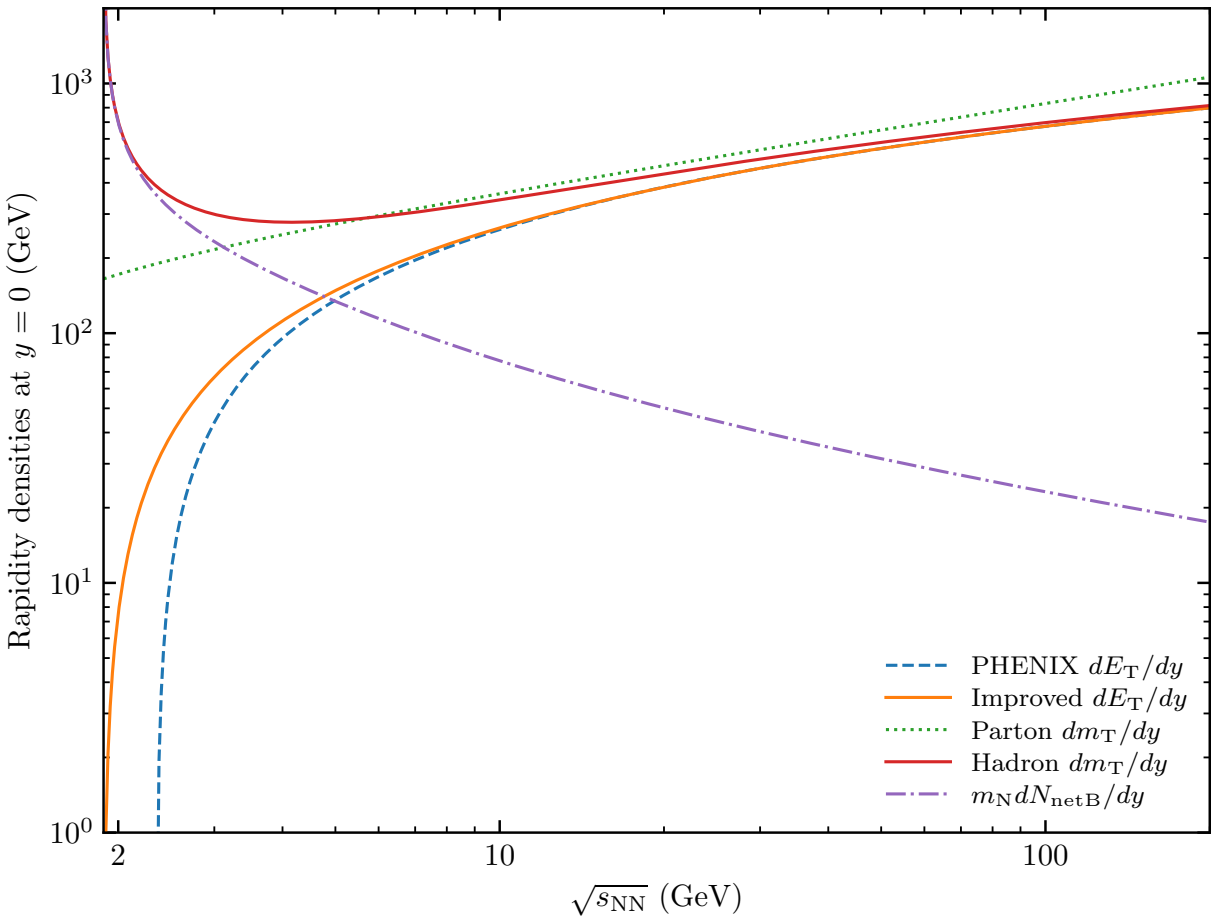

Figure A.5: Mid-rapidity ($y = 0$) values of the transverse mass $m_{\rm T}$, transverse energy $E_{\rm T}$, and $m_{\rm N}N_{\rm netB}$ rapidity densities as functions of collision energy $\sqrt{s_{\rm NN}}$. The $dE_{\rm T}/dy$ from the PHENIX Collaboration [44] is also shown for reference.

$\sqrt{s_{\rm NN}} > 4$ GeV for $y_{\rm B}$ or σ_2 make it seem impossible to fit them well with a smooth function. Instead, the new parametrization provides a smooth fit that is overall closer to the individual fit values. For example, the new parametrization overestimates the individual $y_{\rm B}$ values at $\sqrt{s_{\rm NN}} = 8.77$ and 17.3 GeV, which leads to an underestimate of $dN_{\rm netB}/dy(0)$ near these collision energies.

We further assumed that the net-baryon and net-proton dN/dy distributions have the same shape. The conservation of the net-baryon number is then imposed according to the following restriction:

$$\int \frac{dN_{\rm netB}}{dy} dy = 2{\rm A}. \tag{A.9}$$

The parameter C in Eq. (A.5) is then determined at each collision energy [46]. Finally, the Gaussian parameter σ_1 in Eq. (A.5) is calculated using the conservation of total energy of Eq. (2.15) at each collision energy. Lastly, the parameter σ_1 in Eq. (A.5) is calculated by applying the conservation of total energy requirement of Eq. (2.15). In Fig. A.4, the $dN_{\rm netB}/dy$ shape from both old and new parametrizations is compared with the net-proton data at several collision energies. Note that the shape of $dN_{\rm netB}/dy$ is obtained by scaling the parametrization by various factors for the different collision energies. It is clear that the $dN_{\rm netB}/dy$ shape is more sensitive to the $y_{\rm B}$ parameter than σ_2 [46]. Both parametrizations fit well the shape of the data at 2.65 and 4.31 GeV. At $\sqrt{s_{\rm NN}} = 17.3$ GeV, however, the new parametrization peaks at a higher rapidity than the data, which is consistent with its overestimate of the individual $y_{\rm B}$ fit value as shown in Fig. A.3. At 62.4 GeV the new parametrization has relatively lower peak dN/dy values than the data, which is consistent with its underestimate of the corresponding individual $y_{\rm B}$ fit value [46].

Figure A.5 shows the energy dependence of the hadron $dm_{\rm T}/dy(0)$ parametrization in comparison with that of the $dm_{\rm T}/dy(0)$ for initial partons. The two parametrizations are quite close when the collision energy is between $3 < \sqrt{s_{\rm NN}} < 100$ GeV, which includes the energy range of the Beam Energy Scan program at RHIC [35, 36, 37, 38]. Notice the fast increase of the hadron $dm_{\rm T}/dy(0)$ when the collision energy decreases towards the threshold energy E_0. This is a combined effect of the vanishing beam rapidity near the threshold energy and the finite conserved net-baryon number [45]. It is also clear that at very low energies the net-baryon contribution (dot-dashed curve), coming mostly from the incoming nucleons, dominates the total transverse energy of final hadrons. The PHENIX Collaboration's $dE_{\rm T}/dy$ parametrization is also shown for comparison.

Appendix B: Probability Density Functions with Maxwell-Boltzmann Statistics

B.1 Transverse Momentum Distribution $f_{p_{\mathrm{T}}}(p_{\mathrm{T}})$

Several probability density functions that are useful for calculating thermal averages of interest to this research are derived in this section. These results rely on the assumption that the system under consideration has particle energies that follow the Maxwell-Boltzmann statistics ($K = 0$ in Eq. (3.3)). For identical particles with chemical potential μ at a temperature T, the distribution of energies under Maxwell-Boltzmann statistics is given by:

$$f_p(p) = C\left[\exp\left(\frac{\sqrt{p^2+m^2}-\mu}{T}\right)\right]^{-1}. \tag{B.10}$$

Note that the subscript in the above definition is used to distinguish the probability density functions of the momentum p, the transverse momentum p_{T} or the longitudinal momentum p_z from that of the Mandelstam variable s that is discussed in Sec. B.3. In order for the $f_p(p)$ above to be a probability density function, it must satisfy the normalization condition: $\int d^3p f_p(p) = 1$, where the integration is carried out over the entire three-dimensional momentum phase-space. Thus, the three-dimensional integral of $f_p(p)$ reduces to the following single integral over p, where the factor 4π originates from the integration over the two angles in spherical coordinates:

$$\int d^3p f_p(p) = 4\pi C \int_0^\infty dp p^2 \exp\left[\frac{-\left(\sqrt{p^2+m^2}-\mu\right)}{T}\right]. \tag{B.11}$$

The chemical potential is a constant with respect to p, and it is now written in terms of a fugacity $\lambda = \exp(\mu/T)$. Then, one may use the substitution $p = m\sinh(y)$ to obtain the well-known result [114, 115]:

$$\int d^3p f_p(p) = 4\pi C m^2 T \lambda K_2\left(\frac{m}{T}\right). \tag{B.12}$$

The normalization condition of $f_p(p)$ allows one to calculate the constant C in the above equation.

The probability density function for the transverse momentum $f_{p_\mathrm{T}}(p_\mathrm{T})$ is obtained from the normalized $f_p(p)$. Whereas the result of Eq. (B.12) utilized the spherical polar coordinates (p, θ, ϕ), this step will use the cylindrical coordinates of $(p_\mathrm{T}, p_z, \phi)$. Note that the polar angle is θ, and ϕ is the azimuthal angle. Then one may use the substitution $p_z = E_\mathrm{T}\sinh(y)$, where $E_\mathrm{T} = \sqrt{p_\mathrm{T}^2 + m^2}$ is the transverse mass, to obtain

$$f_{p_\mathrm{T}}(p_\mathrm{T}) = \frac{1}{m^2 T K_2\left(m/T\right)} p_\mathrm{T}\sqrt{p_\mathrm{T}^2 + m^2} K_1\left(\frac{\sqrt{p_\mathrm{T}^2 + m^2}}{T}\right) \tag{B.13}$$

The leading term of the function $K_2(m/T)$ is $2T^2/m^2$ as $m \to 0$, so the result in the massless limit becomes

$$f_{p_\mathrm{T}}(p_\mathrm{T}) = \frac{1}{2T^3} p_\mathrm{T}^2 K_1\left(\frac{p_\mathrm{T}}{T}\right). \tag{B.14}$$

The mean values of the transverse momentum $\langle p_\mathrm{T}\rangle$ and of the square of the transverse momentum $\langle p_\mathrm{T}^2\rangle$ are useful quantities for understanding the overall spread, or variance, of $f_{p_\mathrm{T}}(p_\mathrm{T})$. The variance is defined [69] as $\mathrm{var}(p_\mathrm{T}) = \langle p_\mathrm{T}^2\rangle - \langle p_\mathrm{T}\rangle^2$. The mean transverse momentum is given by

$$\langle p_\mathrm{T}\rangle = \frac{1}{4\pi m^2 T \lambda K_2(m/T)} \int d^3p f_p(p) p_\mathrm{T}.$$

Then, using a hyperbolic function, $p = m\,\mathrm{csch}(y)$ yields

$$\langle p_{\mathrm{T}} \rangle = \frac{\pi m^2}{4TK_2(m/T)} \int_0^\infty dy \coth(y)\mathrm{csch}^4(y) e^{-m\coth(y)/T}$$

This integral can be solved using a standard substitution $u = \coth(y)$:

$$\langle p_{\mathrm{T}} \rangle = \frac{\pi}{2m^2 K_2(m/T)} \left(3T^3 + 3mT^2 + m^2 T\right) e^{-m/T}. \tag{B.15}$$

One can easily verify that the result in the limit $m \to 0$ is the well-known $\langle p_{\mathrm{T}} \rangle = 3\pi T/4$ [50]. The result for $\langle p_{\mathrm{T}}^2 \rangle$ is determined by the substitution $p_{\mathrm{T}} = m\sinh(y)$

$$\left\langle p_{\mathrm{T}}^2 \right\rangle = \frac{2m^5}{3m^2 T K_2(m/T)} \int_0^\infty dy \cosh(y)\sinh^4(y) e^{-m\cosh(y)/T}.$$

Next, various identities for the hyperbolic functions, the integral definition of $K_n(x)$, and the recurrence relation for $K_n(x)$ are used to obtain the following closed form expression for the mean of p_{T}^2:

$$\left\langle p_{\mathrm{T}}^2 \right\rangle = \frac{1}{24m^2 T K_2(m/T)} \left[\left(48m^3T^2 + m^5\right) K_1\left(\frac{m}{T}\right) + 8\left(m^4 T + 24m^2 T^3\right) K_2\left(\frac{m}{T}\right)\right] \tag{B.16}$$

One can take the massless limit of Eq. (B.16) to find $\langle p_{\mathrm{T}}^2 \rangle = 8T^2$. Therefore, the variance of the p_{T} spectrum for massless partons whose energies follow a Maxwell-Boltzmann distribution with temperature T is given by [69]

$$\mathrm{var}(p_{\mathrm{T}}) = \left\langle p_{\mathrm{T}}^2 \right\rangle - \langle p_{\mathrm{T}} \rangle^2 = \left(8 - \frac{9\pi^2}{16}\right) T^2. \tag{B.17}$$

B.2 Longitudinal Momentum Distribution $f_{p_z}(p_z)$

The probability density function for the longitudinal momentum $f_{p_z}(p_z)$ may be obtained from $f_p(p)$. Here, the substitution $p_{\mathrm{T}} = p_z/\sinh(\eta)$ is used and similar procedures as described in the previous section enable one to obtain

$$f_{p_z}(p_z) = \frac{1}{2m^2 T K_2\left(m/T\right)} \left(T|p_z| \sqrt{\frac{m^2}{p_z^2} + 1} + T^2 \right) \exp\left(-\frac{|p_z|}{T} \sqrt{\frac{m^2}{p_z^2} + 1} \right). \tag{B.18}$$

The above result applies to massive particles under the Maxwell-Boltzmann statistics; however, massless partons are more applicable to this research. Then, one can take the limit $m \to 0$ to find

$$f_{p_z}(p_z) = \frac{1}{4T^3} \left(T|p_z| + T^2 \right) \exp\left(-\frac{|p_z|}{T} \right). \tag{B.19}$$

Note that the above results also apply to the other components of the momentum, p_x and p_y, due to the symmetry of the three-dimensional momentum space.

B.3 Total Center-of-Mass Energy Squared Distribution $f(s)$

The thermal average of a variable w that depends on the two-parton momentum phase-space is defined to be the following:

$$\langle w \rangle = \frac{\int d^3p_a d^3p_b f_p(p_a) f_p(p_b) w}{\int d^3p_a d^3p_b f_p(p_a) f_p(p_b)}. \tag{B.20}$$

The denominator ensures the correctness even if $f_p(p)$ is not normalized. Next, two different thermal averages are calculated, and a probability density function $f(s)$ is found for each case.

B.3.1 Thermal Average $\langle\sigma\rangle$

In this first case, the thermal average of the cross section $\langle\sigma\rangle$ can be calculated according to

$$\langle\sigma\rangle \propto \int d^3p_a d^3p_b f_p(p_a) f_p(p_b) \sigma(s), \tag{B.21}$$

where it is assumed that the cross section only depends on s. This six-dimensional integral over the two-parton momentum phase-space is difficult in general; fortunately, the task is simplified by applying symmetry arguments. First, one is always free to rotate the coordinate system so that the momentum of the first parton p_a lies along the positive z axis. Therefore, the three-momentum of particle a has spherical symmetry, and the three integrals over d^3p_a reduce to a single integral over dp_a. With the first particle along the positive p_z axis, one is still free to rotate the coordinate system so that the momentum of the second particle p_b has a component along only one of the p_x or p_y directions. Thus, the three-momentum of particle b has azimuthal symmetry, and the three integrals over d^3p_b reduce to two integrals over dp_b and $d\theta$. Here, the angle between the two partons' three-momenta is written as θ.

The application of the above symmetry arguments reduce the volume element

$$d^3p_a d^3p_b = 4\pi p_a^2 dp_a \; 2\pi p_b^2 dp_b \; d\cos(\theta). \tag{B.22}$$

Next, a change of variables [114] is used to express the magnitudes of the two partons' momenta and the angle between them in terms of the Mandelstam s and two other variables. Recall that for massless partons, $s = (p_a^\mu + p_b^\mu)^2 = 2p_a p_b\,(1 - \cos(\theta))$ because s is a Lorentz invariant quantity, depending on the two partons' four-momenta. This relationship between s and $\cos(\theta)$ motivates the choice to change variables from $(p_a, p_b, \cos(\theta))$ to (p_+, p_-, s) in the following way:

$$p_1 = \frac{p_+ + p_-}{2}, \quad p_2 = \frac{p_+ - p_-}{2}, \quad \cos(\theta) = 1 - \frac{2s}{p_+^2 - p_-^2}. \tag{B.23}$$

The Jacobian for this transformation is $J = 1/(p_+^2 - p_-^2)$, so the volume element of Eq. (B.22) becomes

$$d^3p_a d^3p_b = \frac{\pi^2}{2}\left(p_+^2 - p_-^2\right) dp_+ dp_- ds, \tag{B.24}$$

and the integration limits change from $p_a > 0$, $p_b > 0$, $|\cos(\theta)| \leq 1$ to

$$s \geq 0, \quad p_+ \geq \sqrt{s}, \quad |p_-| \leq \sqrt{p_+^2 - s}. \tag{B.25}$$

The numerator of Eq. (B.21) changes to

$$\langle\sigma\rangle \propto \frac{\pi^2}{2}\int_0^\infty ds\ \sigma(s) \int_{\sqrt{s}}^\infty dp_+ e^{-p_+/T} \int_{-\sqrt{p_+^2-s}}^{\sqrt{p_+^2-s}} dp_- \left(p_+^2 - p_-^2\right). \tag{B.26}$$

After the first integral for p_-, we get

$$\langle\sigma\rangle \propto \frac{\pi^2}{3}\int_0^\infty ds\ \sigma(s) \int_{\sqrt{s}}^\infty dp_+ e^{-p_+/T} \sqrt{p_+^2 - s}\left(2p_+^2 - s\right). \tag{B.27}$$

For the second integral for p_+ the substitution $p_+ = \sqrt{s}\cosh(y)$ yields the following

$$\langle\sigma\rangle \propto \frac{\pi^2}{12}\int_0^\infty ds\ \sigma(s) s^2 \int_0^\infty dy \left(\cosh(4y) + 2\cosh(2y) - 3\right) e^{-\frac{\sqrt{s}}{T}\cosh(y)}. \tag{B.28}$$

One then finds

$$\langle\sigma\rangle \propto \frac{\pi^2}{12}\int_0^\infty ds\ \sigma(s) s^2 \left[K_4\left(\frac{\sqrt{s}}{T}\right) + 2K_2\left(\frac{\sqrt{s}}{T}\right) - 3K_0\left(\frac{\sqrt{s}}{T}\right)\right] \tag{B.29}$$

Finally, the recurrence relation $K_n(x)$ simplifies the above result into

$$\langle\sigma\rangle = \frac{1}{64T^5}\int_0^\infty ds\ \sigma(s) \left[s^{3/2}K_1\left(\frac{\sqrt{s}}{T}\right) + 2sTK_2\left(\frac{\sqrt{s}}{T}\right)\right] \tag{B.30}$$

One may then directly read the probability density function of s as [84]

$$f(s) = \frac{1}{64T^2}\left[\left(\frac{\sqrt{s}}{T}\right)^3 K_1\left(\frac{\sqrt{s}}{T}\right) + 2\left(\frac{\sqrt{s}}{T}\right)^2 K_2\left(\frac{\sqrt{s}}{T}\right)\right]. \tag{B.31}$$

One then gets

$$\langle s\rangle = \int_0^\infty ds\ f(s)\ s = 18T^2, \quad \langle\sqrt{s}\rangle = \int_0^\infty ds\ f(s)\ \sqrt{s} = \frac{75\pi}{64}T. \tag{B.32}$$

Note that the above results of Eqs. (B.31) - (B.32) have been compared to the corresponding results for massless partons in ZPC in Sec. 5.2 where there is an excellent agreement between the numerical results and these analytical ones.

B.3.2 Thermal Average $\langle\sigma v_{rel}\rangle$

The relative velocity between two colliding partons is given in Eq. (5.3) and has been used to study the shear viscosity of massless partons under isotropic or non-isotropic two-body scatterings in AMPT [116]. For massless partons that are often used in the ZPC parton cascade [64], the relative velocity reduces to $v_{rel} = s/(2p_a p_b) = 1 - \cos(\theta)$. The thermal average of the cross section $\langle\sigma\rangle$ was used to derive an $f(s)$ in Sec. B.3.1, but now a slightly different thermal average is used to calculate another $f(s)$. For massless partons, the thermal average of the product of the cross section and the relative velocity is given by

$$\langle\sigma v_{rel}\rangle \propto \int d^3p_a d^3p_b f_p(p_a) f_p(p_b)\sigma(s) v_{rel}(\theta). \tag{B.33}$$

The same procedure as is described in Sec. B.3.1 can be used to simplify the numerator of $\langle\sigma v_{rel}\rangle$ as

$$\langle\sigma v_{rel}\rangle \propto \pi^2 \int_0^\infty ds\ \sigma(s) s \int_{\sqrt{s}}^\infty dp_+ e^{-p_+/T} \int_{-\sqrt{p_+^2-s}}^{\sqrt{p_+^2-s}} dp_-. \tag{B.34}$$

Using $p_+ = \sqrt{s}\cosh(y)$, one obtains

$$\langle \sigma v_{rel} \rangle \propto \pi^2 \int_0^\infty ds\ \sigma(s) s^2 \int_0^\infty dy\, (\cosh(2y) - 1)\, e^{-\sqrt{s}\cosh(2y)/T}, \tag{B.35}$$

where the well known identity $\sinh^2(x) = [\cosh(2x) - 1]/2$ has been used to take advantage of the integral definition of the special functions $K_n(x)$. One then gets

$$\langle \sigma v_{rel} \rangle = \frac{1}{32T^5} \int_0^\infty ds\ \sigma(s) s^{3/2} K_1\left(\frac{\sqrt{s}}{T}\right). \tag{B.36}$$

Therefore, the probability density function of s is given in the above equation and can be written as

$$f(s) = \frac{1}{32T^2} \left(\frac{\sqrt{s}}{T}\right)^3 K_1\left(\frac{\sqrt{s}}{T}\right). \tag{B.37}$$

It is straightforward to verify that Eq. (B.37) satisfies the normalization condition. We also get

$$\langle s \rangle = \int_0^\infty ds\ f(s)\ s = 24T^2, \quad \left\langle \sqrt{s} \right\rangle = \int_0^\infty ds\ f(s)\ \sqrt{s} = \frac{45\pi}{32} T. \tag{B.38}$$

Note that the above results of Eqs. (B.37) - (B.38) are compared to the numerical results for colliding massless partons in ZPC in Sec. 5.2. An excellent agreement between the numerical results and these analytical ones suggests that the analytical probability density of s for massless colliding particles is given by Eq. (B.37). However, more work is needed to prove this fact.